Trivalent Cation Dopants and their Influence on the Inductive Effect in Lithium Iron Phosphate

A thesis submitted to the University of Kent
as part of the requirement in the subject of chemistry
for the degree of PhD

Rebekah Attard-Trevisan

School of Chemistry and Forensic Science

June 2025



To the little girl who dreamed of becoming a real scientist:

you've done it.

ACKNOWLEDGEMENTS

They say it takes a village to raise a child. Well, it takes a lot more than that to do a PhD! I am appreciative to many for their help and support throughout this journey, but first and foremost I would like to extend my gratitude to my supervisor, Dr Maria Alfredsson. You believed in me and gave me the chance to pursue this dream of mine, and for that I am forever grateful. In you I have not only found a mentor, but also a friend.

I would also like to thank the MEE Group at the University of Kent headed by my secondary supervisor, Dr Paul Saines, for giving me the opportunity to present and discuss my research in the friendliest environment. Thank you to Prof. Paul Bingham and Dr Alex Scrimshire at Sheffield Hallam University for your collaboration on Mössbauer spectroscopy, and to Dr Paul Thompson at the ESRF for being available at all times of day (and night) during each beamtime. Also, thank you to Dr Ian Johnson and Prof. Jawwad Darr at UCL for providing us with samples.

Lab 212 crew past and present: Matteo, Sally, Ryan, and Orielia (always manifesting good vibes) – I owe you guys for maintaining my sanity in the lab. To the lifelong friends I made while I was here: Amber (my G), Pat, Dan, Holly, Owen, Tom, Toby, Callum, Lewis, Giada, Anna, Kira, Nadia, and so many more – my time at Kent would not have been the same without you. To everyone at Atomki in Debrecen who always took an interest in my research – I extend my thanks to you.

I would also like to thank everyone back in Malta for their support. To my girls: Adi, Elena, Denise, Zahra, Sammut, and Bobi, you have been with me through all of my academic achievements. Thank you, ladies, for supporting me through it all even though you probably had no idea what I was going on about half the time.

The biggest thanks of all goes to my family: to my grandparents, Helen, George, Monica, and Alfred, who watches my endeavours even beyond this realm; to my mother, Edel, for I would not be half the woman I am without you, and to my father, Mario, who saw far more potential in me than I did – both of you are my lifelong cheerleaders and my unwavering pillars of support; to my brother, aunt, uncles, and blended family, you always made me smile when I was feeling homesick; to my cats, your purrs soothed me enormously; and last, but definitely not least, to my boyfriend, Duncan, who believed in me even when I did not believe in myself – thank you for holding me up when the weight of the world became too heavy.

Declaration of Authenticity

I, Rebekah Attard Trevisan, declare that this thesis entitled *Trivalent Cation Dopants and their Influence on the Inductive Effect in Lithium Iron Phosphate,* and all the research presented therein was generated by me.

I declare that I have acknowledged all contributions by others, and unless otherwise stated, all work presented is my own.

This work has not been previously submitted, in part or in whole, for any other academic degree. The copyright of this degree rests with the author.



Rebekah Attard Trevisan

17/06/2025

ABSTRACT

Lithium-ion batteries are an integral part of everyday life, being found in most portable electronics and even some larger electronic devices, such as electric bicycles. They are one of the most important tools of the revolution against fossil fuels and, therefore, a lot of research efforts are focused on improving their utility, efficiency, and general applicability.

Lithium iron phosphate (LFP) is one of the most universally employed cathode materials due to its environmental benignity, cost effectiveness, and non-toxicity. However, despite decades of research on the material, it still presents shortcomings such as low ionic and electronic conductivity, that prevent it from being implemented in large-scale grid applications.

One of the most effective methods of overcoming these limitations is cation doping. Several trivalent cations from across the periodic table (Al, Sc, V, Ho, Yb) were selected to dope LFP at different concentrations, and the physical, structural, and electrochemical effects of these materials are investigated.

In this thesis, various structural and electrochemical analyses are carried out to assess the phase purity, Li-ion diffusion, oxidation states, and local environments of the doped and undoped materials. The discharge capacity is not seen to improve with the presence of the dopants at varying concentrations; however interesting results, such as an increase in electrochemical stability for the holmium-doped LFP, are seen when compared to the undoped analogue.

The redox activity of phosphorus within the phosphate polyanion is explored in a number of samples, namely a commercial sample of LFP (Gelon LFP), in-house synthesised LFP and 1% holmium-doped LFP, and an optimised sample of 20% vanadium-doped LFP. X-ray absorption spectroscopy is performed *ex situ* on electrodes of these materials at different states-of-charge and various elemental edges are probed in order to gain insight into the redox activities of the different elements. Phosphorus is confirmed to be redox active in both the doped and undoped LFP samples, with the presence of the holmium slightly affecting the polarisation of the phosphate when compared to the undoped analogue.

TABLE OF CONTENTS

Preamble

Dedication i

Acknowledgements ii

Declaration of Authenticity iii

Abstract iv

Table of Contents v

List of Figures ix

List of Tables xv

List of Equations xvi

List of Acronyms/Abbreviations xvii

Chapter 1 – Introduction

1.1 A Brief History of Lithium-Ion Batteries 1

1.2 Cathode Materials in Use Today 5

1.2.1 *Polyanionic Cathode Materials* 10

1.3 Lithium Iron Phosphate 12

1.3.1 *Methods for Improvement of LFP* 14

1.3.2 *Doping Mechanisms* 15

1.3.3 *The Inductive Effect* 22

1.4 Overall Aims of the Project 24

Chapter 2 – Methodology

2.1 Synthetic Techniques 27

2.1.1 *Solvothermal Synthesis* 27

2.1.1.1 *Syntheses Implemented* 27

2.1.1.2 *Doped Material Syntheses* 28

2.2 Battery Assembly and Cycling 28

2.2.1 *Coin Cell Assembly* 30

2.2.2 *Pouch Cell Assembly* 30

2.2.3 *Cycling Parameters* 31

2.3 Analytical Measurements 32

2.3.1 *X-Ray Diffraction* 32

2.3.2 *X-Ray Absorption Spectroscopy* 34

2.3.3 *Scanning Electron Microscopy with Energy Dispersive X-Ray Spectroscopy* 41

2.3.4 *Mössbauer Spectroscopy* 44

2.3.5 *Galvanostatic Cycling* 49

2.3.6 *Cyclic Voltammetry* 50

2.3.7 *Electrochemical Impedance Spectroscopy* 52

Chapter 3 – Trivalent Dopants: A Systematic Study

3.1 Chapter Introduction 54

3.1.1 *Chapter Aims* 54

3.1.2 *Choice of Dopants* 54

3.2 Methodology 55

3.2.1 *All Samples* 55

3.2.2 *Structural Characterisation* 56

3.3 Structural Differences 64

3.3.1 *XRD Refinements* 64

3.4 Electrochemistry 69

3.4.1 *Galvanostatic Cycling* 69

3.4.2 *Cyclic Voltammetry* 73

3.4.3 *Electrochemical Impedance Spectroscopy* 78

3.5 Chapter Conclusions 83

Chapter 4 – V-LFP: An Investigation of Excessive Doping

4.1 Chapter Introduction 85

4.2 Methodology 87

4.3 Results 87

4.3.1 *Structural Characterisation* 87

4.3.2 *Electrochemistry* 91

4.3.3 *X-Ray Absorption Spectroscopy* 98

4.4 Chapter Conclusions 104

Chapter 5 – Ho-LFP: A Case Study

5.1 Chapter Introduction 106

5.2 Methodology 107

5.3 Results 108

5.3.1 *Structural Characterisation* 108

5.3.2 *Electrochemistry* 110

5.3.3 *X-Ray Absorption Spectroscopy* 115

5.3.4 *Mössbauer Spectroscopy* 122

5.4 Chapter Conclusions 129

Chapter 6 – Conclusions and Future Work

6.1 General Conclusions 131

6.2 Future Work 133

Final Sections

Reference List 135

Appendix 1: Additional Data Obtained from XRD, SEM, and XAS 150

Appendix 2: Microwave-Assisted Synthesis of LFP 164

LIST OF FIGURES

1.1 General schematic of the main components of a battery 1

1.2 Crystal structure of $LiCoO_2$ 6

1.3 Crystal structure of $LiMn_2O_4$ 8

1.4 Crystal structure of $LiMPO_4$ (M = Mn, Fe, Co, Ni) 9

1.5 Discharge curves of $LiMPO_4$/C (M = Mn, Fe, Co) 12

1.6 Crystal structure of LFP 13

1.7 Cyclability of (a) pristine LiFePO4/MWCNT and LiFePO4/PEDOT; (b) pristine LiFePO4 nanorods and MWCNT-coated LiFePO4 nanorods at different discharge rates from C/10 to 10C 15

1.8 (a) Rate capabilities of LiFePO4 & $LiFe_{0.97}V_{0.03}PO_4$ at various charge rates; (b) Charge/discharge curves for $LiFe_{0.97}V_{0.03}PO_4$ 18

1.9 Conductivity measurements for analogues of Mn-doped $LiFePO_4$ 19

1.10 Nyquist plots of $LiFePO_4$/C and $LiFe_{0.985}Cu_{0.015}PO_4$/C 20

1.11 Nyquist plots of $LiFePO_4$/C and Cl-doped $LiFePO_4$/C 21

1.12 Charge/discharge curves of pristine and Cl-doped $LiFePO_4$/C 21

1.13 Simplified molecular orbital diagram of FeO_6 23

1.14 Illustration of the inductive effect through the Fe–O–P linkage 23

2.1 Schematic diagram of a CR2032 coin cell 30

2.2 Schematic diagram of a pouch cell 31

2.3 Voltage *vs* time graph indicating the various SOCs of a cycle 32

2.4 Schematic representation of Bragg's Law 33

2.5 XAS spectrum with regions of interest annotated 34

2.6 Schematic depicting the fluorescence and Auger effects in XAS 36

2.7 Schematic illustrating the principle of backscattering interactions 37

2.8 Octahedral ligand field splitting of *d*-orbitals of transition metals 38

2.9 Schematic diagram of XMaS BM28 beamline at the ESRF 40

2.10 Schematic diagram of B18 beamline at DLS 40

2.11 Schematic diagram of the basic components of SEM 42

2.12 Illustration of several signals produced in SEM 43

2.13 Demonstration of recoil-free nuclear radiation 44

2.14 Illustration of the interactions that occur during ^{57}Fe Mössbauer spectroscopy 45

2.15 Correlation between coordination number of ^{57}Fe with isomer shift and quadrupole splitting 47

2.16 Schematic diagram of a ^{57}Fe Mössbauer spectrometer 48

2.17 Typical cyclic voltammogram for a reversible reaction 50

2.18 CVs for (a) reversible; (b) quasi-reversible; (c) irreversible electron transfer 51

2.19 Nyquist plot highlighting the different regions of resistance 53

2.20 Equivalent circuit model used to fit EIS spectra 53

3.1 Background-subtracted PXRD patterns of 1% Ho-LFP, 1% Yb-LFP, and undoped LFP 57

3.2 PXRD patterns of 1%, 3%, and 5% Al-doped LFP 57

3.3 (a) Peak at ~ 35.7 °2θ of Al-doped LFP XRD; (b), (c) in literature 58

3.4 PXRD patterns of 1%, 3%, and 5% Sc-doped LFP 59

3.5 SEM-EDX mapping of carbon-coated undoped LFP 60

3.6 SEM-EDX mapping of (a) Ho-LFP; (b) Yb-LFP; (c) V-LFP 61

3.7 SEM-EDX maps and spectra of 1%, 3%, and 5% Al-LFP 62

3.8 SEM-EDX maps and spectra of 1%, 3%, and 5% Sc-LFP 63

3.9 Rietveld refinement of undoped LFP against ICSD-92198 64

3.10 (a) % Estimated lattice strain for each sample; (b) Estimated lattice strain for Al- and Sc-doped samples across the <1 1 0> plane 66

3.11 Average crystal domain size calculated for each sample 69

3.12 Charge-discharge curves after 1 and 5 cycles for LFP & Gelon LFP 70

3.13 Charge-discharge curves after 1 and 5 cycles for (a) Al-LFP; (b) Sc-LFP 71

3.14 Charge-discharge curves after 1 and 5 cycles for V-LFP, Ho-LFP, and Yb-LFP 72

3.15 Cyclic voltammograms after 1 and 5 cycles for (a) undoped LFP; (b) Ho-LFP; (c) Yb-LFP 74

3.16 Cyclic voltammograms for (a) Al-LFP after 1 cycle; (b) Al-LFP after 5 cycles 76

3.17 Cyclic voltammograms for (a) Sc-LFP after 1 cycle; (b) Sc-LFP after 5 cycles 77

3.18 EIS and their fits after 1 and 5 cycles for (a) undoped LFP; (b) Ho-LFP 79

3.19 EIS and their fits after 1 and 5 cycles for Yb-LFP 80

3.20 EIS and their fits for Al-LFP (a) after 1 cycle; (b) after 5 cycles 81

3.21 EIS and their fits for Sc-LFP (a) after 1 cycle; (b) after 5 cycles 82

4.1 Crystal structure of LFP illustrating different V occupation sites 85

4.2 XRD patterns of Gelon LFP and V-LFP 89

4.3 (a) XRD patterns of Gelon and V-LFP illustrating the peak at ~45 °2θ; (b)~45 °2θ in literature 89

4.4 Linear combination fitting results of V-LFP 90

4.5 (a) Discharge capacity and (b) coulombic efficiency *vs* cycle number

for Gelon LFP and V-LFP at C/2 and C/10 92

4.6 Galvanostatic cycling curves comparing the first and fifth cycles of Gelon LFP and V-LFP 93

4.7 EIS plots and fits to equivalent circuit after 1 and 5 cycles for (a) V-LFP and (b) Gelon LFP 94

4.8 CV curves for V-LFP and Gelon LFP after the first and fifth cycles 97

4.9 (a) Fe K-edge; (b) P K-edge; (c) V K-edge XANES spectra of Gelon LFP and V-LFP at different SOCs 100

4.10 Energy distribution plot of correlation between P & Fe K-edges 101

4.11 Average Fe-O bond distances correlated with Fe K-edge energy 102

4.12 Correlation plot of Fe–O and V–O bond distances 103

5.1 XRD patterns of 1%, 3%, and 5% Ho-doped LFP 108

5.2 (a) SEM-EDX of Ho-LFP; (b) EDX spectrum of Ho-LFP 110

5.3 Galvanostatic cycling curves for LFP, 1%, 3%, and 5% Ho-LFP 111

5.4 (a) Coulombic efficiency and (b) discharge capacity *vs* cycle number graph for LFP and 1% Ho-LFP at C/5 112

5.5 CV curves of undoped LFP and 1% Ho-LFP after 1 and 5 cycles 113

5.6 (a) EIS plots of undoped LFP after 1 and 5 cycles; (b) EIS plots of 1% Ho-LFP after 1 and 5 cycles 114

5.7 Fe K-edge XANES spectra at different SOCs for Ho-LFP and LFP 115

5.8 P K-edge XANES at different SOCs for (a) Ho-LFP during the first cycle; (b) Ho-LFP and LFP during the fifth cycle 117

5.9 Energy distribution plot of correlation between P & Fe K-edges 118

5.10 Ho L_{III}-edge XANES spectra at different SOCs for Ho-LFP 119

5.11 Correlation plot of Fe–O and Ho–O bond distances 121

5.12 Crystal structure of LFP illustrating the M1 and M2 sites 122

5.13 Mössbauer spectra for LFP and Ho-LFP at OCV 123

5.14 Mössbauer spectra for LFP and Ho-LFP at SOC5 124

5.15 Mössbauer spectra for LFP and Ho-LFP at SOC3 125

5.16 Mössbauer spectra for LFP and Ho-LFP at SOC10 126

5.17 Correlation between isomer shift, quadrupole splitting, and coordination number for LFP and Ho-LFP at different SOCs 128

A-1.1 Rietveld refinement of Gelon LFP against ICSD-92198 153

A-1.2 Rietveld refinement of 1% Ho-LFP against ICSD-92198 153

A-1.3 Rietveld refinement of 1% Yb-LFP against ICSD-92198 154

A-1.4 Rietveld refinement of 20% V-LFP against ICSD-92198 154

A-1.5 Rietveld refinement of 1% Al-LFP against ICSD-92198 155

A-1.6 Rietveld refinement of 3% Al-LFP against ICSD-92198 155

A-1.7 Rietveld refinement of 5% Al-LFP against ICSD-92198 156

A-1.8 Rietveld refinement of 1% Sc-LFP against ICSD-92198 156

A-1.9 Rietveld refinement of 3% Sc-LFP against ICSD-92198 157

A-1.10 Rietveld refinement of 5% Sc-LFP against ICSD-92198 157

A-1.11 SEM images of undoped, V-, Ho-, and Yb-doped LFP 158

A-1.12 SEM images of 1%, 3%, and 5% Al-LFP 159

A-1.13 SEM images of 1%, 3%, and 5% Sc-LFP 159

A-1.14 (a) XAS setup of BM28 at XMaS; (b) Detector measuring XAS; (c) *Ex situ* cathodes on sample holder 161

A-1.15 Graph of Debye-Waller factor *vs* SOC *vs* Fe–O bond distances 161

A-1.16 First derivative plots of the P K-edge XANES of (a) Ho-LFP during the first cycle; (b) Ho-LFP and LFP during the fifth cycle 163

A-2.1 Samples A-F after being dried overnight 164

A-2.2 Galvanostatic cycling curves of samples A – F as cathodes 165

A-2.3 XRD patterns for samples A – F compares with reference 166

A-2.4 SEM-EDX imaging of samples A – F 167

LIST OF TABLES

1.1 List of metals and their electrode potentials 3

1.2 Comparison of ionic radii of the chosen dopant ions 24

1.3 List of samples and their respective compositions 26

2.1 List of electrolytes used throughout this thesis 29

3.1 Lattice parameters of all samples 65

3.2 Discharge capacities of all samples 69

3.3 Li-ion diffusion coefficients of all samples 73

3.4 Solution and charge-transfer resistances of all samples 78

4.1 Sample parameters of Gelon LFP and V-LFP 88

4.2 Solution and charge-transfer resistances of Gelon LFP and V-LFP 95

4.3 Li-ion diffusion coefficients of Gelon LFP and V-LFP 96

5.1 Sample parameters of undoped LFP and Ho-LFP 109

5.2 Fe-O bond lengths obtained from EXAFS analysis 120

5.3 Mössbauer parameters for LFP and Ho-LFP at different SOCs 127

A-1.1 List of arbitrary % strain and particle size for all samples 151

A-1.2 Ho–O bond lengths obtained from EXAFS analysis 162

A1.3 V–O bond lengths obtained from EXAFS analysis 162

LIST OF EQUATIONS

1.1 Manganese disproportionation reaction 8

1.2 Lithium deintercalation equation 11

2.1 Bragg's Law 33

2.2 Beer-Lambert Law 35

2.3 Difference in energy between the emitted γ-ray and the nuclear transition energy in Mössbauer spectroscopy 45

2.4 Theoretical capacity calculation 49

2.5 Coulombic efficiency calculation 49

2.6 Nernst equation 50

2.7 Randles-Ševčik equation 52

3.1 Debye-Scherrer equation 67

4.1 Correlation factor calculation between Fe–O and V–O 103

5.1 Correlation factor calculation between Fe–O and Ho–O 121

LIST OF ACRONYMS/ABBREVIATIONS

LIB	Lithium-Ion Battery
NMC	Lithium Nickel Manganese Cobalt Oxide
LFP	Lithium Iron Phosphate
CV	Cyclic Voltammetry
EIS	Electrochemical Impedance Spectroscopy
PVDF	Polyvinylidene Fluoride
NMP	N-methyl-2-pyrrolidone
EC : DEC	Ethylene Carbonate : Diethyl Carbonate
EC : DMC	Ethylene Carbonate : Dimethyl Carbonate
EC : EMC	Ethylene Carbonate : Ethyl Methyl Carbonate
LiTFSI	Lithium Bis(trifluoromethanesulfonyl) imide
SOC	State-Of-Charge
SEI	Solid-Electrolyte Interphase
CEI	Cathode-Electrolyte Interphase
XRD	X-Ray Diffraction
PXRD	Powder X-Ray Diffraction
XAS	X-Ray Absorption Spectroscopy
XANES	X-Ray Absorption Near-Edge Spectroscopy
EXAFS	Extended X-Ray Fine Edge Structure
LCF	Linear Combination Fit

1. Introduction

1.1. A Brief History of Lithium-Ion Batteries

Batteries have now been a staple of our lives for several decades. They are used to power most things, from small everyday items, such as wristwatches, remote controls, and smartphones, to much larger and more energy-consuming objects including scooters and cars. With the world moving towards more renewable sources of energy, advances and developments in battery technology have spurred reasonable momentum in modern-day research.

The inner workings of a battery, or galvanostatic cell, are fairly straightforward. It is composed of two electrodes – the cathode (positive) and anode (negative) – and an ionic component is transported from one electrode to the other via an electrolyte, which in turn forces the electronic component (the electrons) to pass through an external circuit (**Figure 1.1**). In rechargeable batteries, the ionic and electronic components of the circuit work in a reversible manner, acting also as an electrochemical cell.

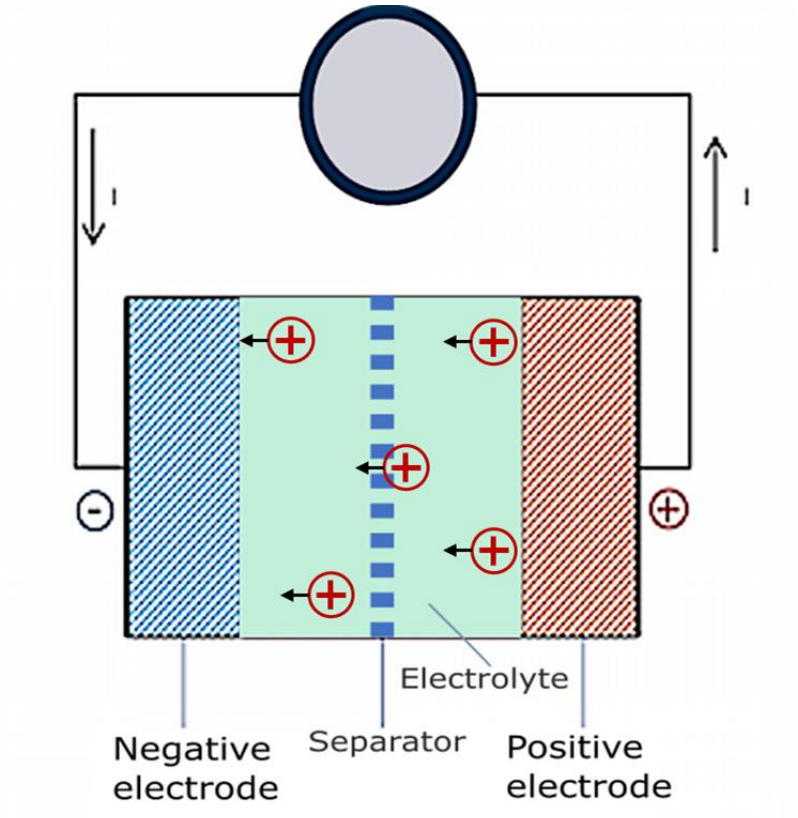

Figure 1.1: General schematic of the main components of a battery.

In a LIB, lithium ions are deintercalated from the cathode and move towards the anode, usually graphite, where they are stored in its' layered structure during charging, and then released back into the cathode upon discharging. This movement of the lithium ions releases electrons at the anode and creates a charge at the positive current collector, causing a current to flow through the device being powered back to the negative current collector.

The creation of the galvanostatic cell is universally attributed to Alessandro Volta and his work in the late 18th century, with an honourable mention of Luigi Galvani. The two would later become synonymous with electronic terms still used until this day, with Volta's name being associated with the unit of voltage, Volt (V), and Galvani's name being used in relation to galvanic processes. Galvani recognised that frogs' legs twitched when charged with an electric spark, thus inciting his interest in bioelectricity and postulating that animals could create electricity, whereas Volta was responsible for the creation of the "voltaic pile," a series of alternating series of zinc and silver discs separated by a rag soaked in silver chloride solution, which he stated created electricity. Volta recognised the critical role of the electrode and electrolyte interphases. The two idealogies both support the hypothesis of energy storage.[1]

In the mid-19th century, more advances were made by French engineer Georges-Lionel Leclanché, who created the concept of carbon-zinc and alkaline cells, and French scientist Gaston Plantè who developed the first lead-acid rechargeable battery. In the early 20th century, another milestone in battery technology was achieved by Swedish engineer Waldmar Jungner who discovered the rechargeable nickel-cadmium battery. Although this technology has nowadays advanced, the underlying principles are still in use in modern-day batteries.[2]

Another important discovery was made in the early 20th century: the potential use of lithium as an electrode by Gilbert Lewis and Frederick Keyes. Their experiments demonstrated that lithium had a higher electrode oxidation potential when compared to sodium and potassium, when compared to the conventional calomel electrode therefore earning the title of "best possible electrode material." This was also evident when measured against the standard hydrogen electrode (**Table 1.1**).[3,4]

Table 1.1: List of metals and their electrode potentials against the standard hydrogen electrode.[4]

Metal	Oxidation potential *vs.* standard hydrogen electrode (V)
Li	3.04
Na	2.71
K	2.93

The need for more portable, longer lasting, less toxic, and cheaper batteries prompted the research and development of lithium-ion batteries. The move from zinc- to lithium-based batteries came with a drastic increase in energy density. Lithium-iodine batteries provided an energy density five times that of zinc-mercury oxide batteries. This revolutionised pacemaker technology, providing users with a non-toxic and more durable device which increased its longevity by almost four times – from two to seven years.[5]

The success of the lithium-iodine battery made way for a new generation of battery, which could meet the requirements of various applications and moving towards a more renewable source of energy. The work of Whittingham, who would later go on to share the Nobel Prize in Chemistry, introduced the concept of intercalation electrodes.[6] He was one of the first to make the correlation between cell reversibility and de/intercalation processes throughout charge cycles, and went on to state that stability of cathode materials depends on the ability of the material to maintain unbroken chemical bonds, which in turn, makes for a reversible reaction.[7]

These materials could easily accept and release lithium ions from their structure thus prolonging the cycle life of the battery. The early work by Whittingham and co-workers used aqueous electrolytes and lithium metal anodes. His work made use of chalcogenide-containing compounds, like Li_xTiS_2, as the framework material for the cathode, which could be easily lithiated and delithiated due to its layered structure and high conductivity.[8] The issues later encountered with such materials were mainly due to the reactivity of the lithium metal anode with the liquid electrolyte, which led to the formation of a solid electrolyte

interphase (SEI) that inhibited the activity of the battery and led to shorts and dendrite formation, occasionally also causing fires.[2,7] These components had to be replaced in order to preserve the battery's safety for consumer use.

In the late 1970s, Murphy and Carides reported the use of non-aqueous components in their batteries, employing Li_2VX_2 (X = S, Se) materials as cathodes, but still implementing lithium metal as the anode.[9] The concept of *lithium rocking chair batteries* had been introduced in the 1980s, where a "lithium sink" material was proposed to act as an anode and a "lithium source" lattice structure material to act as a cathode.[10] Around the same time, Armand worked on the development of polymer electrolyes.[11] These electrolytes replaced the need for aqueous electrolytes, which increased the stability of batteries and decreased the number of side reactions which interfered with the cycling mechanism of the battery.[11,12] It was not until the early 1990s when Japanese manufacturer Sony demonstrated the commercial viability of the *lithium rocking chair battery*, a battery comprised of graphite as an anode and lithium cobalt oxide as a cathode, which eliminated the need for lithium metal anodes.[13,14]

Less than a decade after Whittingham's discovery of intercalation processes as ideal electrode functions, Mizushima, Goodenough and co-workers discovered that transition metal oxides are preferable to sulphides due to their stability at high oxidation states and provision of higher potentials (>4.0 V *vs* Li/Li^+). This led to layered structural oxide materials as cathodes with higher energy density and cell voltage, with the general formula $LiMO_2$ (M = V, Cr, Co, Ni). LiCoO2 had the highest potential (4.7 V *vs* Li/Li^+) thus making it an interesting candidate for further studies.[15] This research spurred a plethora of interest in similar materials, which would revolutionise LIB (Li-ion battery) technology: Thackeray, Goodenough and colleagues put forward spinel-type Mn oxides as cathode materials; Ohzuku and collaborators proposed Ni, Mn, Co oxides; and Padhi, Goodenough *et al.* discovered that olivine-type iron phosphates would make for suitable cathode materials.[16–18]

Materials with improved prospects are still being investigated and developed nowadays to ensure the LIB remains at the forefront of commercial technology. There are many challenges which researchers face, involving more than just the cathode material, such as alternative anode materials, and even aqueous and solid-state electrolytes. All of this exploration is set to transform the conventional battery as we know it, and so, the future of battery technology is a full, exciting and ever-growing one.[19–21]

In 2019, Goodenough, Whittingham and Yoshino were awarded the Nobel Prize in Chemistry for their development in LIBs. Their early work revolutionised the commercial Li-ion battery, since lithium-based cathodes could store up to 10 times more energy than lead-acid batteries, and 5 times as much as nickel-cadmium ones.[22] Lithium releases electrons easily and is also small in size, thus facilitating lithiation and delithiation of polyanionic cathodes and pushing the working voltage of the battery up to ~3.4 V. Implementing a carbon-based electrode to replace lithium metal made Li-ion batteries attractive rechargeable materials for consumer electronics.[23]

1.2. Cathode Materials in Use Today

Novel cathode materials are continuously being discovered which, as well as having improved electrochemical properties, seek to be environmentally sustainable. Recent efforts are being made to decrease the use of toxic materials, such as cobalt and nickel, while still improving the operating voltage window, charge/discharge rate, and specific capacities. The expansion of our understanding of lithium-ion batteries is owed to the intensive research over the last five decades, with the discovery of novel materials and improvement of existing battery technologies playing a crucial role in the advancement of this field.[24] One of the challenges with Li-ion batteries lies within the realm of the cathodes, which limit the energy density of the overall battery.

There are three main oxide families of cathode material commercially used and researched today: layered oxides, spinels, and polyanion-based compounds.[24] All three offer reversibility, facile Li-ion intercalation, and high specific discharge capacity, which make them ideal candidates as battery cathode materials.

One of the layered oxides used commercially is $LiCoO_2$ (**Figure 1.2**), with the Li^+ and Co^{3+} ions in alternate <1 1 1> planes representing the rock salt structure.[25] The large cation size and charge difference between the lithium and cobalt offers good cation ordering, which is critical to the Li-ion diffusion pathway and conductivity.[26] The electronic conductivity of this material is increased further upon charging, where $Li_{1-x}CoO_2$ transforms from insulating to metallic due to the introduction of electron holes into the low-spin $Co^{3+/4+}$ t_{2g}^{6-x} band.[27]

This cathode material was the first one used commercially, and is still widely used nowadays in portable electronics since it has good structural stability and increased electrical conductivity, which in turn offers fast charge-discharge capability with good reversibility. It also has a high operating voltage of ≥4.2 V.[28,29] However, there is a drawback when it comes to the discharge capacity of $LiCoO_2$ being only around 140 mAh g^{-1},[27] which is a major weakness when compared to later generation cathode materials.

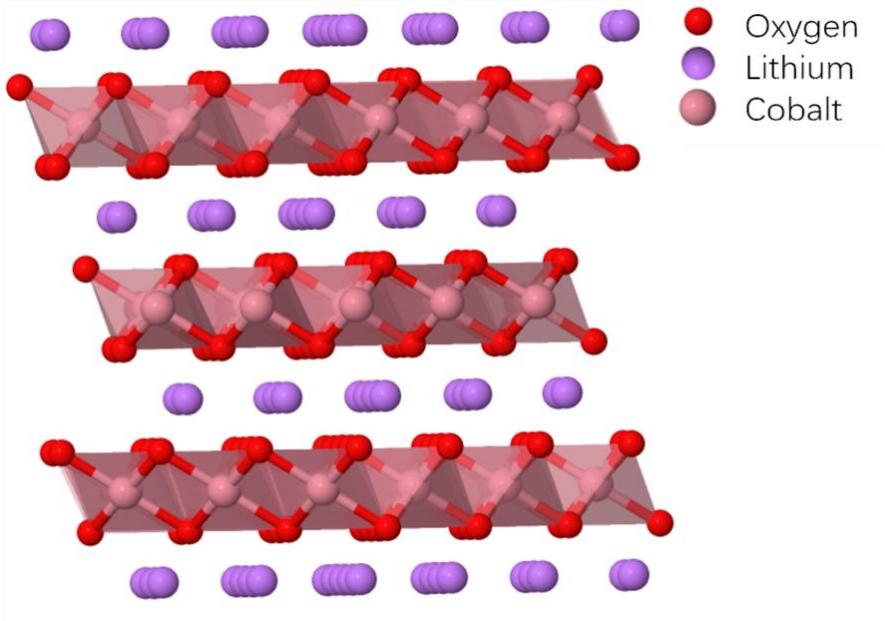

Figure 1.2 Crystal structure of $LiCoO_2$.[30]

Due to this low capacity, it was necessary to research alternate layered oxide materials. This led to the substitution of cobalt with nickel and manganese to give $LiNi_{1-x-y}Mn_xCo_yO_2$, more commonly known as NMC.[31] NMC has gained particular interest over the last decade by the automotive industry as an alternative cathode material for batteries in electrical vehicles.[32]

The two properties leading to the improved battery performance of NMC are chemical and structural stability. The chemical instability suffered by cobalt in $LiCoO_2$ are caused by oxygen release. The origin of this oxygen volatility can be explained by its electronic band structure, where the O 2*p* states lie above the Co 3*d* states.[33] In contrast, the $Mn^{3+/4+}$ band lies above that of the O 2*p* states, ergo oxygen release from the lattice is avoided upon incorporation of manganese into the material.[34] Anti-site migration of nickel from octahedral sites in the transition metal

plane to octahedral sites in the Li-ion plane occurs due to a small destabilisation energy of the manganese in the octahedral site, resulting in a phase transition.[35] This leads to voltage decay as the battery is cycled. This structural instability suffered by manganese is mitigated by the presence of cobalt, which has a large octahedral site energy, suppressing cation migration.[36] Since cobalt becomes metallic and manganese remains semiconducting, incorporating both cations in the cathode material offers improved capacity. Decreasing the amount of cobalt and replacing it with manganese also decreases the environmental impact since manganese is abundant and environmentally non-toxic.[37]

Nickel lies neatly between manganese and cobalt in terms of chemical properties. The $Ni^{3+/2+}$ and the $Ni^{4+/3+}$ bands align with the top of the O 2*sp* band, eliminating the need for a voltage step from one redox couple to the other.[34] This means that the Ni^{3+} can be oxidised fully to Ni^{4+} without a decrease in electron density from the oxygen band, and without removal of oxygen. The Ni^{3+} octahedral site stabilisation energy also lies between Mn^{3+} and Co^{3+}, therefore contributing to good structural stability of NMC as a cathode material. The current effort with regards to NMC is to increase the nickel content whilst decreasing the cobalt content in order to increase the capacity of the material and lowering the cost.[38,39]

The most common cathode material from the spinel oxide family is $LiMn_2O_4$ (**Figure 1.3**), where $Mn^{3+/4+}$ ions occupy octahedral sites and Li^+ ions occupy tetrahedral sites. The edge-shared octahedra offer a three-dimensional Li-ion diffusion pathway, contributing to fast Li-ion conductivity.[40] The 3D structural stability along with high electrical and Li-ion conductivity support faster charge-discharge properties for $LiMn_2O_4$ with good reversibility when compared to $LiCoO_2$.[41]

The Li-ion extraction/insertion mechanism offers a working voltage of 4 V with a practical capacity of <130 mAh g^{-1} with approximately 1 lithium ion per 2 manganese ions reversibly extracted per tetrahedral site in the material.[40] In $Li/Li_xMn_2O_4$, when $0 \leq x \leq 1$, the cells discharge at 4 V. This decreases to 3 V when the lithium content is increased to $1 < x \leq 2$. The cubic symmetry of the $Li_xMn_2O_4$ spinel structure is maintained at higher voltages, whereby the electrode expands and contracts isotropically as Li^+ is (de-)intercalated with cycling.[42]

When lithium is inserted into $Li_xMn_2O_4$ at 3 V, a Jahn-Teller distortion effect is triggered, where a cubic to tetragonal phase transition occurs. Despite the

structural stability of the electrode at higher voltages, a slow capacity fade has occurred in the high-voltage range due to a disproportionation reaction of the manganese cation (**Equation 1.1**), whereby the production of Mn^{2+} leads to the dissolution of the electrode into the electrolyte.[42]

$$2Mn^{3+} \rightarrow Mn^{4+} + Mn^{2+} \qquad [\mathbf{1.1}]$$

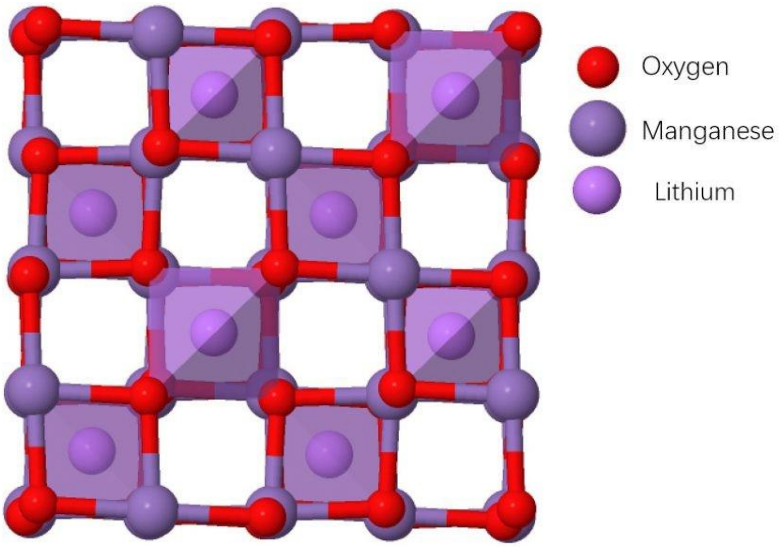

Figure 1.3: Crystal structure of $LiMn_2O_4$.[43]

Advantages of the $LiMn_2O_4$ spinel-type cathodes when compared to layered $LiCoO_2$ cathode materials are the environmental aspect and cost-effectiveness. Manganese is approximately two orders of magnitude less expensive than cobalt, however it tends to be leached from the lattice into the electrolyte upon the presence of acid due to disproportionation of Mn^{3+} to Mn^{4+} and Mn^{2+} (**Equation 1.1**), which makes longevity of the cells an issue because of cathode degradation.[44]

The third example of oxide cathode materials are polyanion oxides. They have become increasingly prevalent because of the stability of the structure and environmental sustainability. In polyanionic cathode materials of the type $Fe_2(XO_4)_3$ (X = Mo, W, and S), the FeO_6 octahedra share their vertices with the XO_4 tetrahedra, which provides an extended three-dimensional –O–Fe–O–X–O– linkage, contributing to their structural stability.[45]

The working voltage in polyanion cathode materials can be raised to as high as approximately 5 V in phosphate materials of the type $LiMPO_4$ (M = Mn, Fe, Co, Ni; **Figure 1.4**) utilising higher energy redox couples, such as $Co^{2+/3+}$ and $Ni^{2+/3+}$. Since the polyanion is fixed in these materials, the redox potential shifts are linked to changes in the M^{2+} cations. The shifts in redox potentials can be described by the changes in M–O covalency, also known as the inductive effect. These changes in covalency are due to the electronegativity of M or the M–O bond lengths as well as –O–M–O–P–O– interactions which are altered when Li^+ is extracted from and inserted into the crystal lattice as the battery is cycled.[45]

The versatility and diversity with polyanions increase when compared to the layered and spinel oxide cathode families. This is evident not only for Li-ion batteries, but also for Na-ion batteries, with materials, such as $Li_3V_2(PO_4)_3$, $Na_3V_2(PO_4)_3$, $Na_3V_2(PO_4)_2F_3$, and $NaFePO_4$ rising in popularity and expanding in implementation on the market.[45–48]

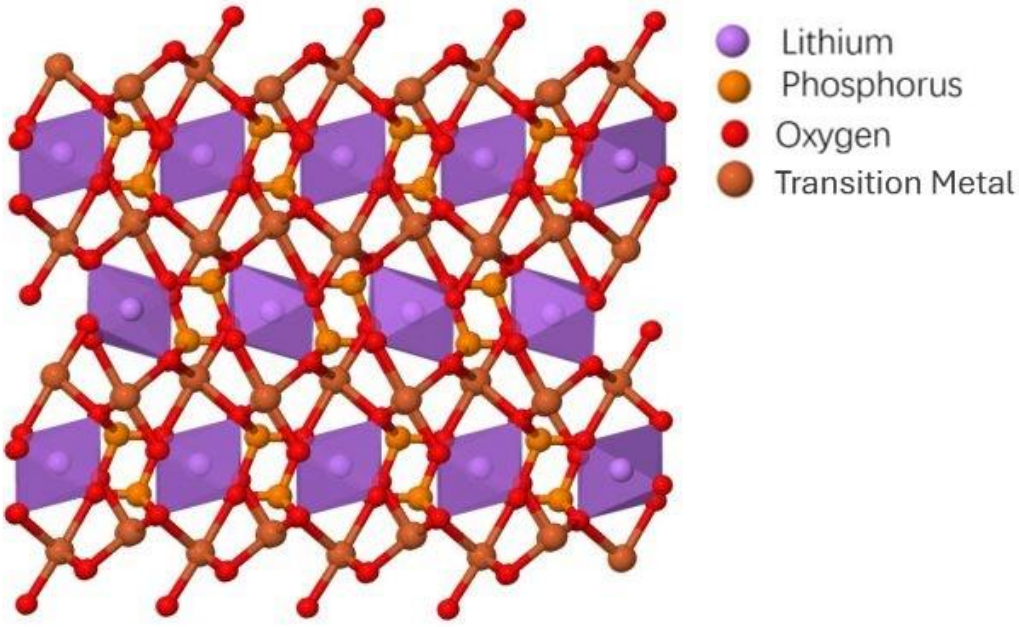

Figure 1.4 Crystal structure of $LiMPO_4$ (M = Mn, Fe, Co, Ni).[49]

There are numerous advantages and disadvantages for all three families of oxides, but perhaps the most important characteristics to consider when assessing their suitability as a potential cathode material are their structural and thermal stability. Whilst layered and spinel oxides offer increased electronic conductivity; the converse is noted in polyanion oxides. This, in turn, increases the manufacturing

costs of polyanion oxide materials since nanosizing and carbon coating steps are required in order to combat this issue. On the other hand, the thermal stability of these materials is remarkable when compared to the layered and spinel oxides, which makes the additional manufacturing cost worthwhile due to the improved safety of the overall batteries when on the market.[50,51] This thesis concentrates on polyanionic phosphate compounds and a more detailed introduction will be given in the following section.

1.2.1. Polyanionic Cathode Materials

There are several compounds that can be classed as polyanionic cathode materials, all having the same structure: tetrahedral polyanionic units of the formula XO_4^{n-} (X = P, S, As, Mo, or W), covalently bonded to MO_6 (M = TM) polyhedra. The strong covalent bonding in the structure makes them better-suited for large-scale Li-ion battery applications since they are safer.[52]

As the strong covalently-bonded oxygen within the polyanion also suppresses oxygen release from the lattice upon charging at higher temperatures, they are favoured over the layered and spinel oxide materials which tend to release oxygen from the lattice upon charging at higher temperatures resulting in chemical instability of the highly oxidised transition metal species.[24]

In the 1950s triphylite, $LiFePO_4$, and lithiophilite, $LiMnPO_4$, were discovered where the Li orthophosphates of Fe^{2+} and Mn^{2+} formed an isomorphous solid solution series with olivine, $(Mg,Fe)_2SiO_4$. NMR was later conducted and the behaviour of the second-nearest-neighbour shifts in a few iron-group phosphates as a function of temperature on a series of mineral specimens of lithiophilite was reported. $LiMPO_4$ (M = Mn, Fe, Co) compounds were proposed to undergo antiferromagnetic or ferromagnetic transitions above helium temperatures. In the 1960s, research efforts were directed to the anisotropy in magnetic properties and electronic structures of $LiFePO_4$ (LFP).[53,54]

In the early 1970s, the world was hit by the petroleum crisis, which sparked an interest in energy storage technologies. The lithium-ion battery was one of the technologies researched and is still extensively studied today, having come a long way since the innovation of the lithium-iodine battery, using Whittingham's design of layered structures and the Li_x–TiS_2 series becoming the preferred material due to

the intercalation mechanism of the lithium ion as the battery is cycled (**Equation 1.2**), which provided minimal crystal distortion and thus being highly reversible.[6]

$$\mathrm{Li} \rightleftharpoons \mathrm{Li}^{+} + e^{-} \qquad [\mathbf{1.2}]$$

Goodenough and colleagues postulated that transition-metal oxides would make better candidates than sulphides as cathode materials, due to their better stability and higher operating voltages (>4 V *vs* Li/Li^+). In the 1980s, a solution to overcome oxides with low working voltages was proposed by Manthiram and Goodenough in the form of polyanion oxide materials.[55,56] They postulated that using oxides containing polyanions such as XO_4^{2-} (X= S, Mo, W) would keep the cost low and overcome the low working voltage issue since Li-ion insertion could still occur within these materials. In a simple oxide such as Fe_2O_3, the $Fe^{2+/3+}$ redox couple would normally operate at <2.5 V *vs* Li/Li^+, however upon the introduction of a polyanion, in a material such as $Fe_2(SO_4)_3$, this is raised to 3.6 V *vs* Li/Li^+.[55]

The next step in this discovery was to incorporate lithium into a material to make it a viable option as a cathode *versus* a carbon anode in a lithium-ion cell. The identification of phospho-olivines of the general formula $LiMPO_4$ (M = Mn, Fe, Co, Ni) as lithium extraction/insertion hosts by Padhi *et al.* was revolutionary, with $LiFePO_4$ being the most extensively studied analogue due to the low cost and environmental benignity of iron.[18,57,58]

The redox potential increases from 3.45 V in $LiFePO_4$ to 4.1 V in $LiMnPO_4$, 4.8 V in $LiCoPO_4$, and 5.1 V in $LiNiPO_4$ due to the changes in the positions of the transition metal redox couples. The original assumption has been that the PO_4^{3-} polyanion is the same for all analogues, i.e. the P–O bond electronegativity is unchanged in the different compounds, so the transition metal cation is the driving force behind the discrepancies in redox energies. The redox energies of the $M^{2+/3+}$ couples tend to increase across the periodic table due to the increase in effective nuclear charge.[59]

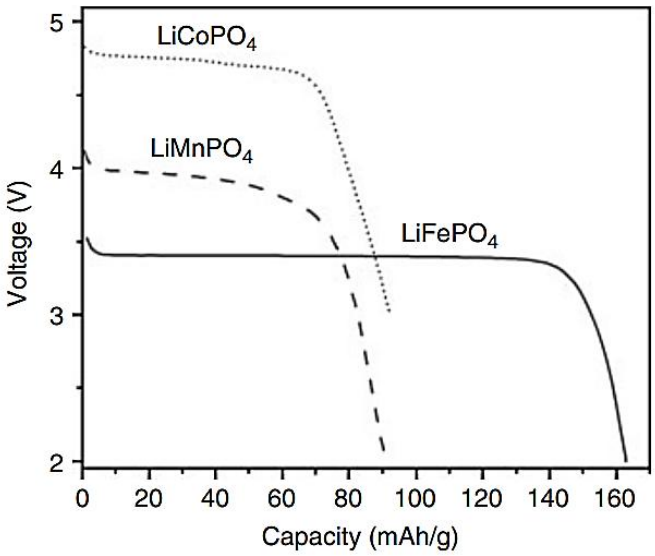

Figure 1.5 Discharge curves of $LiMPO_4$/C (M = Mn, Fe, Co) nanocomposites.[45]

Despite the lowest redox potential amongst the above compounds, $LiFePO_4$ still remains the most attractive material in terms of discharge capacity (**Figure 1.5**), as the internal conductivity of the material is higher than in other $LiMPO_4$ (M = Mn, Co, Ni) analogues. For instance $LiMnPO_4$ contains manganese, which is environmentally friendly and has a favourable $Mn^{2+/3+}$ redox couple at 4.1 V but contributes low practical capacity even at low currents, since it has an electronic conductivity of ~10^{-14} S cm^{-1} and a wide bandgap of ~2 eV in contrast to ~10^{-9} S cm^{-1} and ~0.3 eV, respectively, for $LiFePO_4$.[45]

1.3. Lithium Iron Phosphate

$LiFePO_4$ (LFP, **Figure 1.6**) is the most extensively researched phospho-olivine polyanion oxide as a cathode material. This is due to its environmental benignity, high theoretical capacity of 170 mAh g^{-1}, cost effectiveness, and high thermal stability. LFP has an orthorhombic crystal structure composed of a polyoxyanionic framework, which contains LiO_6 octahedra, and FeO_6 octahedra that share their vertices with PO_4 tetrahedra. This allows for a one-dimensional pathway, created by the edge-shared LiO_6 octahedra across the *b*-axis through which the lithium ions can diffuse.[58,60]

As discussed previously, the strong P–O covalency within the PO_4^{3-} polyanion stabilises the oxygen through the P–O–Fe bridge upon charging, which prevents

oxygen to be discharged from the lattice. This property is what makes this material safer and more stable than the aforementioned simple layered and spinel oxides.[45]

Although LFP is the more attractive candidate for use in cathodes, it has a disadvantage compared to the layered and spinel oxides: low electronic conductivity of 10^{-9} S cm^{-1}, which is considerably less when compared to $LiCoO_2$ and $LiMn_2O_4$. The latter oxides have an electronic conductivity of 10^{-3} S cm^{-1} and $2\times10^{-5} - 5\times10^{-5}$ S cm^{-1}, respectively. The low electronic conductivity of LFP results from the lack of mixed valency between $LiFePO_4$ and $FePO_4$ and the highly localised $Fe^{2+/3+}$ ions linked to the corner-shared FeO_6 octahedra within the crystal lattice. It also suffers from low ionic conductivity due to the arrangement of ions within the crystal lattice, which only allows for a one-dimensional diffusion pathway along edge-shared LiO_6 octahedra.[61] Ionic and electronic conductivity play a crucial role in the Li-ion diffusion mechanism throughout the electrode. Due to these shortcomings, researchers have been concentrating their efforts on improving LFP for larger grid applications.[59]

Another phenomenon that affects the ionic conductivity of LFP is the presence of antisites. The most common type of antisite is the Fe_{Li} antisites (Fe atoms occupying Li-site, and vice versa), which tend to block Li-ion diffusion along the < 0 1 0 > pathway, thus decreasing the ionic conductivity of the material. The synthetic route, synthesis temperature, and reaction time all affect the formation of antisites within LFP.[62,63]

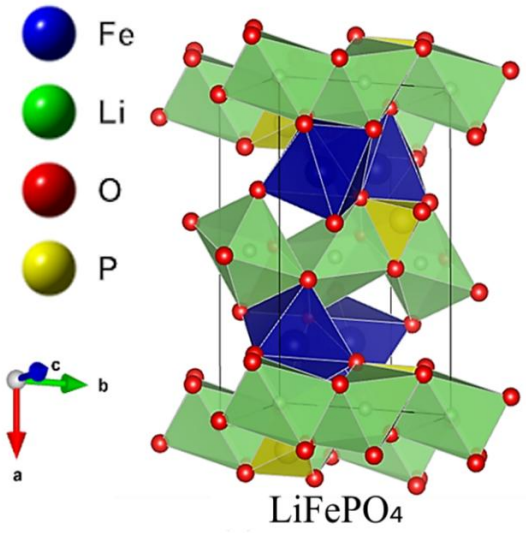

Figure 1.6 Crystal structure of $LiFePO_4$ (LFP); olivine-type structure, orthorhombic space group Pnma.[64]

1.3.1. Methods for Improvement of LFP

Multiple methods have been applied to improve the ionic and electronic conductivity of LFP, including decreasing the particle size in order to decrease the ion and electron diffusion pathway, surface coating with carbon or carbon-containing polymers, and cation doping in Li-, Fe-, and P-sites within the crystal lattice to further increase the electronic conductivity of the material.[65,66]

Initial findings by Padhi and Goodenough in 1997 reported a two-phase reaction mechanism occurring between $LiFePO_4$ and $FePO_4$. However, subsequent studies have shown that the miscibility gap between these phases has been reported to decrease at elevated temperatures, and a single-phase solid solution of Li_xFePO_4 ($0 \leq x \leq 1$) has been described at temperatures above 450 °C. [58,67]

Similarly, a single-phase reaction mechanism has been demonstrated for particles <40 nm. This observation is attractive as the single-phase reaction is reported at room temperature, allowing for the co-existence of $LiFePO_4$ and $FePO_4$. This reaction mechanism was initially reported as two-phase for larger particle sizes, therefore research pertaining to nanoparticle synthesis of LFP became more important.[61]

Multiple studies have been conducted demonstrating that reducing the particle size in LFP decreases the Li-ion diffusion pathway, improving Li-ion diffusion kinetics at room temperature. Despite this, simply nanosizing the particles does not solve the electronic conductivity issue, with reports of pristine LFP nanoparticles still suffering from poor electronic conductivity when implemented in cells.[61,66]

Instead, combining nanosizing LFP with carbon or a conductive polymer coating of the particles improves both the ionic and electronic conductivity. Multi-walled carbon nanotubes (MWCNT), poly(3,4-ethylenedioxythiophene) (PEDOT), and carbon black (CB) have all been used to coat the particles, with promising results observed in terms of long-term cyclability and discharge capacities when compared to the pristine, uncoated LFP (**Figure 1.7**).[45,61]

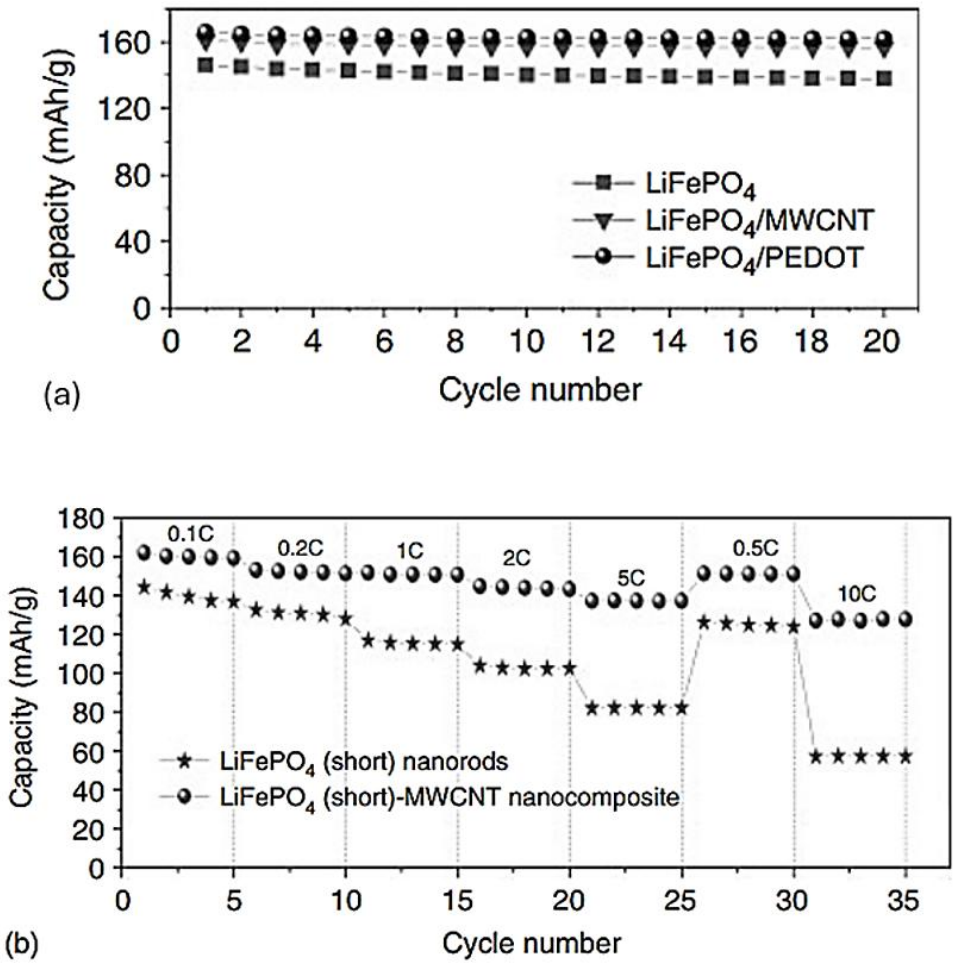

Figure 1.7 (a) Cyclability of pristine $LiFePO_4$, $LiFePO_4$/MWCNT, and $LiFePO_4$/PEDOT; (b) Cyclability of the pristine $LiFePO_4$ nanorods and MWCNT-coated $LiFePO_4$ nanorods at different discharge rates from C/10 to 10C.[45]

Another method that has been explored to overcome the shortcomings of pristine LFP is doping. Doping strategies with various types of dopants have been implemented which have been able to improve the rate performance of LFP due to improvements in both ionic and electronic conductivity of the material.

1.3.2. Doping Mechanisms

The presence of a dopant can create Li-ion diffusion channels or lattice defects, which aid the ionic conductivity of LFP.[68,69] Doping, in turn, enhances the electrochemical performance of the material as it may result in an n- or p-doped material. An important factor to consider is whether the doping is occurring at the surface or in the bulk of the LFP. Bulk doping denotes doping the entire substrate to

stabilise the phase structure as the battery is cycled. Electrochemically inactive species are normally used for this purpose, so as not to interfere with the main redox mechanism which drives the battery. On the other hand, surface doping refers to coating the substrate in dopant ranging from several to tens of nanometres and encasing it in the dopant material. It improves the bulk integrity and structural stability of the material by inhibiting surface reconstruction and adverse surface behaviours.[68]

Bulk doping has been studied extensively since minimal quantity of dopant being present in the crystal lattice of LFP has been known to create new channels to promote and enhance Li-ion diffusion as a battery is cycled.[70,71] This increases the overall Li-ion diffusion of LFP and has been shown to increase discharge capacities, as well as improving the rate capabilities and capacity retention.

It is important to consider the doping sites in the crystal lattice when making a choice of dopant. The ionic radius and formal charge of the dopant will influence the doping site, for example if the ionic radius of the dopant is similar to that of Fe^{2+}, it will likely occupy a Fe-site. Doping with ionic species includes a charge compensating mechanism, for example substituting Fe^{2+} with V^{3+} will result in either a Li^{+} deficiency or O^{2-} vacancies in the lattice structure.

The most common mechanism by which dopants improve the electrochemical performance of LFP is through the creation of Li-ion vacancies in the crystal lattice, facilitating Li-ion diffusion. The enhanced ionic conductivity of the material also results in higher rate capability.[69]

There are three main doping mechanisms through which ion doping can transpire: substitutional doping, interstitial doping, and co-doping. Substitutional doping occurs when a dopant ion directly replaces Li, Fe, P, or O in LFP; interstitial doping is when a dopant ion occupies an interstitial site in the LFP crystal lattice; and co-doping occurs when multiple dopants are introduced in LFP in order to achieve synergistic effects.[72,73]

Doping can occur on any of the cation sites: Li, P, or Fe, and, less commonly, even on the O-site. Li-site doping has shown improvement in the material, wherever high-valent metals with a small ionic radius (e.g. Nb^{5+}, Al^{3+}, Ti^{4+}, K^{+}, Na^{+}) have been used as dopants due to the increase in electron hole mobility in LFP, which changes the material from n-type semiconductor to p-type semiconductor, thus improving conductivity.[74]

The general mechanism in play for improvement of ionic conductivity in LFP through Li-site doping is associated with the shortening of the *b*-axis, which decreases the Li-ion diffusion pathway, therefore facilitating Li-ion mobility and improving ionic conductivity and electrochemical performance of the material.[75,76]

Boron has successfully been doped in the P-site of LFP by Li *et al.*, with the optimal ratio reported to be $LiFeP_{0.98}B_{0.02}O_{4-\delta}/C$. It has been reported that B doping in the P-site of LFP decreases the charge-transfer resistance, improving the mobility of lithium ions. Excessive doping, however, could lead to oxygen defects in the crystal lattice of LFP, which decreases the Li-ion diffusion by immobilising lithium ions upon charging and discharging.[77] Molybdenum has also been used to dope at the P-site of LFP, but with rather negative results. Whilst the measured electronic conductivity of $LiFeP_{0.88}Mo_{0.10}O_4$ was found to be at least two orders of magnitude better than the undoped analogue, the authors reported that the electrochemical performance was considerably worse than nanosized LFP.[78]

The most common site to dope in LFP is the Fe-site. The presence of the dopant in the Fe-site weakens the Li-O bond and increases the Li-ion mobility and, therefore, ionic diffusion of the material. Doping at the Fe-site may introduce a slight lattice distortion, which could reduce the surface energy and obstruct particle growth therefore controlling the particle size and shape, which may improve the electrochemical properties of LFP.[79,80]

Studies involving Fe-site doping in LFP with other transition metals such as V, Mn, Cu, and Zn, amongst many others, show that doping with ≤15% of dopant concentration improves the electrochemical performance of LFP considerably.[81–85] The discharge capacity of $LiFe_{0.97}V_{0.03}PO_4$ is 162.9 mAh g^{-1} at 0.1 C, better than that of the undoped material at 155.2 mAh g^{-1} (**Figure 1.8**), whilst also demonstrating a capacity retention of 96% after 200 cycles.[81]

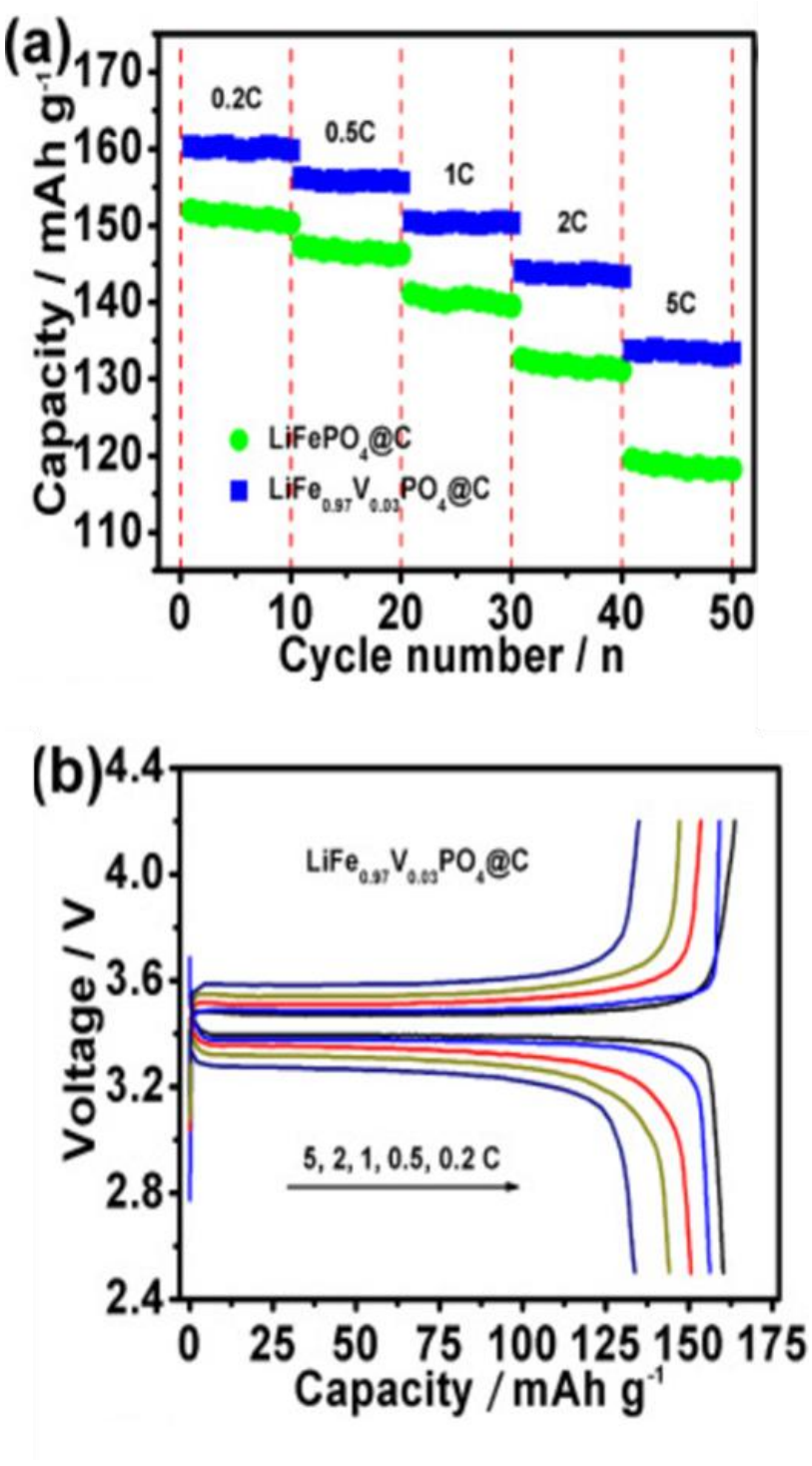

Figure 1.8 (a) Rate capabilities of $LiFePO_4$ & $LiFe_{0.97}V_{0.03}PO_4$ at various charge rates; (b) Charge/discharge curves for $LiFe_{0.97}V_{0.03}PO_4$ at various charge rates.[81]

Gupta *et al.* found that manganese-doped LFP improved the rate capability of the material, however at concentrations higher than 15% the performance of LFP suffered and ionic conductivity decreased (**Figure 1.9**). The presence of Mn in Fe-sites promotes better Li-ion diffusion across the lattice, however above a certain

level of doping, this is restricted, and the charge-transfer process is limited due to the crystal lattice being overly distorted. The excessive doping hinders the Li-ion diffusion by interfering with and distorting the Li-ion diffusion pathway.[85]

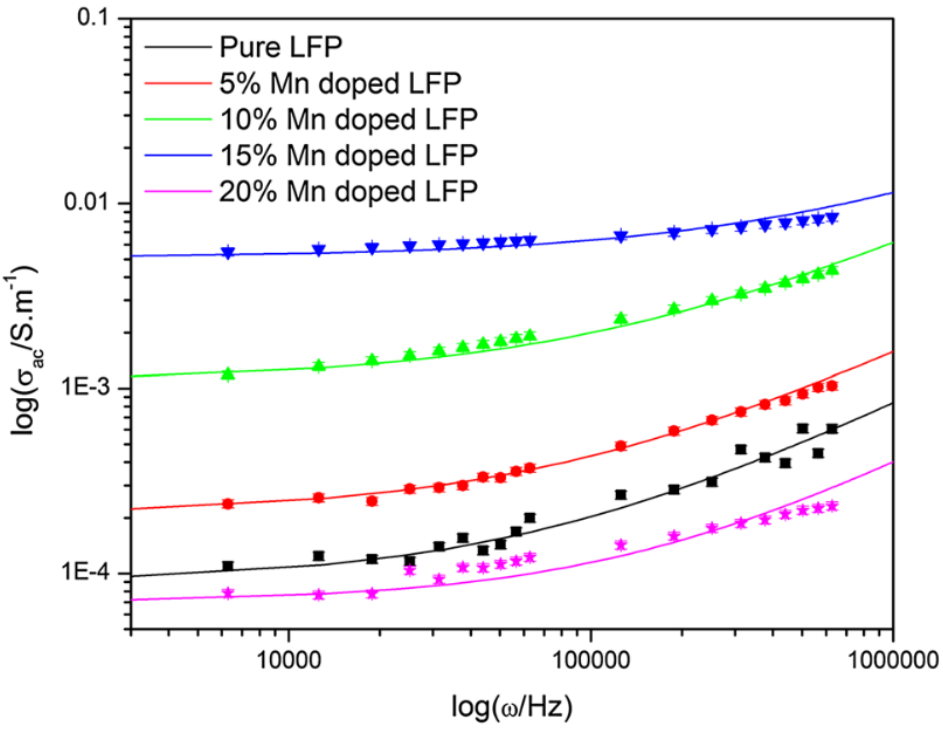

Figure 1.9 Conductivity measurements at RT for all analogues of Mn-doped $LiFePO_4$.[85]

Copper was also found to be a good dopant for LFP since its presence can increase the interplanar spacing in the crystal parallel to the <0 1 0> direction. This, in turn, widens the Li-ion diffusion channels and improves the ionic diffusion of the material. Electrochemical impedance spectroscopy (EIS) measurements showed a marked decrease in internal resistance of Cu-doped LFP when compared to the undoped LFP (**Figure 1.10**). The presence of copper in quantities as low as 1.5% can improve the electrochemical performance of LFP by enhancing the electronic conductivity.[86]

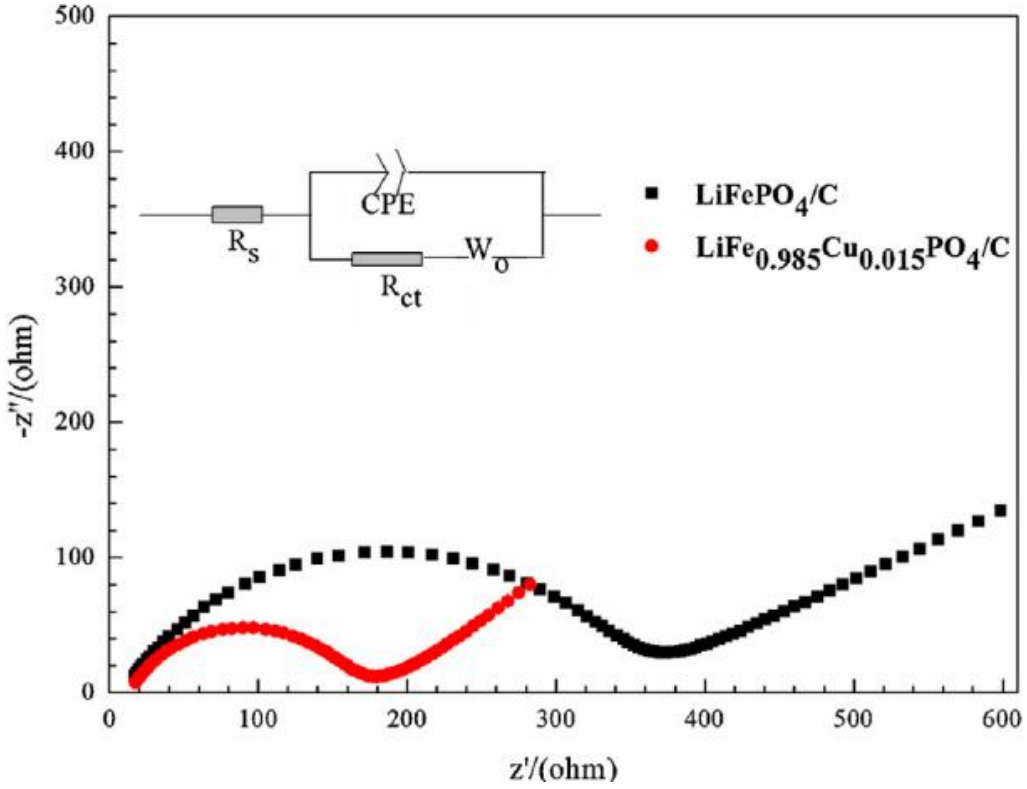

Figure 1.10 Nyquist plots of $LiFePO_4/C$ and $LiFe_{0.985}Cu_{0.015}PO_4/C$ demonstrating the decreased resistance in the Cu-doped LFP.[86]

Non-metallic doping of LFP has also been an avenue that has been explored, with dopants such as some of the halogens, nitrogen, and sulphur. Such dopants often stabilise the internal structure of LFP, which improves its electrochemical performance in terms of cycle and rate capabilities.[87–91]

Liu *et al*. investigated Cl-doping of LFP and reported that it improves the microstructure of LFP, increasing its structural stability, ionic, and electrical conductivity. They performed EIS and found that both the charge-transfer resistance (R_{ct}) and Warburg impedance (Z_W) of the Cl-doped material were decreased when compared to the undoped LFP (**Figure 1.11**), indicating that the presence of Cl improves the diffusion kinetics of the material.[89] These findings were further supported by Sun *et al*., who reported an improved discharge capacity of the Cl-doped LFP when compared to the undoped material at a C-rate of 0.1 C (**Figure 1.12**).[90]

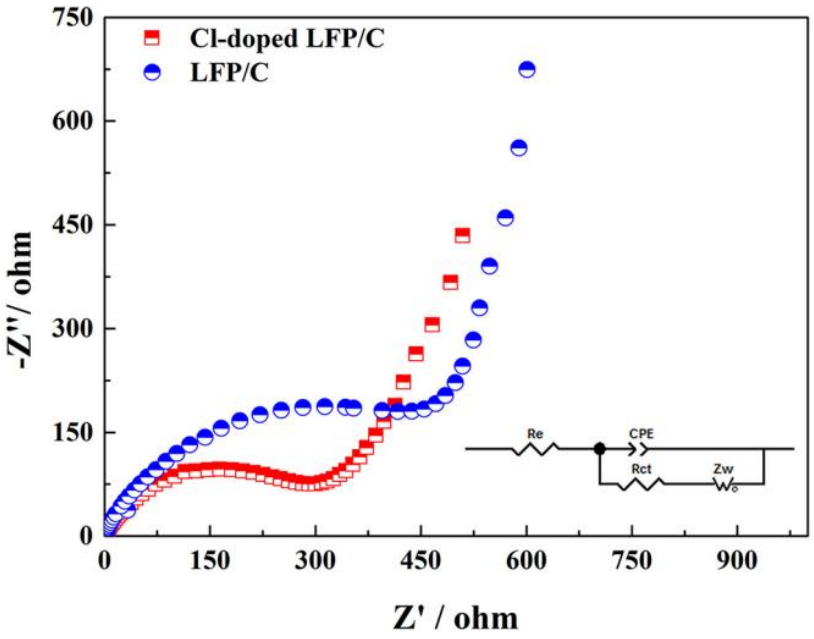

Figure 1.11 Nyquist plots of $LiFePO_4$/C and Cl-doped $LiFePO_4$/C.[89]

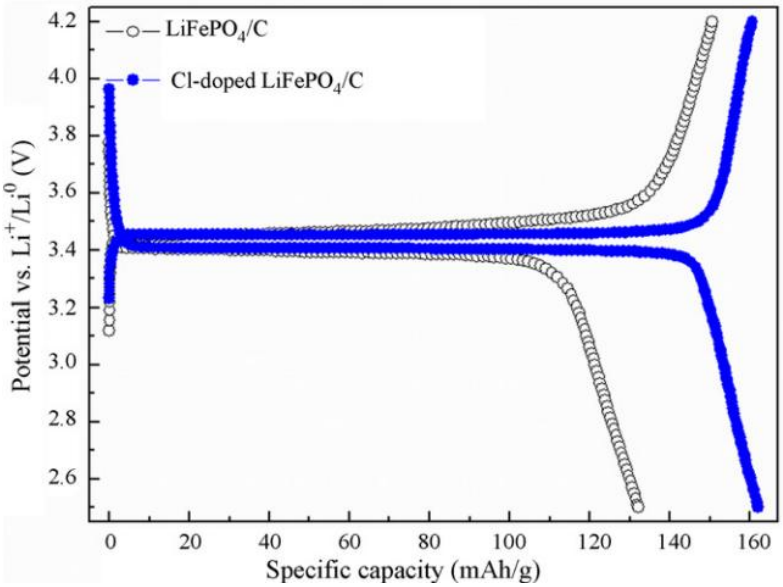

Figure 1.12 Charge/discharge curves of pristine and Cl-doped $LiFePO_4$/C cathodes at 0.1 C.[90]

F-doping of LFP was investigated by Jugović *et al.* and was found to enhance the electrical conductivity from 4.6×10^{-7} S cm^{-1} to 2.3×10^{-6} S cm^{-1}. A small amount of F-doping also reduces both the lattice parameters and the number of antisite defects, allowing for facilitated Li-ion diffusion, thus improving electrochemical performance.[91]

Doping as a method for improvement of ionic and electronic conductivity of LFP has been extensively studied and, coupled with carbon-coating it, is still viewed as one of the most viable options for its improved performance. Doping with minimal amounts can improve the electronic conductivity and Li-ion diffusion rates of the material. The presence of the dopant in LFP may also stabilise the crystal structure and improve its rate capability. All of this combined, therefore, enhances the electrochemical performance of LFP and makes it a better candidate as a cathode material on a larger scale.

1.3.3. The Inductive Effect

Polyanionic cathode materials are of interest in the LIB world due to the fact that they tend to exhibit higher operating voltages for similar redox couples when compared to simple oxides. The reason behind this phenomenon is the inductive effect brought on by the presence of the polyanion.[92,93]

The electronegative phosphorus attracts electrons from the oxygen through the P–O–Fe linkage in the LFP lattice, which in turn weakens the Fe–O bond covalency. As the Fe–O bond covalency is weakened, the P–O covalency increases and stabilises the antibonding Fe^{2+}/Fe^{3+} state, increasing the operating voltage for the redox couple.[92] The presence of the phosphate group boosts the voltage of the transition metal redox couple when compared to its other polyanionic compounds, with an operating voltage of 2.8 V in Li_2FeSiO_4 *versus* 3.0 V in $LiFeBO_3$ *versus* 3.4 V in $LiFePO_4$.[94,95]

The FeO_6 octahedron possesses mixed ionic-covalent character due to the hybridisation of the Fe 3*d* and O 2*p* atomic orbitals.[96] In a simplified model, the minority spin electron of a high-spin octahedral Fe^{2+} $t_{2g}^4e_g^2$ configuration occupies an antibonding t_{2g} orbital that mixes with O $2p_\pi$ orbitals (**Figure 1.13**). This covalent mixing within the FeO_6 complex of LFP results in a quantum mechanical repulsion between the bonding and antibonding orbitals which increases the energy of the t_{2g} orbital, and consequently also raises the energy of the Fe^{2+}/Fe^{3+} redox couple.[97]

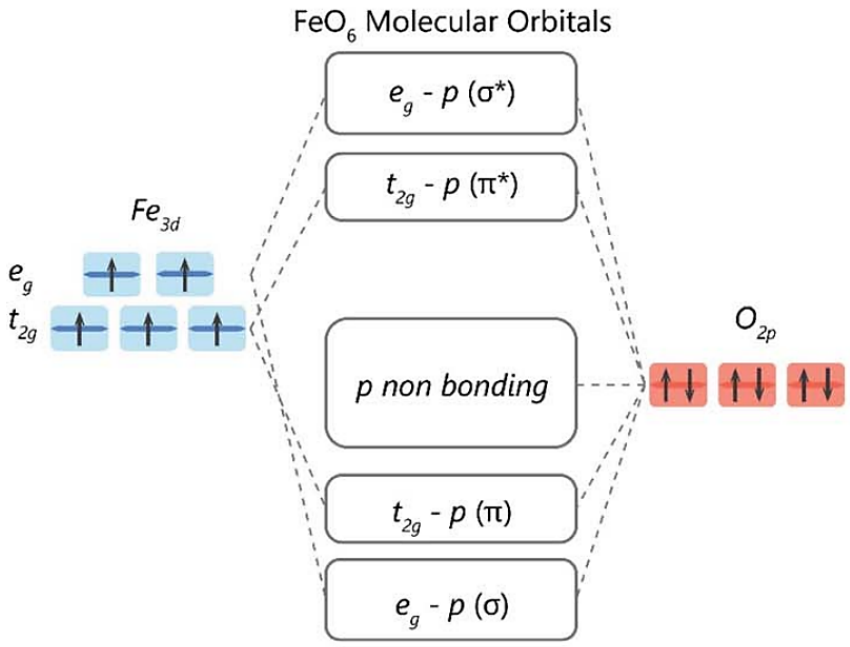

Figure 1.13: Simplified molecular orbital diagram of FeO_6 depicting the different bonding and antibonding states and hybridisation of the Fe 3d and O 2p atomic orbitals.[96]

The countercation, P, shares a common O with Fe in a Fe–O–P linkage and controls the strength of the Fe–O covalency through the inductive effect, thus the stronger the P–O bonding, the weaker the Fe–O bonding.[97] When LFP is delithiated, the P–O bond becomes polarised due to the overlap of the O 2*p* with the Fe 3*d* orbitals increasing, resulting in the spin states having a high degree of covalency (**Figure 1.14**). In LFP however, there is less covalent character and the Fe 3*d* states form narrow bands above the O 2*p* states with minimal orbital mixing. The P–O bonds form states below the main O 2*p* bands.[98]

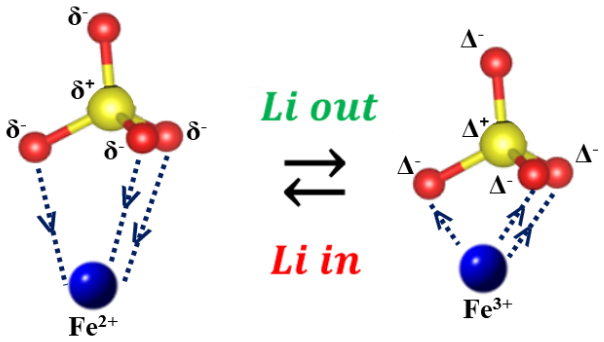

Figure 1.14: Illustration of the inductive effect through the Fe–O–P linkage in LFP as the battery is cycled.

The inductive effect has spurred further interest in the application of polyanionic materials in LIB technology. In particular, this interest is driven by the fact that the working voltages of Mn^{2+}/Mn^{3+}, V^{3+}/V^{4+}, and Fe^{2+}/Fe^{3+} which are too low to be commercially viable as simple oxides, can be raised to >3 V as phosphates. LFP was chosen as the focus of the thesis in order to see how different trivalent dopant concentrations will affect the polarisation of the P–O–Fe linkage.

1.4. Overall Aims of the Project

This thesis aims to investigate the effects of trivalent doping on LFP, particularly whether the presence of the dopant improves the electrochemical properties of the material, and also whether the inductive effect of the polyanion is enhanced as a result of the dopant's presence within the crystal lattice.

To understand how Fe-site cation doping affects structural as well as electrochemical properties of LFP, a series of trivalent dopants from across the periodic table have been researched. The dopants were purposely chosen to give an insight into the different ionic sizes and properties of elements from across the periodic table, ranging from main group elements and transition metals to lanthanides, and to facilitate doping preferentially at the Fe-site in LFP.

The ionic radii of the chosen dopants (**Table 1.2**) vary considerably, with the smallest ion being Al^{3+} with an ionic radius of 0.535 Å, and the largest ion being Ho^{3+} at 0.901 Å. The ionic radius of Sc^{3+} is the closest to that of Fe^{2+} and Li^{+}, whilst V^{3+} has an ionic radius similar to Fe^{3+}.

Table 1.2 Comparison of ionic radii of the chosen dopant ions and $Fe^{2+/3+}$.[99]

Element	Ionic Radius (Å)
Li^{+}	0.760
Fe^{2+}	0.780 (high-spin)
Fe^{3+}	0.645 (high-spin)
Al^{3+}	0.535
Sc^{3+}	0.745
V^{3+}	0.640
Ho^{3+}	0.901

Yb^{3+}	0.868

The inductive effect in the phosphate polyanion of LFP has been of interest since the strong P–O covalency in the polyanion stabilises the structure during Li-ion diffusion. The Fermi level of the $Fe^{2+/3+}$ redox couple is decreased through the Fe–O–P bridge, which results in a discharge voltage of ~3.45 V *vs* Li/Li^{+}.[100] This project has two aims: to understand the function of the PO_4^{3-} polyanion during battery cycling by following the electrochemical redox activity at the P-site of LFP; and to establish if structural properties and ionic mobility can be linked to the structural and electronic properties of PO_4^{3-} ion.

This intends to be done through probing the P K-edge of various analogues of LFP by using X-Ray Absorption Spectroscopy (XAS). The X-Ray Absorption Near Edge Spectroscopy (XANES) portion of the P K-edge should give information, such as local structure and oxidation state. Coupled with the electrochemical measurements, information on the activity of the phosphate polyanion can be obtained. By monitoring the specific correlations between the phosphorus' redox activity and its electrochemical properties, the presence of the PO_4^{3-} inductive effect can be elucidated as the battery is cycled.

Along with the crystallographic and electrochemical analyses done on the materials, further insights are to be gathered through P, Fe, and V K-edge, and Ho L_{III}-edge XAS and Mössbauer spectroscopy, which aim to give a better understanding of the materials and their function at different states-of-charge of the battery. This will help with the comprehension of LFP and its doped analogues when implemented as a cathode in batteries. The comparison of dopants from across the periodic table will help bridge gaps in the research, aiding the understanding of doping mechanisms and quantities and their effects on LFP, both as a material and as a cathode.

The premise of **Chapter 3** is to give an overview of the dopants and elicit comparisons between the effects of different stoichiometric doping levels of aluminium and scandium, particularly, with emphasis on the electrochemistry, whilst in **Chapter 4** the effect of a high concentration of vanadium doping is explored more extensively with more element-specific techniques such as XAS. In **Chapter 5** holmium doping of LFP is investigated since it is not as broadly investigated as a dopant, with further analysis of the materials implemented such as XAS and Mössbauer spectroscopy.

Table 1.3 List of samples and their respective compositions.

Sample Name	Sample Composition	Chapter/s
Undoped LFP	$LiFePO_4/C$	3, 5
Gelon LFP	$LiFePO_4/C$	3, 4
V-LFP	$LiFe_{0.80}V_{0.20}PO_4/C$	3, 4
Ho-LFP	$LiFe_{0.99}Ho_{0.01}PO_4/C$	3, 5
3% Ho-LFP	$LiFe_{0.97}Ho_{0.03}PO_4/C$	5
5% Ho-LFP	$LiFe_{0.95}Ho_{0.05}PO_4/C$	5
Yb-LFP	$LiFe_{0.99}Yb_{0.01}PO_4/C$	3
1% Al-LFP	$LiFe_{0.99}Al_{0.01}PO_4/C$	3
3% Al-LFP	$LiFe_{0.97}Al_{0.03}PO_4/C$	3
5% Al-LFP	$LiFe_{0.95}Al_{0.05}PO_4/C$	3
1% Sc-LFP	$LiFe_{0.99}Sc_{0.01}PO_4/C$	3
3% Sc-LFP	$LiFe_{0.97}Sc_{0.03}PO_4/C$	3
5% Sc-LFP	$LiFe_{0.95}Sc_{0.05}PO_4/C$	3

2. Methodology

This chapter starts by presenting the synthetic approaches to LFP and its doped derivatives in this thesis. The battery assembly method is then described, followed by a brief description of the theory behind the electrochemical measurements implemented. Different structural and chemical analysis techniques of the raw materials as well as measurements carried out on electrodes are then explained, and an overview of the principles applied is also given. A commercially available LFP material purchased from Gelon Lib Group Co., Ltd. was also implemented to compare the in-house synthesised materials with an optimised analogue of LFP.

2.1. Synthetic Techniques

A number of synthetic approaches have been implemented to produce LFP during this project, such as hydrothermal and microwave-assisted syntheses. The most common approach to LFP synthesis, however, is through a solvothermal route, with it being the preferred method even on a commercial scale.[66,101–106]

2.1.1. Solvothermal Synthesis

Solvothermal synthesis is the preferred technique for LFP production since it is a facile and cheap approach, often using a one-pot method and green solvents. The general principle is a one-pot synthesis, with all reagents added in a solvent while stirring, then being transferred to an autoclave and heated under pressure at a low temperature for a prolonged period of time.

2.1.1.1. Syntheses Implemented

The syntheses used in this project were adapted from Wang *et al.*, whereby a one-pot approach in ethylene glycol was employed for the synthesis of LFP.[66] $LiOH{\cdot}H_2O$ (>99%, Sigma-Aldrich), ≥85% H_3PO_4 (ThermoFisher Scientific), and $FeSO_4{\cdot}7H_2O$ (>99%, Sigma-Aldrich) were utilised as the starting materials and added stepwise to ≥98% ethylene glycol (ThermoFisher Scientific) in a stoichiometric ratio of 3 : 1 : 1. The reaction was carried out under a N_2 atmosphere with stirring at room temperature. The suspension was then transferred to a Teflon-lined autoclave and heated to 180 °C for 15 hours, before being washed several times with deionised water by centrifuging, then dried in a vacuum oven at 80 °C overnight.

The as-synthesised LFP was carbon-coated by being added to a 15% sucrose solution with stirring and heating at 80 °C until evaporation. The powder was transferred to a ceramic crucible and heated to 700 °C under Ar atmosphere for 5 hours. Once cooled to room temperature, the black LFP powder was characterised to ensure material purity.

2.1.1.2. Doped Material Syntheses

The doped LFP materials were synthesised following the same method as the undoped: through a 'one-pot' solvothermal method. The same starting materials and solvent were used, however stoichiometric amounts of dopant nitrate were added replacing the Fe salt, yielding $LiFe_xM_{1-x}PO_4$ (M = Al, Sc, Ho, Yb; x = 0.01, 0.03, 0.05) using $Al(NO_3)_3{\cdot}9H_2O$, $Sc(NO_3)_3{\cdot}H_2O$, $Ho(NO_3)_3{\cdot}5H_2O$, and $Yb(NO_3)_3{\cdot}H_2O$ (Sigma-Aldrich) as the dopant source. The 20% V-doped LFP analogue was obtained from colleagues at University College London, synthesised as described by Johnson *et al.*, and used as received.[107]

2.2. Battery Assembly and Cycling

Before assembling and cycling the batteries, the doped and undoped LFP had to be cast as electrodes. All electrodes were made up as slurries using 5% polyvinylidene fluoride binder in *N*-methyl-2-pyrrolidone solvent (5% PVDF in NMP; Sigma-Aldrich) and super pure carbon (ThermoFisher Scientific) as the conductive additive. Ratios of active material (doped/undoped LFP), carbon, and binder varied from 90 : 5 : 5 to 80 : 10 :10, with the former being used more regularly. The active material and carbon additive in appropriate ratios were wet ball-milled using zirconia grinding beads at 400 rpm for 10 minutes three times in absolute ethanol (Fristch Pulverisette 7) then dried in a vacuum oven at 80 °C overnight before speed mixing with the appropriate ratio of binder. After the slurry was speed mixed, a doctor blade was used to tape-cast it onto an aluminium foil current collector at a thickness of 170 – 180 μm, which was then dried in a vacuum oven at 80 °C overnight. Once dry, the electrodes were cut into discs (13/16 mm in diameter) and pressed using a pellet press to ensure minimal contact issues between cathode material and current collector when implemented in half-cells *versus* Li/Li^+ anode.

The electrolytes used throughout the project were 1 M lithium hexafluorophosphte ($LiPF_6$) in either 1:1 v/v ethylene carbonate and

diethylcarbonate (EC:DEC) or 1:1 v/v ethylene carbonate and dimethylcarbonate (EC:DMC) (Sigma-Aldrich) employed for general testing and cycling. When samples were prepared for beamtime experiments, a solution of 1 M lithium bis(trifluoromethanesulfonyl) imide (LiTFSi) in EC:DEC or EC:DMC was prepared in-house and used instead so as to ensure no external source of phosphorus other than the LFP was present when measuring the P K-edge. A better overview of this is presented in **Table 2.1**.

Table 2.1: List of electrolytes and salts used for the experiments carried out throughout this thesis.

Experiment	Cathode	Electrolyte	Salt
Benchmarking (Galvanostatic cycling, CV, EIS)	Gelon LFP	1 M $LiPF_6$	1:1 v/v EC : DMC
	20% V-LFP		
	Undoped LFP	1 M LiTFSI	1:1 v/v EC : DEC
	1% Ho-LFP		
	1% Yb-LFP		
	1% Al-LFP		
	3% Al-LFP		
	5% Al-LFP		
	1% Sc-LFP		
	3% Sc-LFP		
	5% Sc-LFP		
XAS Measurements	Gelon LFP	1 M LiTFSI	1:1 v/v EC : DMC
	20% V-LFP		
	Undoped LFP	1 M LiTFSI	1:1 v/v EC : DEC
	1% Ho-LFP		
Mössbauer Spectroscopy	Undoped LFP	1 M LiTFSI	1:1 v/v EC : DEC
	1% Ho-LFP		

2.2.1. Coin Cell Assembly

Since the cathode was the electrode of interest for this project, all batteries were assembled as half-cells against Li/Li^+, with CR2032 coin cells being the main cell type. All components of the coin cell were dried under vacuum at 65 °C for 24 hours before being introduced into the Ar-filled glove box, and it was ensured that O_2 and H_2O levels in the glove box were <0.5 ppm before assembling batteries. The coin cells were constructed as per the schematic in **Figure 2.1**, with all internal components made out of stainless steel and glass fibre separators (Whatman), and then crimped in the Ar-filled glove box.

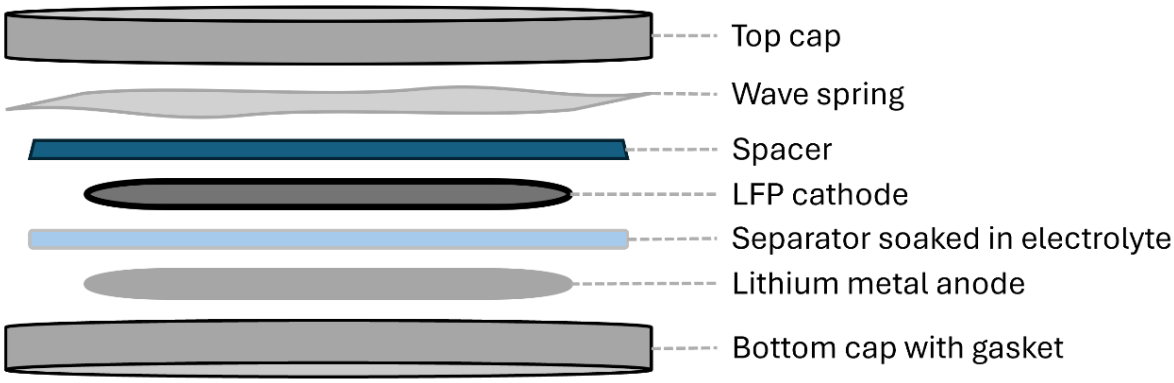

Figure 2.1 Schematic diagram of a CR2032 coin cell and its internal components.

2.2.2. Pouch Cell Assembly

Pouch cells were used when coin cells were unsuitable for the experiment at hand, for example, when the samples were required for XAS measurements. This was due to the fact that most components of the CR2032 coin cells were stainless steel which could interfere with the Fe K-edge measurements of the samples. Pouch cells are composed of laminated aluminium pouch material, positive aluminium and negative nickel tabs, and a glass fibre separator (**Figure 2.2**). The LFP cathode and Li-metal anode, along with the electrolyte were introduced in the Ar-filled glovebox, then the pouch cell was heat-sealed for cycling under vacuum.

To prepare *ex-situ* samples for the XAS experiments, the pouch cell is sandwiched between two glass slides in order to increase contact between the electrodes. The cycled pouch cells were removed from the cycler at chosen stages during the cycling process and introduced into the Ar-filled glovebox where the

cathodes were retrieved, washed with electrolyte, and stored under argon until required for analysis.

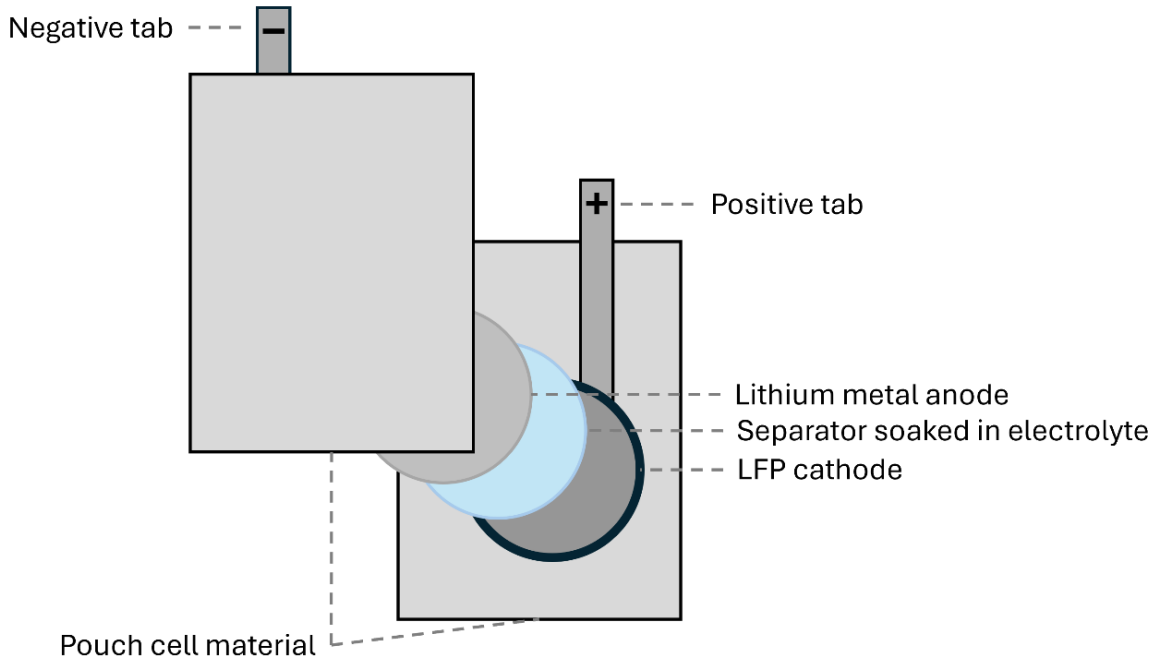

Figure 2.2 Schematic diagram of a pouch cell with all its internal components.

2.2.3. Cycling Parameters

All cells were cycled on a BioLogic VMP3 Multichannel Potentiostat. Galvanostatic cycling was carried out between 2 – 4 V and 2.4 – 3.9 V at various charge rates of C/2, C/5, and C/10. Cyclic voltammetry (CV) was performed at a dE/dt rate of 0.2 mV/s between -2 – 4 V, and electrochemical impedance spectroscopy (EIS) was measured in the frequency range of 1 MHz to 50 mHz with an amplitude of 1 mV over a voltage range of -2 – 4 V.

For XAS measurements, the cells were stopped at different states-of-charge (SOCs) (**Figure 2.3**). The cells were cycled up to 5.5 times to ensure that all solid-electrolyte interphase (SEI) formation had occurred, and to compare the materials after the first and fifth cycles, and various states-of-charge (SOCs) in-between.

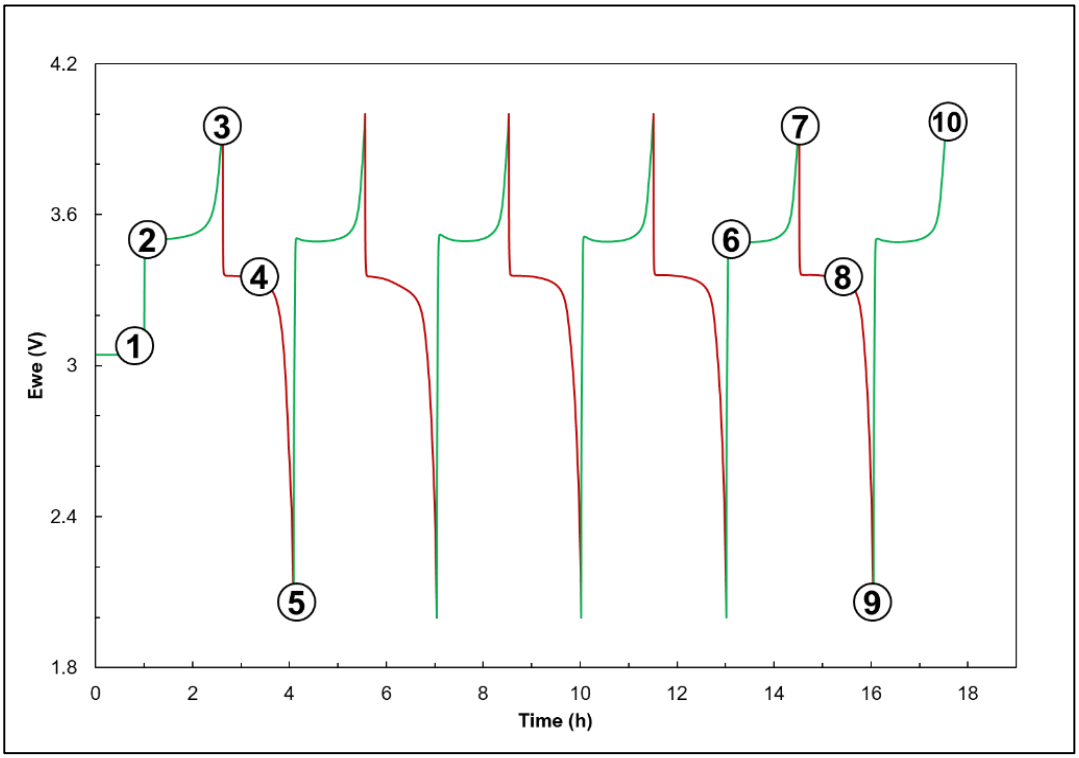

Figure 2.3: Voltage vs. time graph indicating the various SOCs of battery cycling.

2.3. Analytical Measurements

2.3.1. X-Ray Diffraction

X-Ray Diffraction (XRD) is the main analytical technique used to investigate crystalline substances. When an X-ray interacts with matter, a number of interactions occur, which lead to different absorption and scattering effects. Rayleigh scattering is an elastic scattering which occurs when the X-ray interacts with the electrons surrounding atomic nuclei, whereby the energy of the scattered wave remains the same and it retains its phase relationship to the incident wave, causing the X-ray photons impacting the atoms to scatter. However, since crystalline solids are ordered and periodic, the resulting scattered radiation will be constructive or destructive which leads to distinctive diffraction phenomena that can be used to explore the crystal structure of different materials.[108,109]

When an incident X-ray beam interacts with a material, the beam is elastically scattered by the electrons in the atoms present which start oscillating and create constructive and destructive interference. When the scattered X-rays are in-

phase, the former occurs producing strong diffraction peaks, whereas when the scattering is out-of-phase, the latter occurs and no peak is observed.

The main principle of XRD can be described by Bragg's Law:

$$n\lambda = 2d_{\mathrm{hkl}}\sin\theta \qquad [\mathbf{2.1}]$$

where n is the order of diffraction, λ is the wavelength of the incident X-ray beam, d_{hkl} is the lattice spacing, and θ is the angle of the diffracted beam with respect to the *hkl* atomic planes of the crystal (**Figure 2.4**). Diffraction occurs for each lattice plane of a crystalline material, in a direction that satisfies Bragg's law: the path difference between the scattered beams needs to be equal to an integer of the X-ray's wavelength and constructively interfere.[109]

In powder XRD (PXRD), the X-rays interact with multiple small crystals in random orientation, creating a circular diffraction pattern. The intensities of the diffracted circles in this pattern are then plotted at the scattering angles (2θ), which gives a 2D plot known as the powder pattern. The diffraction pattern observed is the Fourier transform of the electron density, which is given by the evaluated X-ray scattering factor, and the crystal structure can be obtained from the pattern if the electron density function is calculated at every point in a unit cell.[109]

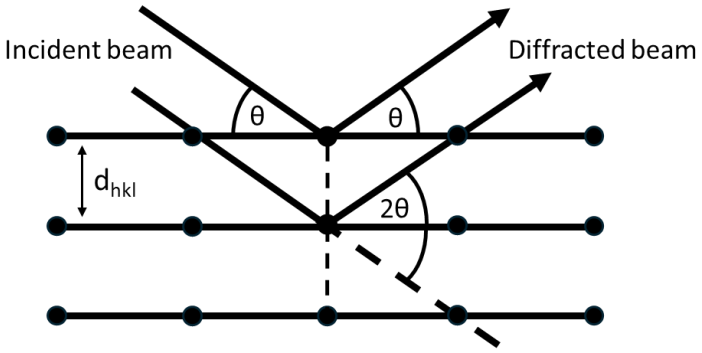

Figure 2.4: Schematic representation of the main principles of Bragg's Law.[109]

During this project, powder XRD was performed on a Rigaku MiniFlex Powder Diffractometer, with Cu-Kα radiation (λ = 1.5418 Å) over the 2θ range 10 –

70°, and a step-size of 0.05°. From the XRD patterns, structural changes in the dopant samples are identified when compared to the pure LFP material, as well as ensuring phase purity of the synthesised materials.

2.3.2. X-Ray Absorption Spectroscopy

X-Ray Absorption Spectroscopy (XAS) is comprised mainly of two regions: X-ray absorption near-edge structure (XANES) and extended X-ray absorption fine structure (EXAFS) (**Figure 2.5**). XANES pertains to the measurement of electronic transitions from core states of an element to the excited electronic states, whereas EXAFS relates to the electronic transitions that occur beyond the LUMO into the continuum. Together, these techniques give us information about electronic structure, neighbouring atoms, coordination numbers, bond distances, and oxidation numbers of the absorbing atom. XAS is specific to each absorbing element, therefore information about each constituent element of a compound can be studied and give an insight into the mechanisms occurring within LFP.[110]

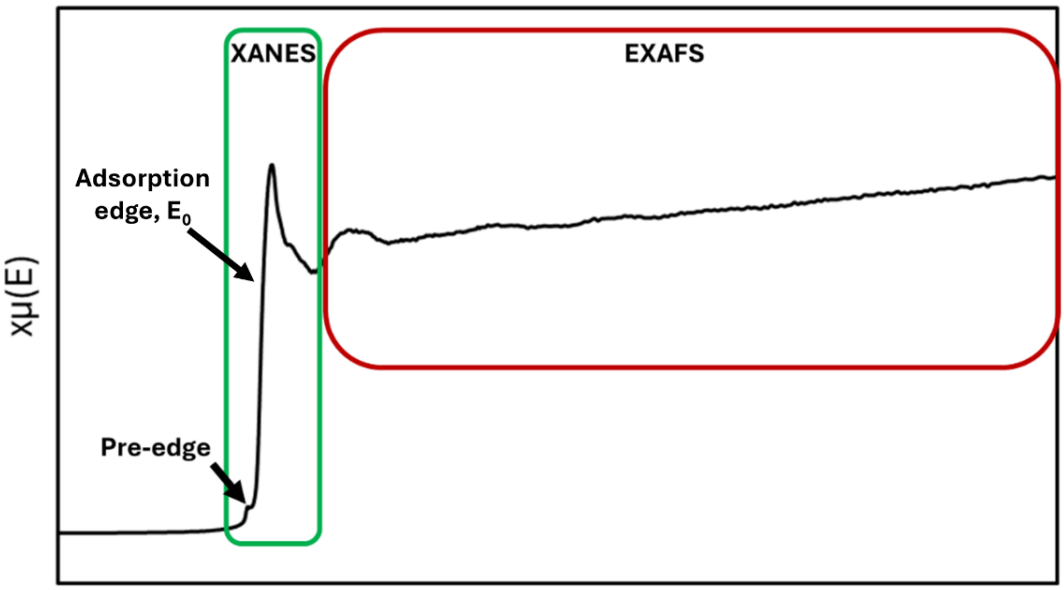

Figure 2.5: XAS spectrum with regions of interest annotated.

When an atom of a specific element is bombarded with an X-ray in an XAS setup, a core electron absorbs the X-ray and becomes excited, resulting in the creation of an electron hole. Once absorbed, two things may happen: a higher energy

level electron falls into the core hole, ejecting an X-ray (the photoelectric effect, K_α or K_β), specific to the absorbing atom, known as fluorescence energy; or the Auger effect, wherein an electron from a higher energy level falls into the electron hole and the energy liberated through this process is transferred to a second electron called an Auger electron, which is then ejected into the continuum (**Figure 2.6**). Only a fraction of this energy is required to overcome the binding energy of the Auger electron, so the rest is retained as kinetic energy. Since the initial ionisation is non-selective, the core hole may be in various shells, so there will be multiple possible Auger transitions for a single element varying in intensity.[111] However, since the measurements carried out in the thesis were done in fluorescence mode, Auger effects were not considered.

The adsorption edge of the measured element during the XAS experiment can be determined through the Beer-Lambert law:

$$E_0 = \log\frac{I_0}{I} \qquad [\mathbf{2.2}]$$

Where E_0 is the adsorption edge, I_0 is the incident beam intensity, and I is the transmitted beam intensity. The adsorption of an electron at an element-specific energy gives rise to an *adsorption edge* (white line) in the energy spectrum if the energy is varied across the specific binding energy of the K-level core electron (**Figure 2.5**). The adsorption edge is part of the XANES region of the spectrum.

The XANES portion of the XAS spectrum ranges from about 20 eV before the main absorption edge energy, E_0, to around 50 eV thereafter.[112] The most important piece of information obtained from the absorption edge, or white line, is the oxidation state of the absorbing element. E_0 increases with increasing oxidation state due to the effective number of positive charges changing due to 1*s* core hole shielding effects. The higher the oxidation state, the more positive overall charge resulting in higher electron binding energy, thus requiring more energy to excite a core electron, which in turn results in a higher E_0.[110]

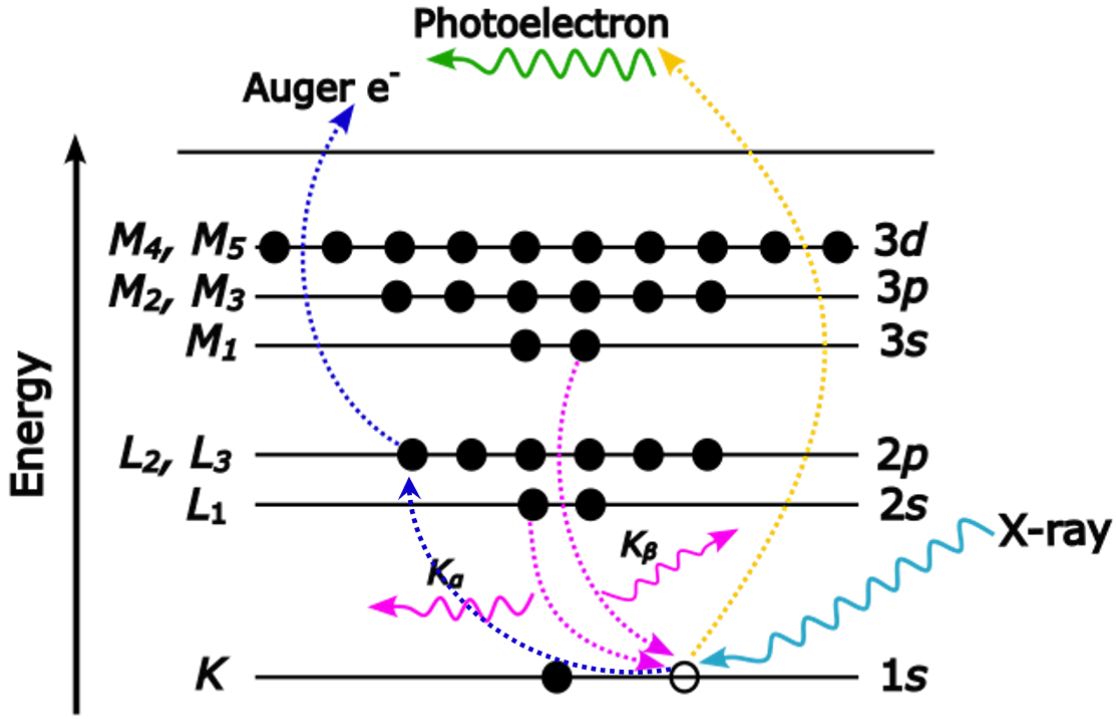

Figure 2.6: Schematic depicting the fluorescence and Auger effects that occur when a core electron absorbs an X-ray during XAS measurements.

In K-edge measurements, the 1*s* → n*p* transitions are the main contributors to the XANES spectra, where n*p* represents the lowest unoccupied *p* orbital of the absorbing atom. This is usually an intense, allowed transition with $\Delta l = 1$, where *l* is the orbital momentum quantum number, giving a sharp white line feature in the XANES spectrum.[109]

When measuring a transition metal K-edge with partially occupied *d*-orbitals, the pre-edge features offer considerable information, such as coordination environment of the element being probed. Pre-edge features provide an insight into the coordination environment of the absorbing atom and arise due to forbidden processes (e.g. $\Delta l = 2$) resulting from 1*s* → (n-1)*d* transitions.[110,112]

The EXAFS segment of the XAS spectrum starts at around 50 eV from E_0 and can extend to a few keV afterwards into the oscillating portion of the spectrum. These oscillations are generated by both constructive and destructive interferences produced by the ejected photoelectron scattering, caused by the neighbouring atoms of the absorbing atom. These interferences produce wave-like patterns in the spectrum which gives an insight into coordination numbers, bond distances, and neighbouring atom information.[112] An incident X-ray is absorbed by a central atom,

and the photoelectron is backscattered from the surrounding atoms and the backscattered wave from these atoms is in phase with the outgoing wave from the central atom, which leads to an increased absorption coefficient at E_1. At a higher energy, E_2, with a shorter photoelectron wavelength, the backscattered wave destructively interferes with the outgoing wave(**Figure 2.7**). This interference results in a decrease in the cross-section of the waves, which consequently leads to the wave-like pattern observed as the EXAFS spectrum.[110]

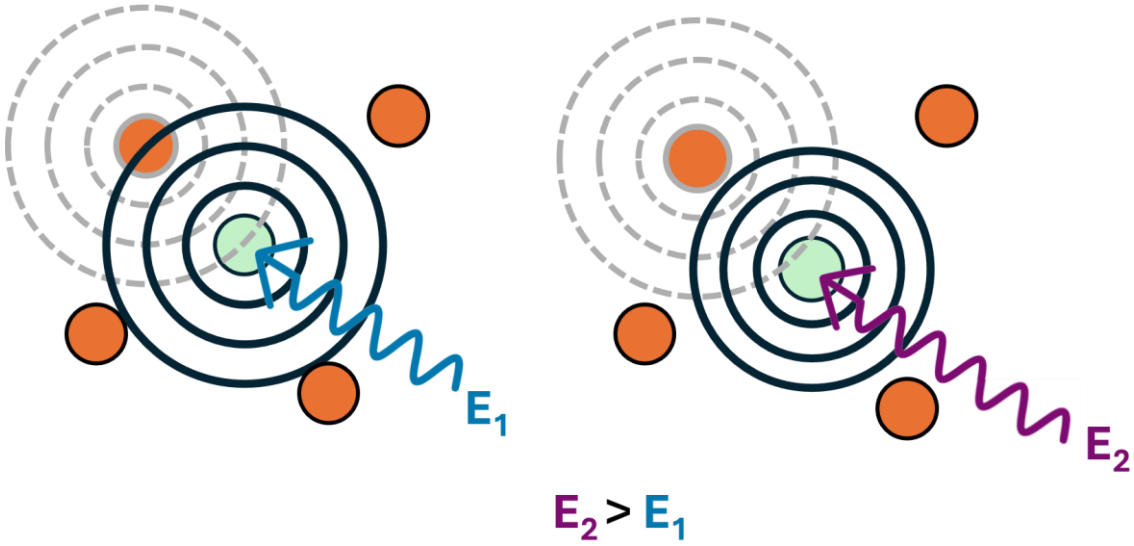

Figure 2.7: Schematic depicting the interactions of the incident X-rays (E_1 & E_2) with the central absorbing atom (green) and its outgoing wave (solid circles), resulting in a backscattering wave (dashed circles) from the surrounding atoms (orange).

During the measurement of the Fe K-edge, a gradual increase in E_0 value is seen as the battery is charged and the lithium ions are extracted from the crystal lattice. The change of Fe^{2+} in LFP (and Ho-LFP) to Fe^{3+} is denoted by the increase in energy of the white line portion of the XANES spectra. This strong shift in the main edge can be attributed to the Fe 1*s* → continuum transitions, with the pre-edge features denoting weaker dipole forbidden Fe 1*s* → 3*d* transitions.[60]

The phosphate oxygen atoms, which are octahedrally coordinated to iron, results in a ligand field which splits the Fe 3*d* states into t_{2g} and e_g states. This gives rise to the pre-edge feature in the XANES portion of the spectra, with the mixing of

O 2*p* and Fe 3*d* orbitals increasing the transition probability of the 1*s* to 3*d* orbitals, which is dipole forbidden.[60]

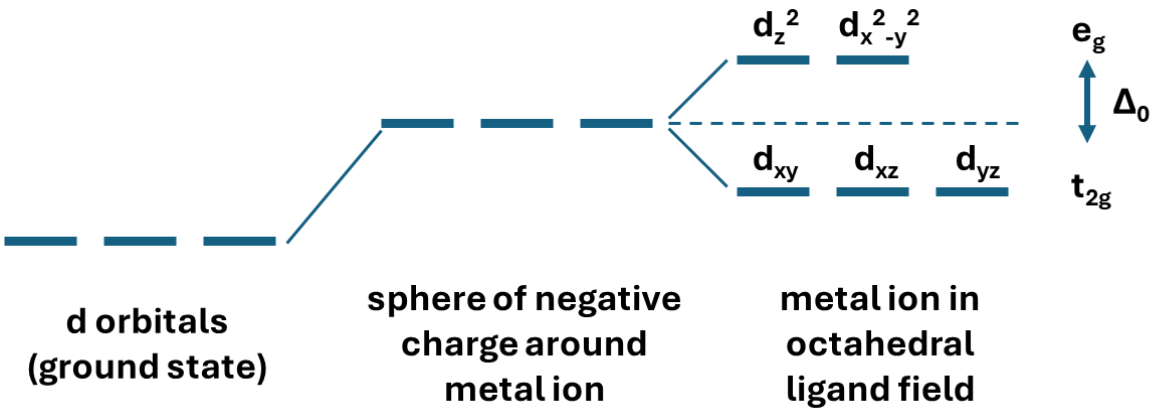

Figure 2.8: Octahedral ligand field splitting of the d-orbitals of transition metal ions.

P K-edge XANES spectra originate from the transition of a P 1*s* electron to an unoccupied antibonding state of the phosphate polyanion, formed by the overlap of the P sp^3 hybrid and O 2*p* orbitals. In LFP, this state must lie above the $Fe^{2+/3+}$ redox couple, however in the mixed valent system, the Fe^{3+} empty states lie above the Fe^{2+} occupied states. Mixing of the minority spin states of the Fe^{3+} ions and the antibonding states of the phosphate anions would occur due to the overlap of the $Fe^{2+/3+}$ redox couple with the unoccupied antibonding state of the phosphate anion. Within a two-phase system, i.e. LFP and iron phosphate, the fraction within which this interaction would occur increases proportionally with the concentration of Fe^{3+} ions as the LFP is delithiated.[113,114]

The beamlines used throughout this project were BM28 at the European Synchrotron Radiation Facility (ESRF, Grenoble, France; **Figure 2.8**) and B18 at Diamond Light Source (DLS, Didcot, United Kingdom; **Figure 2.9**).[115,116] XAS measurements were performed using similar setups at each beamline where the beam is collimated using Si or Pt/Si mirrors. It then passes through a double crystal monochromator, which filters the incoming beam and tapers the X-rays to the required wavelengths. A focusing mirror, or harmonic rejection mirror, is necessary to further focus the beam on the sample, preventing any anomalies as data is

collected. Beam size is further adjusted through a series of slits, which are adapted according to the requirements of the sample being measured.

Ex situ XAS measurements were performed on the cathodes under vacuum (~10^{-6} bar) at 298 K on the BM28 beamline at the ESRF, with emission spectra recorded in fluorescence mode using a Si <1 1 1> monochromator and a primary toroidal focusing mirror, followed by two harmonic rejection mirrors with an incidence angle of 6 mrad. At BM28, the metal K-edges were measured using the same chamber setup as for the P K-edges in fluorescence mode, while on B18 the samples were measured in transmission mode using pouch cells to keep the sample atmosphere inert.

The Demeter version 0.9.26 software package and Larch version 0.9.80 software package were used to process and normalise all XAS data obtained.[117,118] EXAFS oscillations were extracted using a k-range of 2.5 – 9.5 $Å^{-1}$ for all edges and k^2-weighted data for the Fourier Transform. The k-range was selected in order to investigate the first shell data, and to truncate the noise at higher k values.

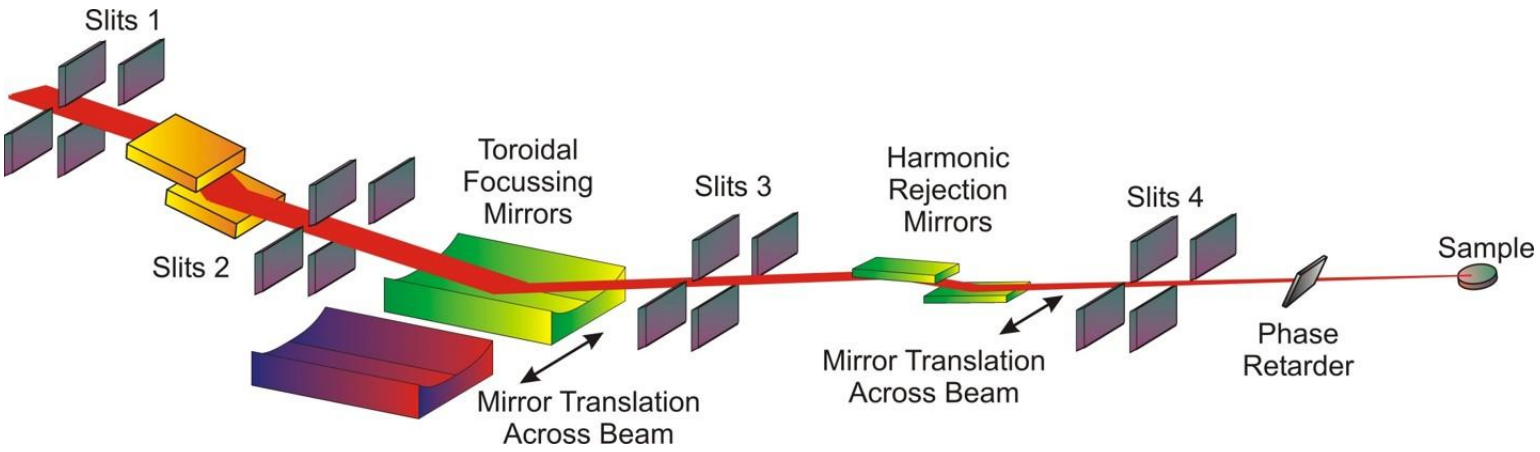

Figure 2.9 Schematic diagram of the optical configuration of the XMaS BM28 beamline at ESRF.[115]

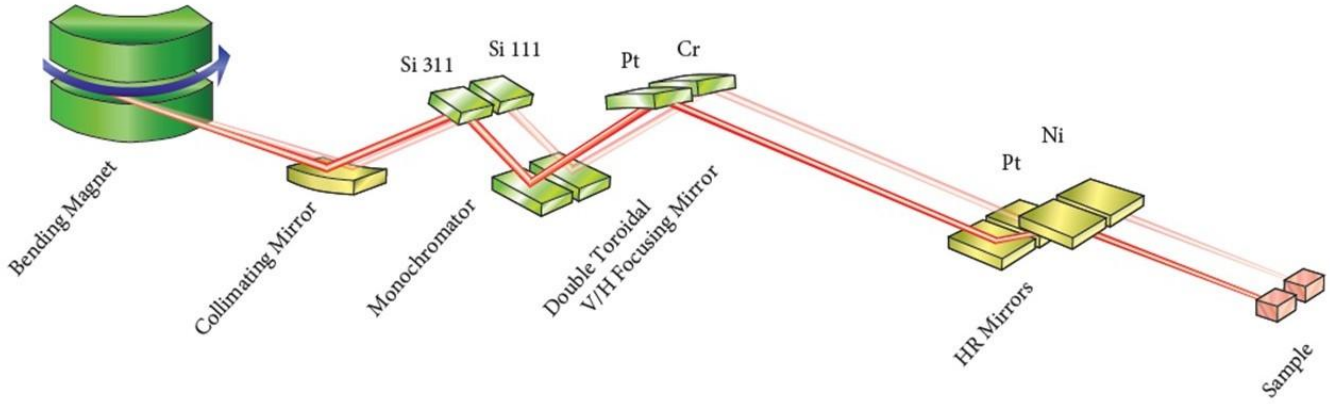

Figure 2.10 Schematic diagram of the optical layout of B18 beamline at DLS.[116]

2.3.3. Scanning Electron Microscopy with Energy Dispersive X-Ray Spectroscopy

Scanning Electron Microscopy with Energy Dispersive X-Ray Spectroscopy (SEM-EDX) is an effective tool for visualisation of samples coupled with elemental analysis.

The SEM technique is comprised of an electron microscope which utilises a beam of electrons that is focused through a series of lenses, which interacts with the sample to generate an image (**Figure 2.11**). When the electron beam comes into contact with the sample, secondary electrons (SE), backscattered electrons (BSE), and characteristic X-rays are produced. Specialised detectors are used to detect the SE, BSE, and X-rays which are then processed, generating an image and providing information about the sample shape, size, and elemental composition.[119]

When the electron beam interacts with the sample, signals are produced which are used to construct an image. The interactions between the beam and the sample are either elastic or inelastic. Elastic scattering occurs when the incident electrons are deflected by the atomic nucleus or outer shell electrons of the sample, resulting in minimal energy loss and a directional change in the scattered electrons. When the incident electrons are scattered through an angle greater than 90 degrees, BSE are produced, whereas when the primary beam transfers energy to the sample, there is inelastic scattering which ionises the atoms, resulting in SE (**Figure 2.12**). Other signals are also produced when an electron beam strikes a sample, such as Auger electrons and characteristic X-rays.[120]

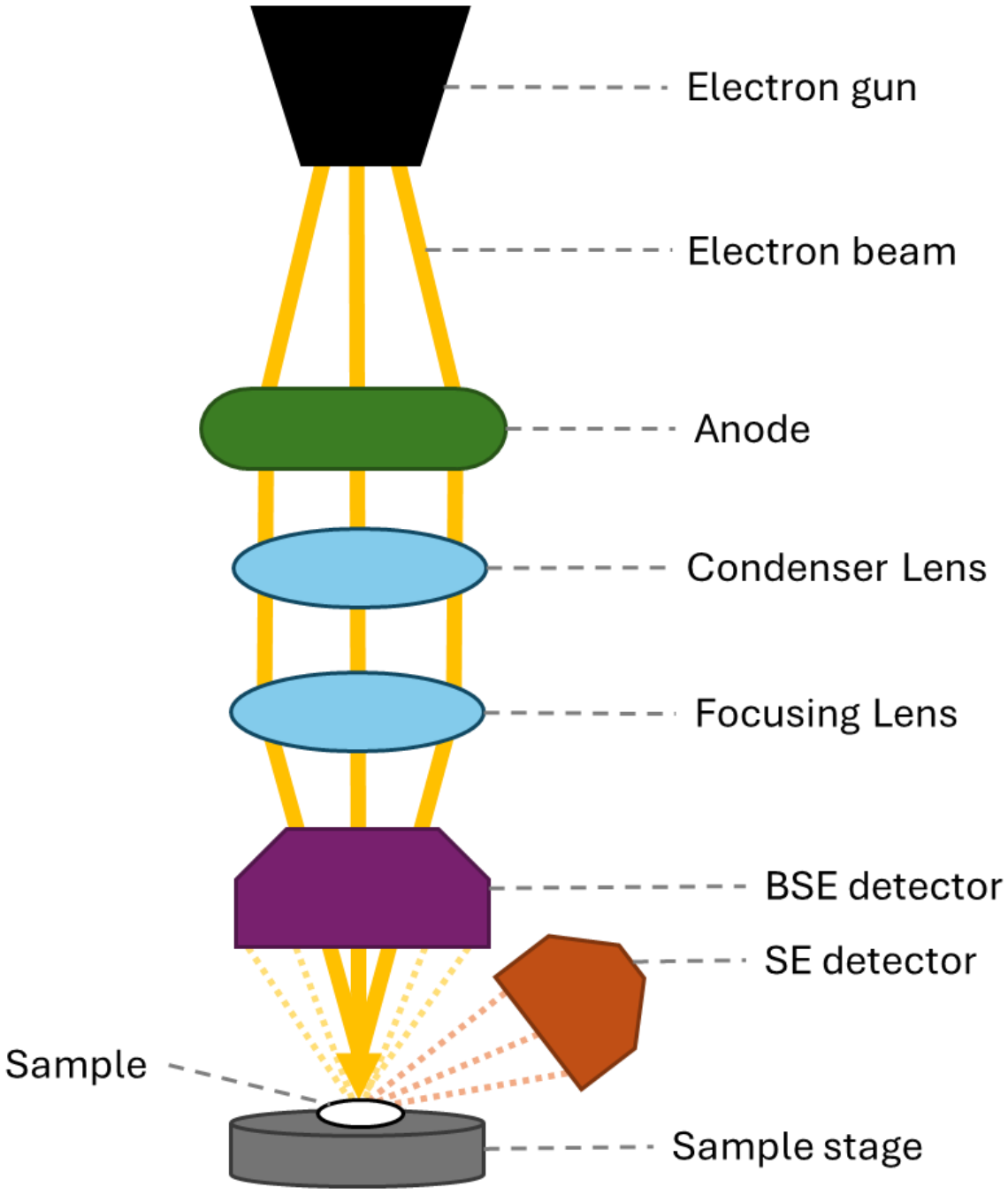

Figure 2.11: Schematic diagram of the basic components and working mechanism of SEM.

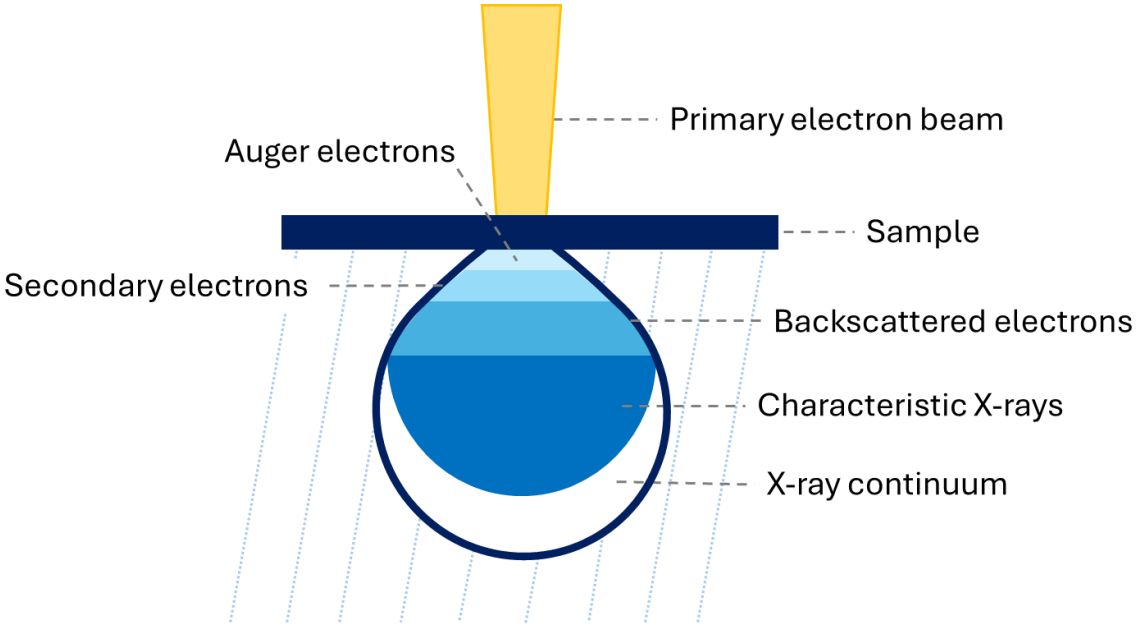

Figure 2.12: Illustration of several signals produced by electron beam-sample interaction in SEM and their regions of detection.

For topological analysis, SE mode is most commonly used since the incident electrons have low energy so detection can only be attained up to a few nanometres. Secondary electrons are generated when a K-shell electron is ejected from the target sample by a primary or additional secondary electron. SE mode thus gives good information about the topology and morphology of the surface of the sample.[119] SE mode was employed throughout this project.

Energy Dispersive X-ray (EDX) spectroscopy allows for elemental information to be obtained from a sample. When the primary electron beam displaces an electron from the core shells of the sample, an outer-shell electron replaces it and releases energy in the form of X-rays. The released X-rays are characteristic to the elements being measured, thus allowing for elemental analysis of the sample. Coupled with SEM imaging, EDX is a powerful tool which allows for site-specific elemental mapping of a sample, which can help identify materials and impurities, as well as carry out compositional analysis.[121]

SEM was carried out on a Hitachi S3400N SEM using a probe current of 15 kV and SE mode, with EDX elemental mapping performed using AZtec Version 4.0 software by Oxford Instruments NanoAnalysis.

2.3.4. Mössbauer Spectroscopy

Mössbauer spectroscopy is useful at identifying different Fe-site, oxidation state, and Fe-related defects within iron-containing compounds. Site determination is the most useful application of Mössbauer spectroscopy, and it finds its uses across multiple fields such as geochemistry, organic and inorganic chemistry, biochemistry, and metallurgy. Site analysis can help estimate quantitatively the fractions of Mössbauer atom (in this case, iron) sites at structurally distinct positions in the same phase as the corresponding pattern intensities.[122,123]

The main principle of Mössbauer spectroscopy is the Mössbauer effect which states that when atoms are held closely in crystalline atomic structures, the gamma radiation emitted by their nuclei is virtually recoil-free. The emitted gamma-photon has the exact frequency that corresponds to the transition energy between the ground and excited states of the nucleus, so when this photon collides with a similar nucleus in a tight crystalline structure, absorption may occur (**Figure 2.13**). Since nuclear energy levels are distinctly defined, only a photon with the exact transition energy may excite another nucleus.[124,125]

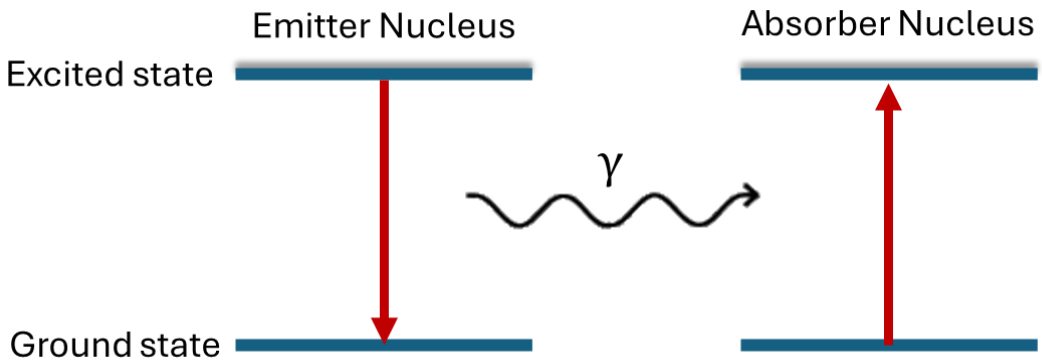

Figure 2.13: Demonstration of recoil-free nuclear radiation.

The nuclear states are very closely defined, so a small change in photon energy will destroy the resonance, which makes Mössbauer spectroscopy ideal for measurements of miniscule nuclear energy differences. The smallest energy variations, magnetic fields at the nucleus, and asymmetry or distortion in the shape of the lattice enveloping the atom are enough to create shifts and splits in the absorption line, producing a visible effect known as hyperfine interactions.[124]

Hyperfine interactions can be categorised into three main sections: chemical isomer shift (CS or IS, mm s^{-1}), nuclear quadrupole splitting (QS or ΔEQ, mm s^{-1}), and the nuclear Zeeman effect, also known as the magnetic dipole interaction (B_{eff} or H, T). The chemical isomer shift stems from the Coulomb interaction of the nuclear charge distribution over the radius of the nucleus in its ground and excited states, as well as the electron charge density at the nucleus. Shielding effects of valence electrons will affect the *s*-electron density at the nucleus, so the isomer shift will depend mostly on the ionisation state of the atom (**Figure 2.14**).[124,125]

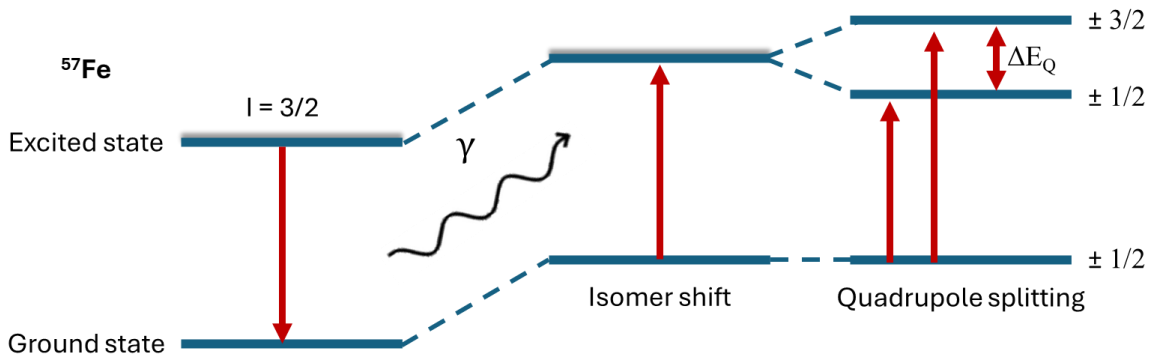

Figure 2.14: Illustration of the magnetic isomer shift and quadrupole splitting interactions that occur during ^{57}Fe Mössbauer spectroscopy.

Nuclear quadrupole splitting arises from interactions between the electron field gradient (EFG) at the nucleus and the electron quadrupole moment, eQ, of the nucleus itself. The ^{57}Fe excited state (I = 3/2) will be split by the EFG into a pair of doublets (I_z = ±1/2, ±3/2). The nuclear Zeeman effect occurs when the nuclear magnetic dipole moment interacts with the external applied magnetic field on the nucleus, resulting in magnetic dipole splitting, which appears as a sextet pattern in a Mössbauer spectrum.[124–126] Combining all hyperfine interactions, the difference in energy between the emitted γ-ray and the nuclear transition energy, ΔE, can be expressed as:

$$\Delta E = \mu H + QVE + \text{cont} < R^2 > \rho(0) \qquad [\mathbf{2.3}]$$

Where μ is the nuclear magnetic moment, Q is the nuclear quadrupole moment, E is the EFG, R^2 is the mean square nuclear charge radius, and $\rho(0)$ is the electron density at the nuclear site, with each component of the equation representing the three principal interactions observed in Mössbauer spectroscopy.[127]

Both the electric quadrupole interaction and the magnetic dipole interaction will produce spectra containing multiple lines, which can provide a large amount of information about the iron environment/s within the material. The three hyperfine interactions can be rendered both as a product of a nuclear term, which is constant for a given γ-ray transition, and as an electronic term, which can vary depending on the chemistry of the absorbing material.[127]

The most common type of Mössbauer isotope is ^{57}Fe, since iron is the most abundant multivalent element and a direct decay product of ^{57}Co. The conditions for recoil-free radiation to occur must be met, ergo the majority of nuclear transitions must be zero-phonon transitions. The lifetime of the excited nuclear state should be long enough so as to ensure good resolution and short enough to prevent unnecessary sensitivity to external vibrations.[126]

Doublets are the most common type of spectrum obtained for iron(II)- and iron(III)-containing species, which have an isomer shift and quadrupole splitting that depend on the coordination number of iron (**Figure 2.15**). Through analysis of these doublets, octahedral and tetrahedral symmetry can be determined. Generally, the hyperfine interactions that control the individual elementary patterns are mainly determined by the nearest neighbouring atoms of the iron atoms being measured.[122,128]

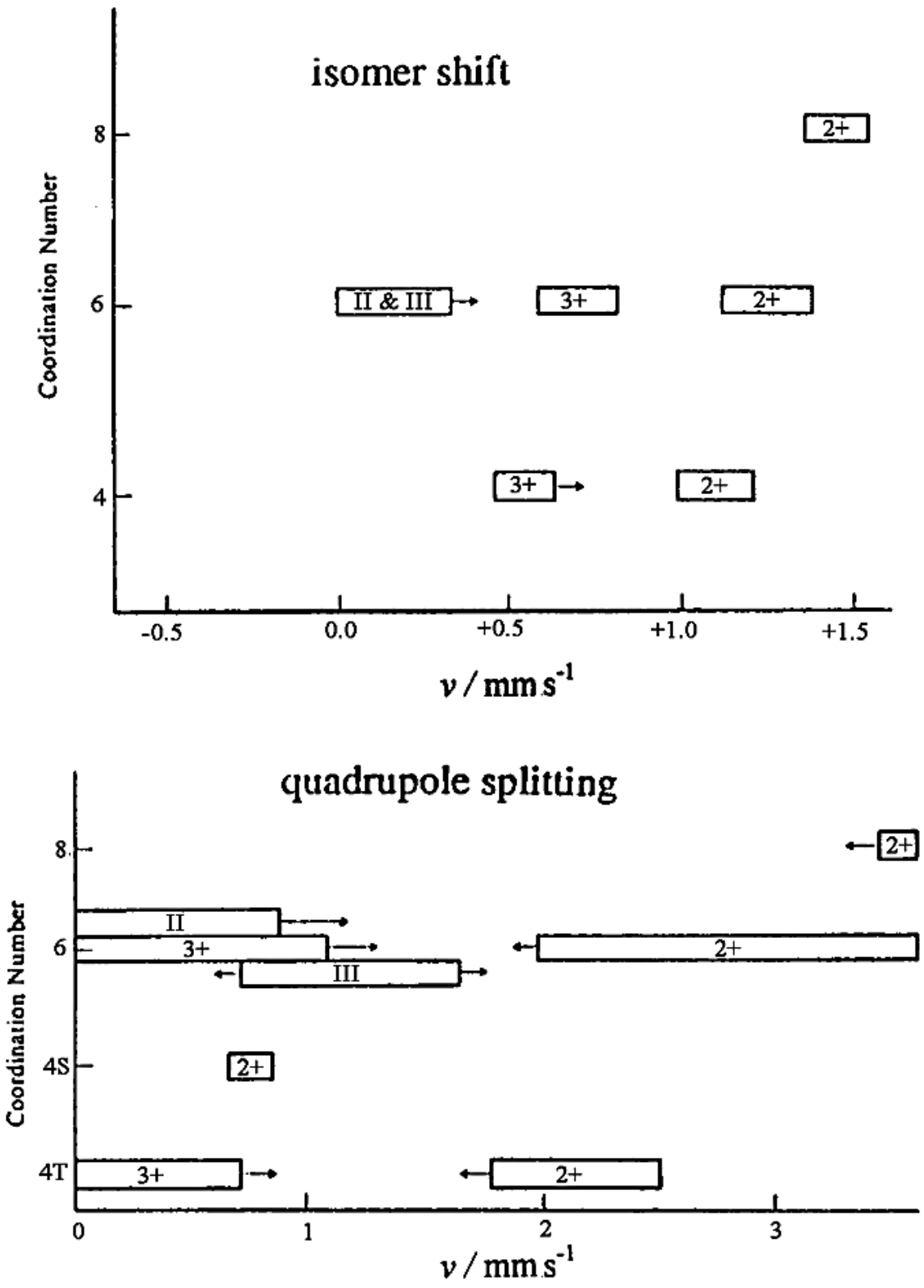

Figure 2.15: Correlation between coordination number of ^{57}Fe with isomer shift (top) and quadrupole splitting (bottom).[122]

Mössbauer measurements were carried out by Dr Alex Scrimshire and Prof Paul Bingham at Sheffield Hallam University using ^{57}Co in a rhodium matrix as the source material, which is encapsulated in a titanium allow holder with a brazed beryllium window and sealed by laser welding (Ritverc Isotope Products). The sample holder is 1 inch in diameter and made of copper, with a 25 Ω heater and 1.5-inch-long temperature sensor (**Figure 2.16**). The heat from the system is removed using a water-cooled heat exchanger and compressor (Sumimoto HC-4E). The resonant absorption energy of the incident gamma ray is tuned to 14.41 keV. The detectors are filled with a 95:5 ratio of argon and methane since the incoming radiation ionises the inert gas producing a series of ion pairs, which eventually need to be quenched. A thin tungsten filament is fixed along the length of the detector aligned with the direction of the collimated gamma-photons being detected. A bias voltage of ~2.5 kV is applied to the filament, resulting in the production of an anode which in turn causes the casing to act as a cathode whereby the ions can be detected. The charge recorded as a voltage pulse is then fed to amplification systems and recorded by a spectrometer (WissEI CMCA-550 module) and data is collected. The Recoil fitting software was used to fit the collected data.[127,129]

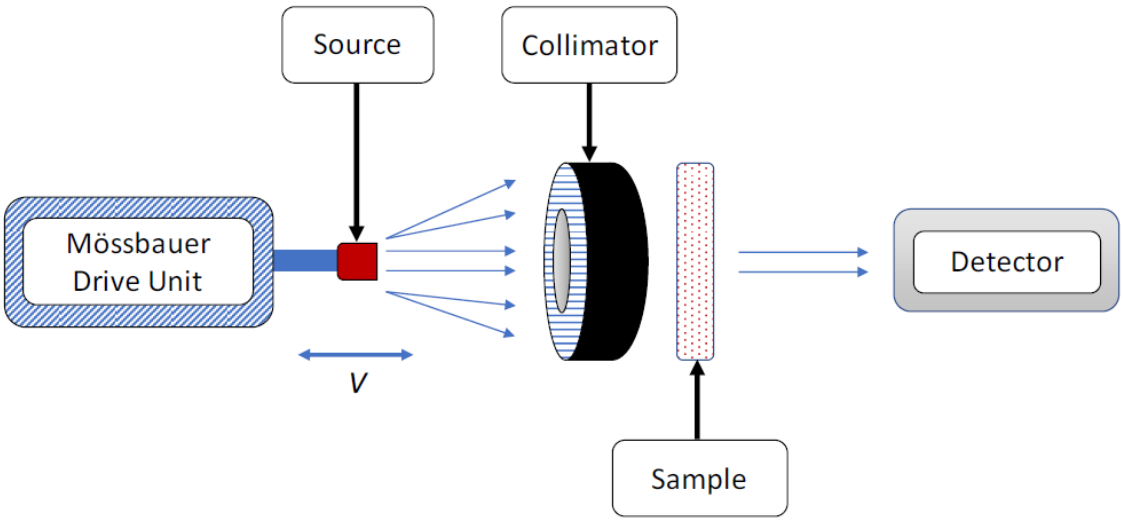

Figure 2.16: Schematic diagram of a transmission ^{57}Fe Mössbauer spectrometer (provided by Dr A. Scrimshire, SHU).[127]

2.3.5. Galvanostatic Cycling

Galvanostatic cycling is the most frequently used technique to study a battery's cycling capability, capacity, coulombic efficiency, lifetime, and performance. Usually, these parameters are assessed based on the C-rate, as it will affect the above properties. The C-rate is the rate at which a battery is discharged relative to its maximum theoretical capacity. At a rate of 1C, the battery will discharge in 1 hour, while at a C-rate of C/2 the battery will discharge in 2 hours, while at 2C the battery will discharge in 30 minutes, and so forth.[130] The C-rate is used to directly compare different materials and material loadings.

The specific capacity is the maximum energy per unit weight stored by a battery, measured in mAh g^{-1}. Conventionally, it is compared to the theoretical specific capacity of the material being measured in order to assess its performance. Theoretical capacity is calculated through **Equation 2.4**:

$$Q = \frac{nF}{M} \qquad [\mathbf{2.4}]$$

where Q is the theoretical capacity, n is the number of lithium ions per unit formula (in the case of LFP, n = 1), F is the Faraday constant, and M is the molecular mass of the electroactive material being measured.

Coulombic efficiency (CE; **Equation 2.5**) is the percentage ratio of the capacity attained from the electrode during discharge compared to the charge capacity of the electrode. CE is affected by numerous factors, for example solid-electrolyte interphase (SEI) formation, electrolytic decomposition, side reactions occurring within the cell, C-rate, temperature, *etc.*

$$\text{CE } \% = \frac{\text{Discharge capacity}}{\text{Charge capacity}} \times 100 \qquad [\mathbf{2.5}]$$

Coin and pouch cells of all doped and undoped LFP samples were galvanostatically cycled as half-cells *versus* Li/Li^+ on a BioLogic VMP3 Multichannel Potentiostat at C-rates of C/5 and C/10 between 2 – 4, and 2.4 – 3.9 V, depending on the experimental setup.

2.3.6. Cyclic Voltammetry

Cyclic voltammetry (CV) is an electrochemical technique used to investigate the oxidation and reduction processes of molecular species that occur within electrochemical environments. Different kinds of information can be obtained from CV, including electrode kinetics, anodic and cathodic reactions, and voltages, as well as reaction reversibility. A cyclic voltammogram for a reversible reaction has two distinct peaks (**Figure 2.17**): one for the oxidation, or anodic, reaction (forward scan) and one for the reduction, or cathodic, reaction (backward scan).

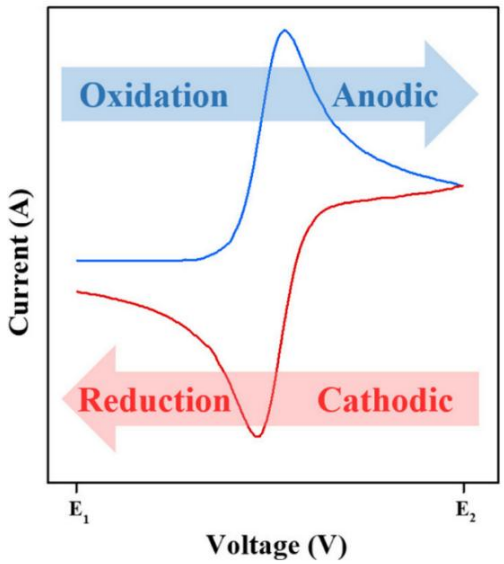

Figure 2.17 Typical cyclic voltammogram shape for a reversible reaction.[131]

The Nernst equation (**Equation 2.6**) is used to relate the potential of an electrochemical cell (E) to the standard potential of a species (E_0) and the relative activities of the oxidised ([Ox]) and reduced ([Red]) species in the system at equilibrium, with F as the Faraday constant, R representing the universal gas constant, T as the temperature in Kelvin, and n as the number of electrons involved in the redox mechanism. For a redox reaction involving one electron, n can be omitted from the reaction as it would be equal to 1.[132]

$$E = E^0 + \frac{RT}{nF}\ln\frac{[\mathrm{Ox}]}{[\mathrm{Red}]} \qquad [\mathbf{2.6}]$$

A reaction is deemed reversible if it meets certain criteria (**Figure 2.18**). The difference between the cathodic and anodic peak potentials (ΔE_p) is 2.22 (RT/F), which is calculated for the forward scan as 59 mV for a reaction to be considered reversible.[133] If the analyte is stable when reduced and can be successfully reoxidised, the reaction is considered reversible. Conversely, if a reaction occurs upon reduction that alters the analyte and prohibits its reoxidation, the redox is considered irreversible. Electron transfer kinetics between the electrode and analyte determine whether a reaction is reversible or irreversible. In the case of the former, when there is a low energy barrier for electron transfer, the Nernstian equilibrium is reached. In the case of the latter, when the energy barrier is high, ΔE_p is larger and the redox reaction is slower.[132]

CV is important for Li-ion battery research since it gives an insight into electrochemical factors and how they affect reaction parameters such as voltage and current, as well as providing information about the Li-ion diffusion rates, intercalation, and redox reactions.[131]

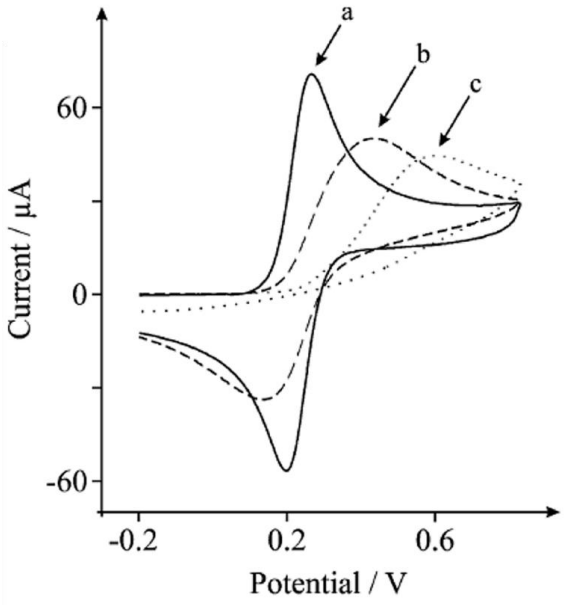

Figure 2.18: CVs for (a) reversible, (b) quasi-reversible, and (c) irreversible electron transfer.[134]

The redox mechanisms undergone in Li-ion batteries tend to be quasi-reversible, since cathodic and anodic peaks depend on the scan rate (v). The cyclic voltammogram of such redox reactions shows gradual peak shifts to higher potential values. The magnitude of the current, i_p, as well as the Li-ion diffusion coefficient,

D, can be obtained from the Randles- Ševčík equation (**Equation 2.7**), where n is the number of electrons involved in the redox mechanism, A is the area of the electrode, C is the concentration of active material, and v is the scan rate.[131]

$$i_p = \pm(2.69 \times 10^5)\, n^{3/2}\, AC\, \sqrt{Dv} \qquad [\mathbf{2.7}]$$

All CV measurements were carried out on a BioLogic VMP3 Multichannel Potentiostat using CR2032 coin cells of undoped and doped LFP cathodes *versus* Li/Li^+ anodes. All scans were performed at a dE/dt rate of 0.2 mV/s between -2 – 4 V.

2.3.7. Electrochemical Impedance Spectroscopy

Electrochemical impedance spectroscopy (EIS) is often used in conjunction with CV, as they are complementary techniques providing a further insight about the electrochemical reactions and properties occurring within an electrochemical cell.

EIS uses a sinusoidal wave of a set frequency to excite the electrochemical system. The resulting current and potential responses are then measured and used to calculate the electrochemical impedance, Z, of the cell.[135] There are two major impedance components: the in-phase, or real, Z` component, and the out-of-phase, or imaginary, –Z`` component. Both components are conventionally represented on a Nyquist plot, where the imaginary –Z`` is plotted against the real Z`.[136]

The internal resistance of an electrochemical cell can be divided into three main categories: electrolyte resistance, reaction resistance, and diffusion resistance. The physical phenomena that control impedance are dependent on the frequency. High frequency impedance (~1 kHz) is mainly caused by Li-ion diffusion in the electrolyte, while at intermediate frequences (1 – several hundred Hz) the impedance is dominated by Li-ion transfer reactions, and at low frequencies (<1 Hz) it is the Li-ion diffusion within the electrode that controls the impedance. A detailed analysis of the Nyquist plot (**Figure 2.19**), therefore, allows for a comprehensive analysis of different reaction mechanisms in different parts of the battery.[136]

Typically, analysis of impedance spectra is executed through equivalent circuit modelling, where an equivalent circuit model is used to fit each component and event occurring within the battery. From the fitting, parameters such as charge-transfer resistance (R_{ct}), Li-ion diffusion coefficients (D), and solution resistance (R_s) can be obtained.[135]

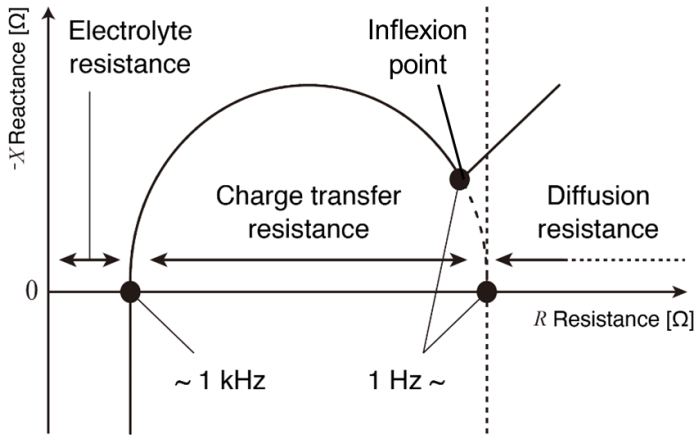

Figure 2.19 Nyquist plot highlighting the different regions of resistance within a battery.[137]

All EIS measurements were carried out on a BioLogic VMP3 Multichannel Potentiostat on CR2032 coin cells of undoped and doped LFP cathodes *versus* Li/Li^+ anodes. Impedance was measured in the frequency range of 1 MHz to 50 mHz with an amplitude of 1 mHz over a voltage range of -2 – 4 V.

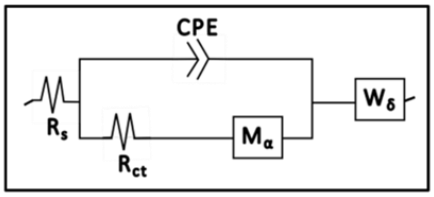

Figure 2.20: Equivalent circuit model used to fit electrochemical impedance spectra throughout this thesis.

All EIS plots were fitted to equivalent circuits composed of the solution resistance, R_s, the charge-transfer resistance which signifies the resistance imparted by the reactions occurring between the electrodes and electrolyte, R_{ct}, a restricted diffusion element, M_α, a constant phase element which represents the double layer capacity, CPE, and the Warburg impedance linked to Li-ion diffusion, W_δ (**Figure 2.20**)

3. Trivalent Dopants: A Systematic Study

3.1. Chapter Introduction

Doping has been used as a method of improvement for LFP for decades, however few comparisons have been made using dopants from across the periodic table. Similar elements are usually used in comparative studies, like first-row transition metals, or lanthanide metals.[138,139] This chapter, however, strives to make comparisons between different types of elements when used as dopants in LFP. The common factor of the selected elements: their trivalent oxidation state. In this chapter Al^{3+}, Sc^{3+}, and Yb^{3+} are researched at length, with V^{3+} discussed in more detail in **Chapter 4** and Ho^{3+} discussed more extensively in **Chapter 5**.

3.1.1. Chapter Aims

The overall aim of this study is to investigate the effects of different trivalent cations when implemented as dopants in LFP. As previously stated, there are numerous reports of dopants with similar chemical and physical properties, such as different transition metals, however there is a lack of comparison amongst elements from different groups or periods. The importance of using elements from across the periodic table stems from the absence of comparative studies pertaining to different kinds of cations.

The variety of elements selected for this study aims to achieve a well-rounded understanding of different factors which affect LFP in terms of stability, cyclability, efficiency, and capacity. The trivalent state was important as, in this oxidation state, cations tend to preferentially dope at the Fe-site therefore a fair assessment can be made since all dopants would target the same site for doping.

3.1.2. Choice of Dopants

Since the purpose of this study is to systematically compare different trivalent dopants, it is important to select a variety of different cations from across the periodic table. Different factors are involved in the selection process, such as cation size, position in the periodic table, novelty of dopant, and most importantly, the ability of the dopant to occupy a trivalent oxidation state.

It is important to have at least one well-reported dopant as part of this study, in order to be able to compare the dopant's effectiveness on LFP, hence vanadium being discussed at a later stage in this thesis.

In terms of novelty, only a few or no studies have been carried out on aluminium and scandium, respectively, whereas certain lanthanides have previously been researched, however the number of studies are few and knowledge is lacking in the area, consequently leading to the selection of ytterbium, and later holmium, in this study.[139,140]

The chosen dopants were thus able to provide an insight into how dopants from different groups across the periodic table can affect the crystal structure of LFP, as well as its performance when implemented as a cathode. The ionic radii of the selected dopants vary between 0.535 to 0.901 Å.

3.2. Methodology

3.2.1. All Samples

Synthesising an undoped analogue was imperative as it afforded a benchmark for the comparison of the doped derivatives. Synthesis was carried out as outlined in section **2.1.1.1** using a one-pot green approach, followed by carbon-coating and calcining before being implemented as a cathode.

Synthesis of the doped analogues was carried out as outlined in section **2.1.1.2**, where different stoichiometric quantities of dopants were implemented until a phase-pure sample was obtained. For Yb a 1% stoichiometric concentration of dopant is used, as higher concentrations showed impurity peaks in the PXRD data. The chosen dopant quantities for the aluminium and scandium analogues were 1, 3, and 5%, with an indication that this was the dopant threshold due to an impurity phase of $AlPO_4$ and $ScPO_4$ arising in the XRD pattern recorded for 5% Al- and Sc-LFP.

3.2.2. Structural Characterisation

XRD was employed to determine sample purity before proceeding with slurry preparation, battery assembly, and electrochemical characterisation. The instrumentation and parameters used were outlined in section **2.3.1** and the sample preparation was carried out by grinding the sample using an agate mortar and pestle. All measurements were carried out using a zero-background sample holder with some Vaseline grease for powder adhesion.

PXRD Rietveld refinements were carried out using GSAS-II software against LFP CIF file ICSD-92198.[128,141] The lattice parameters are listed in section **3.3.1**. Background subtractions were applied to all samples as part of the refinement process. The background was subtracted from all patterns collected in order to be able to compare between different dopant concentrations without any iron fluorescence effects or residue present due to the grease used when mounting the samples onto the sample holder. A third-order Chebyshev polynomial function was employed to avoid over-fitting, and then a peak-picking programme was used to select the main corresponding peaks. All characteristic LFP peaks were present in the sample pattern, indicating good sample purity.

Figure 3.1 shows the PXRD patterns obtained for 1% Ho- and Yb-doped LFP compared to the undoped analogue. The Ho-doped phase shows no extra peaks at doping levels ≤1%, while minor $YbPO_4$ impurity phases are indicated at around 20 and 26 °2θ, which were not eliminated by sintering.[142]

Figure 3.2 shows the PXRD patterns for all levels of Al-doped LFP. As indicated in the figure, there is a minor $AlPO_4$ impurity phase emerging when the doping level increases to 5%. The same occurrence can be seen in the Sc-doped LFP, where a $ScPO_4$ impurity phase is identified in **Figure 3.4** for the 5% Sc-LFP sample.

Although the Al^{3+} dopant was chosen for its likelihood at doping at the Fe-site in LFP, at higher concentrations it is reported that Al^{3+} prefers occupying Li-sites. This is confirmed by the upshift in the XRD pattern at ~35.7 ° (*hkl* plane <3 1 1>) for the 3% and 5% Al-LFP analogues. Li-site doping by LFP has been reported in literature by aluminium, denoted by the shift of the aforementioned peak in the XRD patterns.[63,143] A comparison of this peak for the synthesised samples compared to those extracted from literature is presented in **Figure 3.3**.

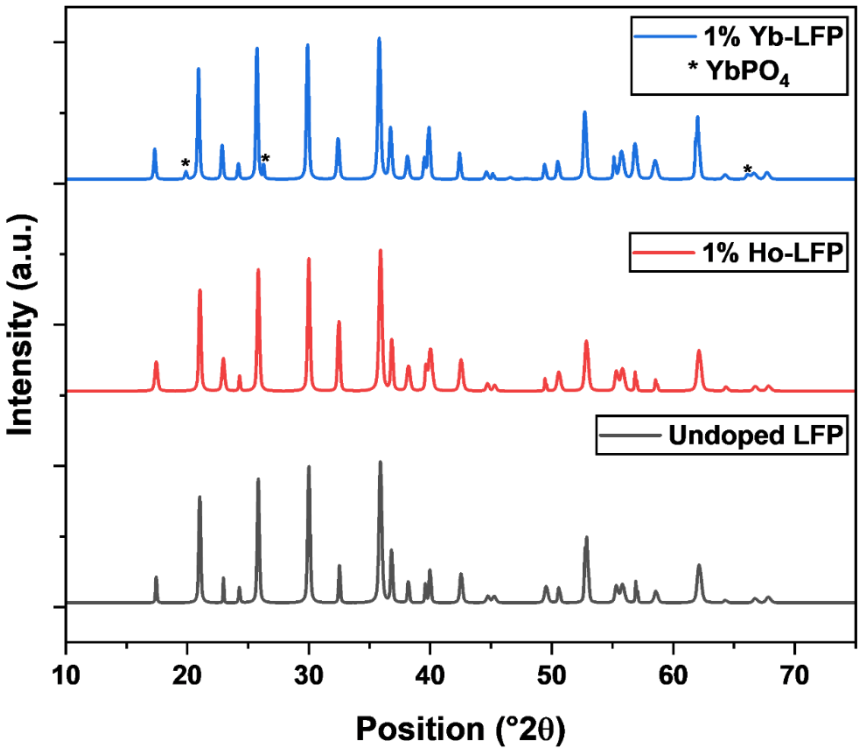

Figure 3.1: Background-subtracted PXRD patterns of 1% Ho- and Yb-doped LFP compared to the undoped LFP analogue.

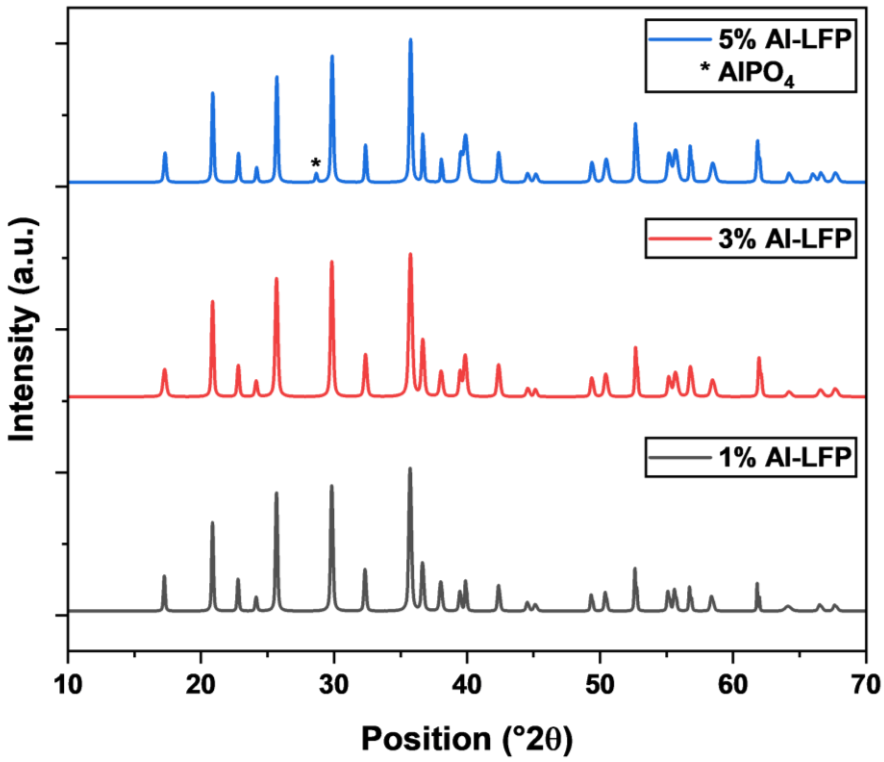

Figure 3.2: Background-subtracted PXRD patterns for the three levels of Al-doped LFP. The peak at ~27 ° 2θ indicates an emerging $AlPO_4$ impurity phase.[144]

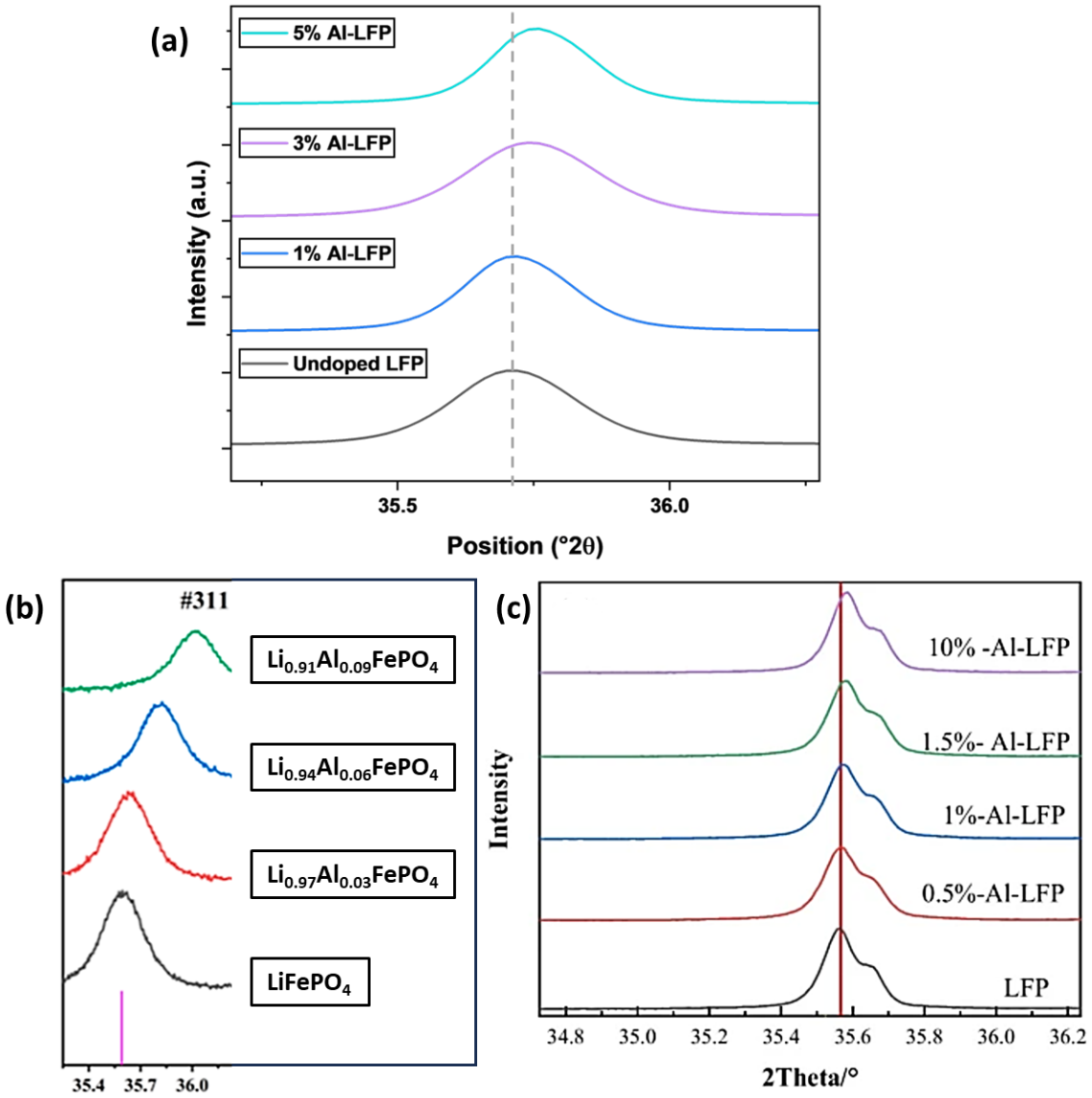

Figure 3.3: (a) Peak at ~35.7 ° <3 1 1>, extracted from the XRD patterns for the Al-doped samples, (b) Upshift in peak corresponding to lattice plane <3 1 1> with increasing Al concentration;[63] (c) Upshift in peak at ~35.6 ° as Al concentration is increased.[143]

Evidence of Li-site doping in Al-doped LFP is further supported by the decrease in volume with increasing aluminium concentration. At 1% Al-doping, the volume is calculated to be 291.022 Å^3, whilst at 3% and 5% Al-doping the volumes are 290.945 Å^3 and 290.963 Å^3, respectively. Having a smaller ionic radius than Li^+ (0.760 Å), the presence of Al^{3+} (0.535 Å) results in an overall decrease in volume of the material.[63,143,145]

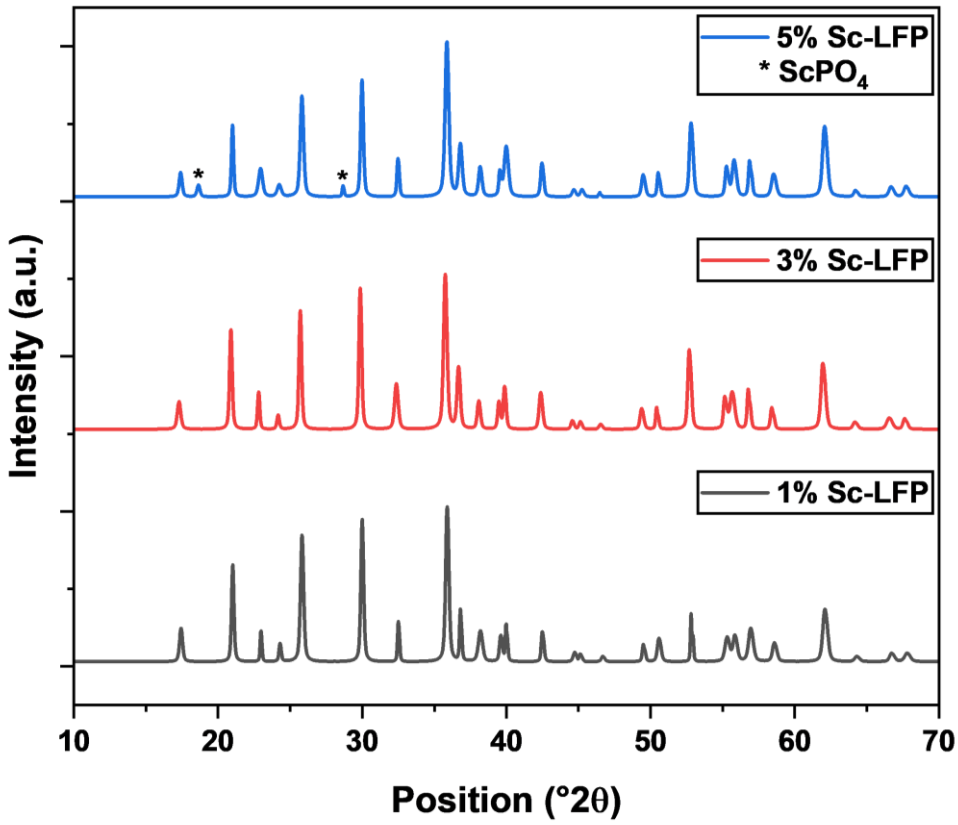

Figure 3.4: Background-subtracted PXRD patterns for the three levels of Sc-doped LFP. The peaks at ~20 ° and ~27 ° 2θ indicates an emerging $ScPO_4$ impurity phase.[146]

SEM-EDX of the carbon-coated samples was performed to gain an insight into the sample morphology and homogeneity of constituent elements across the sample. This step is more important for the doped analogues, since it is important to gauge whether the dopant is evenly distributed throughout the sample. These measurements were carried out by grinding a small amount of sample and sonicating it in a minimal quantity of ethanol, then depositing one drop of this suspension on a sticky carbon tab adhered to a stainless-steel SEM stub. Once the ethanol had evaporated, the edges of the stub were covered in copper tape in order to prevent charging by the sample when placed in the SEM-EDX instrument. Section **2.3.3** outlines the operational procedures employed for SEM-EDX throughout this thesis. EDX mapping was done on all constituent elements within the limit of detection for the undoped sample to assess their homogeneity across the grain selected for analysis (**Figure 3.5**).

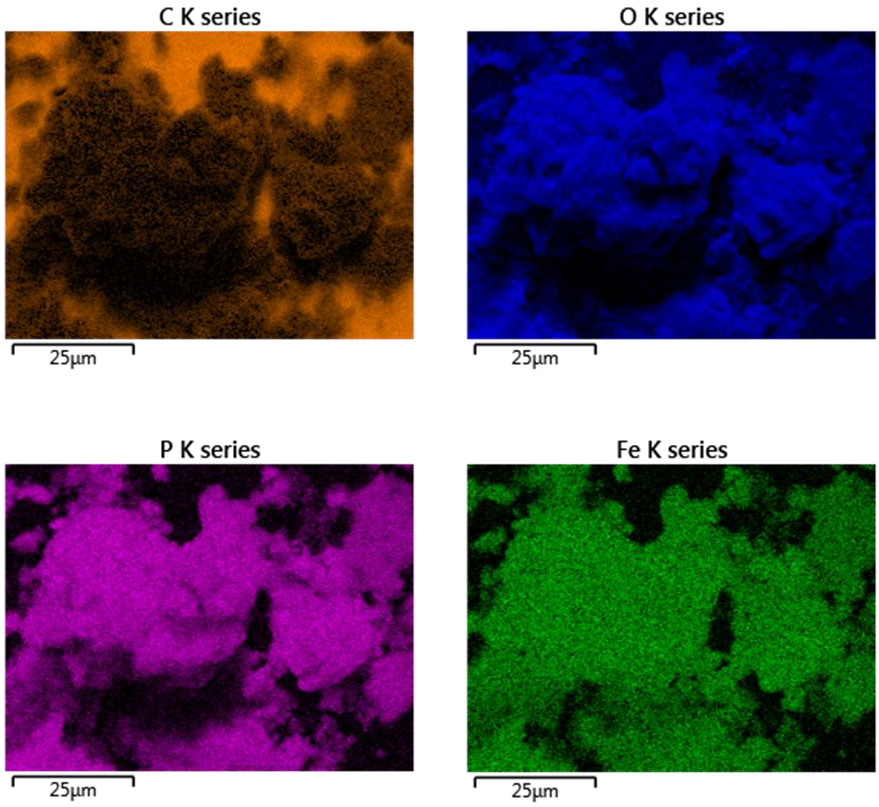

Figure 3.5: SEM-EDX mapping of carbon-coated undoped LFP showing distribution of C, O, P, and Fe across the sample.

The EDX mapping of each lanthanide- and vanadium-doped sample shows a homogenous distribution of dopant across the sample (**Figure 3.6**). The image contrast is enhanced in order to visualise the distribution better since the quantity of lanthanide dopant present is small (**Figure 3.6 (a)** & **(b)**). The EDX spectra also indicated the presence of the dopant in each sample measured, however due to the large amount of carbon present, the values measured are arbitrary and this technique was simply used as a tool to confirm the presence of the dopant. Despite the high concentration of 20%, the vanadium is still evenly distributed across the grain (**Figure 3.6 (c)**).

Since there were different levels of aluminium dopant used, a sample of each concentration was used for SEM-EDX analysis. Section **2.3.3** outlines the operational procedures employed for SEM-EDX throughout this thesis.

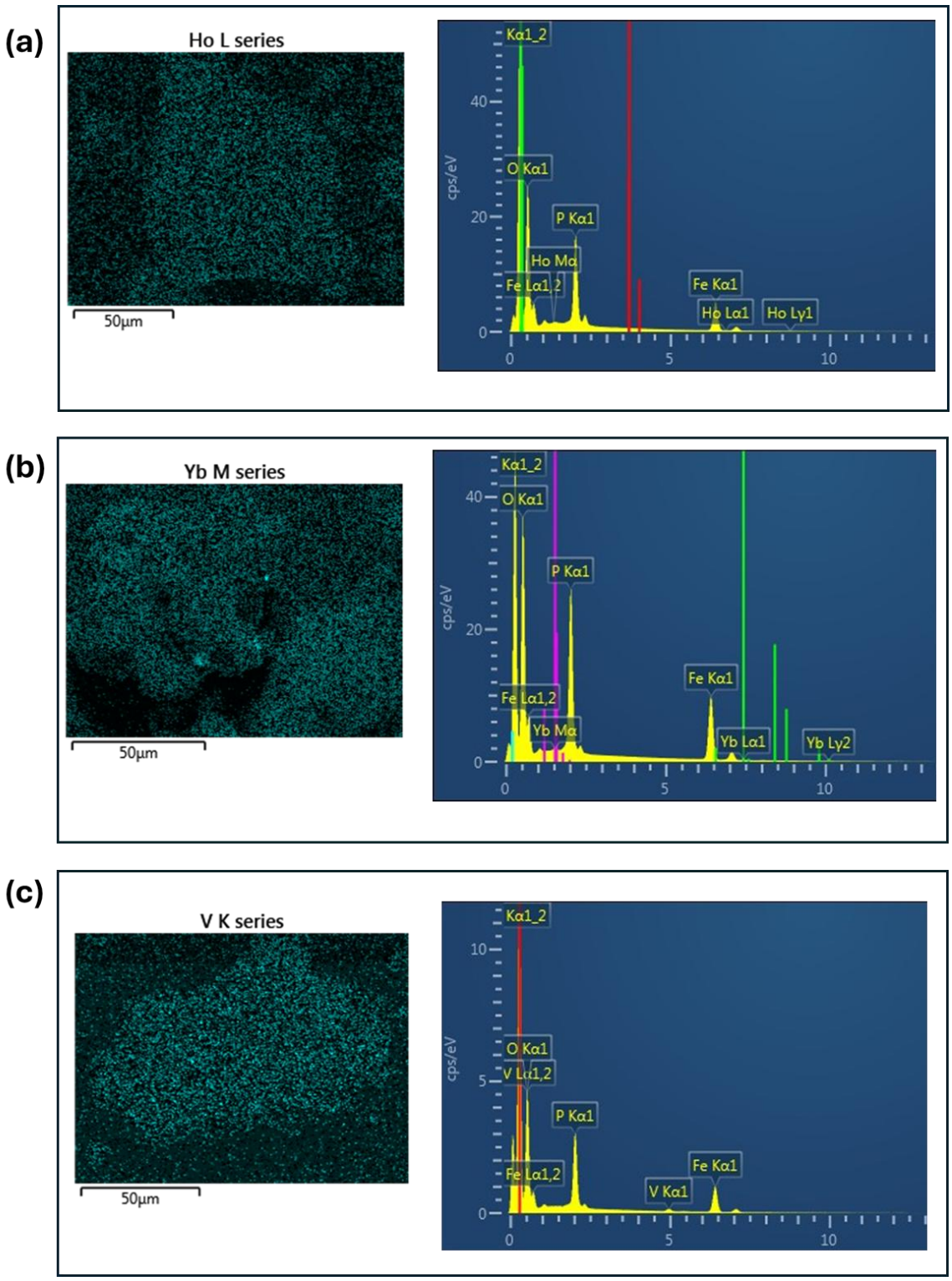

Figure 3.6: SEM-EDX mapping and spectrum indicating the presence of (a) Ho in 1% Ho-LFP; (b) Yb in 1% Yb-LFP; and (c) V in 20% V-LFP.

From **Figure 3.7** it is noted that as the aluminium concentration increases above 3%, both the EDX mapping and spectra indicate that the amount of Al-doping in the sample does not increase. Instead, this suggests that there is a maximum amount of Al-doping occurring in the sample, i.e. close to 3%.

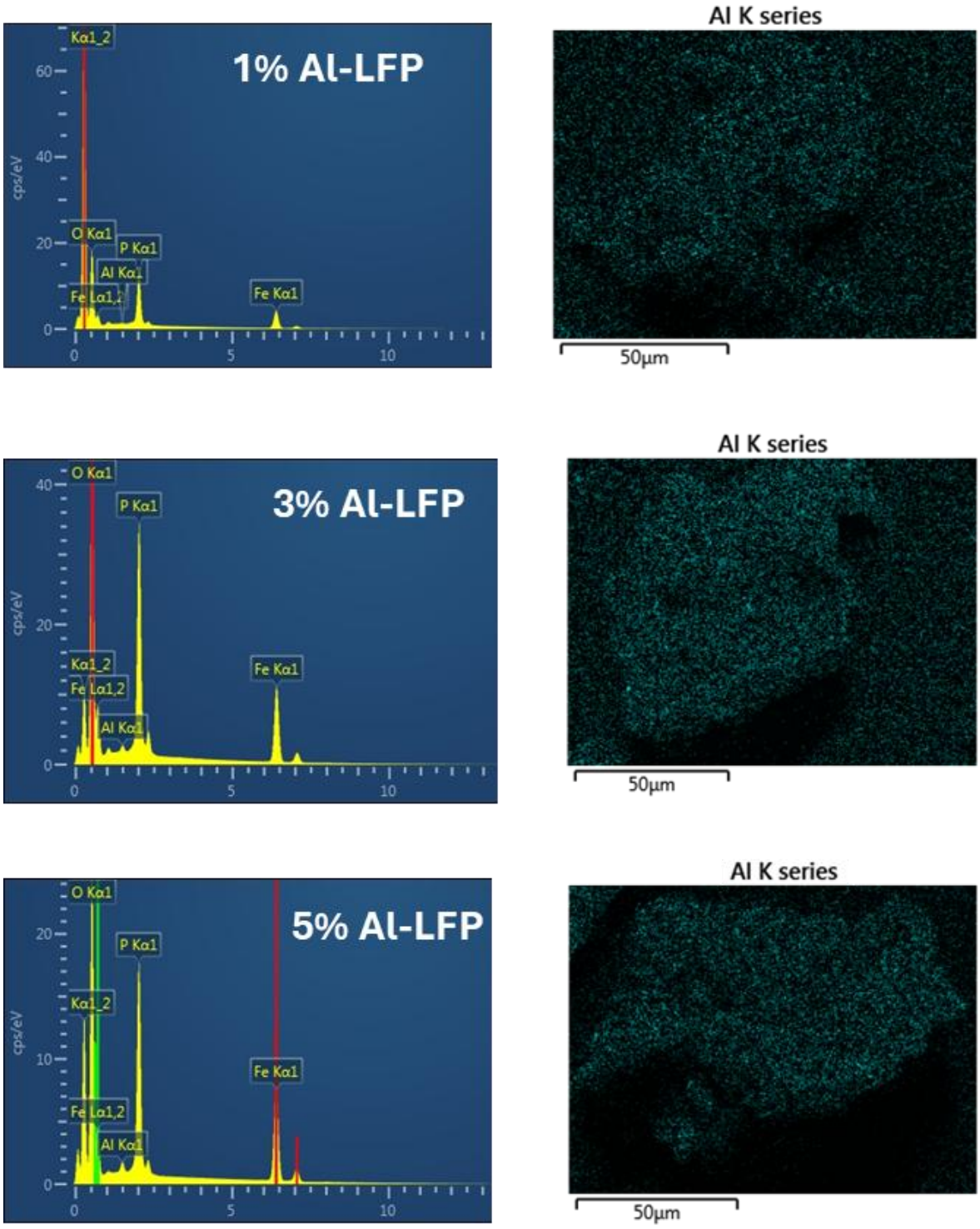

Figure 3.7: SEM-EDX maps and spectra showing the different concentrations of Al, indicating minimal difference in Al concentration between the 3% and 5% samples.

A similar study, as performed for aluminium, using SEM-EDX was employed to determine the scandium concentration in the samples (**Figure 3.8**). For Sc-

doping there appears to be a higher concentration of scandium present in the 5% Sc-LFP sample, however this could be due to the $ScPO_4$ impurity.

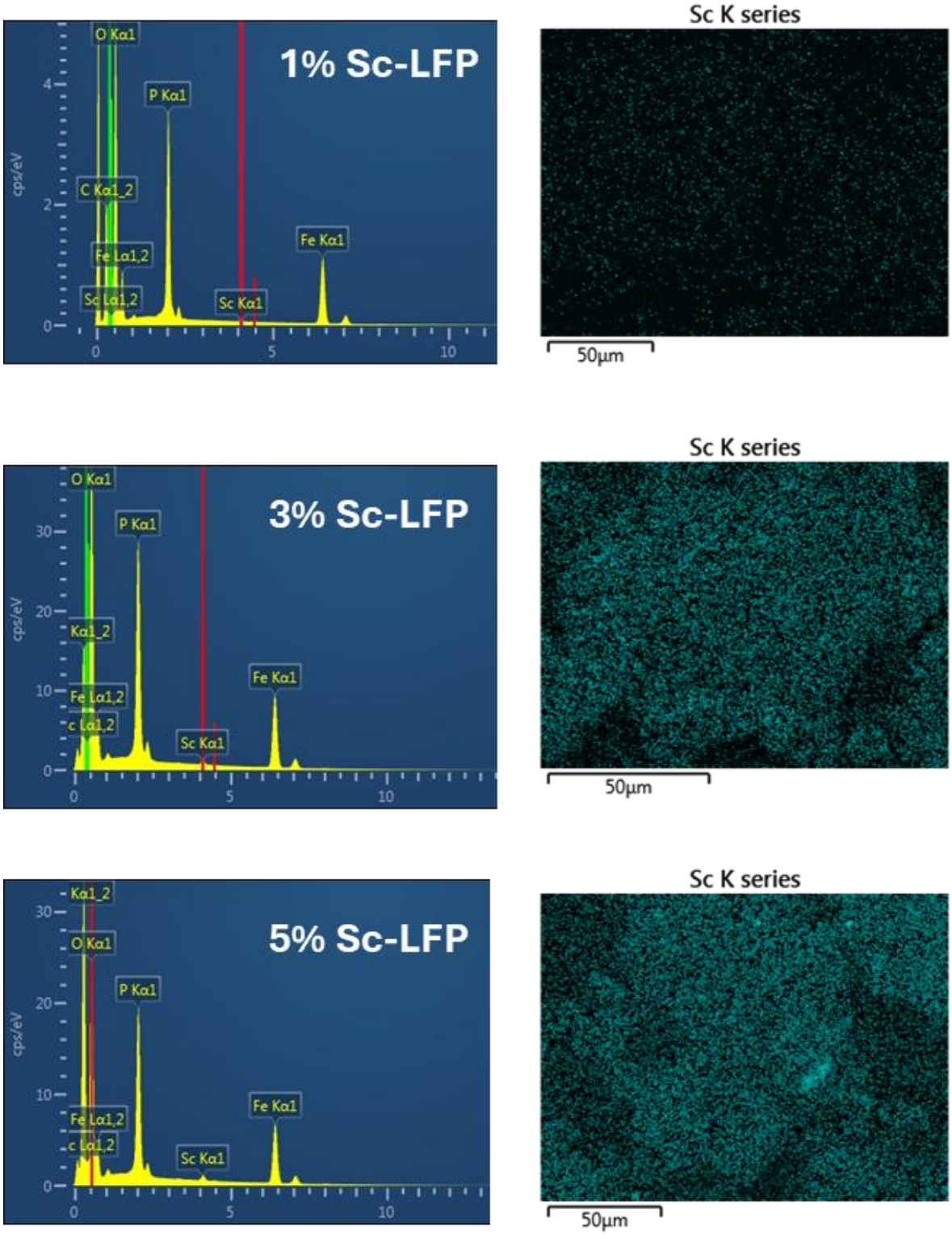

Figure 3.8 SEM-EDX maps and spectra showing the different concentrations of Sc, indicating minimal difference in Sc concentration between the 3% and 5% samples.

3.3. Structural Differences

3.3.1. XRD Refinements

XRD refinements were carried out on all synthesised samples, as well as a commercially available LFP material purchased from Gelon Lib Group Co., Ltd. and the V-LFP analogue synthesised by colleagues at UCL.[107] GSAS-II was the software used for all refinements, and they were performed against LFP CIF file ICSD-92198.[128,141]

The Rietveld refinement carried out on the undoped LFP synthesised in-house can be seen in **Figure 3.9** where 'obs' denotes the recorded XRD pattern and 'LFP' refers to the CIF file used in the refinement (ICSD-92198).[128] All other refinements can be seen in **Appendix I**.

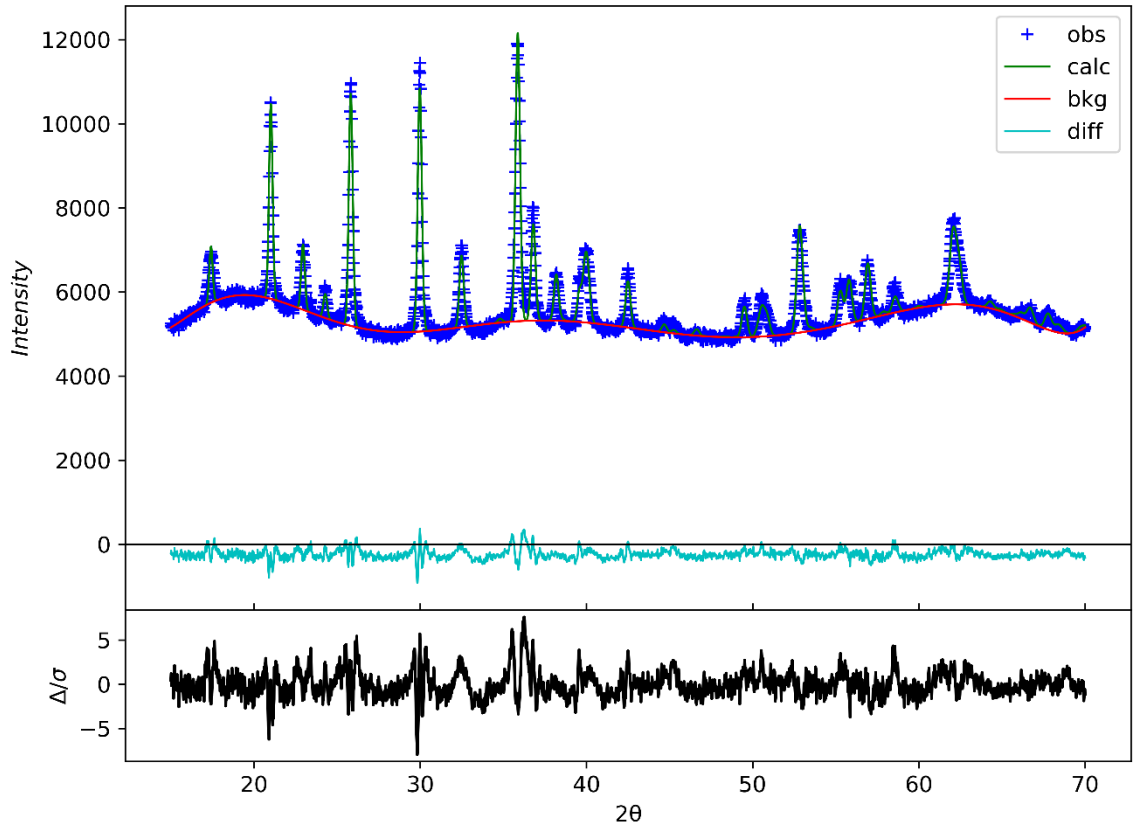

Figure 3.9 Rietveld refinement of undoped LFP against LFP ICSD-92198 CIF file using GSAS-II; R_W = 1.999%.

The lattice parameters and cell volumes are listed in **Table 3.1**, with detailed estimates of lattice strain for each analogue found in **Appendix I.**

Table 3.1: Lattice parameters, weighted residual %, and goodness-of-fit values of all the samples measured throughout this thesis.

Sample	a (Å)	b (Å)	c (Å)	Volume (Å^3)	Weighted residual, R_W %	Goodness-of-fit (GOF)
ICSD 92198	10.329	6.006	4.691	291.023	–	–
Gelon LFP	10.327(5)	6.006(2)	4.692(3)	291.001(2)	2.743	4.41
LFP	10.319(3)	6.004(3)	4.695(1)	290.916(2)	1.999	1.50
1% Ho-LFP	10.321(4)	6.005(2)	4.693(2)	290.967(1)	3.019	2.89
1% Yb-LFP	10.317(1)	6.000(5)	4.700(5)	290.949(3)	2.924	2.15
20% V-LFP	10.316(4)	5.999(2)	4.700(2)	290.873(1)	2.379	6.66
1% Al-LFP	10.325(5)	6.005(2)	4.694(2)	291.022(1)	3.674	2.11
3% Al-LFP	10.320(8)	6.006(3)	4.694(3)	290.945(2)	3.406	3.25
5% Al-LFP	10.321(1)	6.005(4)	4.694(4)	290.963(3)	3.500	1.64
1% Sc-LFP	10.321(1)	6.004(5)	4.696(4)	290.980(3)	4.105	2.28
3% Sc-LFP	10.323(8)	6.005(3)	4.695(3)	291.004(2)	3.866	3.98
5% Sc-LFP	10.323(1)	6.003(7)	4.696(6)	291.039(4)	3.396	3.12

It is difficult to follow any trends between cell volumes and doping concentrations. Only for the Sc-doped samples there seems to be a small increase in volume when dopant is added. Gelon LFP and V-LFP show larger volumes which are justified since they were obtained externally and not synthesised in-house. Instead, the volumes decrease when the concentration of Al-doping increases. This could be attributed to aluminium occupying different sites in the structure as doping varies.

Four different *hkl* plane directions were selected to gather an estimate of lattice strain percentage along different axes and planes of the samples (**Figure 3.10 (a)**). The largest variation and highest strain amongst samples is seen along the *c*-axis across the <0 0 2> *hkl* plane, whereas the least variation is observed along the *b*-axis across the <0 2 0> *hkl* plane direction. The values obtained for strain are used as estimates to gain insight into the effects of the dopants.

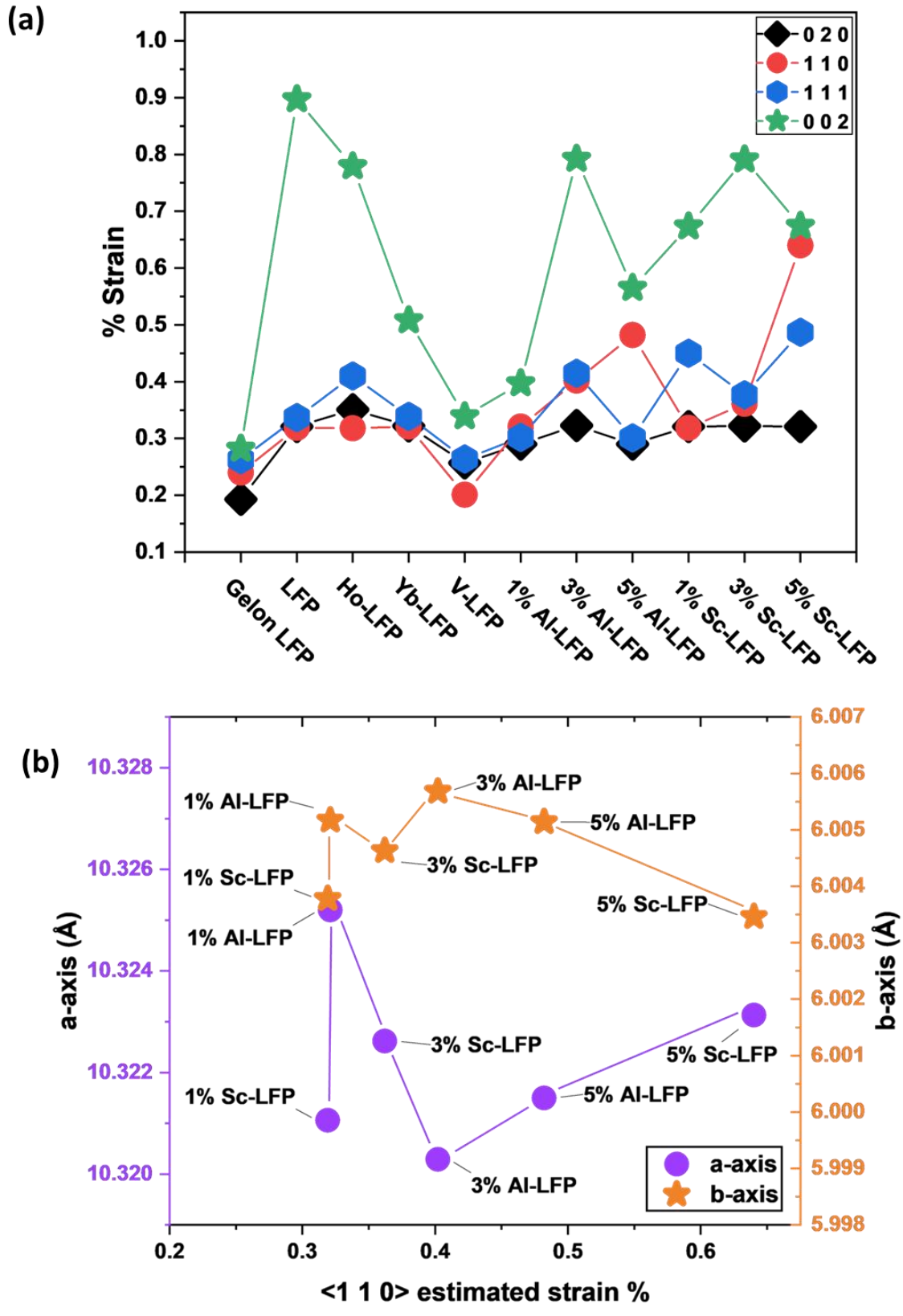

Figure 3.10: (a) % Estimated lattice strain for each sample across four different planes within the crystal lattice; (b) % Estimated lattice strain for Al- and Sc-doped samples across the <1 1 0> plane.

The expected trend would be an increase in strain as the dopants are added to the LFP. For the Al- and Sc-doped samples, however, it is demonstrated that strain has a maximum concentration of 3% particularly along the <0 0 2> plane. This agrees with EDX data previously discussed, showing that there is a maximum concentration achievable at around 3%, since at 5% doping results in lower element intensity, with the excess likely not entering the crystal lattice and sitting on the surface as $AlPO_4$.

Along the <1 1 0> plane, strain is noted to increase with increasing dopant concentration (**Figure 3.10 (b)**). The increase in strain for the Al-doped samples is fairly consistent, with ~ 0.08% increments on shifting from 1% to 3% to 5% dopant concentration. For the Sc-doped samples, the increases in strain are not consistent, with a fairly small increase of 0.042% from 1% to 3% concentration, followed by a large increase of 0.279% in strain from 3% to 5% scandium concentration.

Despite this, there is no trend between the *a-b* lattice parameters and the strain increase. In fact, the Al-doped samples display different behaviours when compared to the Sc-doped samples when plotting lattice parameters *versus* strain. Again, this may be explained by the fact that the doping site differs between Al-LFP and Sc-LFP, i.e., while Sc^{3+} only occupies an Fe-site, resulting in a trend between strain and *a-b* lattice parameters, Al^{3+} has different site occupation so it is more difficult to elucidate a trend. As discussed previously, with increasing Al^{3+} concentration the likelihood of Li-site doping also increases and this was demonstrated by the upshift in the XRD peak at ~35.7 ° (**Figure 3.3 (a)**). This difference in behaviour between Al- and Sc-doping suggests a difference in doping site, with Li-site doping occurring in the Al-LFP and Fe-site doping in the Sc-LFP.

Another property known to affect the electrochemical behaviour is the crystal size. An estimate of the average crystal domain size was calculated using the Debye-Scherrer equation for each of the < *hkl* > planes considered:

$$D = \frac{K\lambda}{\beta \cos\theta} \qquad [\mathbf{3.1}]$$

where D is the particle size, K is the Scherrer constant (0.98), λ is the wavelength of the incident X-ray (in this case, Cu K_{α_1} = 1.54 Å), β is the full width at half maximum, and θ is the Bragg angle of the peak being investigated. The estimates obtained for the crystal domain sizes of the samples were not corrected

for instrumental broadening; therefore, the estimated sizes are likely to be smaller than the actual ones.

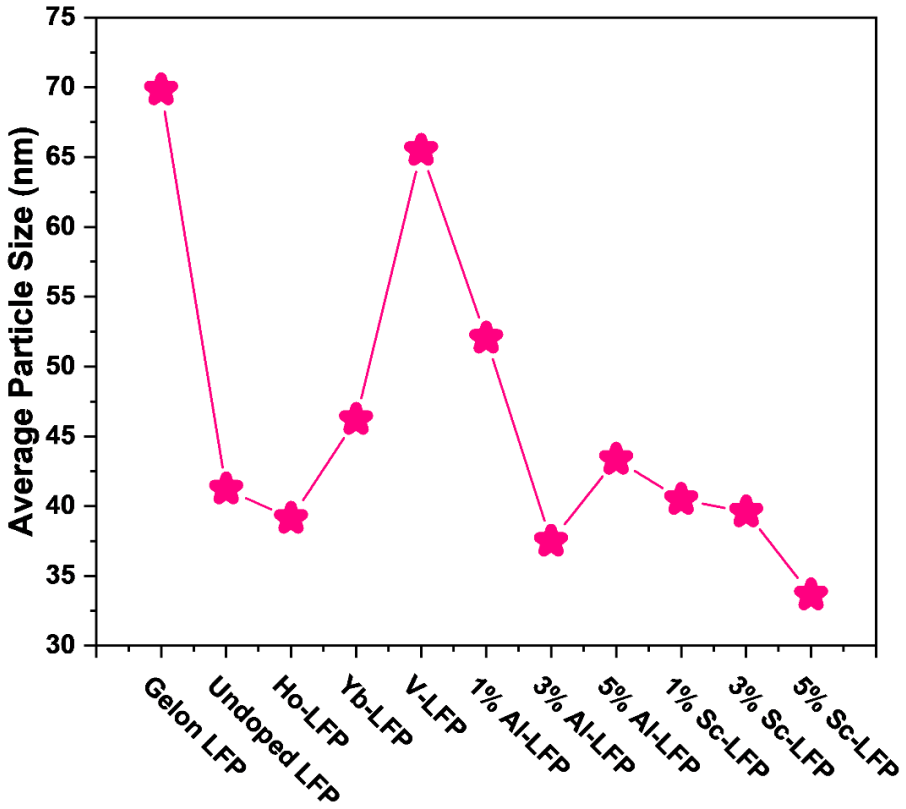

Figure 3.11: Average crystal domain size calculated for each sample investigated using peaks at approximate angles of 17, 24, 25, and 29 °2θ.

An interesting observation can be made with regards to the externally procured samples, Gelon LFP and V-LFP, when compared to those synthesised in-house whereby the average crystal domain sizes for the former are larger than those of the latter (**Figure 3.11**).

A trend can be observed for the Sc-doped samples, where an inverse relationship exists between dopant concentration and crystal domain size. Indeed, this is reduced when doping concentration increases, with a minimum crystal domain size observed for 5% Sc-doping, which could be attributed to the higher concentration of scandium resulting in smaller grains.

The variations in cell lengths are linked to the site occupation of the dopant in the crystal structure of LFP. The drastic decrease in crystal domain size with increasing aluminium concentration (from 1% to 3%) is linked to the Li-site substitution which decreases the volume slightly, and therefore the crystal domain

size of the material. This observation is in agreement with the XRD patterns recorded for the Al-doped LFP samples whereby an upshift of the peak at ~35.7 ° was noted, which was in accordance with Li-site occupation of Al^{3+}, as reported in the literature.[63,143,145]

3.4. Electrochemistry

3.4.1. Galvanostatic Cycling

All materials were cast as electrodes and used as cathodes in both coin and pouch cells. For the purpose of this section, all cathodes were measured at C/10 as coin cells between 2.4 and 3.9 V *versus* lithium metal anode with EC : DEC (1:1 v/v) in 1 M LiTFSI as the electrolyte.

Table 3.2: Discharge specific capacities of all samples after 1 and 5 full charge-discharge cycles.

Sample	Discharge capacity after 1 cycle (mAh g^{-1})	Discharge capacity after 5 cycles (mAh g^{-1})
Gelon LFP	138	143
LFP	102	115
Ho-LFP	108	107
Yb-LFP	96	111
V-LFP	112	127
1% Al-LFP	81	94
3% Al-LFP	85	98
5% Al-LFP	84	108
1% Sc-LFP	106	118
3% Sc-LFP	90	106
5% Sc-LFP	89	90

The above discharge capacity values were obtained after applying the same tests and cycling parameters and measured after the first and fifth charge-discharge

cycles, so as to avoid any bias. The Gelon LFP sample is treated as a reference sample for comparison with literature values.

The charge-discharge curves all follow the same behaviour, with the charge capacity being higher than the discharge capacity due to a number of factors, of which the dominant cause is the cathode-electrolyte interphase (CEI) formation. Similar behaviour is also observed whereby the fifth cycle discharge capacity is higher than the first cycle discharge capacity, which could indicate complete formation of CEI as well as the completion of any side reactions which could interfere with the complete Li-ion extraction/insertion mechanism as the battery is cycled.

From **Table 3.2** it is observed that none of the samples reach the theoretical value of 170 mAh g^{-1} for LFP.[147] As expected, the commercial sample, Gelon LFP (**Figure 3.12**), showed the highest discharge capacities of around 140 mAh g^{-1}, which is understandable since this material has been highly optimised and is distributed for commercial use thus making it a good benchmark. However, for the LFP samples synthesised in-house using the solvothermal method, lower capacities of around 100 mAh g^{-1} were demonstrated.

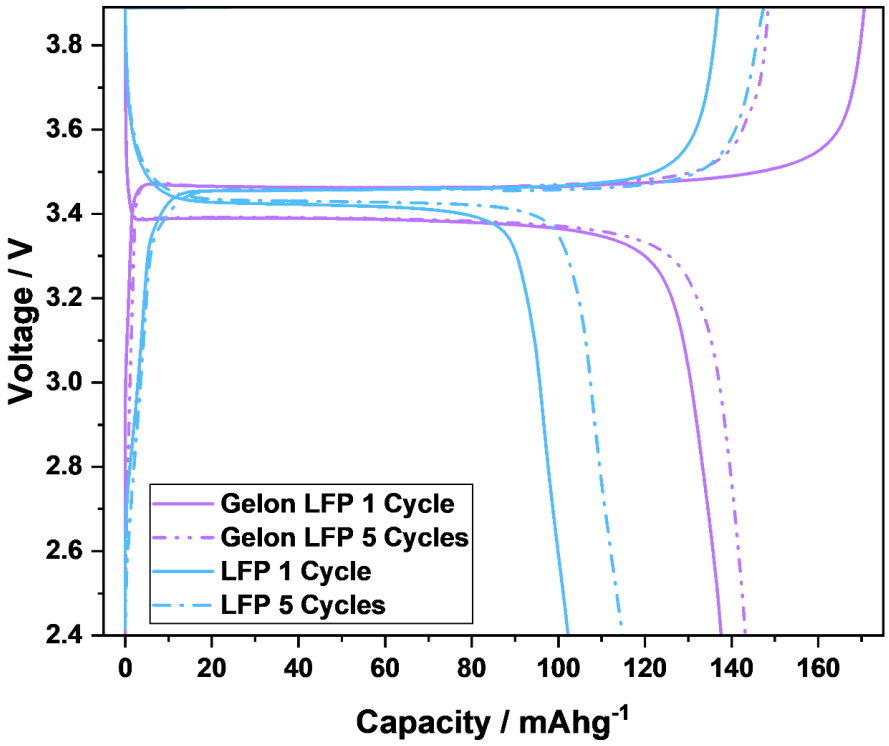

Figure 3.12: Charge-discharge curves after 1 and 5 cycles for Gelon LFP and undoped LFP (synthesised in-house) at C/10.

An interesting trend is noted for the Al- and Sc-doped LFP (**Figure 3.13 (a)** & **(b)**, respectively) whereby an overall increase in capacity was seen with increasing concentrations of aluminium, however, the opposite trend is observed with increasing concentrations of scandium. This could be due to the overall volume of the lattice being smaller for the 5% Al-LFP and 1% Sc-LFP, therefore providing a shorter pathlength for the Li-ion to traverse across, making the overall intercalation and deintercalation processes more efficient. Despite increased specific capacities, they are less than or similar to those observed for the undoped LFP sample. Discharge capacities of ~110-130 mAh g^{-1} for 20% V-LFP, on the other hand, is in good agreement with previous studies by Johnson *et al.* which used 1 M $LiPF_6$ in 3 : 7 v/v in EC : EMC as the electrolyte.[107,148]

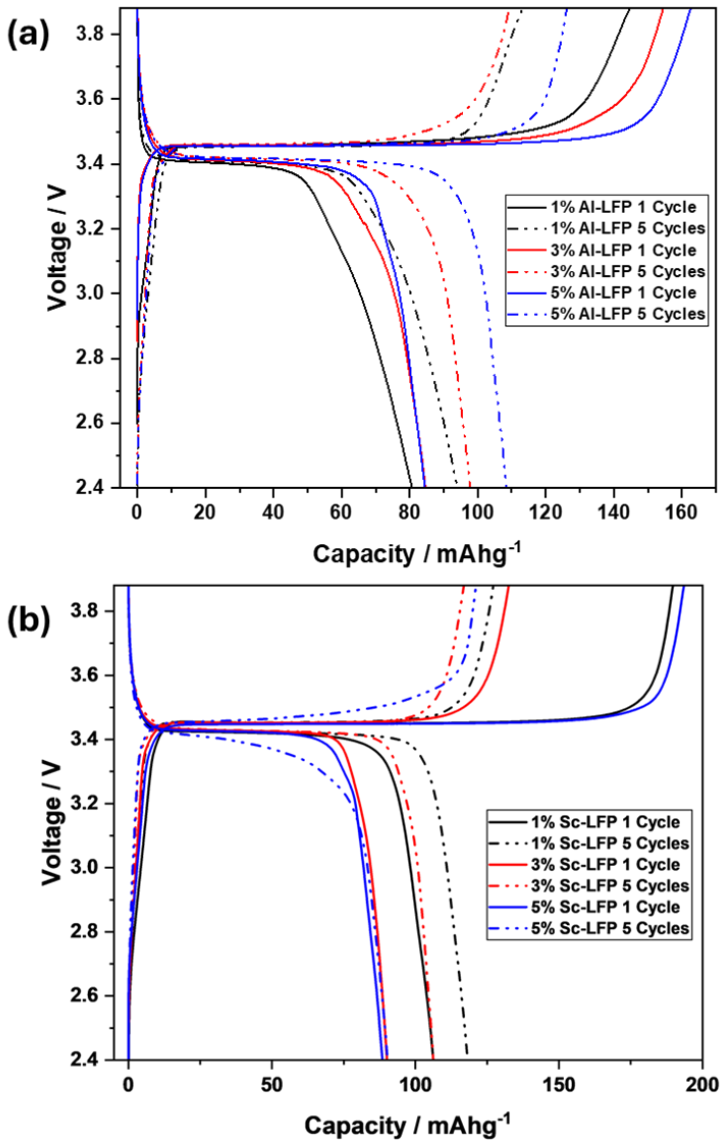

Figure 3.13: Charge-discharge curves after 1 and 5 cycles for different concentrations of (a) Al-LFP and (b) Sc-LFP at C/10.

It is important to note that in the charge-discharge curves of V-LFP (**Figure 3.14**), there is only one plateau observed indicating that even at as high a concentration as 20%, vanadium is not redox active despite the presence of the $LiVP_2O_7$ impurity, which is known to be electrochemically active.

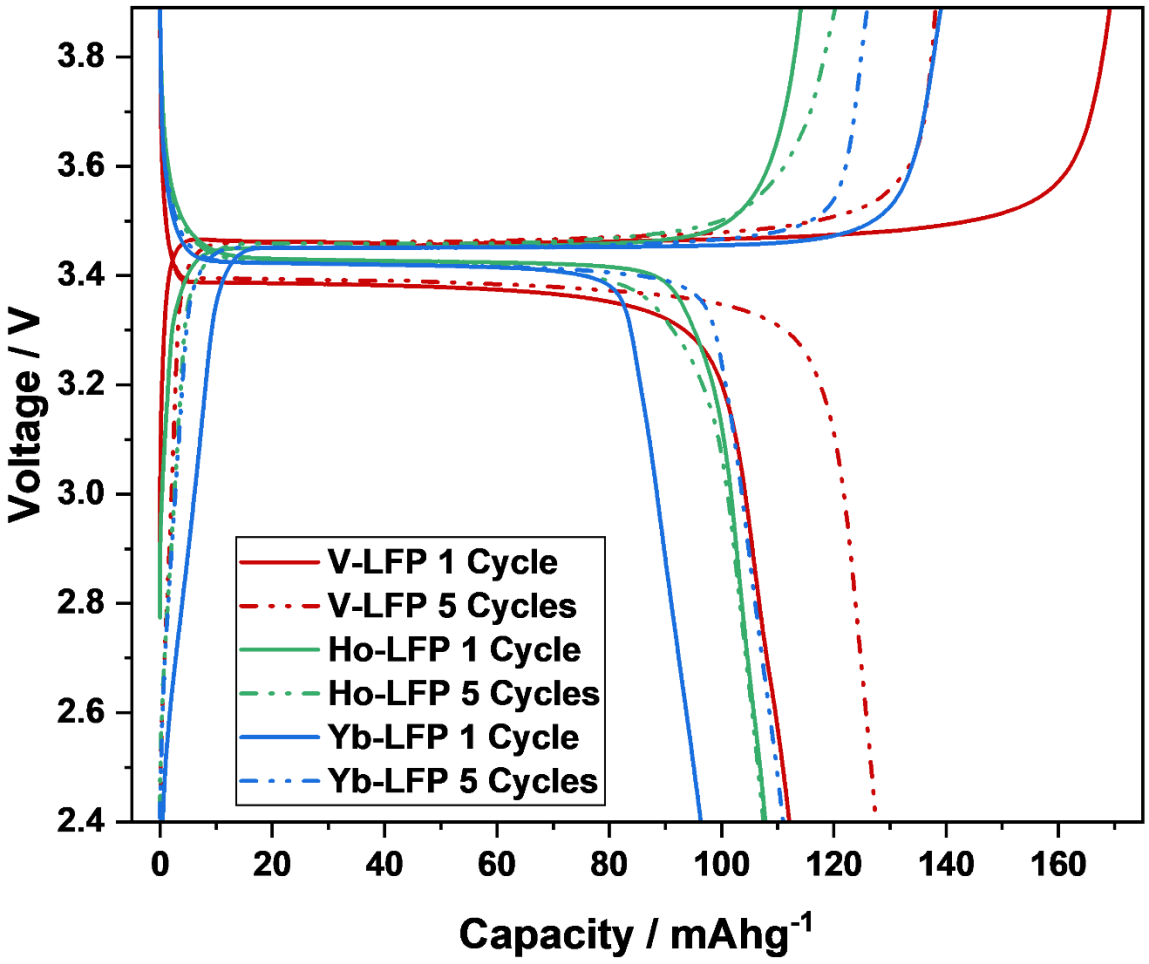

Figure 3.14: Charge-discharge curves after 1 and 5 cycles for V-LFP, Ho-LFP, and Yb-LFP at C/10.

The Yb-LFP showed a marked improvement from the first to the fifth cycle, which was not seen in the Ho-LFP plot where the first and fifth cycles (**Figure 3.14**) gave similar discharge capacities, which indicates a high cycle efficiency for the material. The presence of holmium may improve CEI formation, therefore enhancing the performance of the cell, which showed minimal differences in discharge capacity as it was cycled. Despite the poor improvement in specific capacity as a function of doping in LFP, the polarisation of the samples is improved for low levels of dopants. This is particularly seen in the Ho-, Yb-, and 1% Sc-LFP which show improved hysteresis during cycling (**Figures 3.13 (b)** and **3.14**).

3.4.2. Cyclic Voltammetry

To further understand the cycling behaviours of each material, cyclic voltammetry (CV) and electrochemical impedance spectroscopy (EIS) were carried out after 1 and 5 cycles for each material at C/10.

It is presumed that the Li ions are dominating the transport process, therefore the concentration is assumed to be equivalent to the number of Li ions being transported per charge-discharge cycle. The calculated Li-ion diffusion coefficients are given in **Table 3.3**.

Table 3.3: Li-ion diffusion coefficients for anodic and cathodic processes after 1 and 5 cycles for each material, calculated using the Randles–Ševčík equation.

Sample	**Cathodic D_{app} after 1 cycle (cm^2/s)**	**Anodic D_{app} after 1 cycle (cm^2/s)**	**Cathodic D_{app} after 5 cycles (cm^2/s)**	**Anodic D_{app} after 5 cycles (cm^2/s)**
LFP	0.85×10^{-7}	0.47×10^{-7}	0.91×10^{-7}	0.63×10^{-7}
Ho-LFP	2.63×10^{-7}	2.05×10^{-7}	1.35×10^{-7}	0.86×10^{-7}
Yb-LFP	3.20×10^{-7}	1.83×10^{-7}	2.05×10^{-7}	1.11×10^{-7}
V-LFP	0.69×10^{-7}	0.34×10^{-7}	1.38×10^{-7}	0.89×10^{-7}
1% Al-LFP	0.98×10^{-7}	0.55×10^{-7}	1.30×10^{-7}	0.66×10^{-7}
3% Al-LFP	0.55×10^{-7}	0.32×10^{-7}	1.04×10^{-7}	0.61×10^{-7}
5% Al-LFP	5.55×10^{-7}	0.34×10^{-7}	1.56×10^{-7}	0.88×10^{-7}
1% Sc-LFP	2.53×10^{-7}	1.35×10^{-7}	4.16×10^{-7}	2.16×10^{-7}
3% Sc-LFP	2.64×10^{-7}	1.66×10^{-7}	6.75×10^{-7}	3.03×10^{-7}
5% Sc-LFP	0.94×10^{-7}	0.62×10^{-7}	0.27×10^{-7}	0.16×10^{-7}

The Randles–Ševčík equation was used to calculate the aforementioned Li-ion diffusion coefficients, however it is important to acknowledge that these are better used as estimates due to a number of limitations. The slow scan rate used in collecting the CVs can cause the diffusion layer thickening due to the porous nature of the electrode, and the surface effects can lead to a significant portion of the charge transfer to occur at or near the surface of the electrode, which makes it difficult to

measure bulk diffusion of the material. This is seen in the calculated D_{app} values, which are several orders of magnitude higher than those reported in literature for similar materials.[71,100,107]

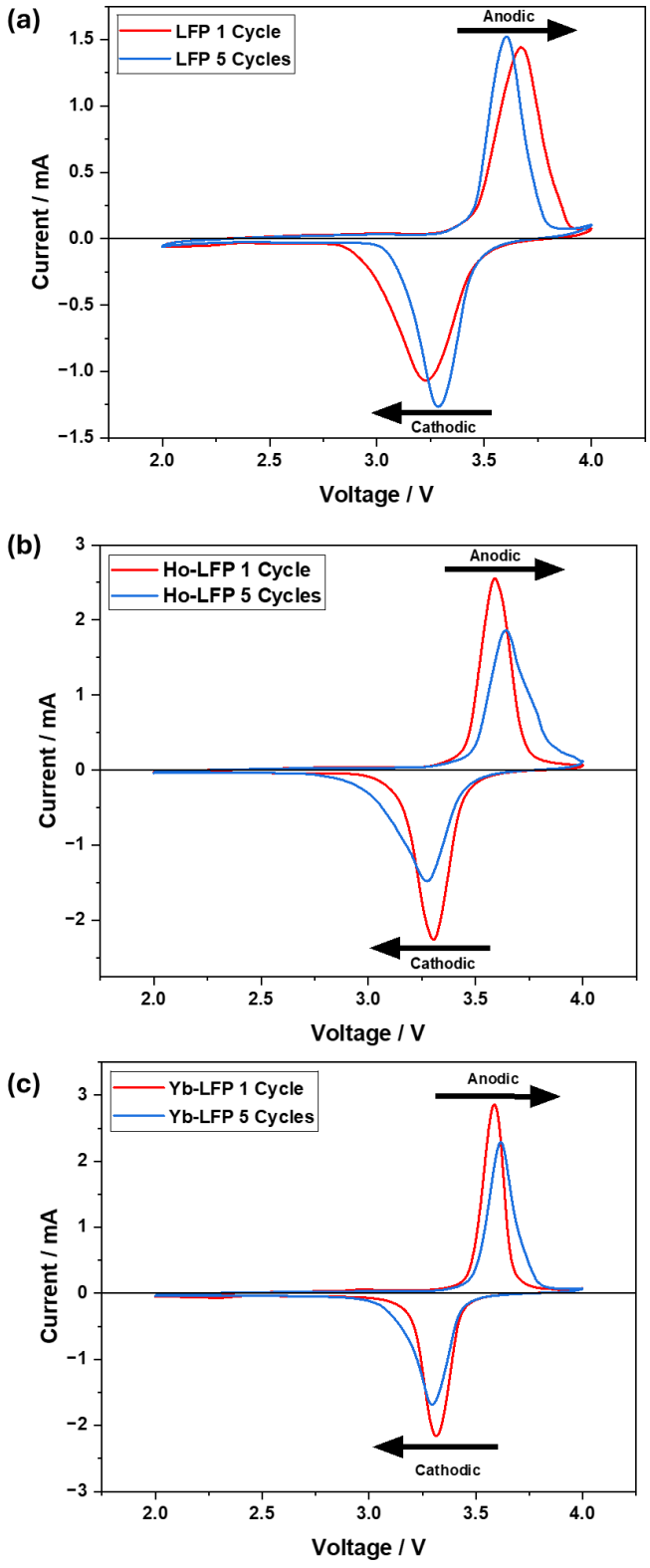

Figure 3.15: Cyclic voltammograms after 1 and 5 cycles for (a) undoped LFP; (b) Ho-LFP; and (c) Yb-LFP.

The cyclic voltammogram for the undoped LFP indicated an improvement in peak current from the first to fifth cycle, with both ip_a and ip_c increasing, whilst peak separation decreased, implying a higher reversibility once the CEI formation is completed (**Figure 3.15 (a)**). On the other hand, Ho-LFP and Yb-LFP showed an opposite trend (**Figure 3.15 (b)** & **(c)**), with peak current decreasing from the first to the fifth cycle, and also showing an increase in the peak separation proposing a reduced reversibility in agreement with the calculated diffusion coefficients that decrease from the first to the fifth cycle. However, overall, despite this decrease both Ho-LFP and Yb-LFP had higher ip_a and ip_c values and diffusion coefficients (**Table 3.3**) for both the first and fifth cycle CVs when compared to the undoped analogue, indicating that the presence of the dopants is increasing the Li-ion mobility therefore resulting in better cycling capabilities.

When discussing the Al-doped LFP analogues, a marked increase in both anodic and cathodic peak currents are observed from the first to the fifth cycle for all concentrations of Al-LFP (1, 3, and 5%; **Figure 3.16**). Peak separation does not change by much from the first to the fifth cycle for 1% Al-LFP, with only a slight increase observed for the 3% and 5% Al-LFP analogues. Also, the diffusion coefficients calculated are similar for all concentrations (**Table 3.3**).

1% and 3% Sc-LFP demonstrate an increase in peak currents and a decrease in peak separation from the first to the fifth cycle (**Figure 3.17**), suggesting improved reversibility as the battery is cycled. This observation agrees with the improved ionic conductivity reported in **Table 3.3**. Instead, the 5% Sc-LFP analogue showed an opposite trend, with a drastic decrease in peak current and significant profile distortion from the first to the fifth cycle. An anomaly appeared in the CV of the first cycle, both upon the anodic and cathodic processes which may indicate interference from an impurity phase that arises due to the higher concentration of dopant, which also agrees with the reported diffusion coefficients which decrease for higher scandium concentrations (**Table 3.3**). The peak profile of the Sc-LFP samples improved from the 1% to the 3% concentration, with a deterioration observed when going to 5% Sc concentration in LFP.

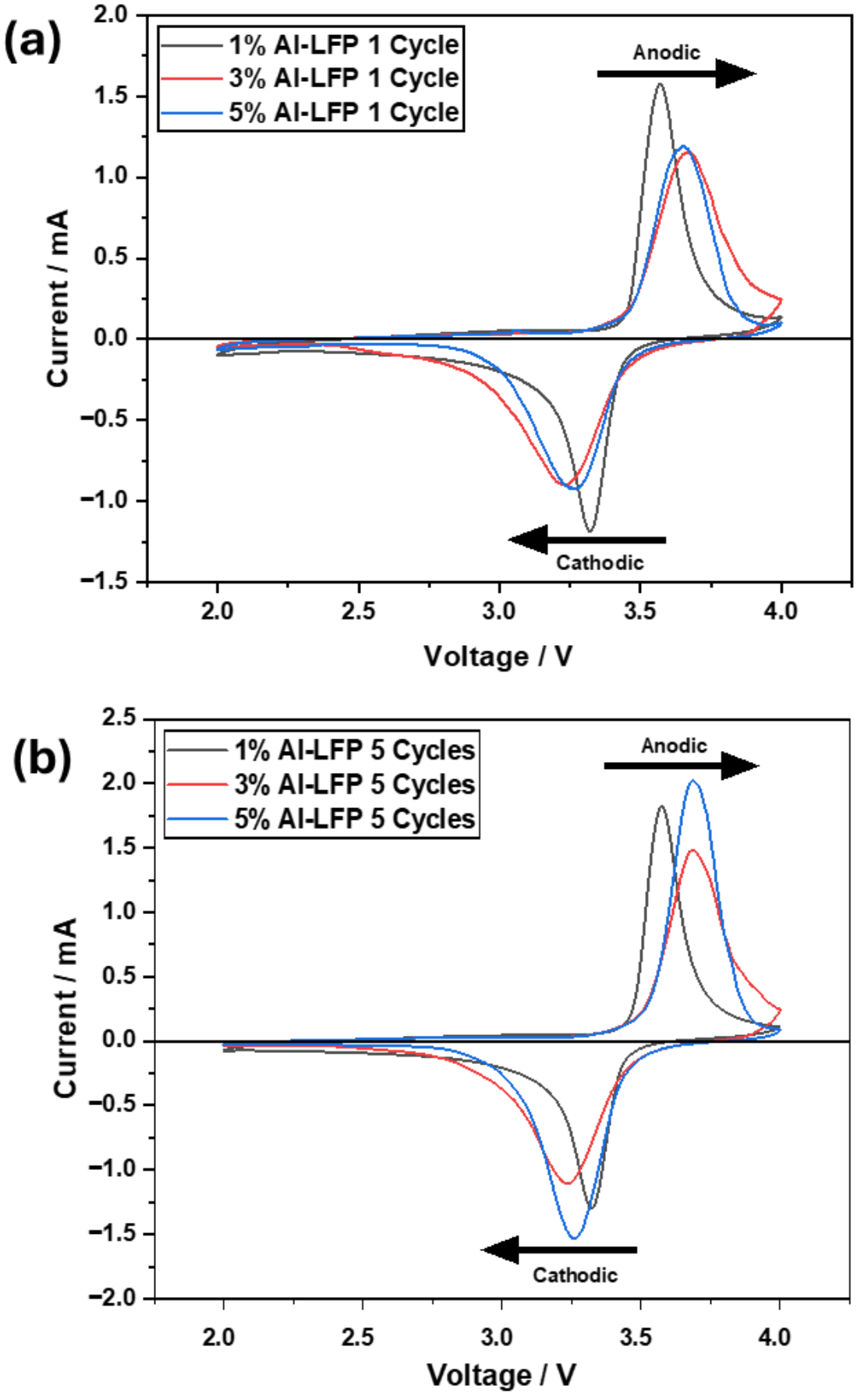

Figure 3.16: Cyclic voltammograms for (a) Al-LFP after 1 cycle and (b) Al-LFP after 5 cycles.

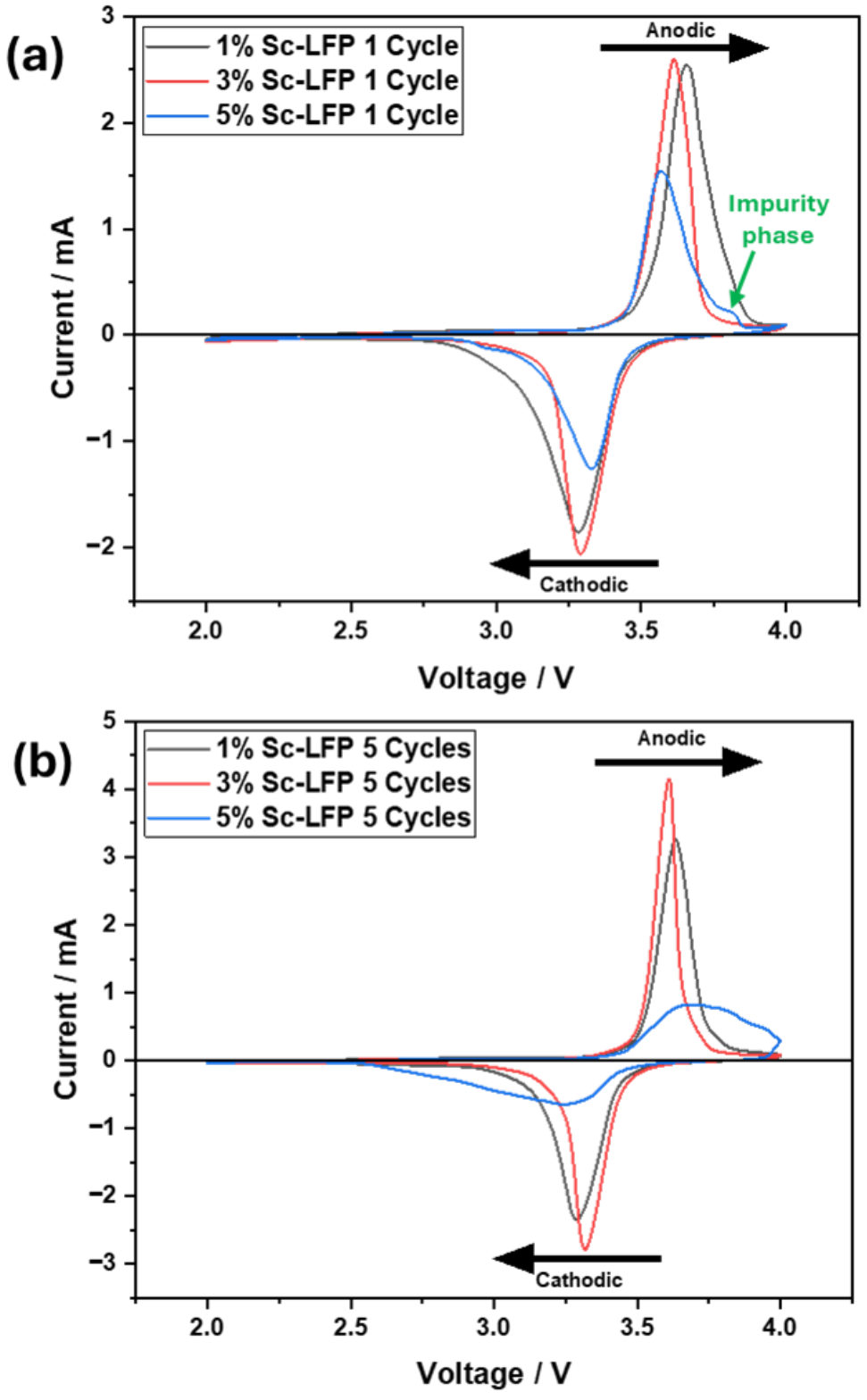

Figure 3.17: Cyclic voltammograms for (a) Sc-LFP after 1 cycle and (b) Sc-LFP after 5 cycles.

3.4.3. Electrochemical Impedance Spectroscopy

In addition to the CV measurements, the samples were also analysed using EIS using a two-electrode system. All impedance spectra were fitted to the same equivalent circuit model, which was comprised of R_s, the solution resistance, R_{ct}, the charge-transfer resistance representing the electrochemical reactions occurring between the electrodes and electrolyte, M_α, a restricted diffusion element, a constant phase element, CPE, which represents double layer capacity, and W_δ which represent the Warburg impedance associated with Li-ion diffusion.

The restricted diffusion element, M_α, was included in the equivalent circuit in order to account for the presence of lattice distortion effects that may be occurring due to the presence of the dopant cations which would, in turn, restrict the Li-ion diffusion as the battery is cycled. Including this element in the equivalent circuit fitting thus takes these effects into account and can adjust the quality of the fits accordingly.

It is important to note that the changes occurring at the lithium metal anode surface are taken into account when discussing the SEI formation and resistance values associated with this phenomenon.

Table 3.4: Solution and charge-transfer resistances after 1 and 5 cycles for each material.

Sample	R_s after 1 cycle (Ω)	R_{ct} after 1 cycle (Ω)	R_s after 5 cycles (Ω)	R_{ct} after 5 cycles (Ω)
LFP	11.57	156.00	12.72	69.10
1% Ho-LFP	6.84	44.39	5.40	189.80
1% Yb-LFP	4.63	54.10	3.69	79.30
20% V-LFP	2.07	157.90	2.34	185.90
1% Al-LFP	3.83	45.73	2.28	53.36
3% Al-LFP	4.17	115.60	4.91	115.70
5% Al-LFP	1.66	251.90	1.29	295.40
1% Sc-LFP	4.88	130.10	1.86	107.90
3% Sc-LFP	1.99	124.10	3.18	114.00
5% Sc-LFP	5.68	63.20	3.14	192.00

The undoped LFP EIS (**Figure 3.18 (a)**) indicates a decrease in resistance from first to fifth cycle, which follows regular impedance behaviour with no secondary phases and complete CEI formation by the fifth cycle. The opposite trend can be observed for Ho-LFP (**Figure 3.18 (b)**), with a drastic increase in R_{ct} seen between cycles 1 and 5, which may indicate incomplete CEI formation after the first cycle. This is further supported from the point of inflexion, which is further away from o Ω.

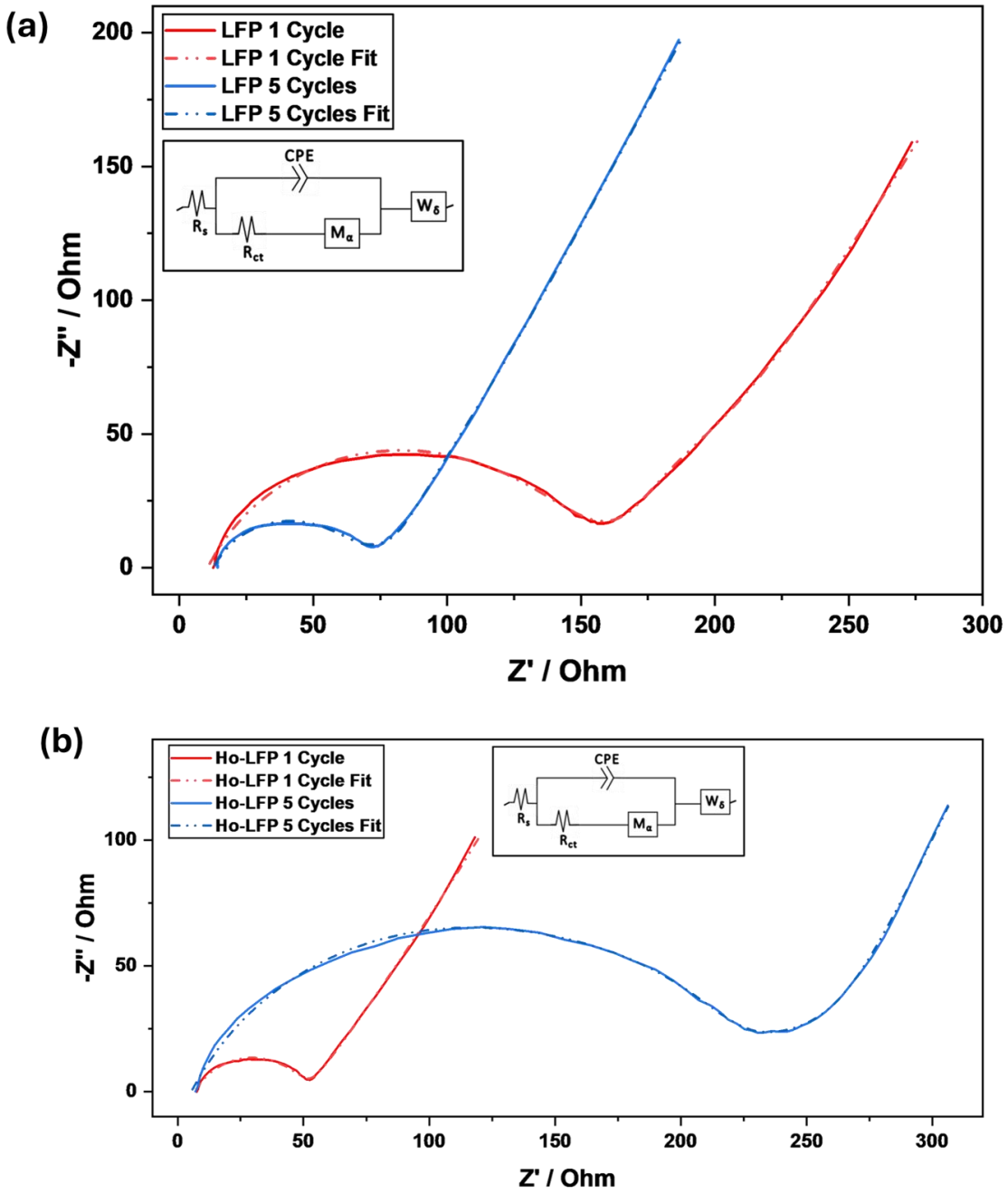

Figure 3.18: Electrochemical impedance spectra and their fits after 1 and 5 cycles for (a) undoped LFP; (b) Ho-LFP.

Yb-LFP EIS (**Figure 3.19**) follow the same trend as that observed for Ho-LFP, where an increase in R_{ct} is observed from the first to the fifth cycle. Both spectra (1st and 5th cycles) indicate the emergence of a second semicircle in the low-frequency region, which may be due to electrolyte-electrode reactions and the formation of CEIs. This could also be attributed to the $YbPO_4$ impurity phase which does not partake in the electrochemistry of the cell and may provide an additional layer of resistance. This can also be seen in the tail of the plot in the spectrum of the fifth cycle, where a curve is observed instead of a straight line representing restricted diffusion.

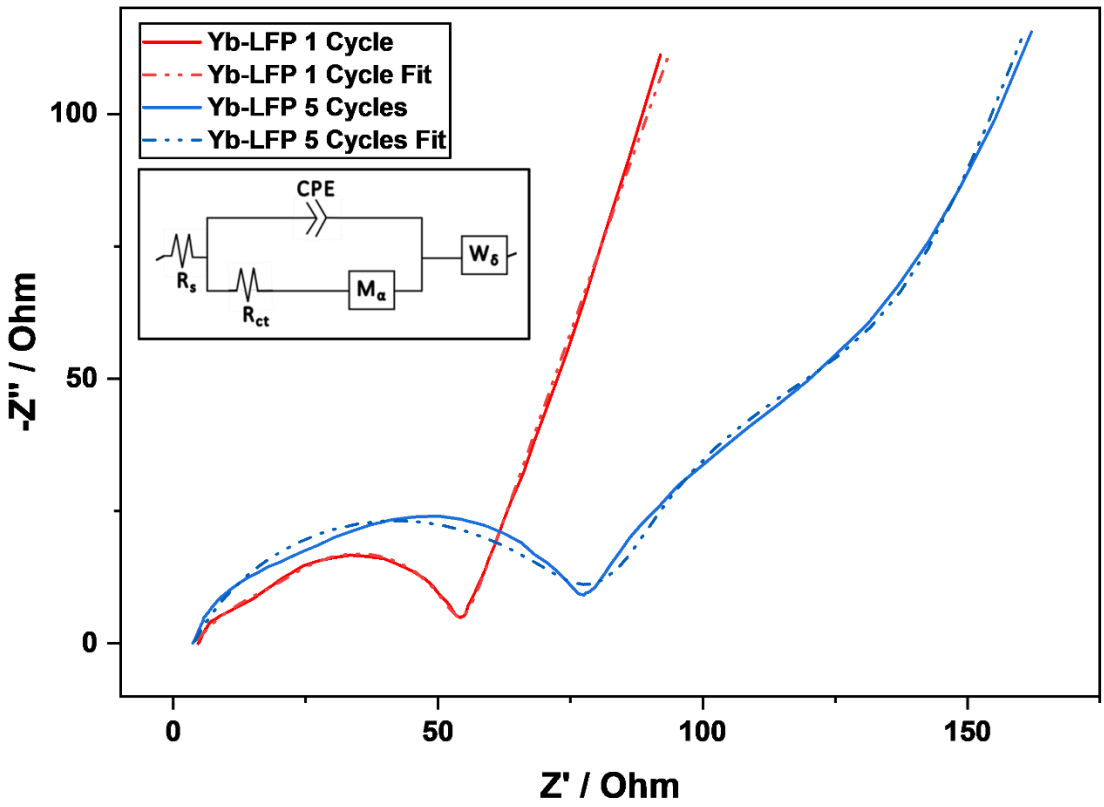

Figure 3.19: Electrochemical impedance spectra and their fits after 1 and 5 cycles for Yb-LFP.

In both Al- and Sc-doped LFP impedance spectra (**Figures 3.20** & **3.21**) the 1% concentration displays the best impedance: a single semicircle in the high-frequency region, followed by a linear Warburg impedance in the low-frequency region. This doping level also exhibits the lowest resistivity.

In fact, the 1% doped Al-LFP gives a value of 45.73 Ω after the first cycle and 53.36 Ω after the fifth (**Table 3.4**). The only other sample which gave a similar value after the first cycle was 1% Ho-LFP with 44.39 Ω. However, this value then increased to 189.90 Ω after the fifth cycle, which is in agreement with the previously discussed formation of CEI (**Figure 3.18 (b)**).

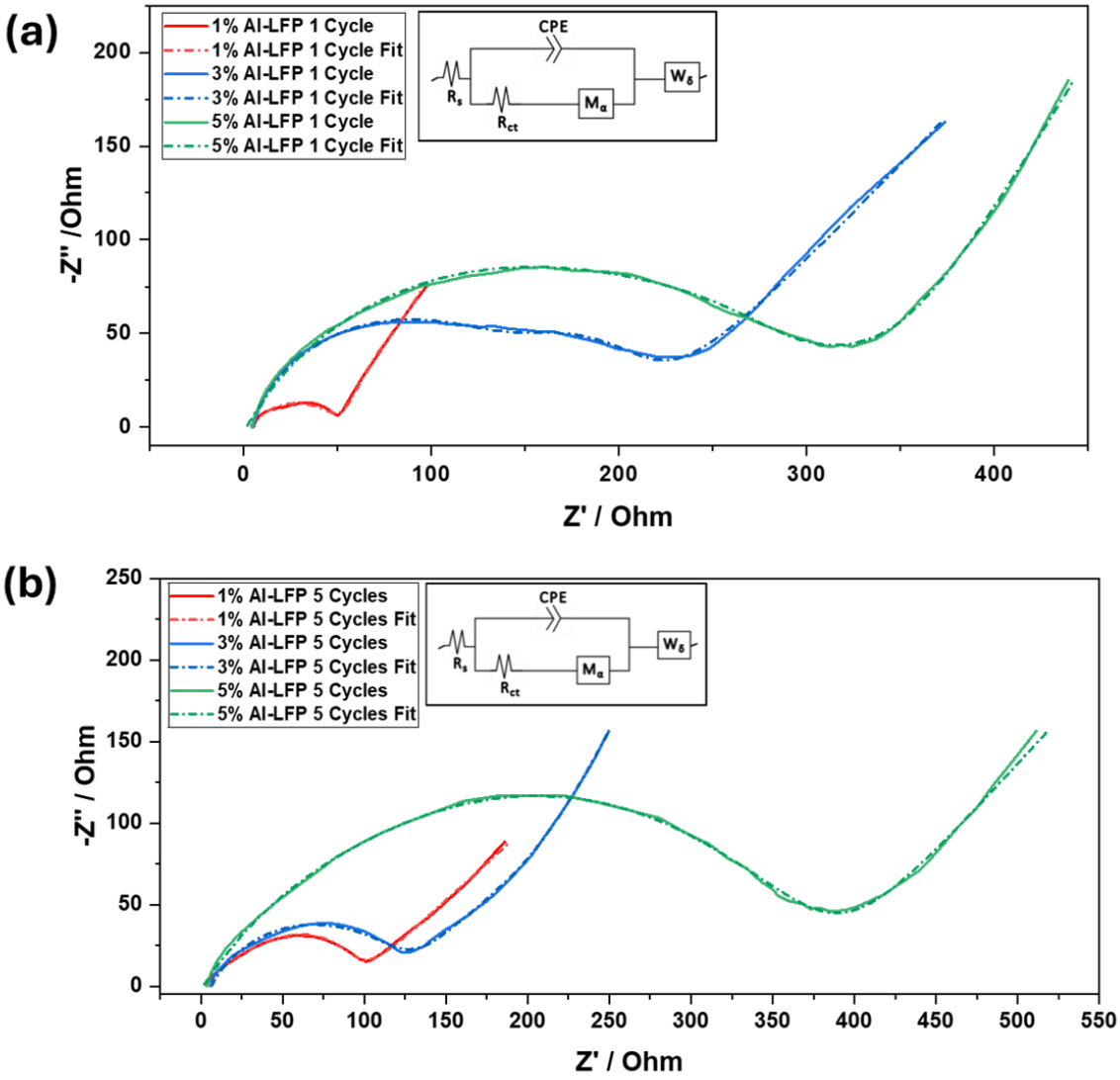

Figure 3.20: Electrochemical impedance spectra and their fits for (a) Al-LFP after 1 cycle and (b) Al-LFP after 5 cycles.

For the 3% and 5% Al and Sc-doped LFP samples, more complicated spectra emerge, with anomalies present at higher frequencies at the first semicircle, resulting in high internal resistances (**Table 3.4**).

These spectra contain features indicating incomplete reactions and possible CEI formation such as the emergence of secondary semicircles and/or curved tails rather than straight lines.

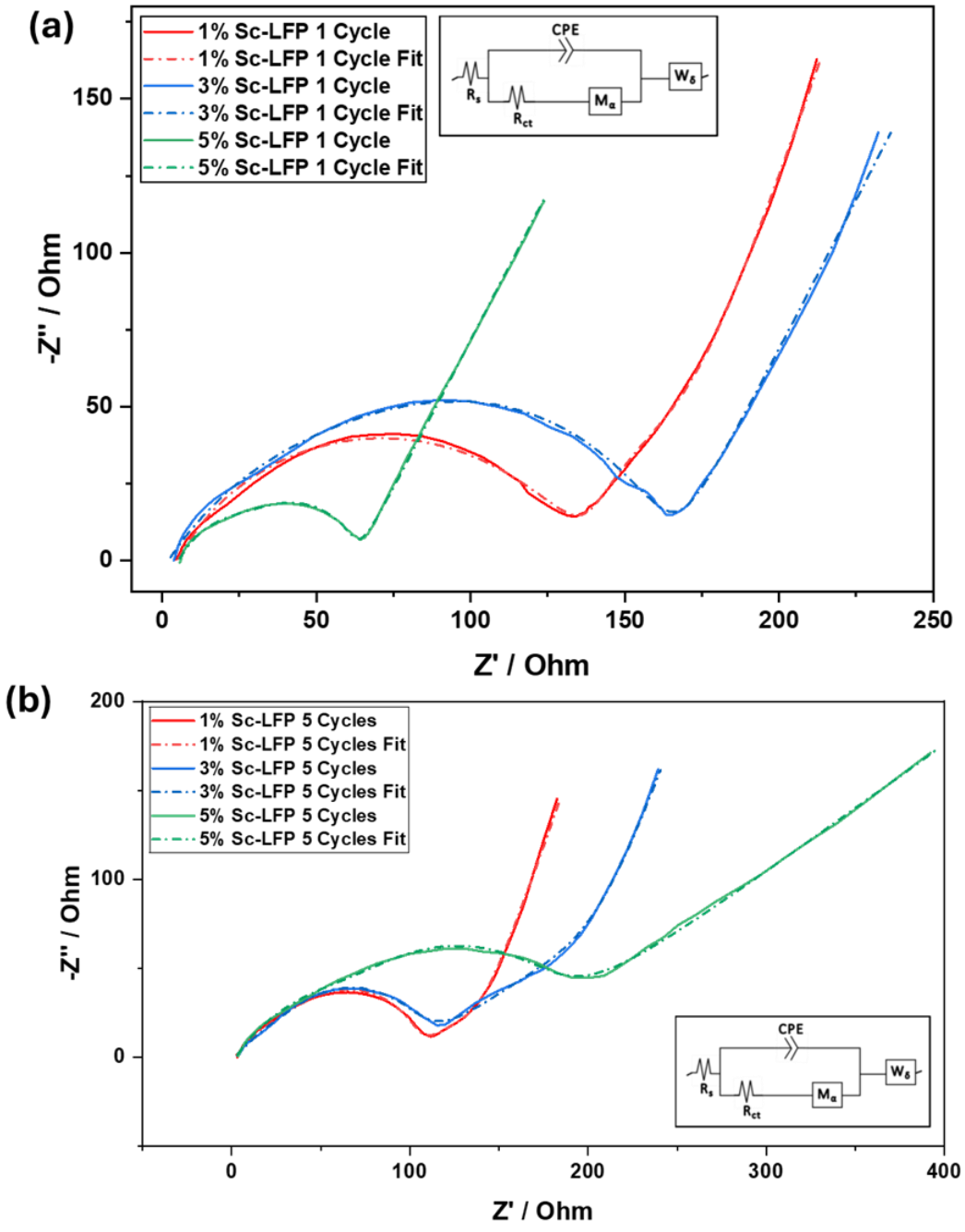

Figure 3.21: Electrochemical impedance spectra and their fits for (a) Sc-LFP after 1 cycle and (b) Sc-LFP after 5 cycles.

The general trend for the EIS studies is an improvement in spectra after 5 cycles for most materials. This could be due to the materials overcoming the SEI layer, thus decreasing the charge-transfer resistance, and facilitating the flow of Li-ions as the battery is cycled further.

3.5. Chapter Conclusions

The commercial sample, Gelon LFP, showed the best electrochemical performance followed by the V-LFP procured from colleagues at UCL.[107] This is unsurprising since these materials were already optimised when received, whereas the samples synthesised in-house were not. This being said, it was interesting to note that the average crystal domain sizes of the latter were all smaller than the former.

Trends were difficult to observe for the Al-doped samples due to the fact that the dopant was not occupying only Fe-sites, unlike the rest of the dopants; however, many were able to be elucidated for the Sc-doped LFP analogues. A decrease in average crystal domain size was noted with increasing scandium concentration, despite the slight increase in volume. An increase was also seen in estimated strain along the <1 1 0> plane with increasing concentration of scandium. However, a decrease in discharge capacity and Li-ion diffusion coefficient was noted at higher concentrations of scandium.

The opposite was observed for the Al-doped samples, where the Li-ion diffusion coefficient and discharge capacity were increasing with aluminium concentration. This is interesting considering that an increase in resistance is also noted at higher concentrations. This opposing trend could be due to the fact that at higher concentrations aluminium is occupying a Li-site, as the increase in resistance is in accordance with the literature.[63,143]

The fact that an impurity phase is present in the 1% Yb-LFP material could have hindered its electrochemical performance when compared to the other dopants. This is notable when comparing its calculated Li-ion diffusion coefficients to the values obtained for the other dopants. Despite this, it showed a better discharge capacity when compared to all Al-doped samples and the 3% and 5% Sc-doped samples. It also exhibited the lowest solution and charge-transfer resistance values after the fifth charge-discharge cycle (except for the undoped analogue), when compared to the other doped materials even though there was residual CEI formation which needed to be overcome. Attempts to leach out the $YbPO_4$ impurity phase using a weak acid were attempted, but proved unsuccessful, and within the scope of this thesis it was not of interest to reduce the concentration of ytterbium further.

From the electrochemical CV and galvanostatic measurements, the 1% Sc-LFP appears to be the best material in terms of balance between capacity and cyclability. However, only considering specific capacity and Coulombic efficiency, the 1% Ho-LFP material surpasses the other dopants in performance. Due to this, a closer investigation has been dedicated to this material and is presented in **Chapter 5**. The electrochemistry of V-LFP and Gelon LFP will be discussed in more detail in **Chapter 4**, as stated previously.

4.V-LFP: An Investigation of Excessive Doping

4.1. Chapter Introduction

Transition metals (TMs) are the most commonly used dopant in lithium iron phosphate, with first-row TMs preferred. The ionic conductivity of LFP has been reported to improve by up to 7 orders of magnitude, from $>10^{-2}$ S cm^{-1} to 10^{-9} – 10^{-8} S cm^{-1} when doped with cations, such as Ni^{2+}, Mo^{4+}, Zr^{4+}, and W^{6+} amongst others.[74,80,149–151]

Vanadium has been used to dope LFP extensively in Li, P, and Fe sites with the latter being the most frequent and effective at improving the cycling capabilities of the material.[81,107,152–163] Addition of minimal quantities of vanadium can aid the Li-ion diffusion in LFP at higher cycle rates by slightly distorting the crystal structure, but not straining the material in such a way that prevents it from reverting to its original structural parameters. This, therefore, improves the overall performance of LFP at higher current densities.[153,163]

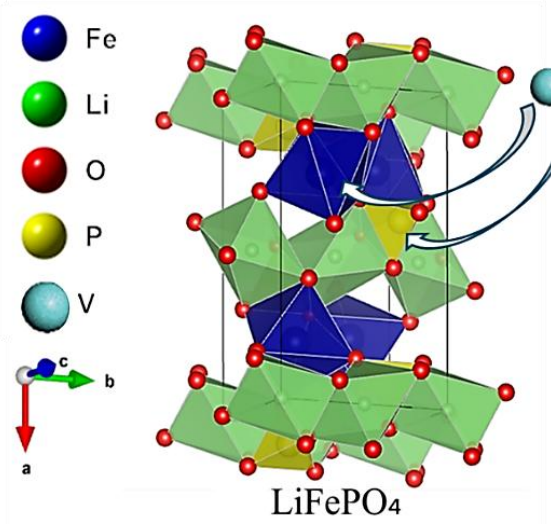

Figure 4.1: Crystal structure of LFP illustrating the different occupation sites of vanadium.

Vanadium is of particular interest as a dopant in LFP due to its multiple oxidation states, giving it the ability to dope at different sites in LFP (**Figure 4.1**), as well as its ability to form several electrochemically active species like $Li_3V_2PO_4$, $LiVOPO_4$, and V_xO_y.[157] It has been shown that the ideal concentration of vanadium as a dopant to improve the cyclability of LFP is between 5 and 10%, with the former showing more promising results.[107,152,160,162]

On the other hand, there has not been much investigation into the effects of higher concentrations of vanadium as a dopant in LFP and how this may affect the Li-ion mobility within the crystal lattice. This has implications for structural and electronic properties of the material with electrochemical performance. 20% V-doping has previously been studied extensively by Johnson and coworkers[107], however the latter study used 1M $LiPF_6$ in 3:7 v/v EC : ethyl methyl carbonate as an electrolyte, while throughout this thesis 1M $LiPF_6$ in 1:1 v/v EC : DMC and 1M LiTFSI in 1:1 v/v EC : DMC were used as electrolytes (**Table 2.1**). The former was used for benchmarking and comparison to literature, whilst the latter was used for XAS measurements. This chapter provides an extension to the detailed structural and electrochemical study by Johnson and coworkers[148,148] by studying the polarisation of the phosphate polyanion during battery cycling to understand whether this is impacted by the presence of vanadium. For completeness and reference with the previous studies, structural and electrochemical data have also been collected since different electrolytes are employed in this thesis.

Our colleagues at UCL have managed to produce a series of V-doped LFP nanoparticles through a continuous hydrothermal flow synthesis.[107] A combination of experimental and theoretical experiments have been used to show that vanadium can occupy both P- and Fe-sites in the LFP lattice, with $LiFe_{0.95}V_{0.05}PO_4$ showing the most promising results, such as a high power output even at high C-rates of 9C. They also managed to synthesise higher concentrations of dopant, such at the 20% V-doped analogue, which is investigated throughout this chapter. [107]

Structural, electrochemical, and spectroscopic analyses have been carried out on both powder and electrode samples of the 20% V-doped material, henceforth referred to as "V-LFP". These data were then compared to powders and electrodes of a commercial sample of undoped LFP (Gelon LFP) in order to elucidate the best comparison possible. The aim of this chapter is to study how the oxidation states of Fe and P K-edges vary during XAS measurements of different SOCs of the materials, and to determine what structural and electronic properties control the electrochemistry of Li-ion batteries. The analysis of the oxidation state and site occupation of vanadium in LFP is important, since it has been shown to attain multiple oxidation states, allowing it to occupy different cation sites in the LFP crystal lattice, with the likelihood of these effects increasing due to the high V concentration of 20% in this sample.

4.2. Methodology

The 20% V-LFP was obtained from I.D. Johnson *et al.* at UCL[107] and the commercial LFP (Gelon LFP) was purchased from Gelon Lib Co. Ltd.. The materials were received carbon-coated and analysed as acquired. The 20% V-LFP was synthesised through a pilot-scale continuous hydrothermal flow synthesis reactor using $VOSO_4$ as the vanadium source and fructose as the carbon source.[107] Gelon LFP is manufactured using a patented methodology involving nanosphere preparation and surface coating technology.[164]

Electrodes were made up as a 90 : 5 : 5 slurries of active material : carbon black : 5% PVDF in NMP binder. Each slurry was then speed-mixed at 3000 rpm for 5 minutes three times, and tape-cast on aluminium foil current collector at a thickness of 170 μm. The electrode cast was then dried in a vacuum oven overnight, and cut into electrode discs of 12.7 mm diameter. Batteries were assembled either as CR2032 coin cells or mylar pouch cells vs. Li/Li^+ anode and cycled between 2 – 4 V at a C-rate of 0.1C. A detailed explanation of the electrolytes used is given in **Table 2.1**.

4.3. Results

4.3.1. Structural Characterisation

The materials were subject to XRD as received, then the patterns were refined using GSAS-II software.[141] The structural data have been previously published by Johnson *et al.*[107] The refinement of the Gelon LFP showed similar parameters to the CIF file used in the refinement (ICSD 92198), whereas the V-LFP showed an overall decrease in lattice parameters. The goodness-of-fit (GOF) was also larger for V-LFP, which could be due to the slight variation in peaks around 30 °2θ (**Figure 4.2**) which indicates a $LiVP_2O_7$ impurity phase previously reported by Johnson *et al.* The lattice parameters and volumes obtained from the Rietveld refinements are also in overall good agreement with those obtained by Johnson *et al.*[107,148]

Table 4.1: Sample parameters of Gelon and V-doped LFP compared to ICSD 92198 CIF file used for Rietveld refinement and to the 20% V-LFP obtained from colleagues at UCL (ΔLFVP(20))[107].

Sample	a (Å)	b (Å)	c (Å)	Volume (Å^3)	Weighted residual, R_W %	Goodness-of-fit (GOF)
ICSD 92198	10.329	6.006	4.691	291.023	–	–
Gelon LFP	10.327(5)	6.006(2)	4.692(2)	291.001(2)	2.743	6.66
V-LFP	10.316(4)	5.999(2)	4.700(2)	290.873(1)	2.379	4.41
ΔLFVP(20) [107]	10.3022 (3)	5.9762 (1)	4.6997 (1)	289.35 (2)	8.44	–

The volume of V-LFP is decreased by 0.128 Å^3 when compared to that of Gelon LFP and by 0.150 Å^3 when compared to the ICSD 92198 CIF file (**Table 4.1**). In **Chapter 3** a detailed analysis of the lattice parameters was reported and it was found that both the *a* and *b* parameters were smaller than the undoped material. This suggests that Li-ion diffusion is hindered in the V-LFP material as the diffusion pathway in the *a*-*b* plane is compressed, further supported by the CV measurements, where the calculated diffusion coefficients can be found later in this chapter in **Table 4.3**.

Zhao *et al.* reported that vanadium can occupy either Fe- or P-sites when doped in LFP. They used XRD analysis to identify the position of vanadium within the crystal lattice and concluded that when V occupies an Fe-site (thus existing as V^{3+}), a low-intensity doublet peak is observed at ~45 °2θ, whereas when V substitutes a P-ion as V^{5+}, a higher intensity singlet peak is observed at the same position (**Figure 4.3 (b)**). In the data recorded for the 20% V-LFP material, a low-intensity doublet is observed at ~45 °2θ, thus alluding to a majority V^{3+} occupation of Fe-sites within LFP (**Figure 4.3 (a)**).[160]

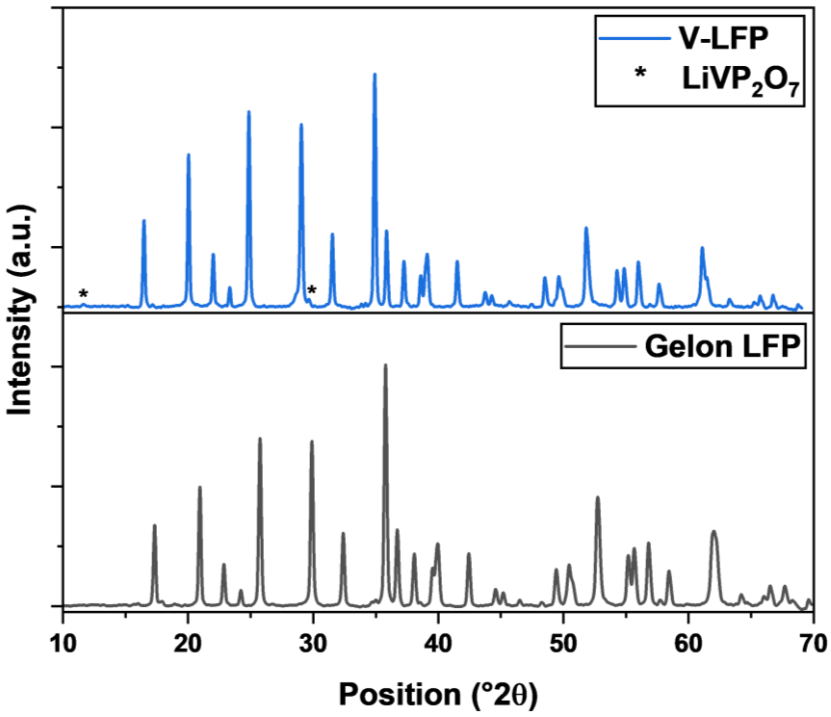

Figure 4.2: Background-subtracted PXRD patterns of V-LFP indicating the $LiVP_2O_7$ impurity peaks[165] (top), and Gelon LFP (bottom).

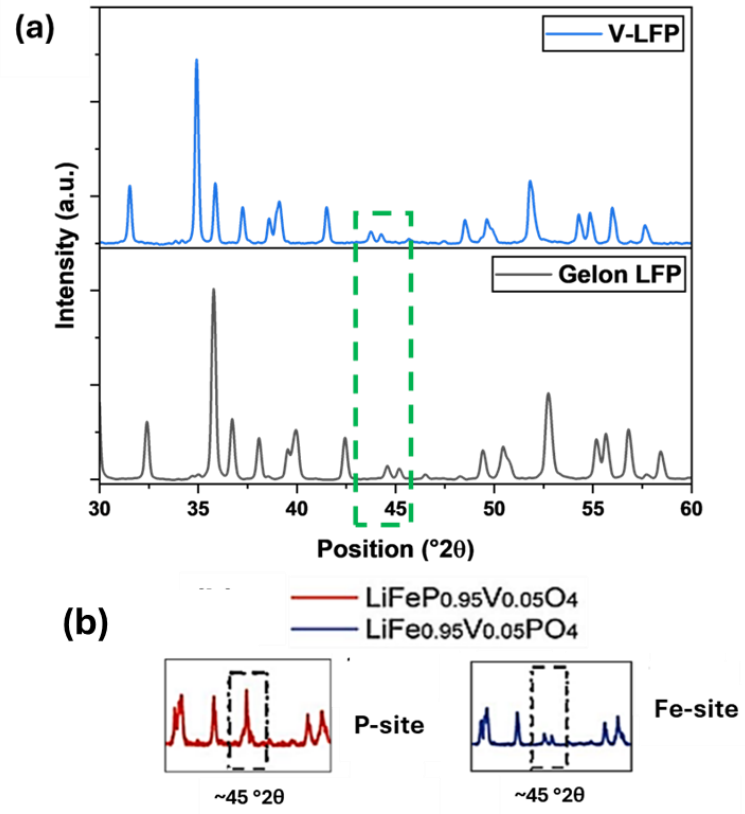

Figure 4.3: (a) Background-subtracted PXRD patterns of LFP and V-LFP indicating the peak at ~45 °2θ, (b) comparing the peaks at ~45 °2θ with literature.[160]

To further analyse the possible occupation site of vanadium within the LFP crystal lattice, it was necessary to determine the main oxidation state of vanadium within the sample. XANES measurements of vanadium standards of various oxidation states, coupled with linear combination fittings (LCF) of the V K-edge of the pristine V-LFP sample support the hypothesis that vanadium is predominantly present as V^{3+} (**Figure 4.2**), with >94% of the fit corresponding to the V^{3+} standard. This thus supports the observation in the XRD pattern that V^{3+} is substituting Fe^{2+} in the LFP lattice during synthesis.

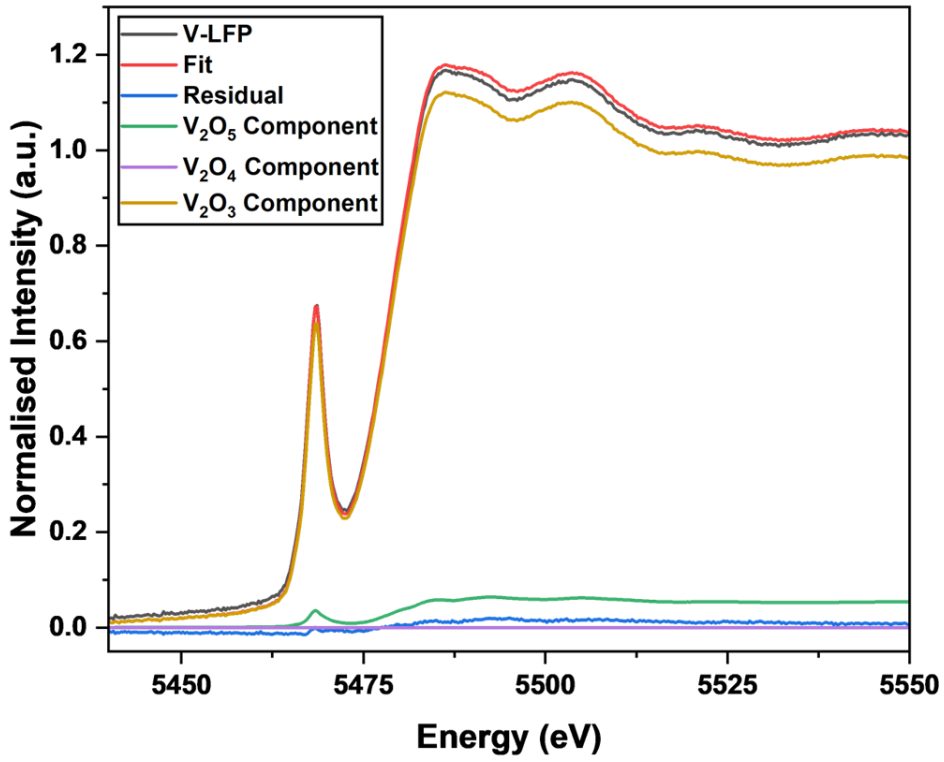

Figure 4.4: Linear combination fitting results of V K-edge spectra of pristine V-LFP fitted against V_2O_3, V_2O_4, and V_2O_5.

To assess the distribution of the constituent elements across the sample, SEM-EDX was carried out and reported in **Chapter 3** (**Figure 3.6 (c)**). Homogenous distributions of the constituent elements were observed across the grain selected for analysis, in agreement with SEM-EDX published by Johnson previously.[148] The vanadium is evenly distributed across the grain, with no particular accumulation of the element in any particular area despite the high concentration of 20% vanadium. Inhomogeneity of elemental distribution may interfere with the Li-ion diffusion during battery cycling, so it is important to assess this before implementing the material as a cathode in cells.

4.3.2. Electrochemistry

In the literature, vanadium doping has been shown to improve the cycling capabilities of LFP. The optimal dopant concentration reported by Johnson *et al.* was found to depend on charge rate, i.e. slower charge rates of 0.3 C favoured doping of 2.5 wt.%, while higher charge rates favour higher V-doping at 5 wt.%.[107] Other studies also demonstrate that the ideal concentration of vanadium in the material is in the region of 5-10%.[157,159,160] The samples we procured from UCL[107] for fluorescence XAS measurements contain 20% vanadium dopant.

Johnson *et al.* ran electrochemical tests on the material while comparing its performance to the samples with lower vanadium concentrations.[107] The 20% V-LFP consistently showed poorer electrochemical performance than the other materials measured, with a discharge capacity of 138 mAh g^{-1} at 0.3C when compared to 169 mAh g^{-1} for the 2.5% V-doped LFP using 1 M $LiPF_6$ in 3:7 v/v EC : ethyl methyl carbonate electrolyte. Despite the presence of a redox active element, vanadium, this was noted to be electrochemically inactive in all concentrations measured.[107] In this study the sample composition is optimised for the XAS measurements within the specific vacuum chamber required to undertake P K-edge XANES measurements. The electrochemical values in this thesis are reported for trend analysis, allowing us to study V-LFP under *ex situ* cycling conditions.

Galvanostatic cycling was carried out on 20% V-LFP and a commercial sample of LFP (Gelon LIB Group, China), which were implemented as cathodes *versus* a Li-metal anode and cycled between 2 – 4 V. Various C-rates were used, namely C/2, C/5, and C/10, in order to gain better insight into the rate capabilities of the materials. Efficiency studies were carried out at C/2 and C/10, whilst XAS samples were cycled at C/5. Galvanostatic cycling, CV and EIS investigations comparing the first and fifth cycle were conducted at C/10 between 2.4 and 3.9 V.

Both materials underwent 18 cycles, and the results were then compared for the different C-rates of C/2 and C/10 (**Figure 4.5**). The commercial sample (Gelon LFP) showed similar average coulombic efficiencies at both C-rates (97.9% at C/2; 98.0% at C/10), whereas V-LFP demonstrated a higher average coulombic efficiency at C/2 (94.6%) when compared to C/10 (88.0%) (**Figure 4.5 (b)**). Both materials showed higher discharge capacities at C/10, with Gelon LFP having an average discharge capacity of 149 mAh g^{-1} at C/10 when compared to 118 mAh g^{-1} at C/2, and V-LFP having a discharge capacity of 121 mAh g^{-1} at C/10 when compared to

101 mAh g^{-1} at C/2 (**Figure 4.5 (a)**). A greater loss of capacity from C/10 to C/2 is experienced by Gelon LFP which loses ~30 mAh g^{-1}, when compared to V-LFP which loses ~20 mAh g^{-1}. These measurements were repeated multiple times and an average was taken.

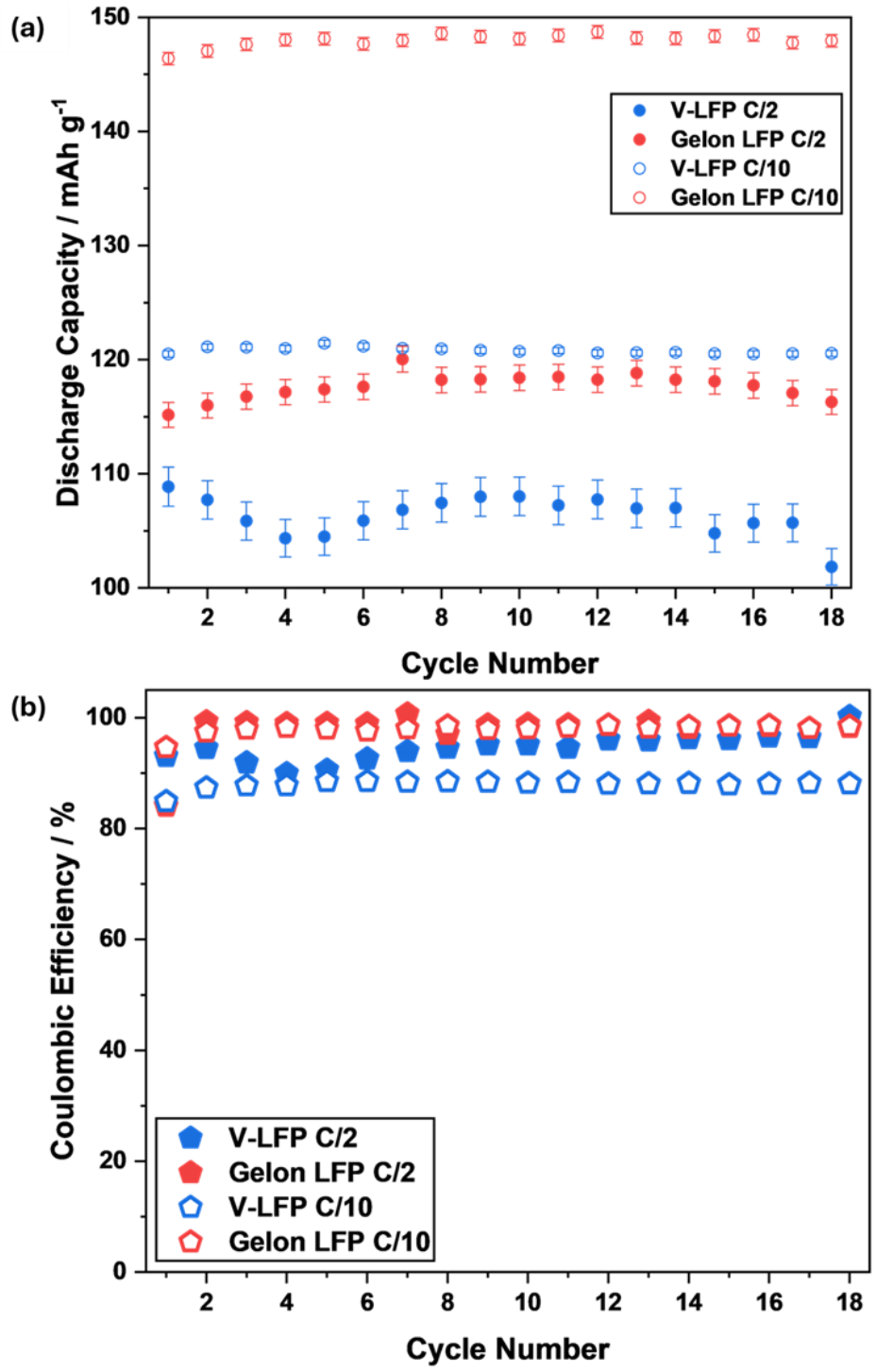

Figure 4.5: (a) Discharge capacity with error bars and (b) coulombic efficiency vs. cycle number for Gelon LFP and V-LFP at C/2 and C/10.

Galvanostatic cycling curves (**Figure 4.6**) show a comparison between the first and fifth cycles of Gelon LFP (denoted LFP) and V-LFP. All curves exhibit a single flat discharge plateau at ~3.39 V, which is identified as the phase transition from $FePO_4$ to $LiFePO_4$ as the Li^+ ion is intercalated as the battery is discharged.[166] [167] The first discharge capacity of V-LFP is 113 $mAhg^{-1}$, and that of LFP is 137 $mAhg^{-1}$, with the fifth discharge capacity being 128 and 143 mAh g^{-1} for V-LFP and LFP, respectively. The theoretical capacity for $LiFe_{0.80}V_{0.20}PO_4$ can be calculated to be ~136 $mAhg^{-1}$, which would make the obtained discharge capacity after the fifth cycle very close to this. The lack of a second discharge plateau in the V-LFP curves indicate that V is redox inactive, which may explain the lower discharge capacities recorded since electrochemically inactive V^{3+} is occupying the electrochemically active Fe^{2+} sites in the LFP crystal lattice.

Both materials undergo an increase in discharge capacity from the first to the fifth cycle however, a greater increase in capacity of 15 mAh g^{-1} is observed for V-LFP, when compared to an increase of 6 mAh g^{-1} for Gelon LFP. Polarisation in the two materials is comparable due to the similarities in electrochemical hysteresis (**Figure 4.6**).

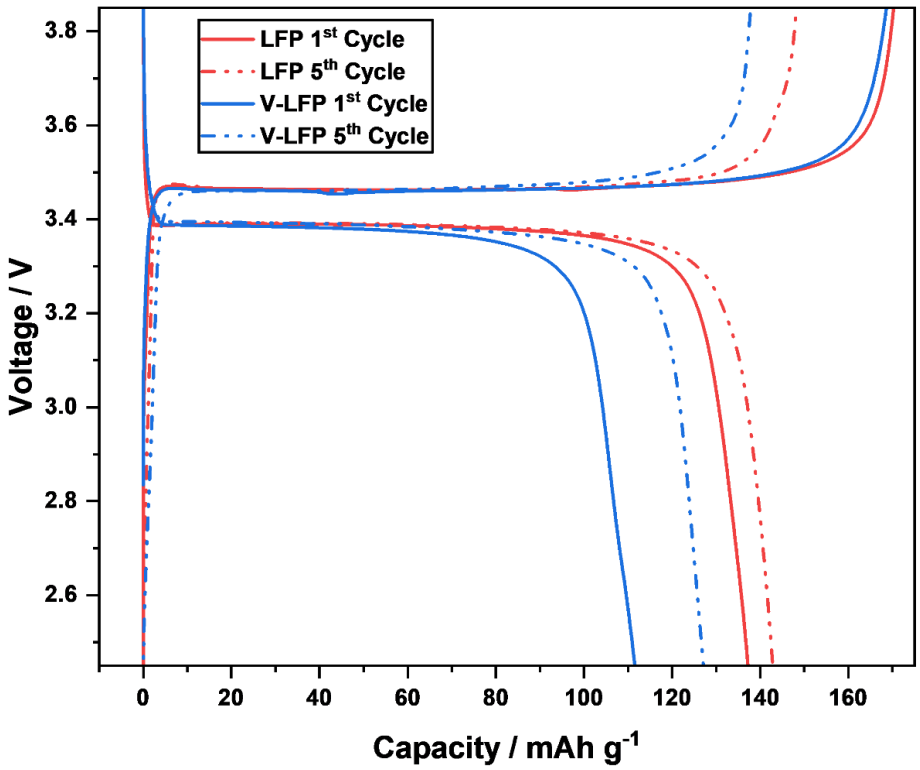

Figure 4.6: Galvanostatic cycling curves comparing the first and fifth charge/discharge cycles of Gelon LFP (LFP) and V-LFP.

One explanation to the observations in the galvanostatic cycling is the high level of dopant present in V-LFP (20%) could contribute to surface disorder due to disproportionation of vanadium ions between the bulk and the surface. This thus results in a charge buildup at the surface (charge spacing), which fades as the material is cycled, suppressing surface polarisation and leading to an increase in discharge capacity from the first to the fifth cycle.[168] EIS measurements support this hypothesis since the curves recorded for V-LFP indicate that the material displays a capacitor behaviour denoted by a change in gradient in the Warburg impedance in the low-frequency region (**Figure 4.7 (a)**).

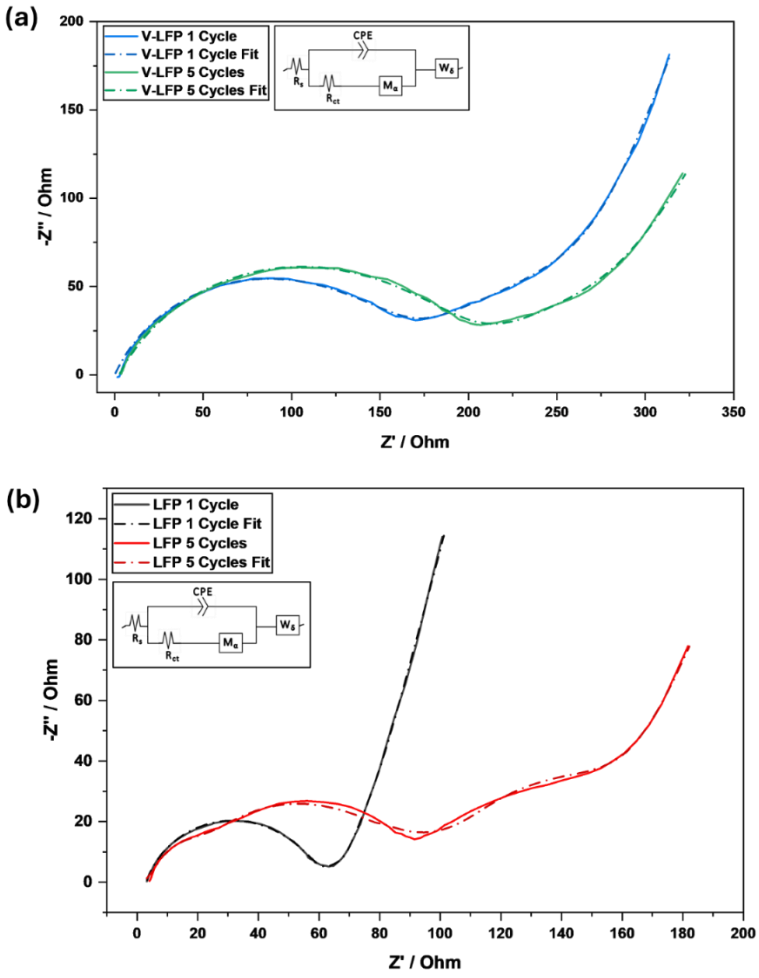

Figure 4.7: EIS plots and fits to equivalent circuit (inset) after 1 and 5 cycles for (a) V-LFP and (b) Gelon LFP (denoted LFP).

The Nyquist plots for V-LFP (**Figure 4.7 (a)**) are similar after both 1 and 5 charge-discharge cycles and are composed of a depressed semicircle in the high-frequency region denoting R_{ct}, followed by a curve in the low-frequency region which represents slightly restricted Li-ion diffusion, a combination of M_{α} and W_{δ}.

The capacitor behaviour observed in V-LFP is due to the contribution of surface concentrations of V^{3+}. This charge buildup at the surface of V-LFP causes a repulsion between Li^+ in the electrolyte and V^{3+} ions, which leads to capacitor behaviour, thus increasing the overall resistance within the battery. This charging effect, along with the lattice distortion leads to slower Li-ion diffusion as the battery is cycled. This behaviour has been previously reported by Johnson *et al.* using 1 M $LiPF_6$ in 3:7 v/v EC : EMC electrolyte, suggesting that electrolyte effects, in this case, are smaller.[107]

The Nyquist plot of Gelon LFP (**Figure 4.7 (b)**) after the first cycle exhibits a semicircle in the high-frequency region which can be attributed to the charge-transfer resistance (R_{ct}) at the electrode/electrolyte interphase, followed by a slope representing the diffusion resistance of Li-ions in the bulk of the electrode – Warburg impedance. When EIS was measured after the fifth cycle, the plot changed significantly with a depressed semicircle in the high-frequency region denoting R_{ct}, however it is followed by a second semicircle, and further semicircle in the low-frequency region. The latter semicircle is attributed to the formation of the cathode-electrolyte interphase (CEI) layer which is a result of the multiple cycles undergone by the material. The formation of CEI leads to more restricted Li-ion diffusion, which is confirmed by the Warburg slope of the plot.

The R_s for both materials is similar due to the addition of conductive carbon black during the slurry-making process (**Table 4.2**), as well as the use of the same electrolyte in all cells. The R_{ct}, however, is greatly increased for V-LFP when compared to that of Gelon LFP, which is in accordance with the theory that the high concentration of vanadium doping is hindering the Li-ion diffusion pathways and causing greater internal resistance within the material.

Table 4.2: R_s and R_{ct} values obtained from equivalent circuit fitting after 1 and 5 cycles for V-LFP and Gelon LFP.

Sample	R_s after 1 cycle (Ω)	R_{ct} after 1 cycle (Ω)	R_s after 5 cycles (Ω)	R_{ct} after 5 cycles (Ω)
V-LFP	2.07	157.90	2.34	185.90
Gelon LFP	2.98	55.88	3.07	90.09

The Li-ion diffusion pathway throughout both materials can be investigated through cyclic voltammetry. Both V-LFP and Gelon LFP undergo a quasi-reversible process involving a single-electron redox mechanism, with a symmetric transition observed for the latter, and a more asymmetric transition observed for the former, after both the first and fifth cycles (**Figure 4.8**).

The asymmetric transition observed in the V-LFP cyclic voltammogram after the first cycle can be associated with the presence of the excess vanadium distorting the crystal structure of LFP, which hinders the diffusion pathway of the Li-ions. The asymmetry of the V-LFP CV decreases from the first to the fifth cycle, further supporting the hypothesis that the material is behaving more similarly to the undoped analogue as it is cycled. The distorted shape of the V-LFP CV after the first cycle is similar to that reported by Johnson and coworkers for 20% V-doped LFP using 1 M $LiPF_6$ in 3:7 v/v EC : ethyl methyl carbonate, indicating minimal electrolyte effects.[107]

Table 4.3: Apparent diffusion coefficients for the charge and discharge processes of Gelon LFP and V-LFP.

Diffusion Coefficients	**Gelon LFP (after 1 cycle)**	**Gelon LFP (after 5 cycles)**	**V-LFP (After 1 cycle)**	**V-LFP (After 5 cycles)**
Anodic D_{app} (cm^2/s)	2.79×10^{-7}	7.61×10^{-7}	0.69×10^{-7}	1.38×10^{-7}
Cathodic D_{app} (cm^2/s)	1.50×10^{-7}	4.45×10^{-7}	0.34×10^{-7}	0.89×10^{-7}

The apparent diffusion coefficients calculated for V-LFP are lower for both the anodic and cathodic processes when compared to the D_{app} values calculated for Gelon LFP (**Table 4.3**). This is a reflection of the asymmetric shape of the V-LFP cyclic voltammograms (**Figure 4.8**), which have a less steep gradient than the cyclic voltammograms of Gelon LFP. The asymmetry of the cyclic voltammograms can again be linked to the presence of the excessive vanadium which is hindering the Li-ion diffusion by distorting the crystal lattice of LFP, thus allowing for a slower redox process and lower diffusion coefficients. Once again, the limitations of this

calculation are taken into account and the values obtained are to be considered as estimates for comparative purposes.

The buildup of positive charge at the particle surfaces could also lead to a slower diffusion coefficient for V-LFP.[168] This charge repulsion between Li^+ ions in the electrolyte and at the surface could contribute to the wider, more asymmetric shape of the cyclic voltammograms, especially after the first cycle. As the battery is cycled further the shape of the cyclic voltammogram becomes slightly more symmetrical, as is seen after the fifth cycle. The double peak observed at the anodic site after 1 cycle can also be associated with bulk and surface charging behaviours of V-LFP, where the charge is dissipated and the bulk behaviours overtake those at the surface the more cycles the battery undergoes, thus behaving more similarly to undoped LFP.

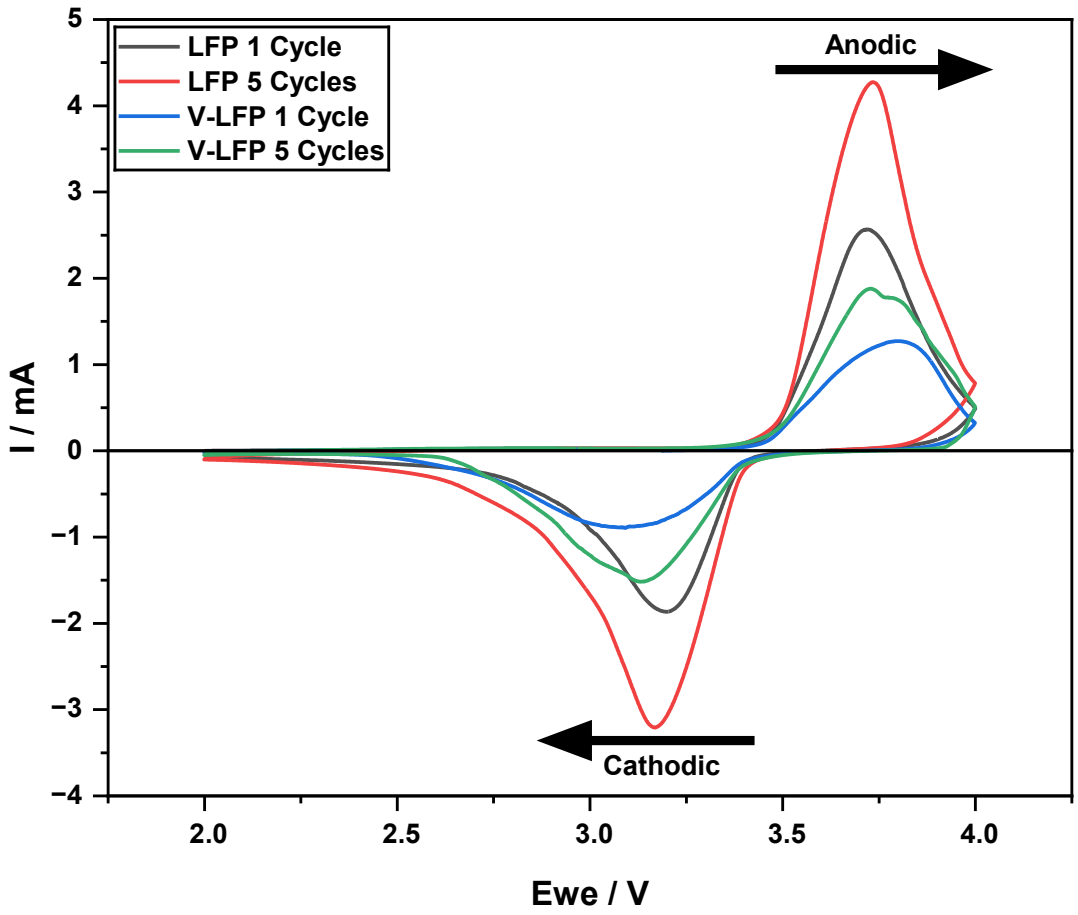

Figure 4.8: CV curves for V-LFP and Gelon LFP (denoted LFP) after the first and fifth charge-discharge cycles.

4.3.3. X-Ray Absorption Spectroscopy

XAS measurements were conducted on ex-situ electrodes that were stopped at various SOCs. The Fe K-edge, P K-edge, and V K-edge were measured and the XANES spectra for each edge are plotted as **Figure 4.9**. For the Fe K-edge, and V K-edge EXAFS was also collected for analysis, and Fe–O and V–O bond lengths were calculated for the measured samples.

The Fe K-edge XANES (**Figure 4.9 (a)**), measured for both materials, shows that the iron is redox active, indicated by a reversible shift in K-edge energy as the iron is oxidised from Fe^{2+} to Fe^{3+} as the battery is charged. The presence of vanadium within the material does not affect the iron redox mechanism as both materials are able to reach the same Fe^{3+} state upon charging.

There are also insignificant differences in the pre-edge features of the Fe K-edge XANES spectra of the Gelon and V-doped LFP corresponding to the $1s \rightarrow 3d$ electronic transitions, a usually spin-forbidden process which is partially allowed because of Fe *d*- and O s*p*-state mixing. The pre-edge features in the charged spectra, i.e. when iron is in the +3-oxidation state, occur at a higher energy than those in the discharged Fe^{2+} spectra due to the electrons being tightly bound to the nucleus in Fe^{3+} therefore requiring a higher energy input for the $1s \rightarrow 3d$ electronic transition to occur. The decrease of the edge intensity from the discharged SOCs (Fe^{2+}) to the charged SOCs (Fe^{3+}) is a reflection of the decreased number of unoccupied *d* states of Fe ions due to charge compensation upon the loss of Li^+ as the battery is charged.[169] The same trends and chemical changes are observed for both the Gelon LFP and V-LFP, which indicates that the presence of the vanadium dopant does not interfere with the iron redox activity. The isosbestic point at ~ 7158 eV confirms that the stoichiometric changes undergone by the materials are related in a reversible phase transition.

The P K-edge XANES data collected for Gelon LFP and V-LFP indicate that the phosphorus is redox active in both materials, with a clear upshift in energy noted for the charged samples as the lithium is deintercalated (**Figure 4.9 (b)**). There are no significant differences between the doped and undoped materials, following the same trends as in the Fe K-edge XANES.

The upshift in the P K-edge position is a result of an electron redistribution within the phosphate polyanion. The phosphorus in PO_4^{3-} is known to backbond to the Fe^{3+} ions, which is observed in the XANES spectrum as the presence of a pre-

edge feature in the oxidised P K-edge spectrum (**Figure 4.9(b)**). The shift to higher energies in the P K-edge XANES confirms the theory that, as the iron is oxidised from $Fe^{2+} \rightarrow Fe^{3+}$ and the Li-ion is deintercalated, there is an electron redistribution within the phosphate polyanion, resulting in higher electron density and contraction of the Fe^{3+}–O bond, which is confirmed by the Fe K-edge EXAFS analysis (**Figure 4.11**).

The emergence of pre-edge features in the charged SOC spectra can be ascribed to the interaction between the Fe 3*d* and P 3*p* states through the shared O atom in the Fe–O–P linkage, as the Fe^{3+}–O bond distance is shorter than the Fe^{2+}–O distance. These states undergo hybridisation which introduces higher covalency in the structure and is in line with the oxidation undergone by Fe^{2+} to Fe^{3+} upon the loss of Li^+.[114,170] The formation of the prominent pre-edge features (**Figure 4.9 (b)**) is evidence of the Fe–O–P backbonding that occurs as the battery is charged. This observation maintains the hypothesis that the phosphate polyanion indirectly contributes to the high specific capacity in phosphate-based materials through this inductive effect.

A direct correlation between P and Fe E_0 energies for both Gelon and V-doped LFP can be made (**Figure 4.10**) for each SOC. This proves that the $Fe^{2+} \leftrightarrow Fe^{3+}$ redox mechanism is directly coupled to the electron charge redistribution occurring at the PO_4^{3-} anion site. This clear correlation demonstrates that the phosphate polyanion is electrochemically active as the battery is cycled, regardless of the presence of the dopant cation. A dipole moment is induced in the phosphate polyanion due to an electron charge transfer from the P atom to the O atom, generated by the oxidation of Fe^{2+} to Fe^{3+} upon the loss of Li^+ as the battery is charged, which in turn leads to a decrease in the Fe–O bond distance. There is no evidence that the phosphate anion behaves differently in the V-doped LFP when compared to the undoped Gelon LFP as the Fe and P K-edge E_0 correlation graph shows the same trends (**Figure 4.10**). This suggests that the dopant does not contribute to an additional capacity through the inductive effect. This is discussed further in **Chapter 5**, section **5.3.3**.

There is no shift to higher or lower energies for the different SOCs in the V K-edge measured (**Figure 4.9 (c)**), demonstrating that the vanadium is electrochemically inactive during battery cycling.[157] This observation is in agreement with the single plateau seen during galvanostatic cycling.

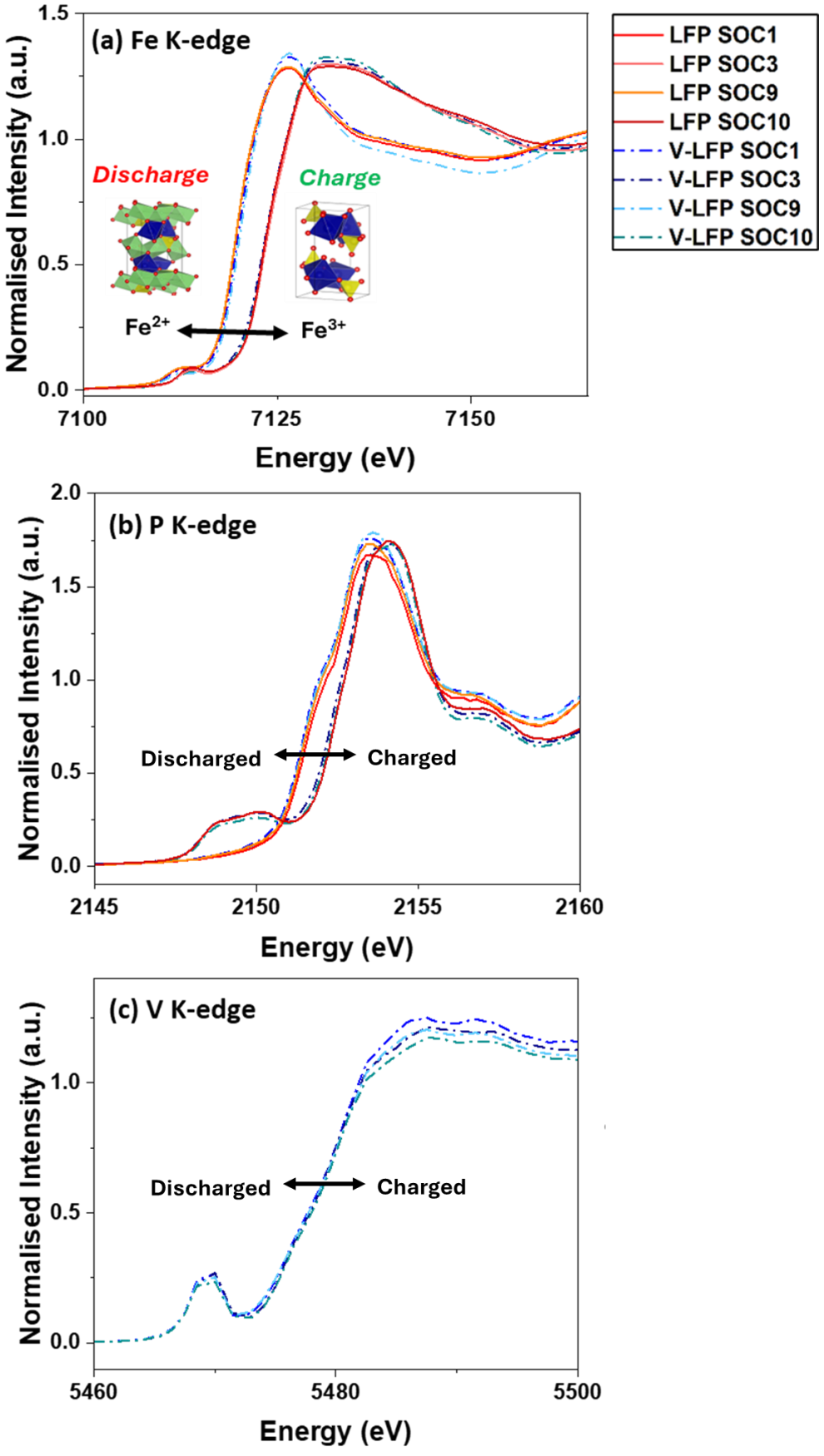

Figure 4.9: (a) Fe K-edge, (b) P K-edge, and (c) V K-edge XANES spectra of Gelon LFP (denoted LFP) and V-LFP comparing the different edges of both materials at different SOCs.

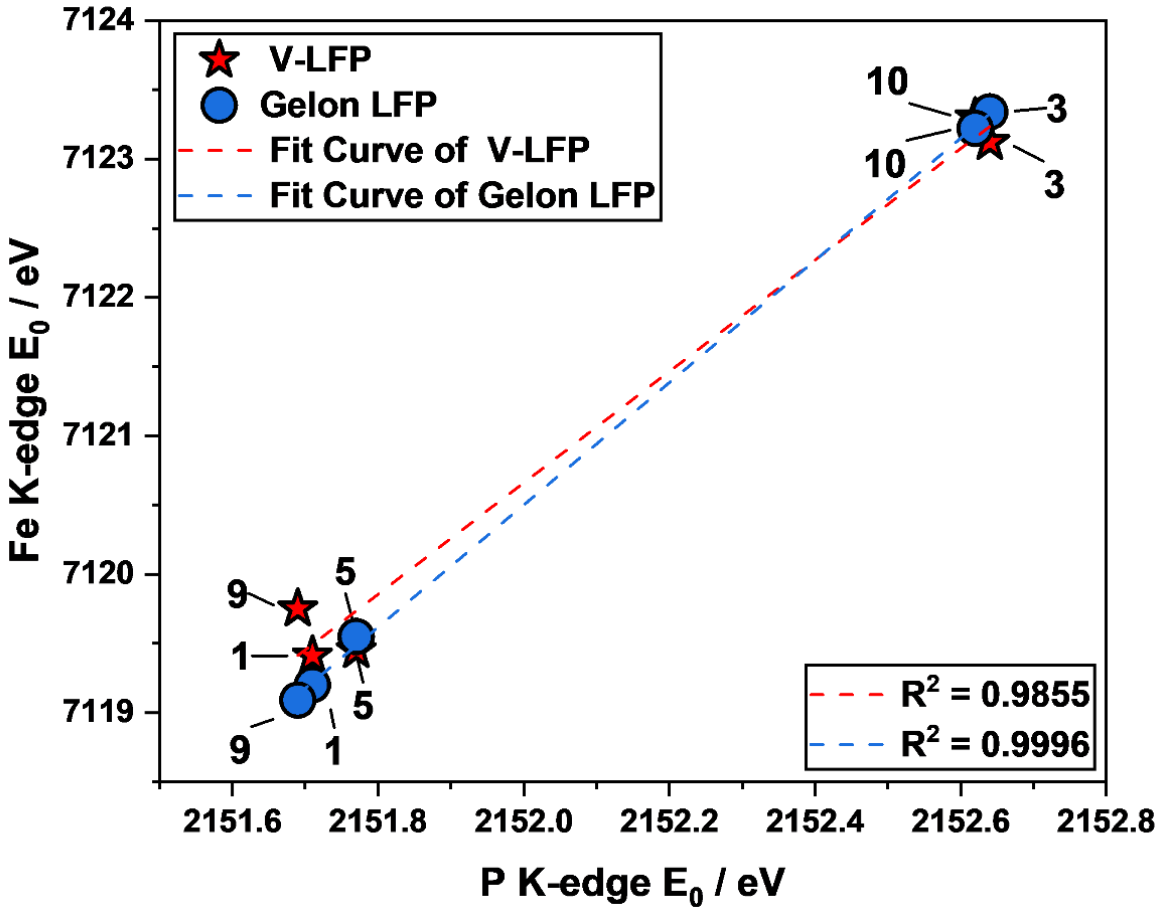

Figure 4.10: Energy distribution plot indicating correlations of P & Fe K-edge energies at different SOCs, indicated by the numbers in the graph

Fe and V K-edge EXAFS fitting were carried out to determine the Fe–O and V–O bond lengths of Gelon LFP and V-LFP samples using Artemis software.[117]

A correlation between Fe K-edge E_0 energy and Fe-O bond lengths can be made (**Figure 4.11**) for both Gelon and V-LFP. After 5 cycles, the crystal lattice is not significantly distorted, showing similar values for the discharged SOCs 1 and 9, and the charged SOCs 3 and 10. The V-LFP Fe–O bond distances for SOC1 (2.109 Å) and SOC9 (2.093 Å) fall within the margin of error in terms of discrepancy.

Whilst E_0 remains relatively constant as a function of SOC during battery cycling, changes can be noted in the Fe–O bond distances at each respective SOC. This cannot be caused by the pristine material being oxidised, but by a reconstruction/relaxation of the material as the battery is cycled. At the charged state, both Gelon and V-LFP have a similar structure, so the change in Fe–O bond distance is independent of the SOC. However, the bond distances in V-LFP are larger than those of Gelon LFP when the battery is in a charged state. There is a greater

difference in Fe–O bond distance between SOC1 and SOC9 for V-LFP, when compared to Gelon LFP. This could be due to the excess vanadium causing an insulating layer within the material, thus distorting the crystal lattice resulting in a shorter Fe–O bond in SOC9. CV measurements of V-LFP after 5 cycles (**Figure 4.8**) agree with this hypothesis as a second peak in the forward scan is noted which could be corroborated with the bulk and surface charging behaviours of the excess V^{3+}.

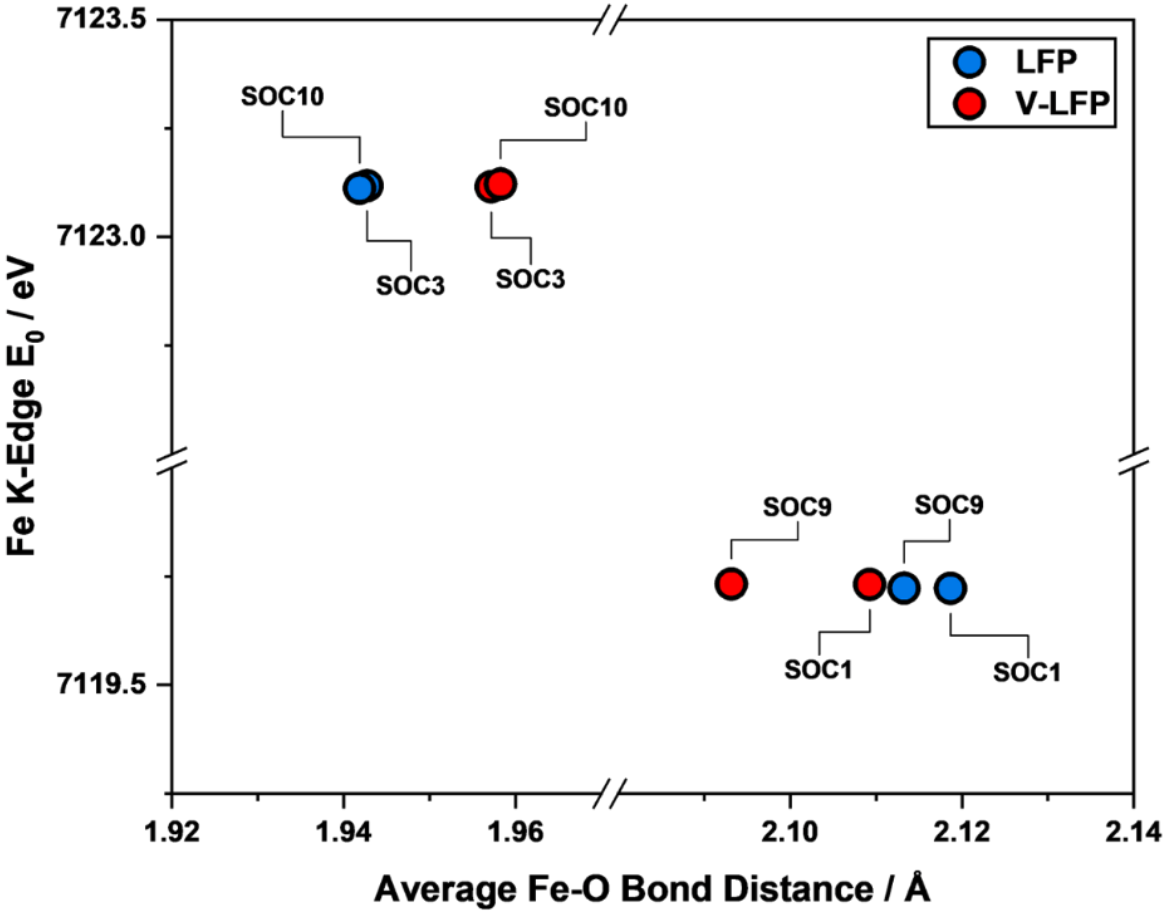

Figure 4.11: Average Fe-O bond distances obtained for V-LFP & Gelon LFP (denoted LFP) correlated with the Fe K-edge energy.

A correlation plot for Fe–O and V–O bond lengths for the different V-LFP SOCs (**Figure 4.12**) determined that, since vanadium is occupying Fe-sites in the crystal lattice, the V–O bond lengths were altered slightly as the battery was cycled to reflect the change in Fe–O bond lengths undergone upon the loss of the Li^{+} ion as Fe^{2+} is oxidised to Fe^{3+}, therefore leading to a contraction of the crystal lattice.

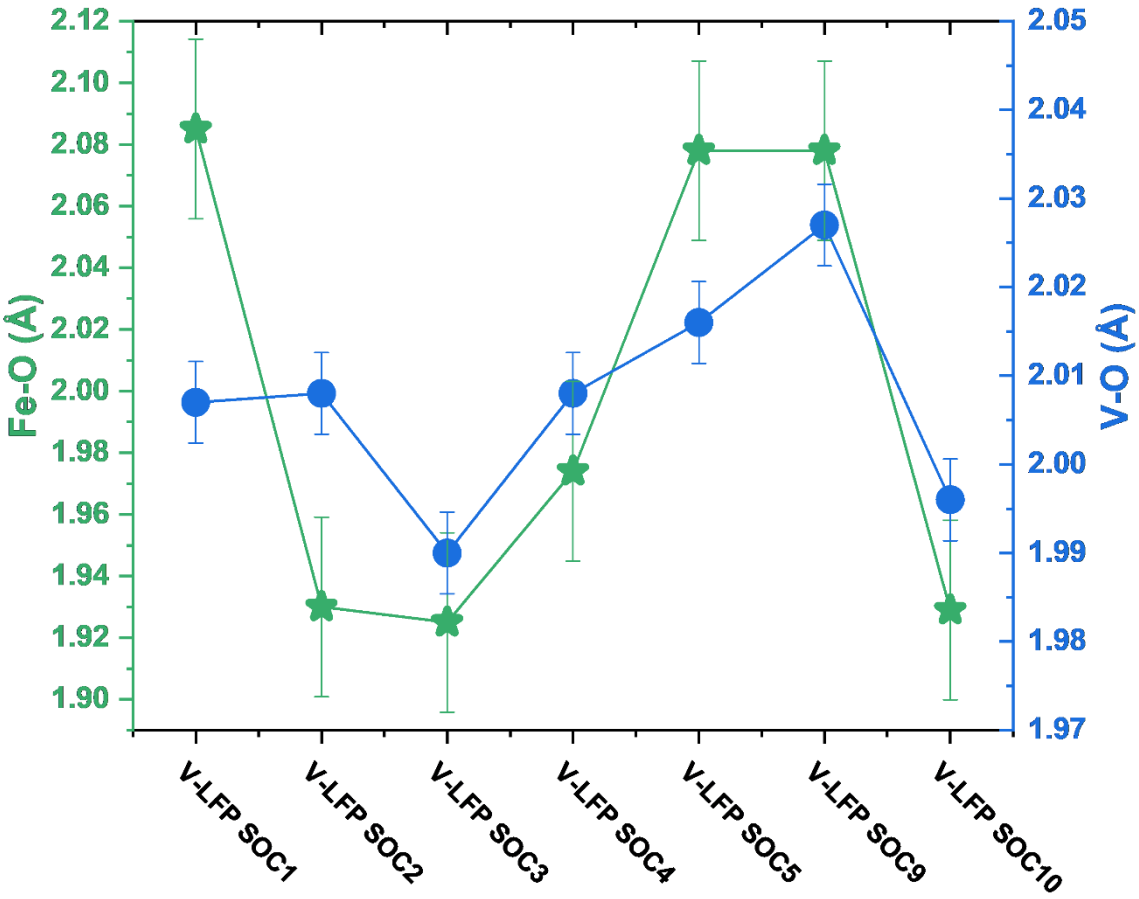

Figure 4.12: Correlation plot of Fe-O and V-O bond distances for each V-LFP SOC.

A correlation factor can be calculated to further emphasise the corroboration between the Fe–O and V–O bond distances obtained:

$$\text{Correl}(\text{Fe–O}, \text{V–O}) = \frac{\sum(\text{Fe–O} - \overline{\text{Fe–O}})(\text{V–O} - \overline{\text{V–O}})}{\sqrt{\sum(\text{Fe–O} - \overline{\text{Fe–O}})^2 \sum(\text{V–O} - \overline{\text{V–O}})^2}} \qquad [4.1]$$

where $\overline{\text{Fe–O}}$ and $\overline{\text{V–O}}$ are the average bond distances, and Fe-O and V-O are the corresponding bond distances at each SOC. The Correl(Fe–O, V–O) value is calculated to be 0.749, indicating a fairly good correlation between the two bond distances.

4.4. Chapter Conclusions

A commercial sample of LFP, Gelon LFP, and a 20% vanadium-doped sample of LFP, V-LFP, were cycled and measured at different SOCs throughout battery cycling. V-LFP exhibited a lower discharge capacity overall, regardless of C-rate, when compared to the undoped analogue, which is due to the electrochemically inactive vanadium dopant occupying electrochemically active Fe(II) sites within the crystal lattice of LFP. The electrochemical inactivity of the vanadium dopant was confirmed through galvanostatic cycling, where only one charge/discharge plateau was observed, corresponding to the $Fe^{2+} \leftrightarrow Fe^{3+}$ redox mechanism and XAS measurements.

The apparent Li-ion diffusion coefficient, calculated using the Randles–Ševčík equation, is lower for V-LFP than Gelon LFP, which is in accordance with the literature where higher concentrations of V-dopant reduced Li-ion transport in the material.[155] This is a result of lattice distortion, as well as formation of V-containing impurity phases, such as $LiVP_2O_7$, which may impede the Li-ion diffusion channels.[107] The presence of such a high concentration of vanadium in the sample (20%) may also lead to the formation of charge repulsion at the surface of the material between Li^+ and excess V^{3+} cations, which contributes to supercapacitor behaviour and further decreases the Li-ion diffusion coefficient.

The occupation of Fe-sites by the vanadium dopant was confirmed through linear combination fittings of V K-edge XANES data, where it was concluded that vanadium is present primarily as V^{3+} in V-LFP. From the V K-edge XANES spectra, the redox inactivity of vanadium in V-LFP was further confirmed as there were no noticeable edge energy shifts at the different SOCs measured.

There is a clear correlation between the Fe and P K-edge energies in both materials, which proves that the phosphate polyanion is electrochemically active and directly coupled to the $Fe^{2+} \leftrightarrow Fe^{3+}$ redox mechanism as the battery is cycled, and that the presence of the dopant cation does not affect this. However, there is no evidence to suggest that V-doping contributes further to the inductive effect.

From the EXAFS fittings, it can be concluded that the iron is redox active in both Gelon and V-doped LFP, with Fe–O bond lengths decreasing as the battery is charged and Li^+ is deintercalated, instead the V–O bond lengths in V-LFP only decrease slightly to accommodate for the lattice contraction brought about by the decrease in Fe^{3+}-O bond length upon delithiation.

In literature, it is found that the optimum vanadium concentration to ameliorate the electrochemistry of LFP ranges from 3-5%.[107,152,155,160] This can explain the issues encountered throughout this chapter, such as supercapacitor behaviour and impurity phases present, since the concentration of vanadium in V-LFP was 20%. At lower concentrations, when vanadium is implemented as a dopant in LFP, the cycling capabilities, discharge capacity, and Li-ion diffusion of the material have been demonstrably improved overall.

5. Ho-LFP: A Case Study

5.1. Chapter Introduction

Rare earth (RE) elements have been used sparingly to dope LFP, however there have been reports of their use in supercapacitors and perovskite materials in secondary batteries.[171,172] REs are comprised of the lanthanide elements, as well as yttrium and scandium in some cases. This is due to their abundance, as well as their similar properties, such as paramagnetism, size, and preferred oxidation state.

Doping with lanthanides has been shown to improve the electrochemical performance of LFP. Minimal doping of just 2% dysprosium improved the discharge capacity of LFP from 136 to 152.6 mAh g^{-1} at 0.1 C, as well as increased the ionic conductivity of the material to 1.9×10^{-2} S cm^{-1}, whilst not disrupting the crystal structure of the LFP.[167] The same effects are seen in Nd-doped LFP, where doping with as much as 6% neodymium improved the material by improving its rate capability and increasing its discharge capacity. EIS also showed that the presence of 6% neodymium decreases the charge-transfer resistance of the material by more than half, from 570.6 Ω to 217.3 Ω, thus improving its performance when implemented in a battery.[173] An improvement was also seen when NMC was doped with dysprosium where cation mixing was decreased since the migration on Ni^{2+} to the Li layer was suppressed, and Li-ion intercalation/deintercalation was facilitated. This goes to show that the introduction of lanthanides in cathode materials can improve their performance.[174]

Cerium and lanthanum have also been used to dope LFP, with the two also co-doping the material. The electronic conductivity of the co-doped material improved to 1.15×10^{-4} S cm^{-1} from 1.04×10^{-8} S cm^{-1} for the undoped LFP.[175] The presence of these dopants improved the electrochemical performance of LFP when doped in minimal quantities of 0.1% to 0.5%, where the coulombic efficiency of the 0.5% co-doped LFP remained stable at ~100%, whilst that of the undoped LFP fluctuated from 98.5-95.9%. This indicates that, despite the large ionic radius of the lanthanides, these elements can be doped into the lattice of LFP without structural disruption and improve the function of the material.[175–178]

Holmium and ytterbium have been previously used to dope LFP, with promising results of improved discharge capacity and decreased polarisation in doping concentrations as low as 1%. A concentration of 2% ytterbium offered a 10

mAh g^{-1} increase in capacity when compared to the undoped analogue at 0.1 C.[179] For 1% Ho-doped LFP, the capacity fade over 100 cycles at 0.1 C was calculated to be 0.0339, which is an improvement over the 0.0593 calculated for the undoped LFP.[140] At higher concentrations, an impurity phase of Ho_2O_3 was seen, which may have interfered with the performance of the material, thus supporting the hypothesis that low concentrations of dopant are enough to improve LFP.[140]

Ho-doping of LFP is of particular interest due to its ability to occupy divalent and trivalent oxidation states, therefore potentially being redox active as the battery is cycled along with the $Fe^{2+/3+}$ redox couple in LFP. Different concentrations of holmium were used to dope LFP in this chapter, however phase purity was affected at concentrations higher than 1%. As a result of this, the 1% Ho-LFP was the main material investigated.

This chapter, therefore, aims to compare the effects of the presence of holmium in LFP with the pristine material. The questions this chapter aims to answer are:

- What is the maximum concentration of holmium that can be incorporated in LFP without impurity phases?
- How does the presence of holmium affect the electrochemistry of LFP?
- Is the holmium redox active as the battery is cycled?
- Does the holmium affect the induction effect of the phosphate polyanion?

5.2. Methodology

$LiFe_{1-x}Ho_xPO_4$ (x = 0.01, 0.03, 0.05) was synthesised according to section **2.1.1.2** using a one-pot green approach, with $Ho(NO_3)_3{\cdot}5H_2O$ (Sigma-Aldrich) used as the main source of holmium. The material was then carbon coated with a 15% sucrose solution and calcined at high temperature under an Ar atmosphere before being implemented as a cathode. All the materials investigated in this chapter were synthesised in-house.

Electrodes were made up as a 90 : 5 : 5 slurries of active material : carbon black : 5% PVDF binder. Each slurry was then speed-mixed at 3000 rpm for 5 minutes three times, and cast as sheets on aluminium foil as the current collector. The electrode was tape-cast at a thickness of 170 μm and dried in a vacuum oven overnight. The electrode sheet was cut into discs of 12.7- or 16-mm diameter,

depending on the cell type being investigated. Half-cells were assembled either as CR2032 coin cells or pouch cells using a 3.4 µm-thick mylar window *vs.* Li/Li$^+$ anode and cycled between 2.4 – 3.9 V at a C-rate of 0.1 C. The electrolytes used for each experiment are listed in **Table 2.1**.

5.3. Results

5.3.1. Structural Characterisation

XRD measurements were carried out to characterise the materials prior to being implemented as cathodes. An impurity phase of Ho_2O_3 was observed for the 3% and 5% Ho-doped LFP, which was not seen in the 1% Ho-doped LFP, so the latter was used as the main material for analysis and will henceforth be referred to solely as "Ho-LFP" (**Figure 5.1**).

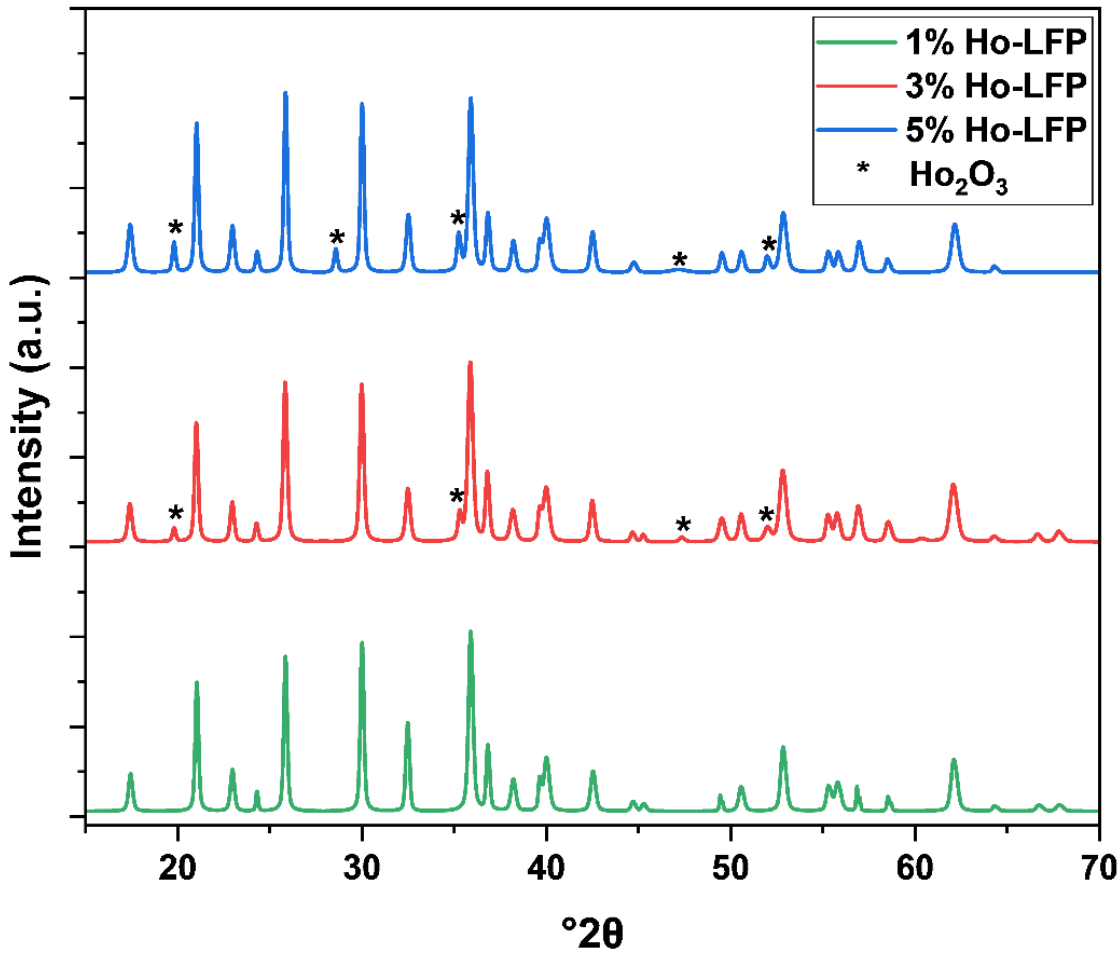

Figure 5.1: Background-subtracted PXRD patterns of 1%, 3%, and 5% Ho-doped LFP with Ho_2O_3 impurity peaks denoted by asterisks. [180]

XRD refinements were carried out on the 1% Ho-LFP material and lattice parameters obtained were compared to those of the undoped analogue, as can be seen in **Table 5.1**. The reflections at higher 2θ angles absent in the 5% Ho-LFP pattern could be due to incorrect background subtraction where slightly lower-intensity peaks could have been underfit.

Table 5.1: Sample parameters of undoped and 1% Ho-doped LFP compared to ICSD 92198 CIF file used for Rietveld refinement.

Sample	**a (Å)**	**b (Å)**	**c (Å)**	**Volume (Å³)**	**Weighted residual, R_W %**	**Goodness-of-fit (GOF)**
ICSD 92198	10.329	6.006	4.691	291.023	–	–
LFP	10.319(3)	6.004(3)	4.695(1)	290.916(2)	1.999	1.50
Ho-LFP	10.321(7)	6.005(3)	4.693(3)	290.967(2)	3.019	2.89

Compared to the CIF file, the lattice parameters of the undoped and Ho-doped LFP are smaller, however there is a slight increase seen in the a, b, and volume parameters of the doped analogue when compared to the undoped one. This is justified by the presence of the holmium which is a larger cation than any of the constituent elements of LFP.

SEM-EDX was carried out on the samples to assess the homogeneity of the constituent elements across the samples (**Figure 5.2 (a)**). EDX mapping showed that there was an even distribution of holmium dopant across the sample, and the presence of holmium was further confirmed by the EDX spectrum (**Figure 5.2 (b)**).

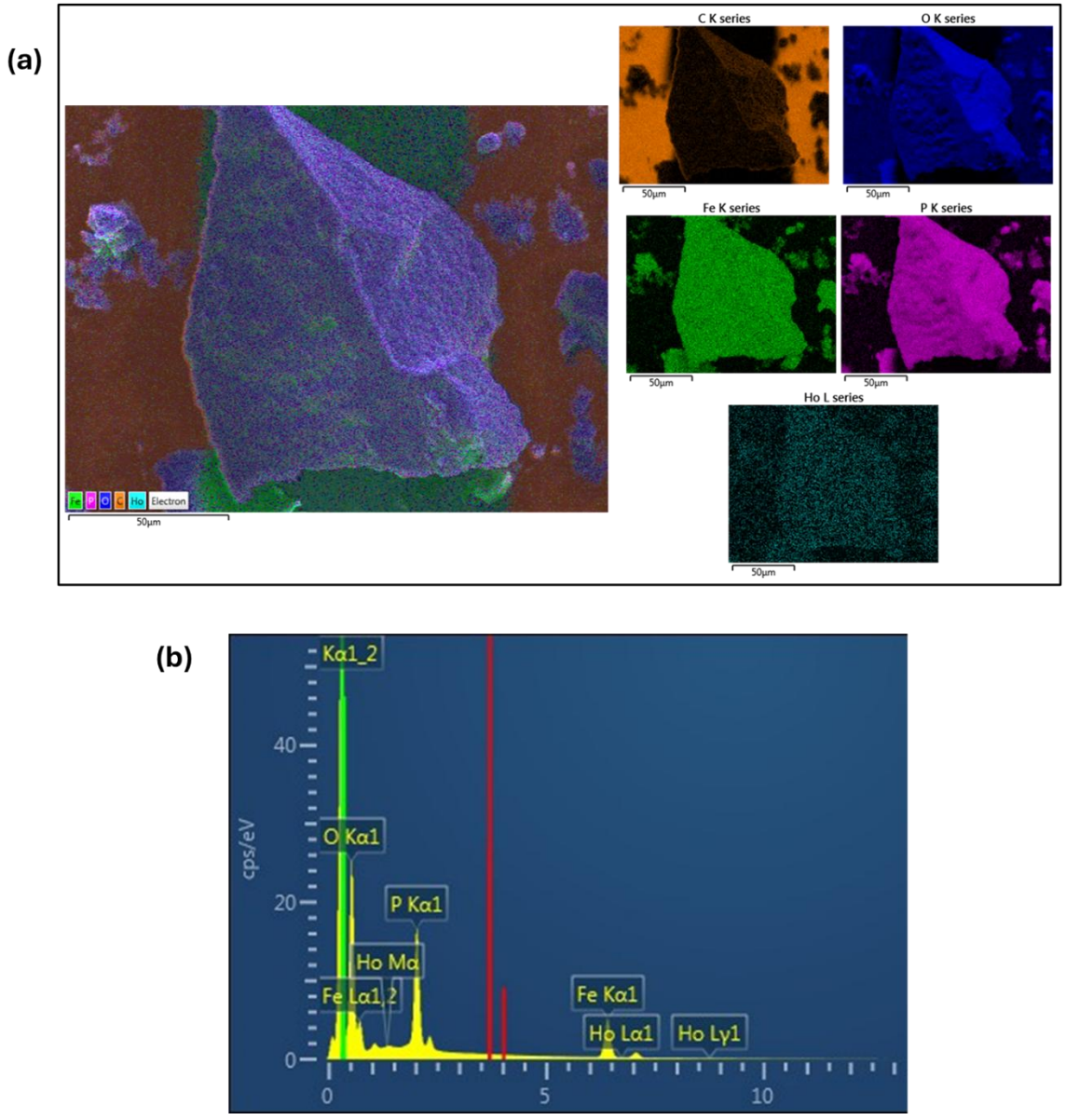

Figure 5.2: (a) SEM-EDX of Ho-LFP mapping its constituent elements; (b) EDX spectrum indicating the presence of holmium within the sample.

5.3.2. Electrochemistry

Galvanostatic cycling was carried out on undoped, 1%, 3%, and 5% Ho-doped LFP *vs.* Li/Li^+ in 1 M $LiPF_6$ in EC/DEC electrolyte as coin cells and cycled at a C-rate of C/10, then the discharge capacity was compared for each analogue (**Figure 5.3**). $LiFe_{0.99}Ho_{0.01}PO_4$ showed improved performance with a discharge capacity of 138 $mAhg^{-1}$, compared to $LiFePO_4$ (122 mAh g^{-1}). $LiFe_{0.97}Ho_{0.03}PO_4$ is close to undoped LFP with a specific capacity of 122 $mAhg^{-1}$. The lowest discharge capacity was observed for $LiFe_{0.95}Ho_{0.05}PO_4$ at 109 $mAhg^{-1}$. This implies that the impurity phase

of Ho_2O_3 present in the 3% and 5% Ho-doped LFP is hindering the Li-ion diffusion when the material is cycled, therefore leading to lower discharge capacities.

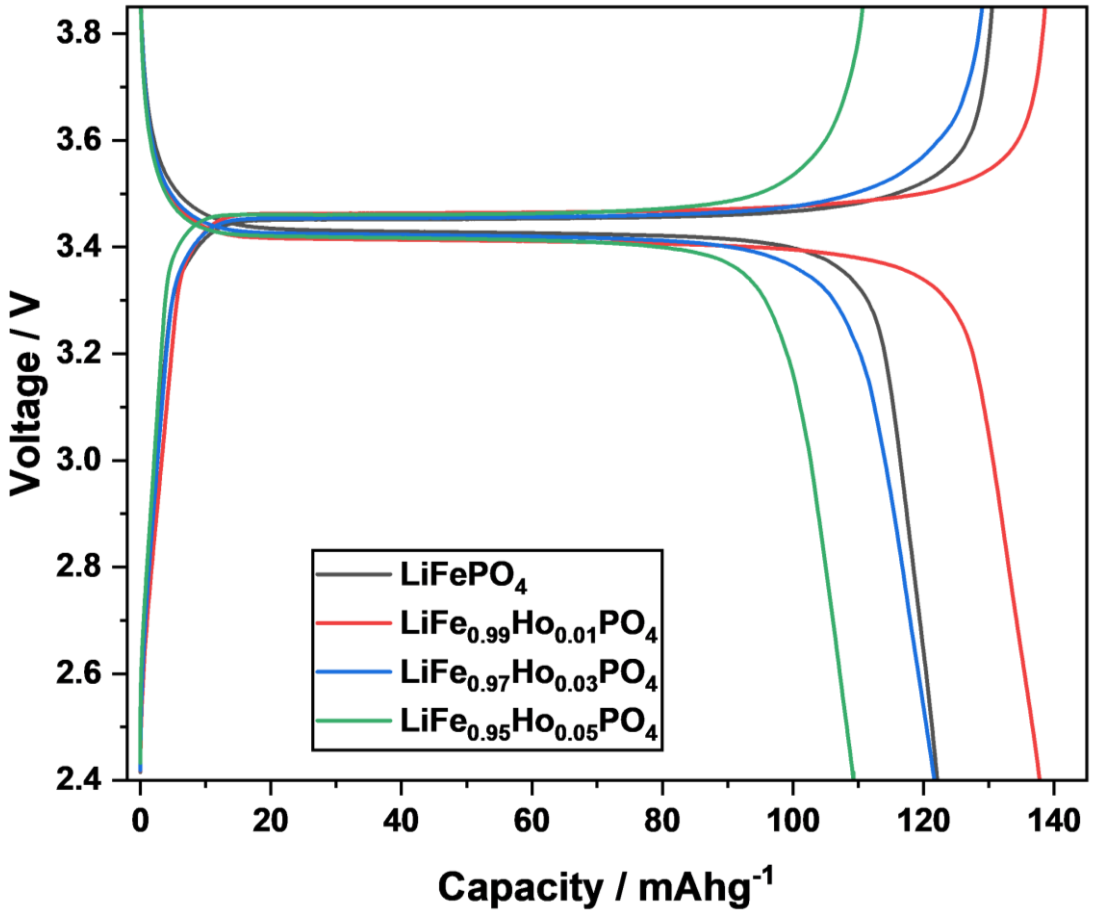

Figure 5.3: Galvanostatic cycling curves for undoped LFP, 1%, 3%, and 5% Ho-LFP at C/10.

The cycling efficiency of the 1% Ho-LFP was measured over 16 cycles at a cycle rate of C/5 and compared to the undoped analogue (**Figure 5.4 (a)**).

Increasing the capacity rate from C/10 to C/5 results in a lower average specific capacity of 108.7 mAh g^{-1} after the first cycle with an increase to 115.6 mAh g^{-1} by the final cycle (**Figure 5.4 (b)**). The Coulombic efficiency of Ho-LFP shows a maximum of 95.01% after the first cycle and a minimum of 81.7% after 16 cycles. The corresponding values for undoped LFP are: specific capacity of 98.1 mAh g^{-1} to 119.1 mAh g^{-1} after 13 cycles. The specific capacities for the subsequent cycles are lower (**Figure 5.4 (b)**). However, the Coulombic efficiency is improved when compared to that of Ho-LFP, at around 97%. Despite the overall performance of LFP

being better in terms of obtaining larger efficiencies and discharge capacities, the Ho-LFP showed greater stability, especially when comparing the discharge capacities of both materials. There was greater fluctuation observed for LFP, with capacity dropping and recovering at multiple points as the cell was cycled.

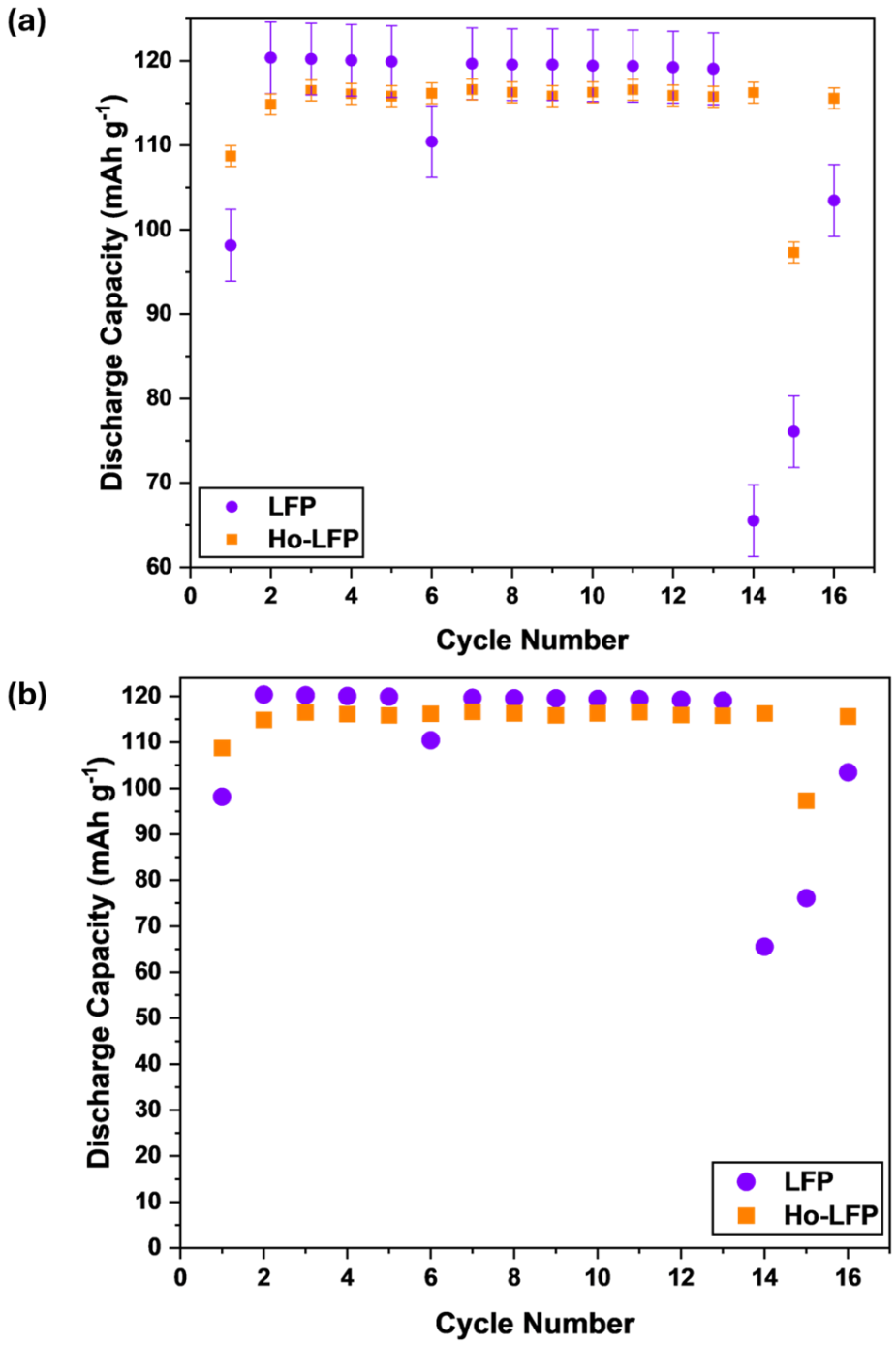

Figure 5.4: (a) Coulombic efficiency versus cycle number graph and (b) discharge capacity versus cycle number graph for LFP and 1% Ho-LFP over 16 cycles at C/5.

Cyclic voltammetry (CV) was performed after 1 and 5 cycles (**Figure 5.5**), followed by electrochemical impedance spectroscopy (EIS; **Figure 5.6**) to gain further insights into the Li-ion diffusion mechanism and internal resistance of the material. One redox peak is seen throughout all scans confirming the Li-ion diffusion is the dominating process and, therefore, only one redox mechanism is occurring, i.e. the holmium present in the material is redox inactive.

An improvement in peak profile is seen in the undoped analogue from the first to the fifth cycle, with the opposite observed for the 1% Ho-doped LFP (**Figure 5.5**). Despite this, the Li-ion apparent diffusion is higher for the latter after both 1 and 5 cycles. This observation supports the hypothesis that the presence of the dopant within the crystal lattice facilitates Li-ion diffusion.

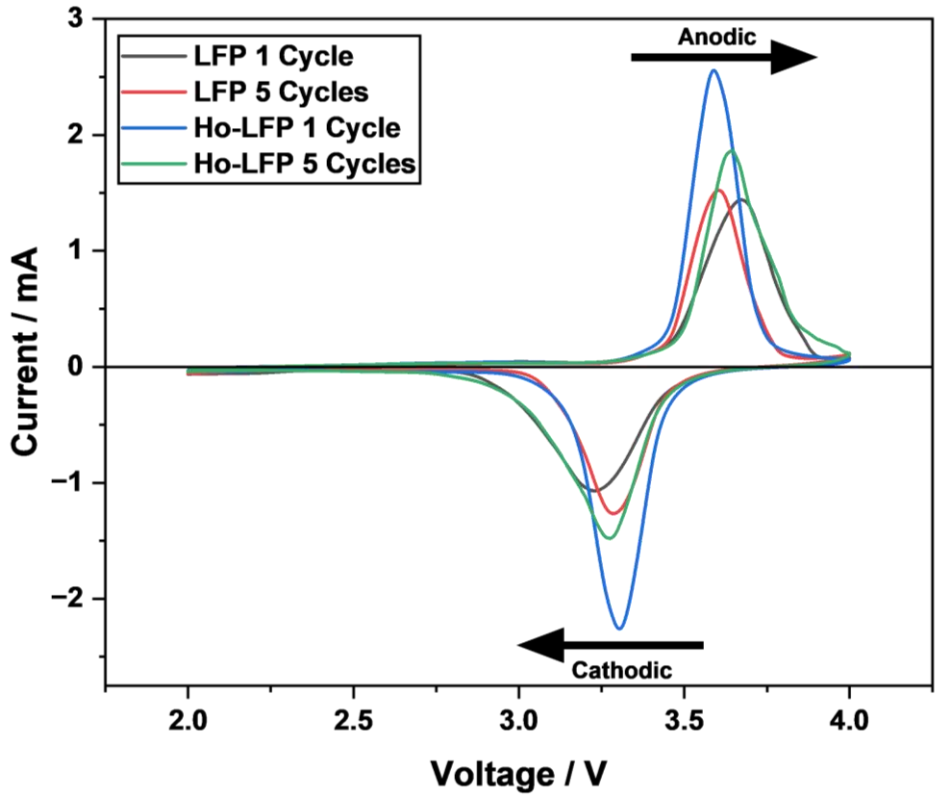

Figure 5.5: CV curves of undoped LFP and 1% Ho-LFP after 1 and 5 cycles.

The EIS plots follow the trends observed by the CV curves, i.e., higher conductivity an improvement from the first to fifth cycle for the undoped LFP (**Figure 5.6 (a)**). However, the opposite is observed for the 1% Ho-doped LFP (**Figure 5.6 (b)**).

All four EIS plots follow the expected impedance shape: a semicircle in the high-frequency region followed by a straight line in the low-frequency region. This

indicates that there are no extraneous reactions interfering with the redox and that the dominating process is the Li-ion de/intercalation.

The increase in resistance from the first to fifth cycle in the case of 1% Ho-LFP may be attributed to slight lattice distortion due to the presence of the dopant, leading to a structural disorder in the material as it is cycled, where the dopant blocks the diffusion channels and hinders the structural ordering observed in LFP. The decrease in resistance from the first to the fifth cycle seen in the case of LFP could confirm the complete formation of CEI by the fifth cycle.

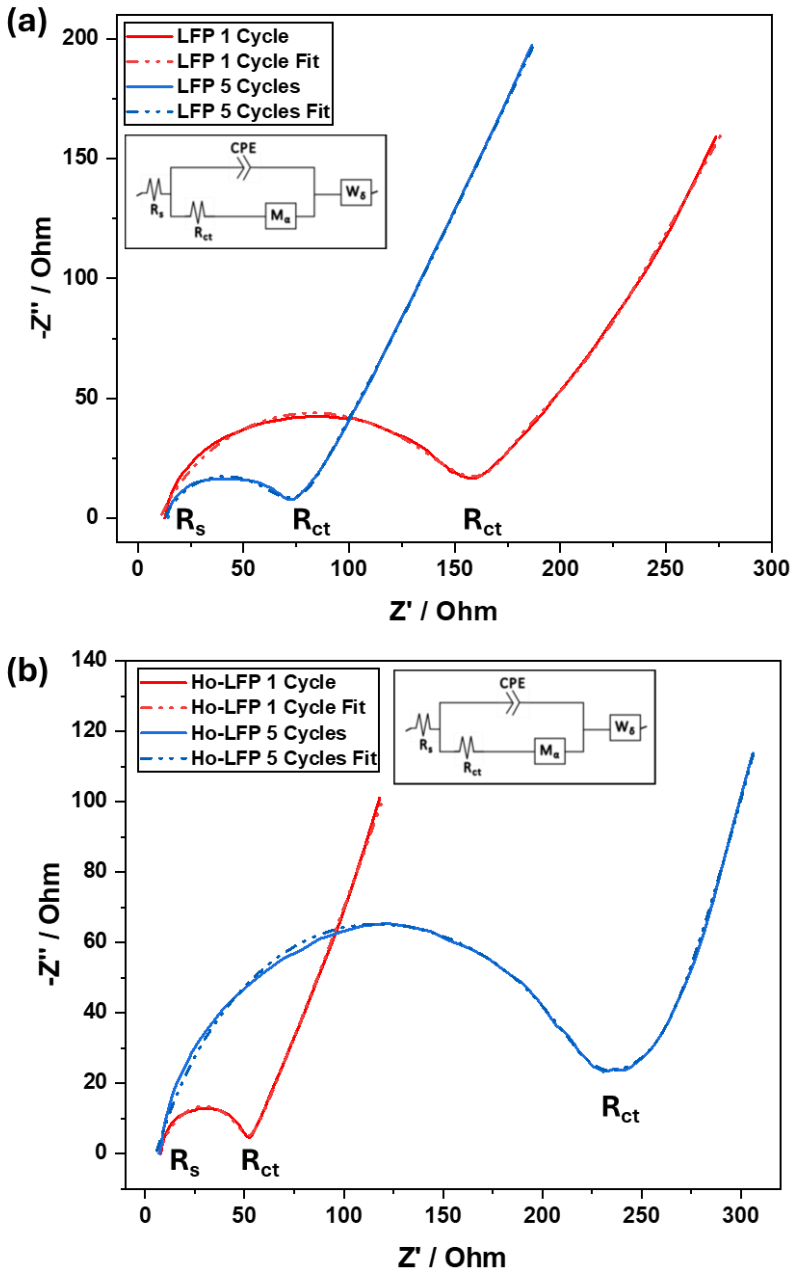

Figure 5.6: (a) EIS plots of undoped LFP after 1 and 5 cycles; (b) EIS plots of 1% Ho-doped LFP after 1 and 5 cycles.

5.3.3. X-Ray Absorption Spectroscopy

XAS measurements were conducted on *ex-situ* electrodes that were stopped at various SOCs. The electrodes were implemented as half-cells *vs* Li/Li^+ in 1 M LiTFSI in EC/DEC electrolyte and constructed as pouch cells. The Fe K-edge, P K-edge, and Ho L_{III}-edge of the samples were measured. For the Fe K-edge, EXAFS was also collected and analysis was carried out to determine Fe-O bond lengths obtained for the measured samples.

A reversible shift to higher energies is seen for the Fe K-edge of all samples (**Figure 5.7**) as the battery is charged. This upshift in energy is due to the iron oxidising from Fe^{2+} to Fe^{3+} as the Li^+ is deintercalated and charge compensation occurs. As the Li^+ is reinserted into the lattice upon discharging, the Fe^{3+} is reduced to Fe^{2+}, which is represented by the shift in the Fe K-edge XANES to lower energies. From **Figure 5.7** it is confirmed that for Ho-LFP the Fe^{3+} is oxidised to the same state as LFP, while in the discharged state the Fe^{2+} K-edge value of Ho-LFP is slightly downshifted than observed for LFP.

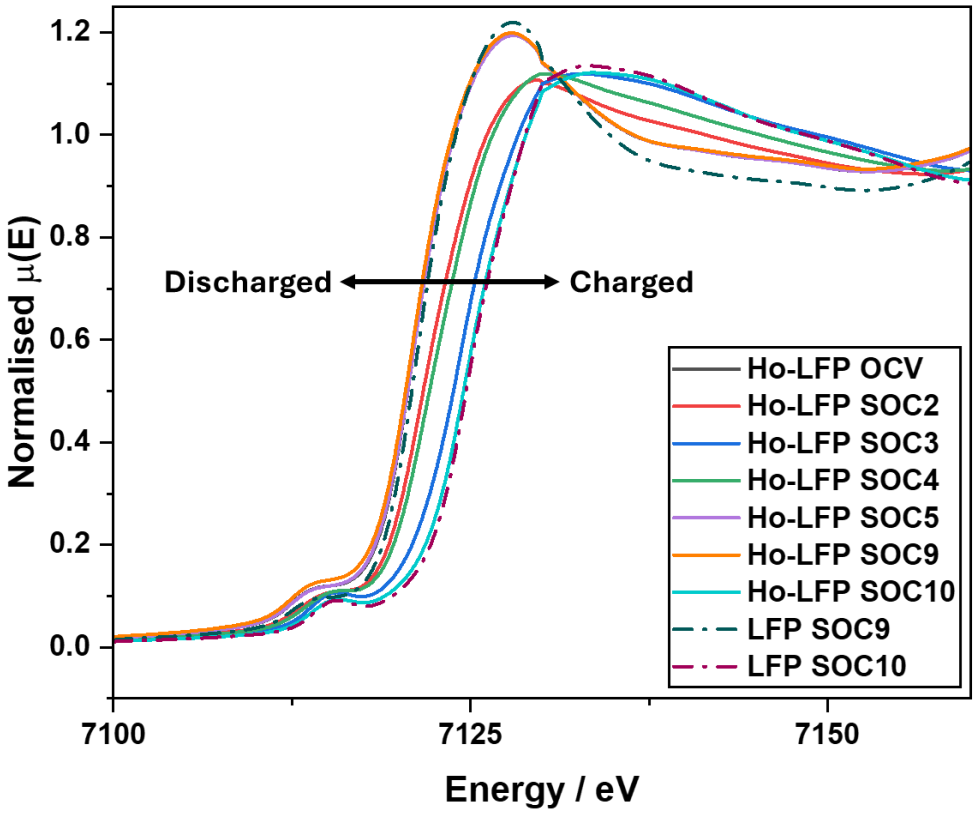

Figure 5.7: Fe K-edge XANES spectra for Ho-LFP at different SOCs during the first and fifth charge-discharge cycles and LFP at different SOCs during the fifth charge-discharge cycle at C/10.

The P K-edge XANES spectra (**Figure 5.8**) demonstrate an upshift in energy as the battery is charged to higher SOCs, illustrating the inductive effect of the phosphate polyanion as a dipole is induced upon Li-ion extraction.

The pre-edge features observed in the $FePO_4$ structure upon delithiation are due to the backbonding phenomenon from the phosphorus to the iron. The phosphate polyanion, PO_4^{3-}, occupies a tetrahedral coordination which contributes to orbital hybridisation, forming P sp^3 hybrid orbitals. The main edges (E_0) of the P K-edge XANES spectra are associated with the transition of a P 1*s* electron into an unoccupied state formed by the overlap of the P sp^3 hybrid orbital with the O 2*p* orbitals.[113]

As Li^+ is deintercalated from LFP, E_0 moves towards higher energies as charge compensation occurs upon the loss of lithium, where Fe^{2+} is oxidised to Fe^{3+}, resulting in more covalent Fe–O bonds. Polarisation of the oxygen ions towards the phosphorus ion occurs as the iron is oxidised from oxidation state Fe^{2+} to Fe^{3+}, which induces the formation of a dipole within the phosphate polyanion. The partial negative charges induced on the oxygen ions results in a shortening of the Fe^{3+}–O bonds and an increase in covalency, thus reducing the covalency of the P–O bonds.

There is a small discrepancy between the Ho-LFP and LFP P K-edge XANES spectra (**Figure 5.8 (b)**) where there is a slightly larger energy difference between the charged and discharged SOCs of the latter. This may indicate that the presence of holmium is polarising the material slightly, which results in a greater discrepancy in energy between SOC9 and SOC10, when comparing Ho-LFP with LFP, which contributes to a stronger induced dipole around the phosphate polyanion in the Ho-doped sample.

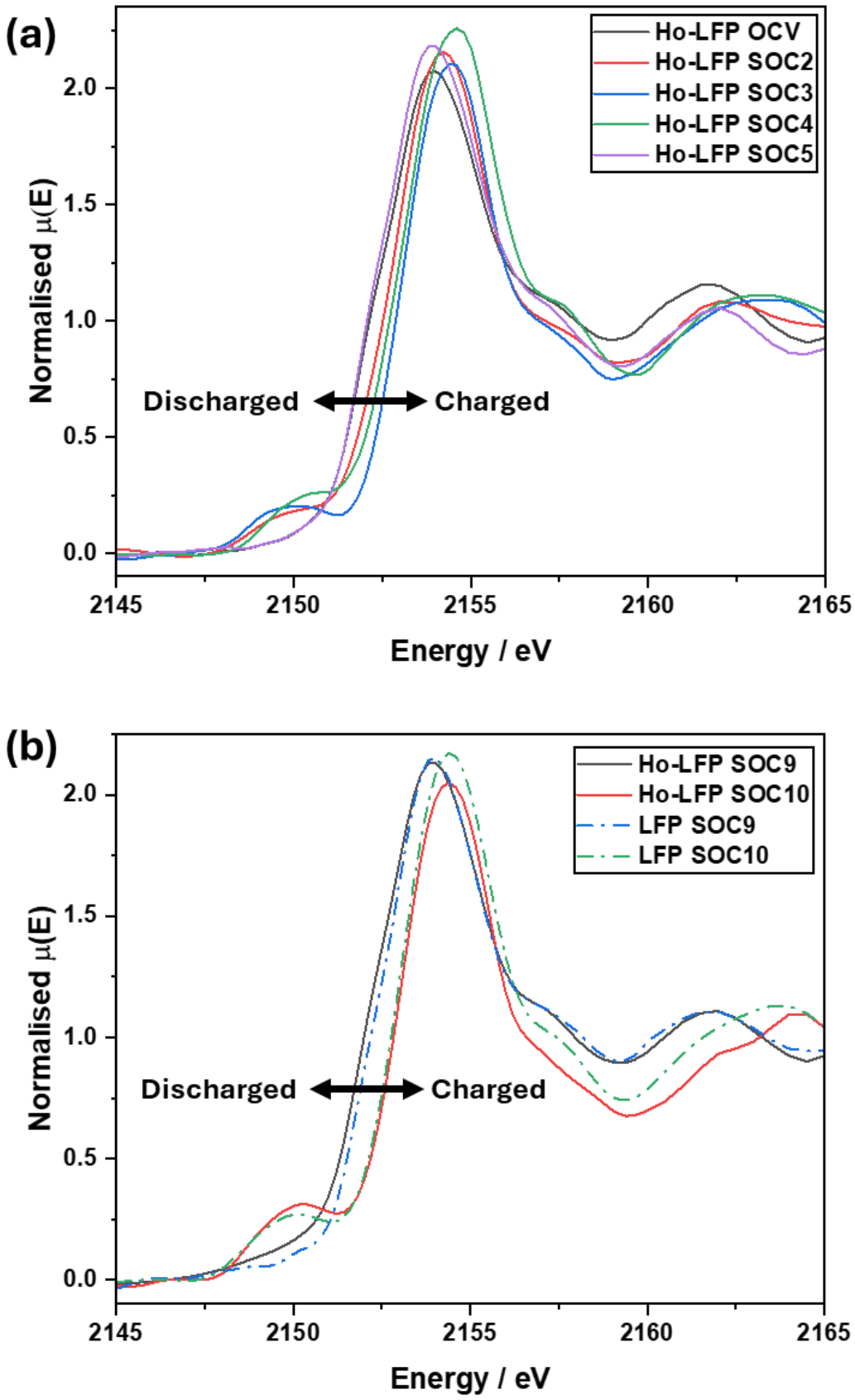

Figure 5.8: P K-edge XANES spectra at different SOCs for (a) Ho-LFP during the first charge-discharge cycle and (b) Ho-LFP and LFP during the fifth charge-discharge cycle.

A correlation between P and Fe K-edge E_0 energies can be made for both undoped and Ho-doped LFP (**Figure 5.9**) at each SOC. The fact that the shift in Fe K-edge energy can be directly coupled to that of the P K-edge energy is further proof that the phosphorous is electrochemically active. A dipole moment is induced in the phosphate polyanion due to an electron redistribution upon the loss of Li^+ as the Fe^{2+} is oxidised to Fe^{3+}.

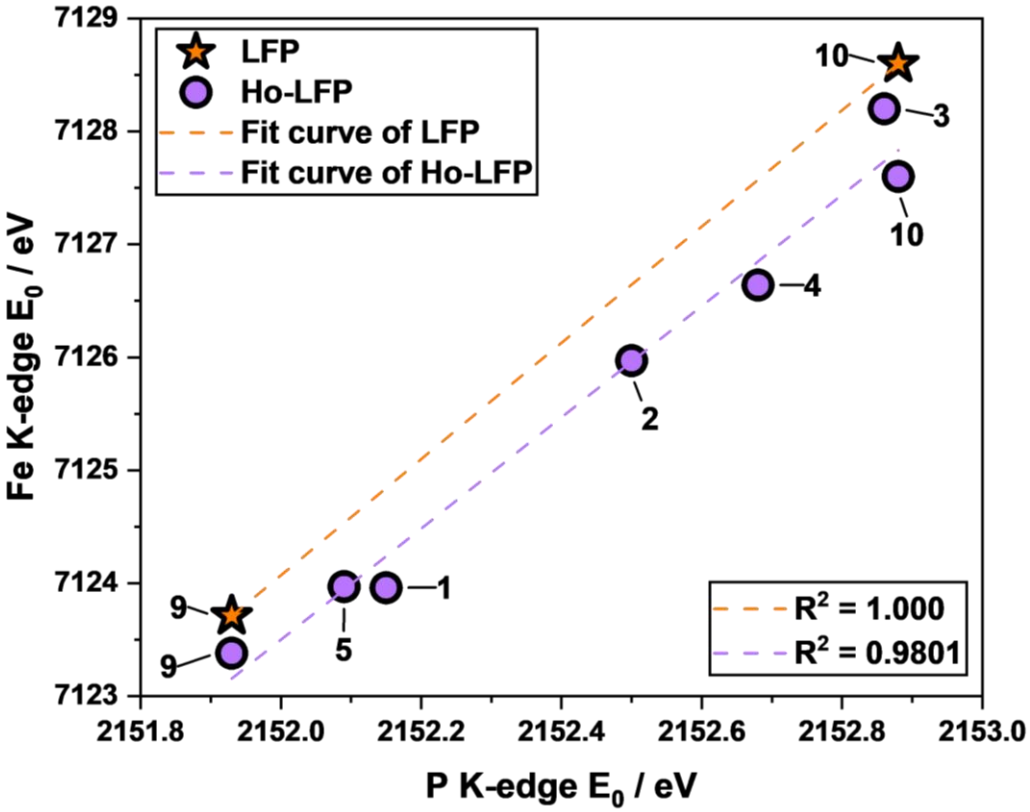

Figure 5.9: Energy distribution plot indicating correlations of P & Fe K-edge energies at different SOCs for Ho-LFP and LFP.

The Ho L_{III}-edge was also measured (**Figure 5.10**) since holmium can occupy both divalent and trivalent oxidation states. If the holmium were redox active as the battery was cycled, a similar trend of energy increase upon charging and decrease upon discharging would have been observed, as for the Fe and P K-edge XANES. However, no change in the edge energy of ~8076 eV was observed for any of the SOCs measured throughout this experiment.

A Ho_2O_3 standard was also measured, which aligns with the sample spectra, therefore further confirming redox inactivity and the fact that holmium is in oxidation state Ho(III). This agrees with the galvanostatic cycling curves where only one redox plateau was observed, linked to the $Fe^{2+/3+}$ redox couple.

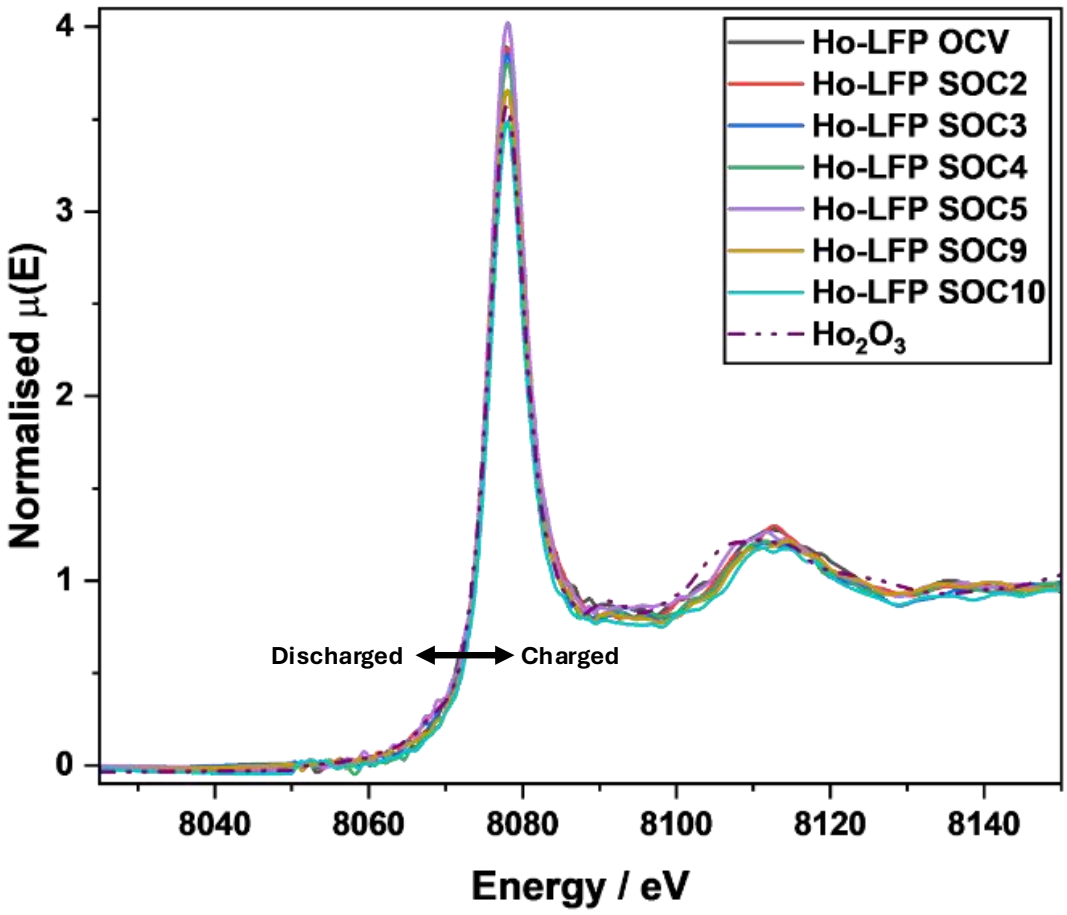

Figure 5.10: Ho L_{III}-edge XANES spectra for all measured SOCs of Ho-LFP.

The intense white line observed for Ho L_{III}-edge XANES is typical of dipole-allowed electronic transitions since X-ray absorption of lanthanide 2*p* core levels explores the unoccupied 5*d* states. Thus, a transition from 2*p* to 5*d* electronic states in trivalent lanthanides results in a very intense E_0 peak. The general appearance and lack of shift in E_0 suggests that the Ho^{3+} coordination environment is similar for all samples measured.[181,182]

EXAFS was also collected for the Fe K-edge and Ho L_{III}-edge of undoped and Ho-doped LFP at different SOCs in order to determine any trends in the Fe–O and Ho–O bond lengths for the materials.

The Fe K-edge EXAFS was collected for all samples and the Fe–O bond lengths obtained from the radial distribution function are listed in **Table 5.2**.

Table 5.2: Fe–O bond lengths obtained from the radial distribution function by fitting the Fe K-edge EXAFS.

Sample	Fe-O (Å)	Debye-Waller factor (σ^2)
Ho-LFP OCV	2.059(2)	0.0156
Ho-LFP SOC2	1.988(4)	0.0121
Ho-LFP SOC3	1.999(8)	0.0022
Ho-LFP SOC4	1.974(6)	0.0074
Ho-LFP SOC5	2.059(2)	0.0110
Ho-LFP SOC9	2.102(9)	0.0077
Ho-LFP SOC10	1.999(3)	0.0032
LFP SOC9	2.076(9)	0.0167
LFP SOC10	1.988(7)	0.0002

A trend can be noted whereby the Fe-O bond lengths decrease upon charging and increase upon discharging. This is in accordance with the XANES data obtained for the relevant SOCs where an increase in energy is seen upon charging, indicating an oxidation from Fe^{2+} to Fe^{3+}, thus decreasing the Fe–O bond distance.

In the Ho-LFP samples, another trend can be observed whereby in the transitory states where Fe^{2+}/Fe^{3+} both exist, the Fe-O bond is shorter than any other SOC. This indicates that the Fe^{3+}–O bond is shorter in the mixed Fe^{2+}/Fe^{3+} state (SOCs 2 and 4) than in the pure Fe^{3+} state (SOC 3 and 10) value where O^{2-} is shared between two Fe^{3+} ions (**Figure 5.11**). The Fe–O bond lengths obtained for SOCs 9 and 10 of Ho-LFP when compared to undoped LFP are slightly larger, indicating that the presence of holmium is affecting the crystal lattice of LFP. This agrees with the volume of the Ho-LFP lattice obtained from the Rietveld refinement (290.267 $Å^3$), which is slightly larger than that obtained for the undoped LFP (290.923 $Å^3$).

Ho L_{III}-edge EXAFS data were collected for all Ho-LFP samples and the Ho–O bond lengths were obtained from the radial distribution function. Slight changes were observed in these bond distances, which agree with the changes observed in the Fe–O bond lengths of corresponding samples.

As the battery was charged, a decrease in Ho–O bond length was observed and the opposite was noted as the battery was discharged. These values of Ho–O

bond lengths are in correlation with the Fe–O bond lengths discussed earlier in this chapter, where the Fe^{3+}–O bond distance is smaller than that for Fe^{2+}–O, thus being reflected in the corresponding Ho–O bond distances due to the contraction of the LFP crystal lattice.

A correlation factor can be calculated to further emphasise the corroboration between the Fe-O and Ho-O bond distances obtained:

$$\text{Correl}(\text{Fe–O}, \text{Ho–O}) = \frac{\sum(\text{Fe–O} - \overline{\text{Fe–O}})(\text{Ho–O} - \overline{\text{Ho–O}})}{\sqrt{\sum(\text{Fe–O} - \overline{\text{Fe–O}})^2 \sum(\text{Ho–O} - \overline{\text{Ho–O}})^2}} \qquad [\mathbf{5.1}]$$

where $\overline{\text{Fe–O}}$ and $\overline{\text{Ho–O}}$ are the average bond distances and Fe-O and Ho-O are the corresponding bond distances at each SOC. This can be calculated to be 0.8366, indicating a fairly good correlation between the two bond distances.

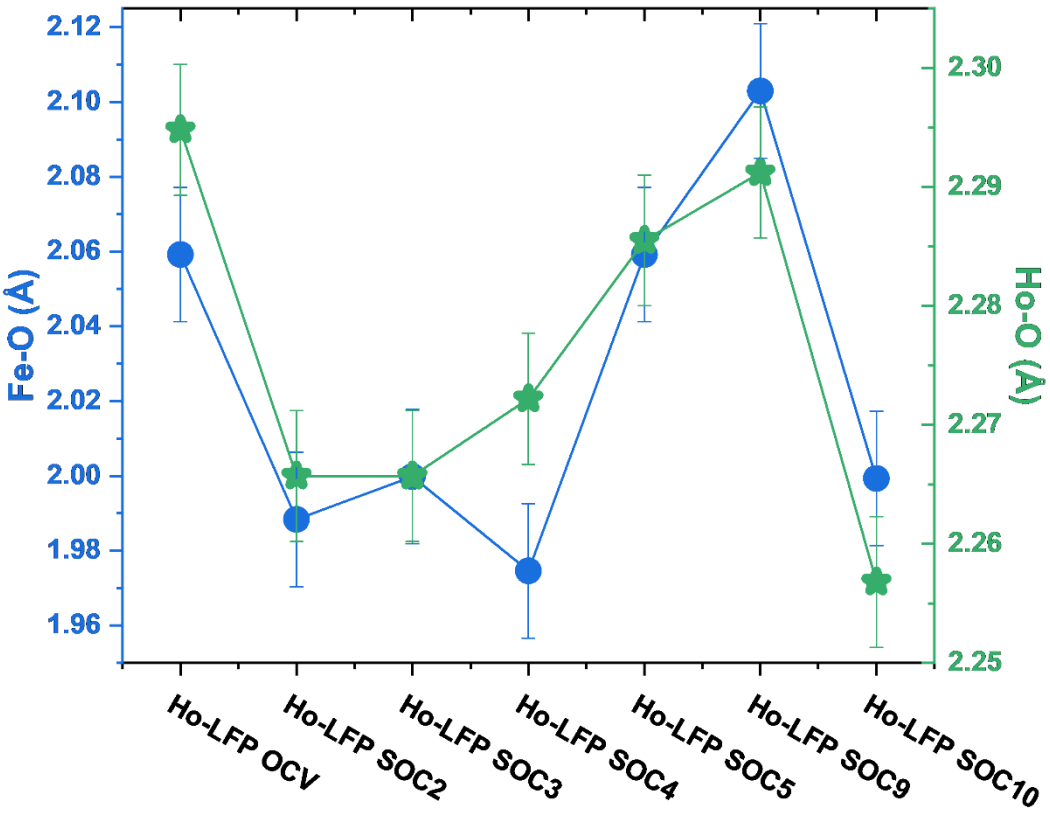

Figure 5.11: Correlation plot of Fe–O and Ho–O bond distances for each Ho-LFP SOC.

5.3.4. Mössbauer Spectroscopy

Mössbauer spectroscopy is a practical tool for identifying Fe-site occupancies in LFP. It gives further information regarding the oxidation state of iron at different SOCs as LFP is cycled, and it can provide an insight into whether the presence of the holmium is interfering or affecting the iron.

The Mössbauer parameters obtained for the LFP and Ho-LFP samples at different SOCs are given in **Table 5.3**, where it can be noted that, apart from LFP SOC10 and Ho-LFP SOC3, two doublets are present within each sample. This is largely due to an electrochemically inactive ferric iron antisite defect present in LFP which has been reported multiple times in literature.[123,128,183,184]

This Fe^{3+} antisite defect can arise in mainly one of two ways:

- Iron replacement, whereby an Fe^{3+} ion occupies an M2 site (**Figure 5.12**) previously occupied by an Fe^{2+} ion due to stoichiometric variations via $3Fe^{2+} \rightarrow 2Fe^{3+}$;
- Site vacancy, whereby $LiFe^{2+} \rightarrow 2Fe^{3+}$ leaving a Li-ion vacancy in the M1 site (**Figure 5.12**).

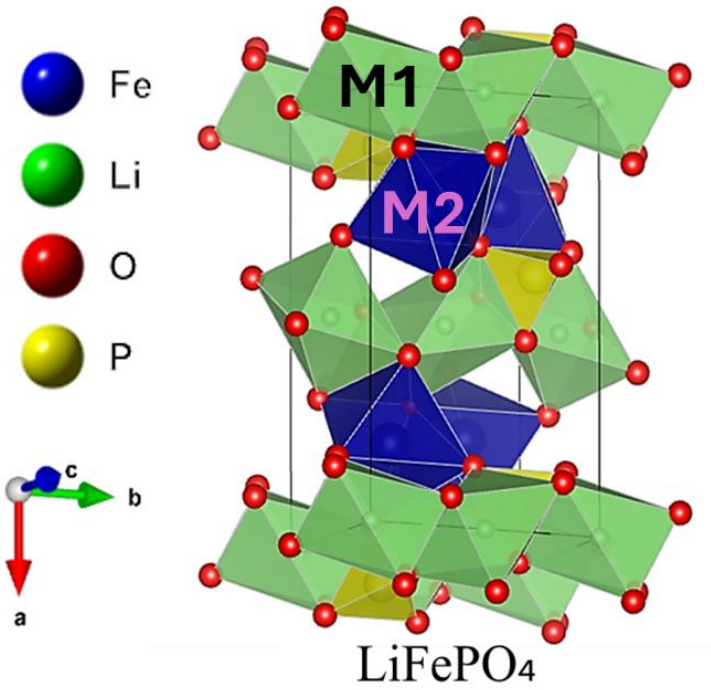

Figure 5.12: Crystal structure of LFP, indicating the M1 and M2 sites, where antisite defects may occur.

The latter situation seems to be the most likely outcome since the isomer shift, δ, values generally observed can be assigned to high-spin Fe^{3+} which is more prone to occupy an M1 site, which positions it as an antisite defect within the LFP crystal structure.[123,128]

The electrodes were implemented as cathodes *vs* Li/Li^+ metal anode using 1 M LiTFSI in EC/DEC electrolyte in pouch cells and cycled at a C-rate of C/10.

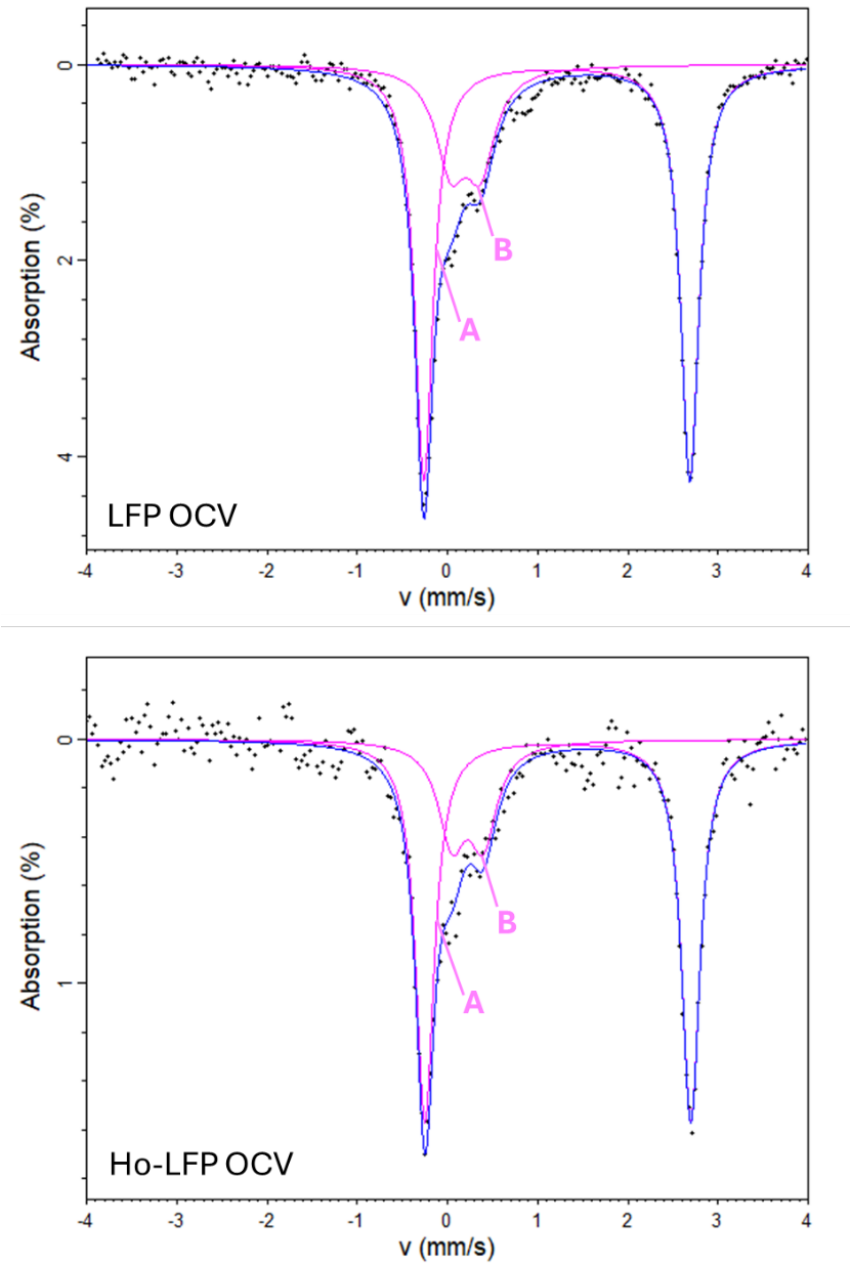

Figure 5.13: Mössbauer spectra collected at room temperature for LFP and Ho-LFP at OCV, with the blue line indicating an overall fit and the pink lines fitted to the separate doublets A & B.

In the discharged SOCs (OCV & SOC5), the dominating oxidation state is Fe^{2+} (**Figures 5.13** & **5.14**). This is notable from the intense doublet (**A**) followed by a very weak doublet (**B**) seen in the Mössbauer spectra. The intense doublet corresponds to high-spin Fe^{2+} in octahedral coordination. The smaller, weak doublet present in all SOCs is assigned to high-spin Fe^{3+} in tetrahedral coordination occupying an M1 antisite defect.[123,128]

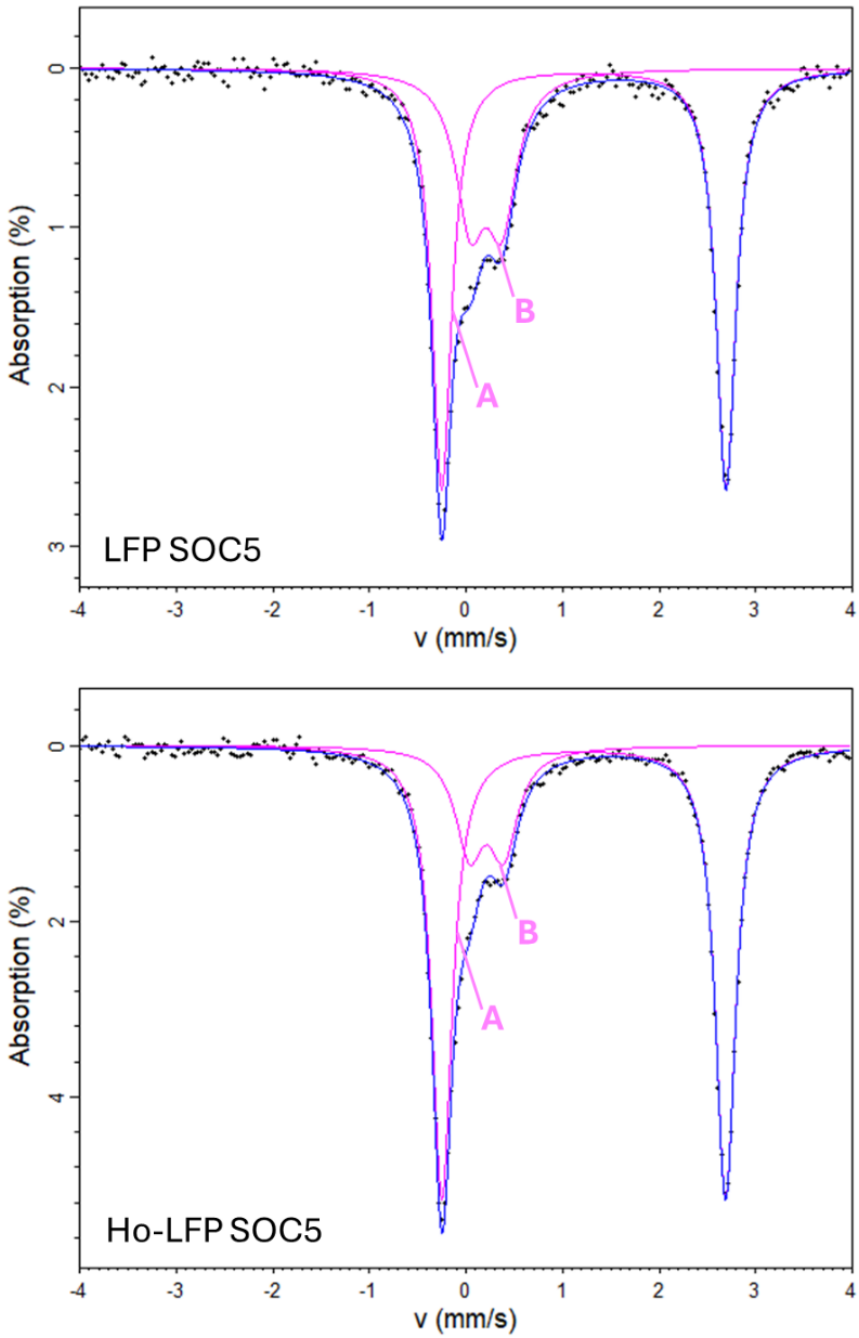

Figure 5.14: Mössbauer spectra collected at room temperature for LFP and Ho-LFP at SOC5, with the blue line indicating an overall fit and the pink lines fitted to the separate doublets A & B.

Undoped LFP and Ho-LFP SOC3, as well as LFP SOC10 Mössbauer spectra contain three doublets (**Figures 5.15** & **5.16 (top)**). The less intense doublets (**B** & **C**) could be due to high-spin Fe^{2+} being present in the sample due to relaxation factors where the oxidised Fe^{3+} could have started to reduce back to Fe^{2+}, and also due to the formation of CEI during the first charge-discharge cycle which prevents some of the lithium from being extracted therefore not oxidising all of the iron.[127]

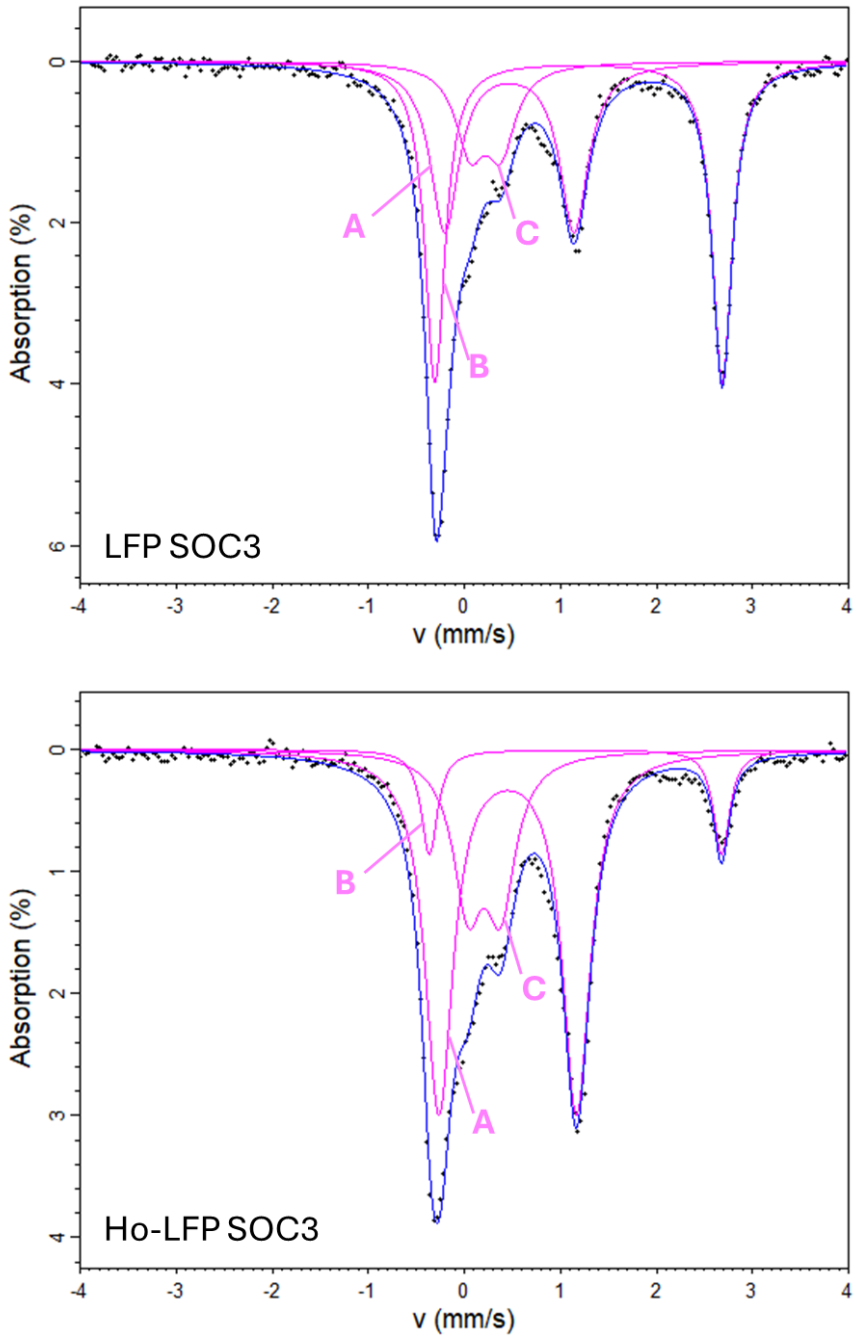

Figure 5.15: Mössbauer spectra collected at room temperature for LFP and Ho-LFP at SOC3, with the blue line indicating an overall fit and the pink lines fitted to the separate doublets A, B & C.

In the charged SOCs (SOCs 3 & 10), the predominant oxidation state is Fe^{3+} (**Figures 5.15** & **5.16**), which is made apparent by the intense doublet (**A**) indicating Fe^{3+} site occupancies. The Fe^{3+} present in these samples is more covalent due to the Fe–O–P backbonding brought on by the phosphate polyanion. In these SOCs the Fe 4*s* electrons are mixing with the O 2*sp* states, the first neighbouring atoms to the Fe atoms being probed in the octahedral site.[123]

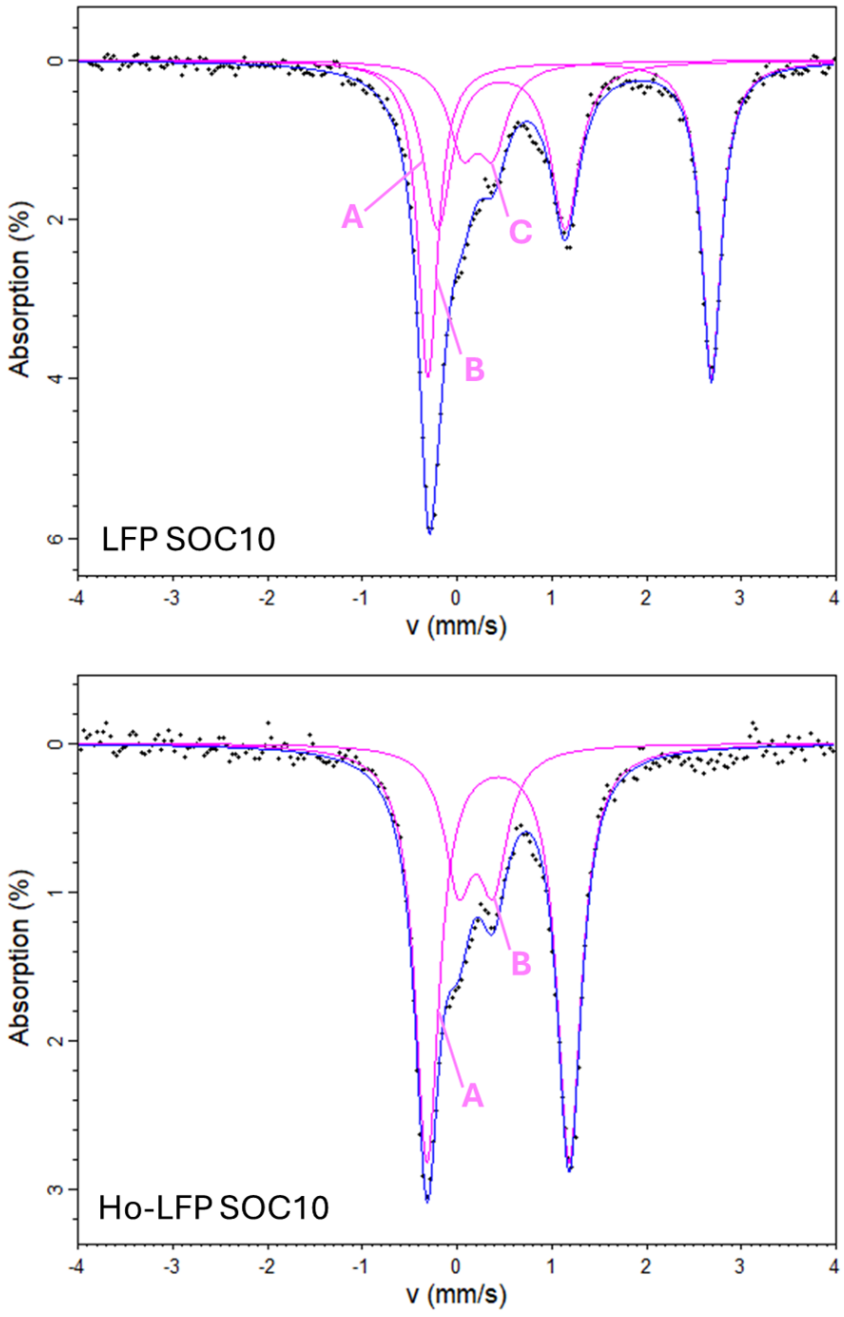

Figure 5.16: Mössbauer spectra collected at room temperature for LFP and Ho-LFP at SOC10 with the blue line indicating an overall fit and the pink lines fitted to the separate doublets A, B & C.

Table 5.3: Mössbauer parameters obtained from fitting the data obtained for LFP and Ho-LFP samples at different SOCs.

Sample	δ (mm s^{-1})	$\Gamma/2$ (mm s^{-1})	Δ (mm s^{-1})	A (%)
LFP OCV	1.214	0.124	2.949	73.12
	0.203	0.201	0.327	26.88
LFP SOC3	1.19	0.125	2.991	47.1
	0.47	0.18	1.347	35.3
	0.221	0.184	0.317	17.6
LFP SOC5	1.222	0.123	2.943	66.52
	0.210	0.186	0.325	33.48
LFP SOC10	0.416	0.142	1.501	79.12
	0.183	0.234	0.372	20.88
Ho-LFP OCV	1.225	0.125	2.947	73.35
	0.226	0.184	0.346	26.65
Ho-LFP SOC3	1.158	0.101	3.042	10.50
	0.209	0.187	0.340	26.80
	0.452	0.176	1.431	62.70
Ho-LFP SOC5	1.220	0.128	2.937	76.71
	0.216	0.177	0.354	23.29
Ho-LFP SOC10	0.434	0.155	1.501	73.00
	0.200	0.184	0.365	27.00

A correlation between isomer shift, δ, quadrupole splitting, Δ, and coordination number of iron for the LFP and Ho-LFP samples measured is plotted in **Figure 5.17**. Clear clustering is observed at coordination numbers 4 and 6, with the clustering at coordination number 4 being composed of high-spin Fe^{3+} of tetrahedral coordination, and that at coordination number 6 being high-spin Fe^{2+} and Fe^{3+} of octahedral coordination, depending on the SOC being measured.

A link can be made between the coordination number of iron and the number of antisites present in the structure, suggesting that there is a level of Fe^{3+} occupancy of M2 sites within all samples. This could be due to stoichiometric disparities owing to differences in grain sizes, whereby larger grain sizes could not have been fully de/lithiated upon charging and discharging, therefore containing different levels of Fe^{2+} and Fe^{3+}.

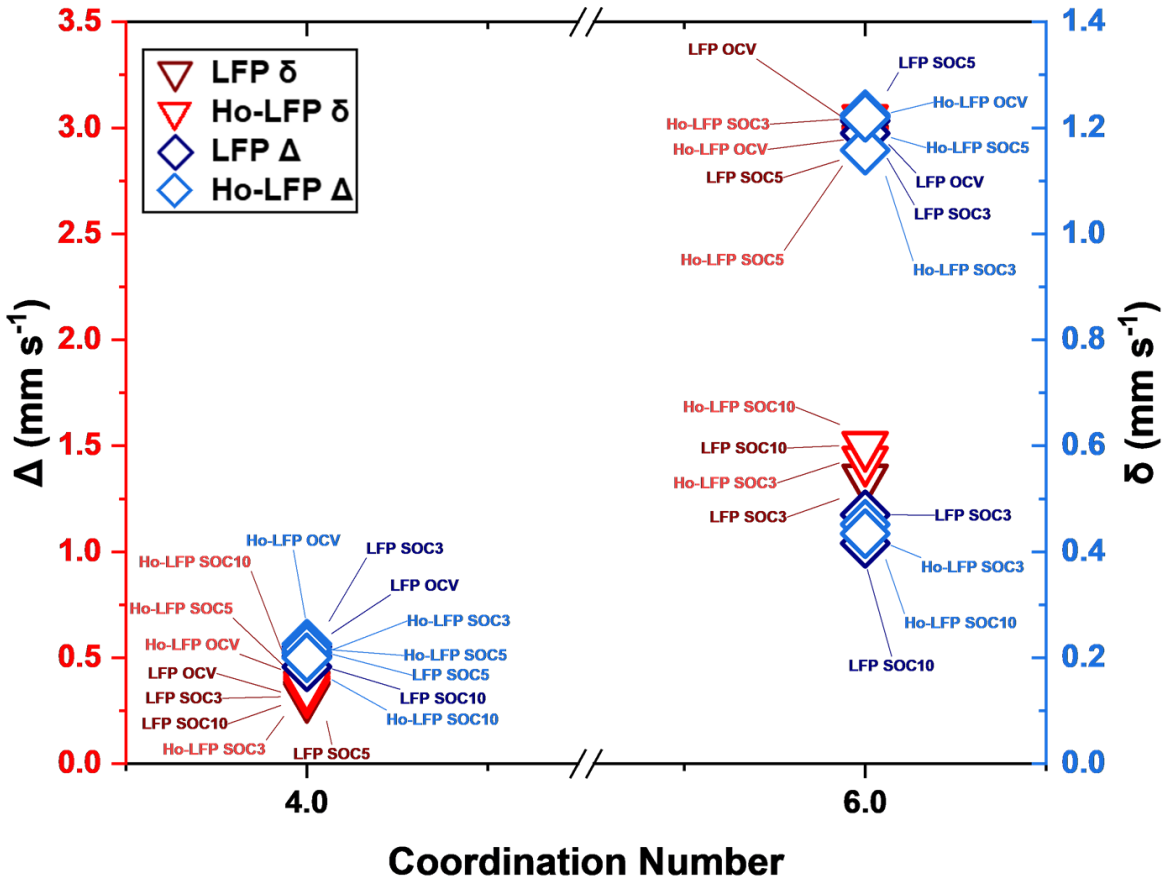

Figure 5.17: Correlation between isomer shift, quadrupole splitting, and coordination number for LFP and Ho-LFP at different SOCs.

The Mössbauer spectra obtained for the measured samples gave a good insight into the coordination environments of iron at different SOCs and there is little to no difference observed between the spectra of undoped and Ho-doped LFP, indicating that the presence of the holmium in the Ho-LFP samples is not interfering with the redox mechanism or the immediate environment of iron. This data is in accordance with the XAS data previously discussed in this chapter.

5.4. Chapter Conclusions

Despite the undoped analogue giving high discharge capacities and coulombic efficiencies, the Ho-LFP displayed greater electrochemical stability in comparison to the undoped LFP, displaying more consistent discharge capacities recorded with respect to LFP. The difference in charge and discharge capacities observed for the Ho-LFP samples was also observed to be reduced, therefore displaying a better cycling capability overall.

The holmium was observed to be redox inactive as the cells of the doped analogue were cycled, as noted from the Ho L_{III}-edge XANES. The holmium dopant was observed not to interfere with the redox mechanism of iron or the phosphate polyanion, since the same trends and mechanisms were observed in both Fe K-edge and P K-edge XANES for the doped and undoped samples.

The EXAFS obtained from the Ho L_{III}-edge showed a minimal change in the Ho-O bond distance, which is corroborated with lattice parameter alterations induced by the contraction of the Fe-O bond upon cycling, therefore further proving that the holmium is redox inactive as the battery is cycled. It is important to consider also that some of the holmium present in the samples could be residual Ho_2O_3 sitting on the surface of the grain based on the identical shape of the Ho L_{III}-edge XANES spectra for the samples and Ho_2O_3. The Ho–O bond distances measured would agree with this statement, since they fall within the 2.23 to 2.32 Å range for the cubic structure of Ho_2O_3.[185]

Observations made from the Mössbauer data agree with the XAS data obtained for the samples. The discharged samples contained a higher degree of Fe^{2+} in high-spin octahedral environments, as observed from the high quadrupole splitting values. The Fe^{3+} site occupancies in the charged samples can be inferred as being more covalent in nature due to their lower isomer shift values.[122] This is corroborated by the P K-edge XANES where pre-edge features are observed in the charged SOCs, indicating a back-donation of electrons occurring from the P *p* states to the Fe 3*d* states.

Furthermore, Mössbauer data confirmed that the presence of holmium within LFP did not interfere with the dominant Fe^{2+}/Fe^{3+} redox mechanism as the battery is cycled, as only two doublets were seen in all spectra related to the different iron species present depending on the SOC. This correlates with the electrochemical data whereby a single plateau was observed and a single peak was seen in the

galvanostatic cycling curves and cyclic voltammograms, respectively, and no shift was detected in the XANES spectra of the Ho L_{III}-edge recorded for the samples.

Considering that the holmium may be sitting in the form of Ho_2O_3, rather than being incorporated into the lattice to give $LiFe_{0.99}Ho_{0.01}PO_4$, the improvement in cyclability could be due to the fact that its presence alters the surface in such a way that it prevents detrimental side reactions, which can lead to improved performance. Further analysis as to the site occupation and composition of the holmium within LFP should be carried out to determine its effects in more detail.

6. Conclusions and Future Work

6.1. General Conclusions

The findings of this thesis not only expand on our knowledge of the electrochemical effects of cation doping in LFP, but also the structural properties of these materials. The investigation of cation doping mechanisms in LFP has revealed the impacts of elemental substitution on this critical cathode material. The complex interplay between dopant type, concentration, and electrochemical performance has been demonstrated. However, despite extensive efforts to enhance the properties of LFP through strategic doping, the results obtained throughout this thesis reveal the resistance of LFP's intrinsic structural and electrochemical properties.

Among the various dopants investigated, the 1% holmium dopant showed the most promising results, whilst the 5% aluminium doping had the poorest outcome. The small ionic radius of aluminium created structural constraints, whereby it preferentially occupied Li-sites over Fe-sites, which became more evident at higher concentrations (3%, 5%), and made trend identification challenging. The samples with higher aluminium concentration also displayed poor ionic conductivity, resulting in poor electrochemical performance.

Scandium doping yielded interesting results, with increasing concentrations correlating with decreased particle size and increased lattice strain along the <1 1 0> plane direction. However, the contrary was seen with discharge capacity and Li-ion diffusion which were decreased. This highlighted the effects of structural modification on electrochemical performance.

Ytterbium doping yielded novel results, especially considering the presence of the $YbPO_4$ impurity phase which could not be eliminated through sintering or leaching. The solution and charge-transfer resistances of this material after 5 cycles were the lowest recorded for any doped material, however it suffered in values calculated for Li-ion diffusion, which may have been a direct consequence of the impurity phase. It was difficult to eliminate this impurity phase since the lowest doping concentration of interest for this thesis was 1%.

The vanadium-doped samples provided an insight into excessive doping. At 20% dopant concentration, V-LFP demonstrated significant performance limitations, including high resistance and impeded Li-ion diffusion. The high concentration of vanadium allowed us to study the oxidation state distribution of V

in LFP and if the V is at any point redox active during cycling. It was confirmed that the dominating oxidation state is V^{3+} and that vanadium is redox inactive, despite the presence of the $LiVP_2O_7$ impurity phase.

This aligns with the literature, where the optimal vanadium concentration has been reported to be between 3-5%, above which the electrochemical performance degrades due to impurity phases and internal charge repulsion which hinders the Li-ion diffusion.[107,152,153,155]

Holmium doping showed particular promise, displaying enhanced stability and polarisation, and reduced overpotential, when compared to the undoped analogue synthesised using the same method. Holmium itself remained redox inactive, with the iron redox couple dominating the redox mechanism of the battery. A minimal amount of holmium was used, at 1% stoichiometric concentration, showing the importance of controlling dopant concentration in LFP improvement approaches.

Comparative analyses with a commercial sample, Gelon LFP, highlighted the challenges of in-house synthesis and material optimisation. Gelon LFP demonstrated superior electrochemical performance, demonstrating the difficulty of reproducing results of commercially optimised battery materials in-house.

Another outcome of this thesis pertained to the electrochemical function of phosphorus within the phosphate polyanion. XAS investigations proved the redox activity of phosphorus at various SOCs of a battery's cycle. Reversible shifts to higher energies in the XANES spectra of the P K-edge were observed for the delithiated (charged) samples. The presence of the dopant did not interfere with this shift, with V-doped and Ho-doped samples being measured. However, a slightly larger gap in energy between the charged and discharged samples of Ho-LFP was observed when compared to the undoped analogue, which could infer that the presence of holmium within the lattice leads to a greater polarisation around the phosphate polyanion that contributes to a stronger induced dipole.

A critical observation can be made regarding cation doping in LFP: doping is not one-size-fits-all. The doping success of different elements depends on a number of factors, such as ionic radius of the dopant, concentration, formal valency, site occupation, and synthetic strategy. The aluminium doping results particularly highlight this, demonstrating how minor structural modifications can alter the performance and electrochemical properties when compared to undoped LFP.

The in-house synthesised materials displayed better polarisation when compared to that of the externally procured materials. The undoped, Ho-, and Yb-doped samples synthesised as part of this thesis had a difference of 0.03 V between the charge and discharge plateaus, whereas the Gelon and V-doped LFP obtained from Gelon Energy Corp Lib Group Co., Ltd. and UCL, respectively, displayed a difference of 0.07 V between the charge and discharge plateaus as the cells were cycled.

This thesis provided a significant understanding of trivalent cation doping in LFP, revealing the interplay between material alteration and performance enhancement. Each dopant element introduced unique challenges with different structural and electrochemical outcomes.

Future investigations should focus on developing multifaceted doping strategies, with importance given to striking a balance between the structural and electrochemical aspects of the doping mechanism. The findings of this thesis emphasise the need for consideration of dopant characteristics, site preferences, and concentration effects in advancing battery material technologies.

6.2. Future Work

There are various other avenues one can take in order to expand the work done in this thesis. Other materials, dopants, and analytical techniques can be explored to gain a better understanding of doping strategies and dopant function in LFP. Furthermore, theoretical calculations can be carried out to complement the work done in this thesis and give a better insight to the potential of cation doping in LFP for implementation of the material on a larger scale.

To make this study more comprehensive different cation dopants of varying oxidation states could be implemented, thus creating a comparative study of dopant behaviours in LFP. A different comparative study assessing the effects of different starting reagents would also prove interesting, as the salts of the starting reagent determine the outcome of the material. Different synthetic methodologies, such as sol-gel, microwave assisted, or solid state could also be employed in order to fine tune the doping parameters for instance site occupancy, concentration, and valency.

Considering the electrochemistry, the effects of different binders on the doped and undoped materials could be explored, using aqueous binders such as

carboxymethyl cellulose (CMC) and polyvinylacetate (PAA) based binders. Another aspect to consider is implementing these cathode materials as full cells *vs* a graphite-based anode, which will help give an indication of functionality on a production level.

Neutron diffraction studies could complement the collected data, especially for the lanthanide-doped analogues. Time-of-flight measurements could give further insight to the effects of the dopant on the charge/discharge mechanism of doped and undoped LFP, as well as help observe the function, if any, of the dopant during the redox mechanism.

As the materials were cycled, the oxygen as part of the phosphate group was studied indirectly through measurements carried out on the P K-edge of undoped, Gelon, Ho-, and V-doped LFP. It would, however, also be interesting to study the effects of the doped and undoped materials at different SOCs on the oxygen directly, which could be done using X-ray Raman scattering.

The lithium-ion insertion and reaction mechanisms can be more closely followed by applying analytical techniques such as X-ray photoelectron spectroscopy (XPS), nuclear magnetic resonance (NMR), and *in operando* XAS, the latter of which could be used to probe different elemental edges as the battery is cycled in real-time. Furthermore, carrying out Mössbauer spectroscopy and O K-edge XAS on all doped samples would be beneficial in expanding the understanding of the inductive effect due to the Fe-O-P linkage and investigating the effects of the dopants on the material more thoroughly.

Adding dopants in different concentrations and carrying out structural and electrochemical characterisations of the resulting materials should, in principle, lead to a LFP design that produces a more structurally sound and stable material with an increased longevity that meets the demands of the market.

REFERENCE LIST

(1) Trasatti, S. 1799-1999: Alessandro Volta's "Electric Pile" Two Hundred Years, but It Doesn't Seem like It. *J. Electroanal. Chem.* **1998**, *460* (1–2), 1–4.

(2) Scrosati, B. History of Lithium Batteries. *J. Solid State Electrochem.* **2011**, *15* (7–8), 1623–1630.

(3) Lewis, G. N.; Keyes, F. G. The Potential of the Lithium Electrode. *J. Am. Chem. Soc.* **1913**, *35* (4), 340–344.

(4) Xu, J.; Dou, S.; Cui, X.; Liu, W.; Zhang, Z.; Deng, Y.; Hu, W.; Chen, Y. Potassium-Based Electrochemical Energy Storage Devices: Development Status and Future Prospect. *Energy Storage Materials* **2021**, *34*, 85–106.

(5) Salkind, A. J. *Proceedings of the Symposium on History of Battery Technology*; 1987.

(6) Whittingham, M. S. Electrical Energy Storage and Intercalation Chemistry. *Science* **1976**, *192* (4244), 1126–1127.

(7) Whittingham, M. S. Chemistry of Intercalation Compounds: Metal Guests in Chalcogenide Hosts. *Prog. in Solid State Chem.* **1978**, *12* (1), 41–99.

(8) Whittingham, M. S. The Role of Ternary Phases in Cathode Reactions. *J. Electrochem. Soc.* **1976**, *123* (3), 315–320.

(9) Murphy, D. W.; Carides, J. N. Low Voltage Behavior of Lithium/Metal Dichalcogenide Topochemical Cells. *J. Electrochem. Soc.* **1979**, *126* (3), 349–351.

(10) Armand, M. B. Intercalation Electrodes. *Mater. for Adv. Batter.*; Murphy, D. W., Broadhead, J., Steele, B. C. H., Eds.; Springer US: Boston, MA, 1980; pp 145–161.

(11) Armand, M. Polymer Solid Electrolytes - an Overview. *Solid State Ion.* **1983**, *9–10*, 745–754.

(12) Armand, M. Charge Transfer at Polymer Electrolytes. *Faraday Discuss. Chem. Soc.* **1989**, *88*, 65.

(13) Nagaura, T.; Tazawa, K. *Prog. in Batter. and Solar Cells*; Cleveland, OH (United States); JEC Press Inc., 1990; Vol. 9.

(14) Scrosati, B. Lithium Rocking Chair Batteries: An Old Concept? *J. Electrochem. Soc.* **1992**, *139* (10), 2776–2781.

(15) Mizushima, K. LixCoO2 (0<x<1): A New Cathode Material for Batteries of High Energy Density. 4.

(16) Thackeray, M. M.; David, W. I. F.; Bruce, P. G.; Goodenough, J. B. Lithium Insertion into Manganese Spinels. *Mater. Res. Bull.* **1983**, *18* (4), 461–472.

(17) Yabuuchi, N.; Ohzuku, T. Novel Lithium Insertion Material of LiCo1/3Ni1/3Mn1/3O2 for Advanced Lithium-Ion Batteries. *J. Power Sources* **2003**, *119–121*, 171–174.

(18) Padhi, A. K.; Nanjundaswamy, K. S.; Goodenough, J. B. Phospho-olivines as Positive-Electrode Materials for Rechargeable Lithium Batteries. *J. Electrochem. Soc.* **1997**, *144* (4), 1188–1194.

(19) Son, S.-B.; Gao, T.; Harvey, S. P.; Steirer, K. X.; Stokes, A.; Norman, A.; Wang, C.; Cresce, A.; Xu, K.; Ban, C. An Artificial Interphase Enables Reversible Magnesium Chemistry in Carbonate Electrolytes. *Nat. Chem.* **2018**, *10* (5), 532–539.

(20) Lin, D.; Liu, Y.; Cui, Y. Reviving the Lithium Metal Anode for High-Energy Batteries. *Nat. Nanotech.* **2017**, *12* (3), 194–206.

(21) Wang, F.; Borodin, O.; Gao, T.; Fan, X.; Sun, W.; Han, F.; Faraone, A.; Dura, J. A.; Xu, K.; Wang, C. Highly Reversible Zinc Metal Anode for Aqueous Batteries. *Nat. Mater.* **2018**, *17* (6), 543–549.

(22) Sheikh, K.; Chen, B. X.; Penn, I. *Lithium-Ion Batteries Work Earns Nobel Prize in Chemistry for 3 Scientists*. https://www.nytimes.com/2019/10/09/science/nobel-prize-chemistry.html (accessed 2022-06-15).

(23) Grandin, K.; Goodenough, J. B. The Pathway to Discovering Practical Cathode Materials for the Rechargeable Li+-Ion Battery. In *The Nobel Prizes 2019*; World Scientific, 2022.

(24) Manthiram, A. A Reflection on Lithium-Ion Battery Cathode Chemistry. *Nat. Commun.* **2020**, *11* (1), 1550.

(25) Mizushima, K.; Jones, P. C.; Wiseman, P. J.; Goodenough, J. B. LixCoO2 (0<x<-1): A New Cathode Material for Batteries of High Energy Density. *15* (6).

(26) Chebiam, R. V.; Kannan, A. M.; Prado, F.; Manthiram, A. Comparison of the Chemical Stability of the High Energy Density Cathodes of Lithium-Ion Batteries. *Electrochem. Commun.* **2001**, *3* (11), 624–627.

(27) Nishizawa, M.; Yamamura, S. Irreversible Conductivity Change of Li1−xCoO2 on Electrochemical Lithium Insertion/Extraction, Desirable for Battery Applications. *Chem. Commun.* **1998**, No. 16, 1631–1632.

(28) Lyu, Y.; Wu, X.; Wang, K.; Feng, Z.; Cheng, T.; Liu, Y.; Wang, M.; Chen, R.; Xu, L.; Zhou, J.; Lu, Y.; Guo, B. An Overview on the Advances of LiCoO2 Cathodes for Lithium-Ion Batteries. *Adv. Energy Mater.* **2021**, *11* (2), 2000982.

(29) Kim, S.; Lee, J.-A.; Lee, D. G.; Son, J.; Bae, T. H.; Lee, T. K.; Choi, N.-S. Designing Electrolytes for Stable Operation of High-Voltage LiCoO2 in Lithium-Ion Batteries. *ACS Energy Lett.* **2024**, *9* (1), 262–270.

(30) *Lithium Cobalt Oxide - LiCoO2 - Conduction animation*. ChemTube3D. https://www.chemtube3d.com/lib_lco-2/ (accessed 2024-07-03).

(31) Chebiam, R. V.; Prado, F.; Manthiram, A. Soft Chemistry Synthesis and Characterization of Layered Li1-xNi1-yCoyO2-δ (0 ≤ x ≤ 1 and 0 ≤ y ≤ 1). *Chem. Mater.* **2001**, *13* (9), 2951–2957.

(32) Baczyńska, A.; Niewiadomski, W.; Gonçalves, A.; Almeida, P.; Luís, R. Li-NMC Batteries Model Evaluation with Experimental Data for Electric Vehicle Application. *Batteries* **2018**, *4* (1), 11.

(33) Ma, X.; Wang, J.; Wang, Z.; Wang, L.; Xu, H.; He, X. Engineering Strategies for High-Voltage LiCoO2 Based High-Energy Li-Ion Batteries. *Electron* **2024**, *2* (3), e33.

(34) Goodenough, J. B. Cathode Materials: A Personal Perspective. *J. Power Sources* **2007**, *174* (2), 996–1000.

(35) Senthil Arumugam, R.; Shunmugasundaram, R.; Safonova, O. V.; Wood, V. Effect of Subtle Changes in Ni^{2+} /Ni^{3+} and Particle Surface Area in $LiNi_{0.5}Mn_{0.5-x}Co_xO_2$ (x = 0.1–0.3) Cathode Materials for Lithium-Ion Batteries. *J. Electrochem. Soc.* **2024**, *171* (5), 050522.

(36) Dixit, H.; Zhou, W.; Idrobo, J.-C.; Nanda, J.; Cooper, V. R. Facet-Dependent Disorder in Pristine High-Voltage Lithium–Manganese-Rich Cathode Material. *ACS Nano* **2014**, *8* (12), 12710–12716.

(37) Venkatraman, S.; Shin, Y.; Manthiram, A. Phase Relationships and Structural and Chemical Stabilities of Charged Li1-xCoO2-δ and Li1-xNi0.85Co0.15O2-δ Cathodes. *Electrochem. Solid-State Lett.* **2003**, *6* (1), A9–A12.

(38) Märker, K.; Reeves, P. J.; Xu, C.; Griffith, K. J.; Grey, C. P. Evolution of Structure and Lithium Dynamics in LiNi0.8Mn0.1Co0.1O2 (NMC811) Cathodes during Electrochemical Cycling. *Chem. Mater.* **2019**, *31* (7), 2545–2554.

(39) Banerjee, H.; Grey, C. P.; Morris, A. J. Stability and Redox Mechanisms of Ni-Rich NMC Cathodes: Insights from First-Principles Many-Body Calculations. *Chem. Mater.* **2024**, *36* (13), 6575–6587.

(40) Armstrong, A. R.; Bruce, P. G. Synthesis of Layered LiMnO2 as an Electrode for Rechargeable Lithium Batteries. *Nature* **1996**, *381* (6582), 499–500.

(41) Gummow, R. J.; De Kock, A.; Thackeray, M. M. Improved Capacity Retention in Rechargeable 4 V Lithium/Lithium-Manganese Oxide (Spinel) Cells. *Solid State Ionics* **1994**, *69* (1), 59–67.

(42) Thackeray, M. M. Structural Considerations of Layered and Spinel Lithiated Oxides for Lithium Ion Batteries. *J. Electrochem. Soc.* **1995**, *142* (8), 2558–2563.

(43) *Lithium Manganese Oxide - LiMn2O4- Conduction animation*. ChemTube3D. https://www.chemtube3d.com/lib_lmo-2/ (accessed 2024-07-03).

(44) Choi, W.; Manthiram, A. Comparison of Metal Ion Dissolutions from Lithium Ion Battery Cathodes. *J. Electrochem. Soc.* **2006**, *153* (9), A1760.

(45) Manthiram, A.; Muraliganth, T. Lithium Intercalation Cathode Materials for Lithium-Ion Batteries. In *Handbook of Battery Materials*; Daniel, C., Besenhard, J. O., Eds.; Wiley, 2011; pp 341–375.

(46) Masquelier, C.; Croguennec, L. Polyanionic (Phosphates, Silicates, Sulfates) Frameworks as Electrode Materials for Rechargeable Li (or Na) Batteries. *Chem. Rev.* **2013**, *113* (8), 6552–6591.

(47) Huang, H.; Yin, S.-C.; Kerr, T.; Taylor, N.; Nazar, L. F. Nanostructured Composites: A High Capacity, Fast Rate Li3V2(PO4)3/Carbon Cathode for Rechargeable Lithium Batteries. *Adv. Mater.* **2002**, *14* (21), 1525–1528.

(48) Jian, Z.; Zhao, L.; Pan, H.; Hu, Y.-S.; Li, H.; Chen, W.; Chen, L. Carbon Coated Na3V2(PO4)3 as Novel Electrode Material for Sodium Ion Batteries. *Electrochem. Commun.* **2012**, *14* (1), 86–89.

(49) *Lithium Iron Phosphate-LiFePO4 - Conduction animation*. ChemTube3D. https://www.chemtube3d.com/lib_lfp-2/ (accessed 2024-07-03).

(50) Nitta, N.; Wu, F.; Lee, J. T.; Yushin, G. Li-Ion Battery Materials: Present and Future. *Materials Today* **2015**, *18* (5), 252–264.

(51) Doughty, D.; Roth, E. P. A General Discussion of Li Ion Battery Safety. *Electrochem. Soc. Interface* **2012**.

(52) Gong, Z.; Yang, Y. Recent Advances in the Research of Polyanion-Type Cathode Materials for Li-Ion Batteries. *Energy Environ. Sci.* **2011**, *4* (9), 3223.

(53) Geller, S.; Durand, J. L. Refinement of the Structure of LiMnPO4. *Acta Crys.t* **1960**, *13* (4), 325–331.

(54) Mays, J. M. Second-Nearest-Neighbor Nuclear Magnetic Resonance Shifts in Iron Group Phosphates. *Phys. Rev.* **1957**, *108* (4), 1090–1091.

(55) Manthiram, A.; Goodenough, J. B. Lithium Insertion into Fe2(*M*O4)3 Frameworks: Comparison of *M* = W with *M* = Mo. *J. Sol. State Chem.* **1987**, *71* (2), 349–360.

(56) Manthiram, A.; Goodenough, J. B. Lithium Insertion into Fe2(SO4)3 Frameworks. *J. Power Sources* **1989**, *26* (3), 403–408.

(57) Padhi, A. K.; Nanjundaswamy, K. S.; Masquelier, C.; Goodenough, J. B. Mapping of Transition Metal Redox Energies in Phosphates with NASICON Structure by Lithium Intercalation. *J. Electrochem. Soc.* **1997**, *144* (8), 2581.

(58) Padhi, A. K.; Nanjundaswamy, K. S.; Goodenough, J. B. Phospho-olivines as Positive-Electrode Materials for Rechargeable Lithium Batteries. *J. Electrochem. Soc.* **1997**, *144* (4), 1188–1194.

(59) Muraliganth, T.; Manthiram, A. Understanding the Shifts in the Redox Potentials of Olivine LiM1–yMyPO4 (M = Fe, Mn, Co, and Mg) Solid Solution Cathodes. *J. Phys. Chem. C* **2010**, *114* (36), 15530–15540.

(60) Deb, A.; Bergmann, U.; Cramer, S. P.; Cairns, E. J. Structural Investigations of LiFePO4 Electrodes and in Situ Studies by Fe X-Ray Absorption Spectroscopy. *Electrochim. Acta* **2005**, *50* (25–26), 5200–5207.

(61) Manthiram, A.; Vadivel Murugan, A.; Sarkar, A.; Muraliganth, T. Nanostructured Electrode Materials for Electrochemical Energy Storage and Conversion. *Energy Environ. Sci.* **2008**, *1* (6), 621.

(62) Pan, X.; Zhuang, S.; Sun, Y.; Sun, G.; Ren, Y.; Jiang, S.; Zhu, B.; Li, X.; Wen, Y. Restraining Formation of Fe-Li Anti-Site Defects via in-Situ Surface Construction on Single-Crystal LiFePO4 Cathode for Extending Fast Charging Lifespan. *J. Alloy. Compd.* **2023**, *968*, 172257.

(63) Xiao, Y.; Zhao, Z.; Zhang, Q.; Qiao, R. Doping $LiFePO_4$ with Al^{3+} : Suppression of Anti-Site Defects and Implications for Battery Recycling. *ACS Omega* **2025**, *10* (1), 1293–1302.

(64) Momma, K.; Izumi, F. VESTA: A Three-Dimensional Visualization System for Electronic and Structural Analysis. *J. Appl. Cryst.* **2008**, *41* (3), 653–658.

(65) Wagemaker, M.; Ellis, B. L.; Lützenkirchen-Hecht, D.; Mulder, F. M.; Nazar, L. F. Proof of Supervalent Doping in Olivine LiFePO $_4$. *Chem. Mater.* **2008**, *20* (20), 6313–6315.

(66) Wang, Y.; Zhu, B.; Wang, Y.; Wang, F. Solvothermal Synthesis of LiFePO 4 Nanorods as High-Performance Cathode Materials for Lithium Ion Batteries. *Ceram. Int.* **2016**, *42* (8), 10297–10303.

(67) Jyoti, J.; Singh, B. P.; Tripathi, S. K. Recent Advancements in Development of Different Cathode Materials for Rechargeable Lithium Ion Batteries. *J. Energy Storage* **2021**, *43*, 103112.

(68) Qian, H.; Ren, H.; Zhang, Y.; He, X.; Li, W.; Wang, J.; Hu, J.; Yang, H.; Sari, H. M. K.; Chen, Y.; Li, X. Surface Doping vs. Bulk Doping of Cathode Materials for Lithium-Ion Batteries: A Review. *Electrochem. Energy Rev.* **2022**, *5* (4), 2.

(69) Zhang, H.; Zou, Z.; Zhang, S.; Liu, J.; Zhong, S. A Review of the Doping Modification of LiFePO4 as a Cathode Material for Lithium Ion Batteries. *Int. J. Electrochem. Sci.* **2020**, *15* (12), 12041–12067.

(70) Pignanelli, F.; Romero, M.; Mombrú, D.; Téliz, E.; Díaz, V.; Castiglioni, J.; Zinola, F.; Faccio, R.; Mombrú, Á. W. Insights of Cobalt Doping on Carbon-Coated LiFePO4 Olivine Nanoparticles Prepared by Citric Acid Combustion Route as Cathodes for Lithium Batteries. *Ionics* **2019**, *25* (8), 3593–3601.

(71) Cao Y.; Luo L.; Du K.; Peng Z.-D.; Hu G.-R.; Jiang F.; Synthesis and Electrochemical Properties of $LiFe_{1-x}Nb_xPO_4$/C Composite Cathode Material by Two-Step Synthesis Route. *Acta Physico-Chimica Sinica* **2013**, *29* (07), 1507–1514.

(72) Yamada, A.; Koizumi, H.; Sonoyama, N.; Kanno, R. Phase Change in LixFePO4. *Electrochem. Solid-State Lett.* **2005**, *8* (8), A409.

(73) Kang, B.; Ceder, G. Battery Materials for Ultrafast Charging and Discharging. *Nature* **2009**, *458* (7235), 190–193.

(74) Chung, S.-Y.; Blocking, J. T.; Andersson, A. S.; Chiang, Y.-M. Electronically Conductive Phospho-Olivines as Lithium Storage Electrodes. *Solid State Ionics: Trends in the New Millenium* **2002**, 85.

(75) Li, J.; Li, S.; Li, Q. High-Density Na-Doped LiFePO4 Synthesised by Co-Precipitation for Lithium Ion Battery. *Mater. Res. Innov.* **2015**, *19* (sup2), S2-133-S2-136.

(76) Yin, X.; Huang, K.; Liu, S.; Wang, H.; Wang, H. Preparation and Characterization of Na-Doped LiFePO4/C Composites as Cathode Materials for Lithium-Ion Batteries. *J.f Power Sources* **2010**, *195* (13), 4308–4312.

(77) Li, Y.; Wang, L.; Liang, F.; Yao, Y.; Zhang, K. Enhancing High Rate Performance and Cyclability of LiFePO4 Cathode Materials for Lithium Ion Batteries by Boron Doping. *J. Alloy. Compd.* **2021**, *880*, 160560.

(78) Kulka, A.; Baster, D.; Dudek, M.; Kiełbasa, M.; Milewska, A.; Zając, W.; Świerczek, K.; Molenda, J. Electrochemical Properties of Chemically Modified Phosphoolivines as Cathode Materials for Li-Ion Batteries. *J. Power Sources* **2013**, *244*, 565–569.

(79) Wang, D.; Li, H.; Shi, S.; Huang, X.; Chen, L. Improving the Rate Performance of LiFePO4 by Fe-Site Doping. *Electrochim. Acta* **2005**, *50* (14), 2955–2958.

(80) Zheng, S.; Wang, X.; Huang, X.; Liu, C. Hydrothermal Synthesis of Ni-Doped Carom-like LiFe0.95Ni0.05PO4 Powders. *Ceram. Int.* **2012**, *38* (5), 4391–4394.

(81) Jiang, S.; Wang, Y. Synthesis and Characterization of Vanadium-Doped LiFePO4@C Electrode with Excellent Rate Capability for Lithium-Ion Batteries. *Solid State Ionics* **2019**, *335*, 97–102.

(82) Baek, D.-H.; Kim, J.-K.; Shin, Y.-J.; Chauhan, G. S.; Ahn, J.-H.; Kim, K.-W. Effect of Firing Temperature on the Electrochemical Performance of LiMn0.4Fe0.6PO4/C Materials Prepared by Mechanical Activation. *J. Power Sources* **2009**, *189* (1), 59–65.

(83) Liu, H.; Cao, Q.; Fu, L. J.; Li, C.; Wu, Y. P.; Wu, H. Q. Doping Effects of Zinc on LiFePO4 Cathode Material for Lithium Ion Batteries. *Electrochem. Commun.* **2006**, *8* (10), 1553–1557.

(84) Zhu, M.; Cheng, L.; Liu, Y.; Li, W.; Hu, P.; Jin, H.; Hu, Y.; Li, Y. LiFePO4/(C+Cu) Composite with Excellent Cycling Stability as Lithium Ion Battery Cathodes Synthesized via a Modified Carbothermal Reduction Method. *Ceramics International* **2018**, *44* (11), 12106–12111.

(85) Gupta, R.; Saha, S.; Tomar, M.; Sachdev, V. K.; Gupta, V. Effect of Manganese Doping on Conduction in Olivine LiFePO4. *J. Mater. Sci.: Mater. Electron.* **2017**, *28* (7), 5192–5199.

(86) Ma, Z.; Fan, Y.; Shao, G.; Wang, L.; Song, J.; Wang, G.; Liu, T. Cupric Ion Substituted LiFePO4/C Composites with Enhanced Electrochemical Performance for Li-Ion Batteries. *Electrochim. Acta* **2014**, *139*, 256–263.

(87) Zhang, B.; Wang, S.; Liu, L.; Wang, J.; Liu, W.; Yang, J. Facile Synthesis of S-Doped LiFePO $_4$ @N/S-Doped Carbon Core–Shell Structured Composites for Lithium-Ion Batteries. *Nanotech.* **2022**, *33* (40), 405601.

(88) Meng, Y.; Li, Y.; Xia, J.; Hu, Q.; Ke, X.; Ren, G.; Zhu, F. F-Doped LiFePO4@N/B/F-Doped Carbon as High Performance Cathode Materials for Li-Ion Batteries. *Appl. Surf. Sci.* **2019**, *476*, 761–768.

(89) Liu, H.; Luo, S.; Yan, S.; Wang, Y.; Wang, Q.; Li, M.; Zhang, Y. A Novel and Low-Cost Iron Source for Synthesizing Cl-Doped LiFePO4/C Cathode Materials for Lithium-Ion Batteries. *J. Electroanal. Chem.* **2019**, *850*, 113434.

(90) Sun, C. S.; Zhang, Y.; Zhang, X. J.; Zhou, Z. Structural and Electrochemical Properties of Cl-Doped LiFePO4/C. *J. Power Sources* **2010**, *195* (11), 3680–3683.

(91) Jugović, D.; Mitrić, M.; Milović, M.; Cvjetićanin, N.; Jokić, B.; Umićević, A.; Uskoković, D. The Influence of Fluorine Doping on the Structural and Electrical Properties of the LiFePO4 Powder. *Ceramics International* **2017**, *43* (3), 3224–3230.

(92) Hautier, G.; Jain, A.; Ong, S. P.; Kang, B.; Moore, C.; Doe, R.; Ceder, G. Phosphates as Lithium-Ion Battery Cathodes: An Evaluation Based on High-Throughput *Ab Initio* Calculations. *Chem. Mater.* **2011**, *23* (15), 3495–3508.

(93) Örnek, A. Positive Effects of a Particular Type of Microwave-Assisted Methodology on the Electrochemical Properties of Olivine Li*M*PO4 (*M* = Fe, Co and Ni) Cathode Materials. *Chem. Eng. J.* **2018**, *331*, 501–509.

(94) Abakumov, A. M.; Fedotov, S. S.; Antipov, E. V.; Tarascon, J.-M. Solid State Chemistry for Developing Better Metal-Ion Batteries. *Nat. Commun.* **2020**, *11* (1), 4976.

(95) Ramana, C. V.; Mauger, A.; Gendron, F.; Julien, C. M.; Zaghib, K. Study of the Li-Insertion/Extraction Process in LiFePO4/FePO4. *J. Power Sources* **2009**, *187* (2), 555–564.

(96) Jiang, B.; Li, L.; Zhang, Q.; Ma, J.; Zhang, H.; Yu, K.; Bian, Z.; Zhang, X.; Ma, X.; Tang, D. Iron–Oxygen Covalency in Perovskites to Dominate Syngas Yield in Chemical Looping Partial Oxidation. *J. Mater. Chem. A* **2021**, *9* (22), 13008–13018.

(97) Padhi, A. K.; Nanjundaswamy, K. S.; Masquelier, C.; Okada, S.; Goodenough, J. B. Effect of Structure on the Fe3 + / Fe2 + Redox Couple in Iron Phosphates. *J. Electrochem. Soc.* **1997**, *144* (5), 1609–1613.

(98) Tang, P.; Holzwarth, N. A. W. Electronic Structure of FePO4, LiFePO4, and Related Materials. *Phys. Rev. B* **2003**, *68* (16), 165107.

(99) Shannon, R. D. Revised Effective Ionic Radii and Systematic Studies of Interatomic Distances in Halides and Chaleogenides. *Acta Cryst.* **1976**, *A32*, 751–767.

(100) Huynh, L. T. N.; Nguyen, H. H. A.; Tran, T. T. D.; Nguyen, T. T. T.; Nguyen, T. M. A.; La, T. H.; Tran, V. M.; Le, M. L. P. Electrode Composite LiFePO4@Carbon: Structure and Electrochemical Performances. *J. Nanomater.* **2019**, *2019* (1), 2464920.

(101) Benedek, P.; Wenzler, N.; Yarema, M.; Wood, V. C. Low Temperature Hydrothermal Synthesis of Battery Grade Lithium Iron Phosphate. *RSC Adv.* **2017**, *7* (29), 17763–17767.

(102) Martins, R.; Gonçalves, R.; Costa, C. M.; Ferdov, S.; Lanceros-Méndez, S. Mild Hydrothermal Synthesis and Crystal Morphology Control of $LiFePO_4$ by Lithium Nitrate. *Nano-Structures & Nano-Objects* **2017**, *11*, 82–87.

(103) Meligrana, G.; Gerbaldi, C.; Tuel, A.; Bodoardo, S.; Penazzi, N. Hydrothermal Synthesis of High Surface LiFePO4 Powders as Cathode for Li-Ion Cells. *J. Power Sources* **2006**, *160* (1), 516–522.

(104) Zhan, T. T.; Jiang, W. F.; Li, C.; Luo, X. D.; Lin, G.; Li, Y. W.; Xiao, S. H. High Performed Composites of LiFePO4/3DG/C Based on FePO4 by Hydrothermal Method. *Electrochim. Acta* **2017**, *246*, 322–328.

(105) Lim, J.; Kang, S.-W.; Moon, J.; Kim, S.; Park, H.; Baboo, J. P.; Kim, J. Low-Temperature Synthesis of LiFePO4 Nanocrystals by Solvothermal Route. *Nanoscale Res. Lett.* **2012**, *7* (1), 3.

(106) Lim, J.; Gim, J.; Kang, S.-W.; Baek, S.; Jeong, H.; Kim, J. Synthesis of $LiFePO_4$ Nanoparticles and Crystal Formation Mechanism during Solvothermal Reaction. *J. Electrochem. Soc.* **2012**, *159* (4), A479–A484.

(107) Johnson, I. D.; Lübke, M.; Wu, O. Y.; Makwana, N. M.; Smales, G. J.; Islam, H. U.; Dedigama, R. Y.; Gruar, R. I.; Tighe, C. J.; Scanlon, D. O.; Corà, F.; Brett, D. J. L.; Shearing, P. R.; Darr, J. A. Pilot-Scale Continuous Synthesis of a Vanadium-Doped LiFePO4/C Nanocomposite High-Rate Cathodes for Lithium-Ion Batteries. *J. Power Sources* **2016**, *302*, 410–418.

(108) *Powder Diffraction: Theory and Practice*; Dinnebier, R. E., Billinge, S. J. L., Eds.; Royal Society of Chemistry: Cambridge, 2008.

(109) Epp, J. X-Ray Diffraction (XRD) Techniques for Materials Characterization. In *Materials Characterization Using Nondestructive Evaluation (NDE) Methods*; Elsevier, 2016; pp 81–124.

(110) Yano, J.; Yachandra, V. K. X-Ray Absorption Spectroscopy. *Photosynth. Res.* **2009**, *102* (2–3), 241–254.

(111) Nilsson, A. Applications of Core Level Spectroscopy to Adsorbates. *Journal of Electron Spectroscopy and Related Phenomena* **2002**, *126* (1–3), 3–42.

(112) Bokhoven, J. A. van; Lamberti, C. *X-Ray Absorption and X-Ray Emission Spectroscopy: Theory and Applications*; John Wiley & Sons, 2016.

(113) Yoon, W.-S.; Chung, K. Y.; McBreen, J.; Zaghib, K.; Yang, X.-Q. Electronic Structure of the Electrochemically Delithiated Li1–xFePO4 Electrodes Investigated by P K-Edge X-Ray Absorption Spectroscopy. *Electrochem. Solid-State Lett.* **2006**, *9* (9), A415–A417.

(114) Franke, R.; Hormes, J. The P K-near Edge Absorption Spectra of Phosphates. *Physica B: Condensed Matter* **1995**, *216* (1–2), 85–95.

(115) *Beamline Details*. https://warwick.ac.uk/fac/cross_fac/xmas/xmasbeamline/description/ (accessed 2024-07-30).

(116) *Beamline Layout and Specifications - - Diamond Light Source*. https://www.diamond.ac.uk/Instruments/Spectroscopy/B18/Specification.html (accessed 2024-07-30).

(117) Ravel, B.; Newville, M. *ATHENA* , *ARTEMIS* , *HEPHAESTUS* : Data Analysis for X-Ray Absorption Spectroscopy Using *IFEFFIT*. *J. Synchrotron Rad.* **2005**, *12* (4), 537–541.

(118) Newville, M. Larch: An Analysis Package for XAFS and Related Spectroscopies. *J. Phys.: Conf. Ser.* **2013**, *430*, 012007.

(119) Abd Mutalib, M.; Rahman, M. A.; Othman, M. H. D.; Ismail, A. F.; Jaafar, J. Scanning Electron Microscopy (SEM) and Energy-Dispersive X-Ray (EDX) Spectroscopy. In *Membrane Characterization*; Elsevier, 2017; pp 161–179.

(120) Zhou, W.; Apkarian, R. P.; Wang, Z. L.; Joy, D. Fundamentals of Scanning Electron Microscopy (SEM). In *Scanning Microscopy for Nanotechnology*; 2007.

(121) Goldstein, J. I.; Newbury, D. E.; Echlin, P.; Joy, D. C.; Lyman, C. E.; Lifshin, E.; Sawyer, L.; Michael, J. R. Generation of X-Rays in the SEM Specimen. In *Scanning Electron Microscopy and X-ray Microanalysis*; Springer US: Boston, MA, 2003; pp 271–296.

(122) Kuzmann, E.; Nagy, S.; Vértes, A. Critical Review of Analytical Applications of Mössbauer Spectroscopy Illustrated by Mineralogical and Geological Examples: (IUPAC Technical Report).

(123) Ali, M.; Tsud, N.; Meena, S. S.; Murugavel, S. Size Dependent Electronic Structure of $LiFePO_4$ Probed Using X-Ray Absorption and Mössbauer Spectroscopy. *Phys. Chem. Chem. Phys.* **2022**, *24* (16), 9695–9706.

(124) *The Mossbauer Effect Theory*. https://faculty.knox.edu/cschulz/M%C3%B6ssbauer/theory.htm (accessed 2024-07-31).

(125) *Mössbauer Spectroscopy: Tutorial Book*; Yoshida, Y., Langouche, G., Eds.; Springer Berlin Heidelberg: Berlin, Heidelberg, 2013.

(126) Dyar, M. D.; Agresti, D. G.; Schaefer, M. W.; Grant, C. A.; Sklute, E. C. MÖSSBAUER SPECTROSCOPY OF EARTH AND PLANETARY MATERIALS. *Annu. Rev. Earth Planet. Sci.* **2006**, *34* (1), 83–125.

(127) Scrimshire, A. Investigations of Catalyst and Energy Storage Materials Using ^{57}Fe Mössbauer Spectroscopy. Doctoral Thesis, Sheffield Hallam University, 2018. https://shura.shu.ac.uk/24809/.

(128) Andersson, A. Lithium Extraction/Insertion in LiFePO4: An X-Ray Diffraction and Mössbauer Spectroscopy Study. *Solid State Ionics* **2000**, *130* (1–2), 41–52.

(129) Rancourt, D. G.; Ping, J. Y. Voigt-Based Methods for Arbitrary-Shape Static Hyperfine Parameter Distributions in Mössbauer Spectroscopy. *Nuclear Instruments and Methods in Physics Research Section B: Beam Interactions with Materials and Atoms* **1991**, *58* (1), 85–97.

(130) MIT Electric Vehicle Team,. A Guide to Understanding Battery Specifications. **2008**.

(131) Kim, T.; Choi, W.; Shin, H.-C.; Choi, J.-Y.; Kim, J. M.; Park, M.-S.; Yoon, W.-S. Applications of Voltammetry in Lithium Ion Battery Research. *J. Electrochem. Sci. Technol* **2020**, *11* (1), 14–25.

(132) Elgrishi, N.; Rountree, K. J.; McCarthy, B. D.; Rountree, E. S.; Eisenhart, T. T.; Dempsey, J. L. A Practical Beginner's Guide to Cyclic Voltammetry. *J. Chem. Educ.* **2018**, *95* (2), 197–206.

(133) Savéant, J.-M. Single Electron Transfer at an Electrode. In *Elements of Molecular and Biomolecular Electrochemistry*; Wiley, 2006; pp 1–77.

(134) Brownson, D. A. C.; Kampouris, D. K.; Banks, C. E. Graphene Electrochemistry: Fundamental Concepts through to Prominent Applications. *Chem. Soc. Rev.* **2012**, *41* (21), 6944.

(135) Wang, S.; Zhang, J.; Gharbi, O.; Vivier, V.; Gao, M.; Orazem, M. E. Electrochemical Impedance Spectroscopy. *Na.t Rev. Methods Primers* **2021**, *1* (1), 41.

(136) Lazanas, A. Ch.; Prodromidis, M. I. Electrochemical Impedance Spectroscopy—A Tutorial. *ACS Meas. Sci. Au* **2023**, *3* (3), 162–193.

(137) *Nyquist Plot for Impedance Measurement of Lithium-ion Batteries | Hioki*. https://www.hioki.com/euro-en/learning/electricity/nyquist.html (accessed 2024-07-31).

(138) Abbate, M.; Lala, S. M.; Montoro, L. A.; Rosolen, J. M. Ti-, Al-, and Cu-Doping Induced Gap States in $LiFePO_4$. *Electrochem. Solid-State Lett.* **2005**, 8, A288.

(139) Zhao, H.; Xia, J.; Yin, D.; Luo, M.; Yan, C.; Du, Y. Rare Earth Incorporated Electrode Materials for Advanced Energy Storage. *Coord. Chem. Rev.* **2019**, *390*, 32–49.

(140) Altin, S.; Yolun, A. Fabrication and Electrochemical Performance of Ho-Substituted C/LiFePO4: Improved Battery Performance. *J. Mater. Sci.: Mater. Electron.* **2021**, *32* (16), 21568–21578.

(141) Toby, B. H.; Von Dreele, R. B. *GSAS-II* : The Genesis of a Modern Open-Source All Purpose Crystallography Software Package. *J. Appl. Crystallogr.* **2013**, *46* (2), 544–549.

(142) Ridley, M.; McFarland, B.; Miller, C.; Opila, E. YbPO4: A Novel Environmental Barrier Coating Candidate with Superior Thermochemical Stability. *Materialia* **2022**, *21*, 101289.

(143) Zou, G.; Chen, K.; Luo, X.; Fu, Q.; Wu, B. Crystal Structure, Morphology, and Electrical Properties of Aluminum-Doped LFP Materials. *Ionics* **2024**, *30* (5), 2549–2563.

(144) Graetsch, H. Two Forms of Aluminium Phosphate Tridymite from X-Ray Powder Data. *Acta Cryst. C* **2000**, *56* (4), 401–403.

(145) Xie, H.; Zhou, Z. Physical and Electrochemical Properties of Mix-Doped Lithium Iron Phosphate as Cathode Material for Lithium Ion Battery. *Electrochim. Acta* **2006**, *51* (10), 2063–2067.

(146) Milligan, W. O.; Mullica, D. F.; Beall, G. W.; Boatner, L. A. Structural Investigations of YPO4, ScPO4, and LuPO4. *Inorganica Chim. Acta* **1982**, *60*, 39–43.

(147) Arouca Maia, B.; Magalhães, N.; Cunha, E.; Correia, N.; Braga, M. H.; Santos, R. M. A Comprehensive Study of LFP-Based Positive Electrodes: Process Parameters' Influence on the Electrochemical Properties. *Batteries* **2025**, *11* (3), 93.

(148) Johnson, I. D. Continuous Hydrothermal Synthesis of Nanomaterials for Rechargeable Battery Applications, University College London, London, **2017**.

(149) Wang, Z.; Sun, S.; Xia, D.; Chu, W.; Zhang, S.; Wu, Z. Investigation of Electronic Conductivity and Occupancy Sites of Mo Doped into $LiFePO_4$ by Ab Initio Calculation and X-Ray Absorption Spectroscopy. *J. Phys. Chem. C* **2008**, *112* (44), 17450–17455.

(150) Li, D.; Huang, Y.; Sharma, N.; Chen, Z.; Jia, D.; Guo, Z. Enhanced Electrochemical Properties of LiFePO4 by Mo-Substitution and Graphitic Carbon-Coating via a Facile and Fast Microwave-Assisted Solid-State Reaction. *Phys. Chem. Chem. Phys.* **2012**, *14* (10), 3634.

(151) Gouveia, D. X.; Lemos, V.; De Paiva, J. A. C.; Souza Filho, A. G.; Mendes Filho, J.; Lala, S. M.; Montoro, L. A.; Rosolen, J. M. Spectroscopic Studies of Li x Fe P O 4 and Li x M 0.03 Fe 0.97 P O 4 (M = Cr , Cu , Al , Ti). *Phys. Rev. B* **2005**, *72* (2), 024105.

(152) Chen, M.; Shao, L.-L.; Yang, H.-B.; Ren, T.-Z.; Du, G.; Yuan, Z.-Y. Vanadium-Doping of LiFePO4/Carbon Composite Cathode Materials Synthesized with Organophosphorus Source. *Electrochim. Acta* **2015**, *167*, 278–286.

(153) Chiang, C.-Y.; Su, H.-C.; Wu, P.-J.; Liu, H.-J.; Hu, C.-W.; Sharma, N.; Peterson, V. K.; Hsieh, H.-W.; Lin, Y.-F.; Chou, W.-C.; Lee, C.-H.; Lee, J.-F.; Shew, B.-Y. Vanadium Substitution of $LiFePO_4$ Cathode Materials To Enhance the Capacity of $LiFePO_4$ -Based Lithium-Ion Batteries. *J. Phys. Chem. C* **2012**, *116* (46), 24424–24429.

(154) Harrison, K. L.; Bridges, C. A.; Paranthaman, M. P.; Segre, C. U.; Katsoudas, J.; Maroni, V. A.; Idrobo, J. C.; Goodenough, J. B.; Manthiram, A. Temperature Dependence of Aliovalent-Vanadium Doping in $LiFePO_4$ Cathodes. *Chem. Mater.* **2013**, *25* (5), 768–781.

(155) Hong, J.; Wang, C. S.; Chen, X.; Upreti, S.; Whittingham, M. S. Vanadium Modified LiFePO4 Cathode for Li-Ion Batteries. *Electrochem. Solid-State Lett.* **2008**, *12* (2), A33.

(156) Hu, C.-W.; Chen, T.-Y.; Shih, K.-S.; Wu, P.-J.; Su, H.-C.; Chiang, C.-Y.; Huang, A.-F.; Hsieh, H.-W.; Chang, C.-C.; Shew, B.-Y.; Lee, C.-H. Real-Time Investigation on the Influences of Vanadium Additives to the Structural and Chemical State Evolutions of LiFePO 4 for Enhancing the Electrochemical Performance of Lithium-Ion Battery. *J. Power Sources* **2014**, *270*, 449–456.

(157) Moretti, A.; Giuli, G.; Nobili, F.; Trapananti, A.; Aquilanti, G.; Tossici, R.; Marassi, R. Structural and Electrochemical Characterization of Vanadium-Doped LiFePO $_4$ Cathodes for Lithium-Ion Batteries. *J. Electrochem. Soc.* **2013**, *160* (6), A940–A949.

(158) Omenya, F.; Chernova, N. A.; Upreti, S.; Zavalij, P. Y.; Nam, K.-W.; Yang, X.-Q.; Whittingham, M. S. Can Vanadium Be Substituted into LiFePO $_4$? *Chem. Mater.* **2011**, *23* (21), 4733–4740.

(159) Zhang, L.-L.; Liang, G.; Ignatov, A.; Croft, M. C.; Xiong, X.-Q.; Hung, I.-M.; Huang, Y.-H.; Hu, X.-L.; Zhang, W.-X.; Peng, Y.-L. Effect of Vanadium Incorporation on Electrochemical Performance of LiFePO $_4$ for Lithium-Ion Batteries. *J. Phys. Chem. C* **2011**, *115* (27), 13520–13527.

(160) Zhao, T.; Xu, W.; Ye, Q.; Cheng, J.; Zhao, H.; Wu, Z.; Xia, D.; Chu, W. Local Structure of Vanadium in Doped LiFePO $_4$. *J. Synchrotron Rad.* **2010**, *17* (5), 584–589.

(161) Hua, N.; Wang, C.; Kang, X.; Wumair, T.; Han, Y. Studies of V Doping for the LiFePO4-Based Li Ion Batteries. *J. Alloy. Compd.* **2010**, *503* (1), 204–208.

(162) Wen, Y.; Zeng, L.; Tong, Z.; Nong, L.; Wei, W. Structure and Properties of LiFe0.9V0.1PO4. *J. Alloy. Compd.* **2006**, *416* (1–2), 206–208.

(163) Liu, H.; Li, C.; Cao, Q.; Wu, Y. P.; Holze, R. Effects of Heteroatoms on Doped LiFePO4/C Composites. *J. Solid State Electrochem.* **2008**, *12* (7–8), 1017–1020.

(164) *Lifepo4 Lithium Iron Phosphate LFP Powder*. https://www.libgroup.net/blog-detail-02.html (accessed 2025-05-07).

(165) Uebou, Y.; Okada, S.; Egashira, M.; Yamaki, J.-I. Cathode Properties of Pyrophosphates for Rechargeable Lithium Batteries. *Solid State Ionics* **2002**, *148* (3–4), 323–328.

(166) Göktepe, H. Effect of Dy $^{3+}$ -Doping on Electrochemical Properties of LiFePO $_4$ /C Cathode for Lithium-Ion Batteries. *J. Chin. Chem. Soc.* **2013**, *60* (2), 218–222.

(167) Göktepe, H. Effect of Dy $^{3+}$ -Doping on Electrochemical Properties of LiFePO $_4$ /C Cathode for Lithium-Ion Batteries. *J. Chin. Chem. Soc.* **2013**, *60* (2), 218–222.

(168) Maier, J. Ionic Conduction in Space Charge Regions. *Prog. Solid State Chem.* **1995**, *23* (3), 171–263.

(169) Canepa, P.; Schofield, E.; Chadwick, A. V.; Alfredsson, M. Comparison of a Calculated and Measured XANES Spectrum of α-Fe2O3. *Phys. Chem. Chem. Phys.* **2011**, *13*, 12826–12834.

(170) Okude, N.; Nagoshi, M.; Noro, H.; Baba, Y.; Yamamoto, H.; Sasaki, T. A. P and S K-Edge XANES of Transition-Metal Phosphates and Sulfates. *J. Electron Spectrosc. Rel. Phenom.* **1999**, *101–103*, 607–610.

(171) Henao, J.; Martinez-Gomez, L. Review: On Rare-Earth Perovskite-Type Negative Electrodes in Nickel–Hydride (Ni/H) Secondary Batteries. *Mater. Renew Sustain. Energy* **2017**, *6* (2), 7.

(172) Chen, K.; Xue, D. Rare Earth and Transitional Metal Colloidal Supercapacitors. *Sci. China Technol. Sci.* **2015**, *58* (11), 1768–1778.

(173) Zhao, M. S.; Zhang, L. Rare Earth Element Aliovalent Doping Substitution and Electrochemical Performance of $LiFe_{1-x}Nd_xPO_4$. *MSF* **2010**, *654–656*, 2883–2886.

(174) Yan, C.; Yang, X.; Zhao, H.; Zhong, H.; Ma, G.; Qi, Y.; Koel, B. E.; Ju, Y. Controlled Dy-Doping to Nickel-Rich Cathode Materials in High Temperature Aerosol Synthesis. *Proc. Combust. Instit.* **2021**, *38* (4), 6623–6630.

(175) Zhang, B.; Xu, Y.; Wang, J.; Lin, J.; Wang, C.; Chen, Y. Lanthanum and Cerium Co-Doped LiFePO4: Morphology, Electrochemical Performance and Kinetic Study from −30 - +50 °C. *Electrochim. Acta* **2019**, *322*, 134686.

(176) Zhao, N.; Li, Y.; Zhi, X.; Wang, L.; Zhao, X.; Wang, Y.; Liang, G. Effect of Ce3+ Doping on the Properties of LiFePO4 Cathode Material. *J. Rare Earths* **2016**, *34* (2), 174–180.

(177) Wang, L.; Jiao, C.; Liang, G.; Zhao, N.; Wang, Y.; Li, L. Effect of Rare Earth Ions Doping on Properties of LiFePO4/C Cathode Material. *J. Rare Earths* **2014**, *32* (9), 895–899.

(178) Luo, S.; Tian, Y.; Li, H.; Shi, K.; Tang, Z.; Zhang, Z. Influence of Lanthanum Doping on Performance of LiFePO4 Cathode Materials for Lithium-Ion Batteries. *J. Rare Earths* **2010**, *28* (3), 439–442.

(179) Göktepe, H. Electrochemical Performance of Yb-Doped LiFePO4/C Composites as Cathode Materials for Lithium-Ion Batteries. *Res. Chem. Intermed.* **2013**, *39* (7), 2979–2987.

(180) Boutahar, A.; Moubah, R.; Hlil, E. K.; Lassri, H.; Lorenzo, E. Large Reversible Magnetocaloric Effect in Antiferromagnetic Ho2O3 Powders. *Sci. Rep.* **2017**, *7* (1), 13904.

(181) Moon, J.; Nilsson, M. Coordination Chemistry of Lanthanides in a AOT–CMPO Solvent Extraction System: UV-Vis and XAFS Studies. *Dalton Trans.* **2018**, *47* (43), 15424–15438.

(182) Röhler, J. Chapter 71: X-Ray Absorption and Emission Spectra. In *Handbook on the Physics and Chemistry of Rare Earths*; Elsevier, 1987; Vol. 10, pp 453–545.

(183) Hannoyer, B.; Prince, A. A. M.; Jean, M.; Liu, R. S.; Wang, G. X. Mössbauer Study on LiFePO4 Cathode Material for Lithium Ion Batteries. *Hyperfine Interact.* **2006**, *167* (1–3), 767–772.

(184) Prince, A. A. M.; Mylswamy, S.; Chan, T. S.; Liu, R. S.; Hannoyer, B.; Jean, M.; Shen, C. H.; Huang, S. M.; Lee, J. F.; Wang, G. X. Investigation of Fe Valence in LiFePO4 by Mössbauer and XANES Spectroscopic Techniques. *Solid State Commun.* **2004**, *132* (7), 455–458.

(185) *Materials Project*. Materials Project. https://next-gen.materialsproject.org/materials/mp-812 (accessed 2025-10-13).

(186) Bezerra, C. A. G.; Davoglio, R. A.; Biaggio, S. R.; Bocchi, N.; Rocha-Filho, R. C. High-Purity LiFePO4 Prepared by a Rapid One-Step Microwave-Assisted Hydrothermal Synthesis. *J. Mater. Sci.* **2021**, *56*, 10018–10029.

(187) Streltsov, V. A.; Belokoneva, E. L.; Tsirelson, V. G.; Hansen, N. K. Multipole Analysis of the Electron Density in Triphylite, LiFePO4, Using X-Ray Diffraction Data. *Acta Cryst. B* **1993**, *49* (2), 147–153.

APPENDIX 1

Additional Data Obtained from XRD, SEM, and XAS

More detailed estimated strain for all samples measured and the particle size estimated for each measured plane, along with the corresponding peak positions can be found in **Table A-1.1**.

Table A-1.1: List of arbitrary % strain and particle size corresponding to specific <h k l> planes and the angles used to calculate these properties.

Sample	<*h k l*>	Peak position (°2θ)	% lattice strain (estimate)	Estimated particle size (Å)
Gelon LFP	0 2 0	29.86	0.193	696
	1 1 0	24.18	0.240	688
	1 1 1	25.70	0.263	591
	0 0 2	17.30	0.282	817
Undoped LFP	0 2 0	29.95	0.321	418
	1 1 0	24.25	0.319	516
	1 1 1	25.80	0.337	460
	0 0 2	17.39	0.897	255
1% Ho-LFP	0 2 0	29.95	0.351	380
	1 1 0	24.25	0.318	516
	1 1 1	25.80	0.410	377
	0 0 2	17.40	0.779	292
1% Yb-LFP	0 2 0	29.95	0.322	418
	1 1 0	24.27	0.321	516
	1 1 1	25.76	0.339	460
	0 0 2	17.35	0.508	454
20% V-LFP	0 2 0	29.88	0.257	522
	1 1 0	24.16	0.201	826
	1 1 1	25.69	0.264	591
	0 0 2	17.30	0.339	680

Sample	<*h k l*>	Peak position (°2θ)	% lattice strain (estimate)	Estimated particle size (Å)
1% Al-LFP	0 2 0	29.79	0.290	464
	1 1 0	24.11	0.321	516
	1 1 1	25.64	0.302	518
	0 0 2	17.23	0.397	583
3% Al-LFP	0 2 0	29.79	0.323	418
	1 1 0	24.11	0.402	413
	1 1 1	25.64	0.415	376
	0 0 2	17.22	0.792	292
5% Al-LFP	0 2 0	29.82	0.290	464
	1 1 0	24.15	0.482	344
	1 1 1	25.66	0.301	518
	0 0 2	17.26	0.565	408
1% Sc-LFP	0 2 0	29.96	0.321	418
	1 1 0	24.27	0.319	516
	1 1 1	25.79	0.450	345
	0 0 2	17.40	0.673	340
3% Sc-LFP	0 2 0	29.81	0.322	418
	1 1 0	24.12	0.361	459
	1 1 1	25.66	0.377	414
	0 0 2	17.25	0.791	292
5% Sc-LFP	0 2 0	29.94	0.321	418
	1 1 0	24.20	0.640	258
	1 1 1	25.76	0.487	329
	0 0 2	17.45	0.674	340

The Rietveld refinement outputs for all samples carried out with GSAS-II software[141] are shown in **Figures A-1.1 – A1.10** where 'obs' denotes the recorded XRD pattern and 'LFP' refers to the CIF file used in the refinement (ICSD-92198).[128]

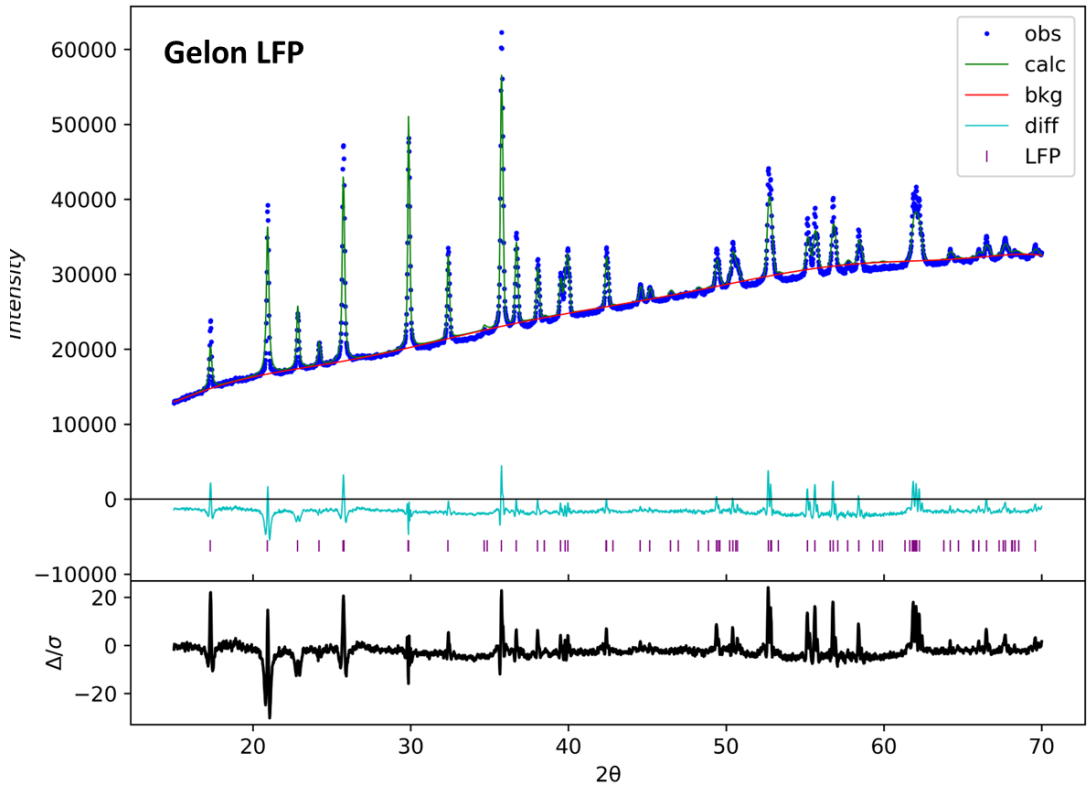

Figure A-1.1: Rietveld refinement of Gelon LFP against LFP ICSD-92198 CIF file using GSAS-II.

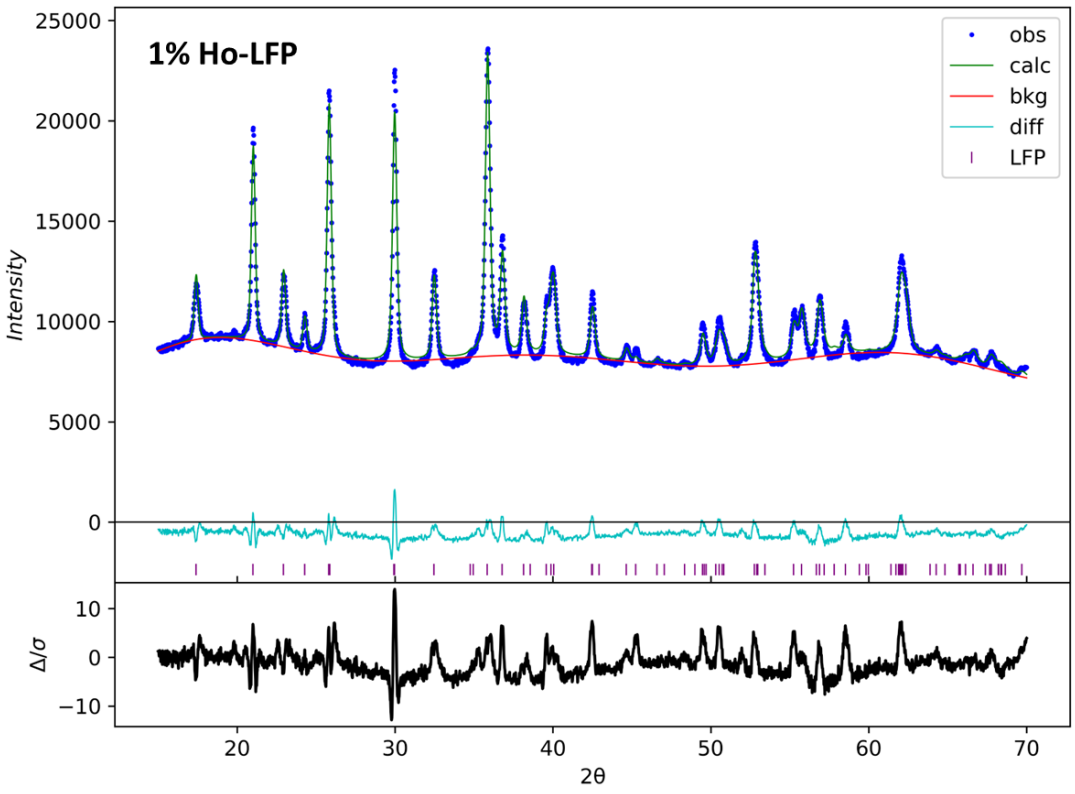

Figure A-1.2: Rietveld refinement of 1% Ho-LFP against LFP ICSD-92198 CIF file using GSAS-II.

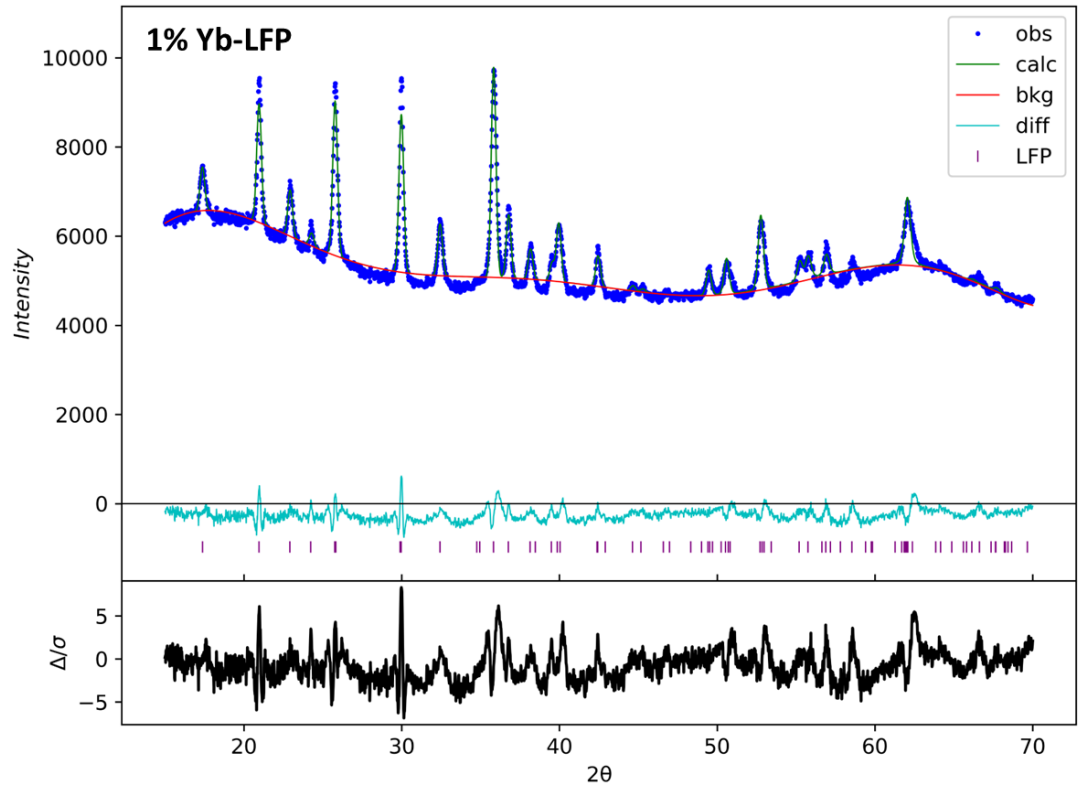

Figure A-1.3: Rietveld refinement of 1% Yb-LFP against LFP ICSD-92198 CIF file using GSAS-II.

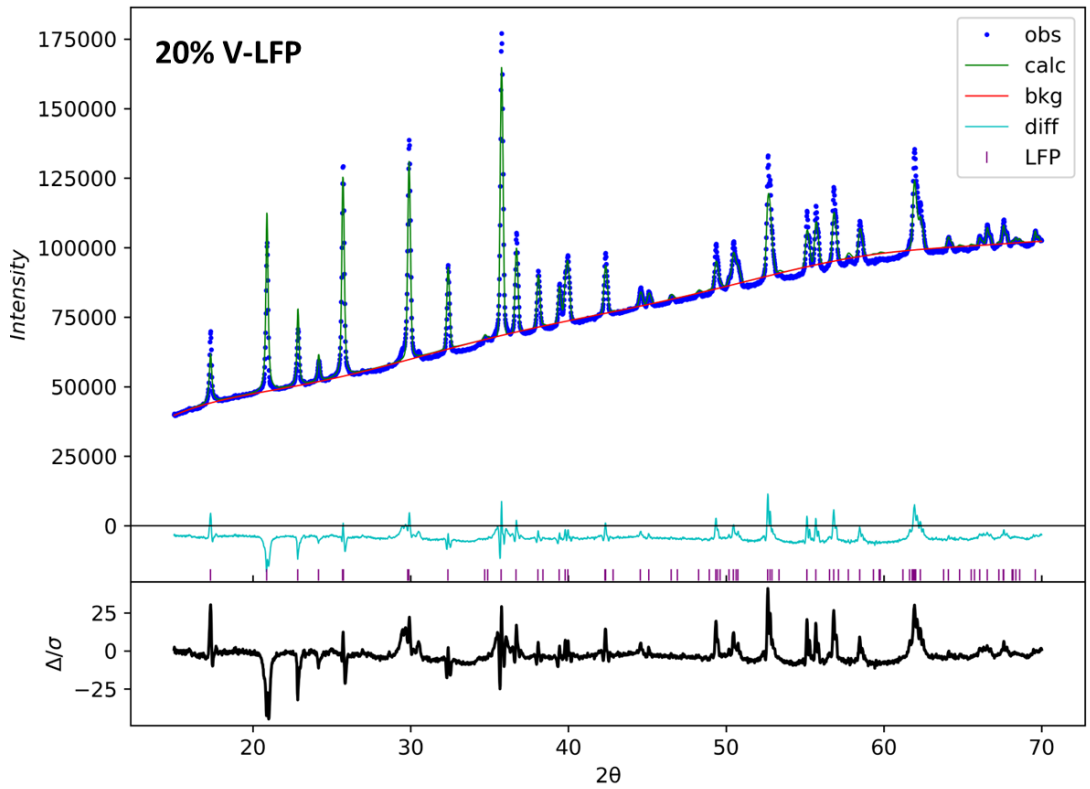

Figure A-1.4: Rietveld refinement of 20% V-LFP against LFP ICSD-92198 CIF file using GSAS-II.

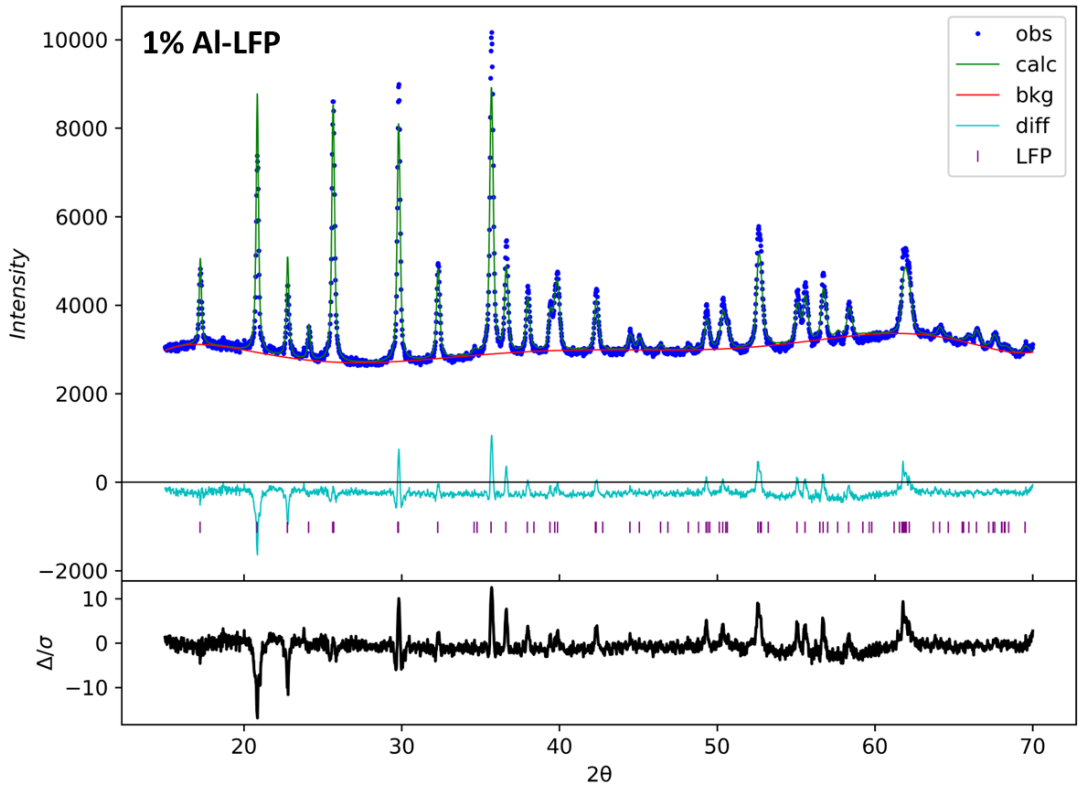

Figure A-1.5: Rietveld refinement of 1% Al-LFP against LFP ICSD-92198 CIF file using GSAS-II.

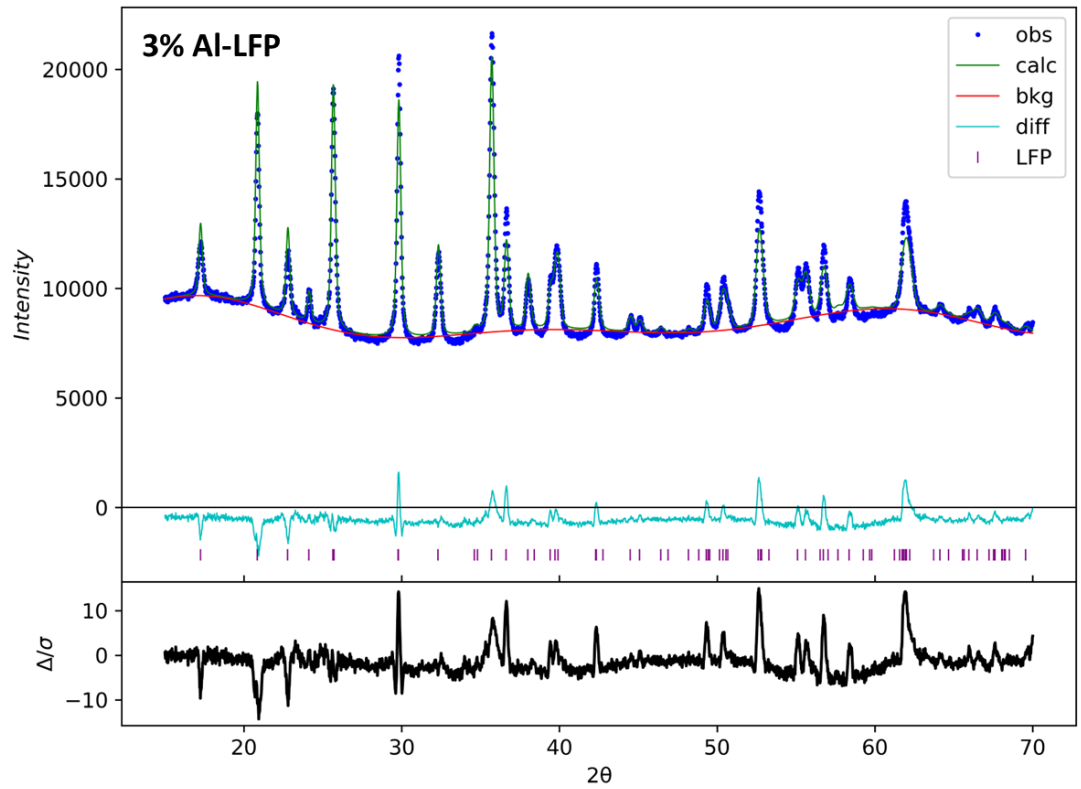

Figure A-1.6: Rietveld refinement of 3% Al-LFP against LFP ICSD-92198 CIF file using GSAS-II.

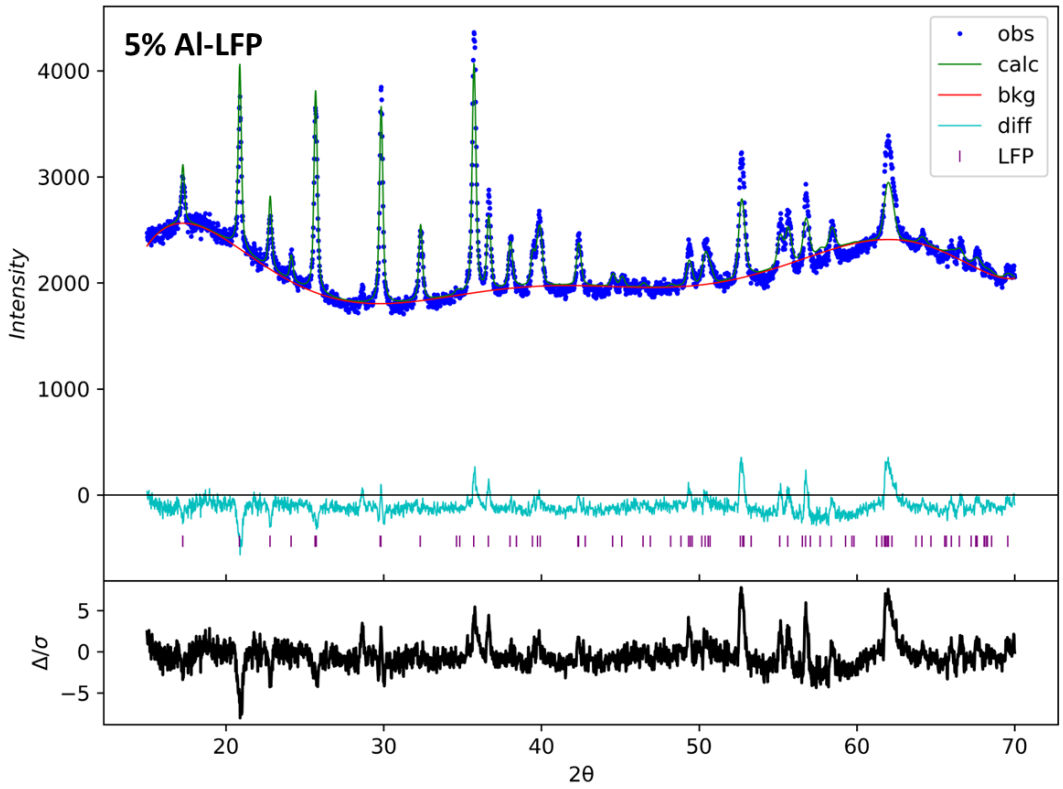

Figure A-1.7: Rietveld refinement of 5% Al-LFP against LFP ICSD-92198 CIF file using GSAS-II.

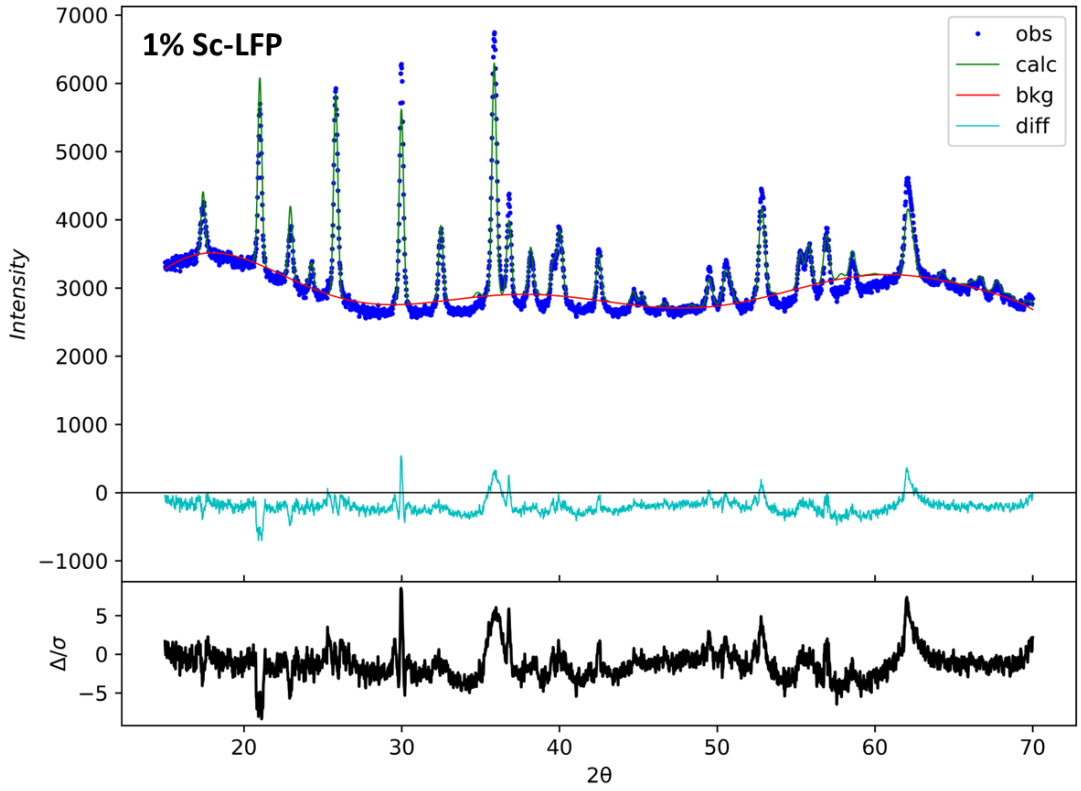

Figure A-1.8: Rietveld refinement of 1% Sc-LFP against LFP ICSD-92198 CIF file using GSAS-II.

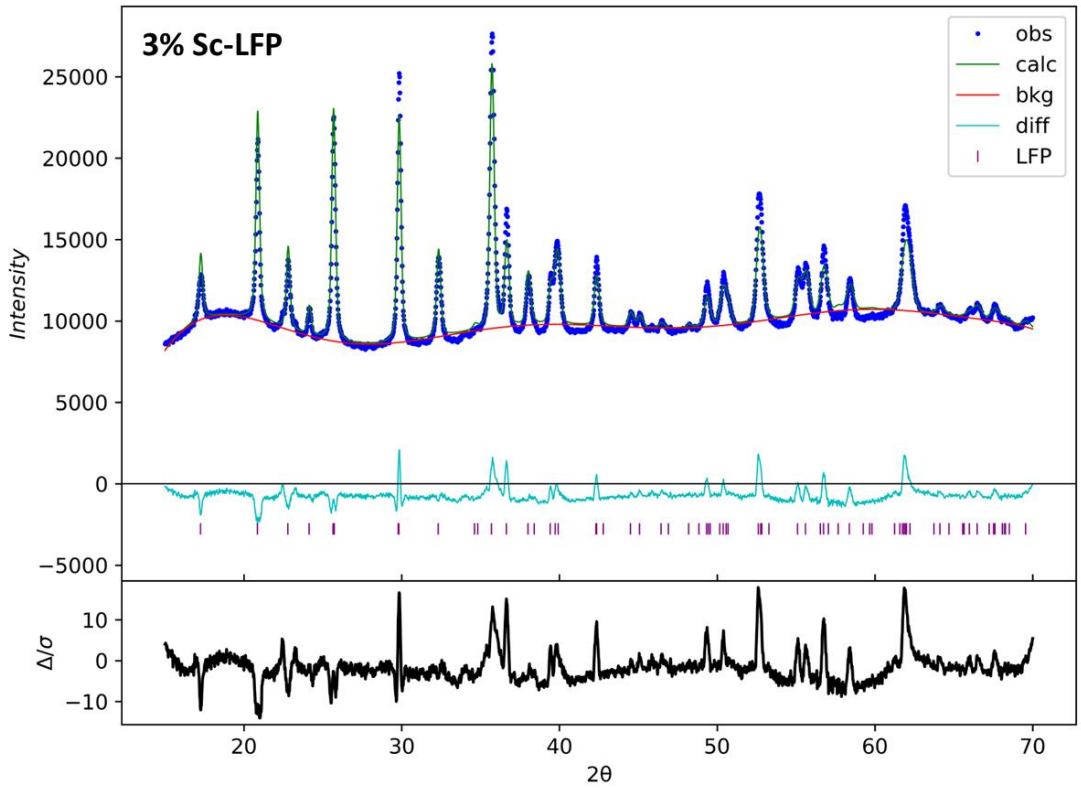

Figure A-1.9: Rietveld refinement of 3% Sc-LFP against LFP ICSD-92198 CIF file using GSAS-II.

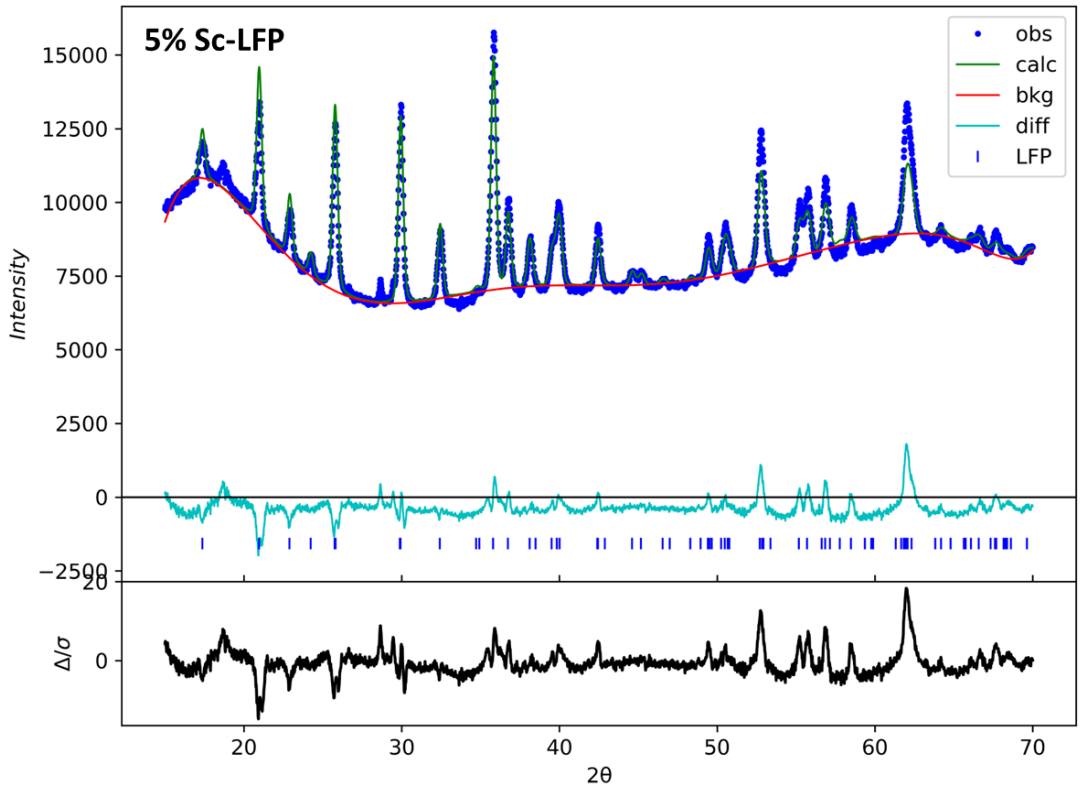

Figure A-1.10: Rietveld refinement of 5% Sc-LFP against LFP ICSD-92198 CIF file using GSAS-II.

The SEM images of each sample are presented in **Figures A-1.11 – A-1.13**. The selected grains were used for EDX mapping, which is presented in the main body of this thesis.

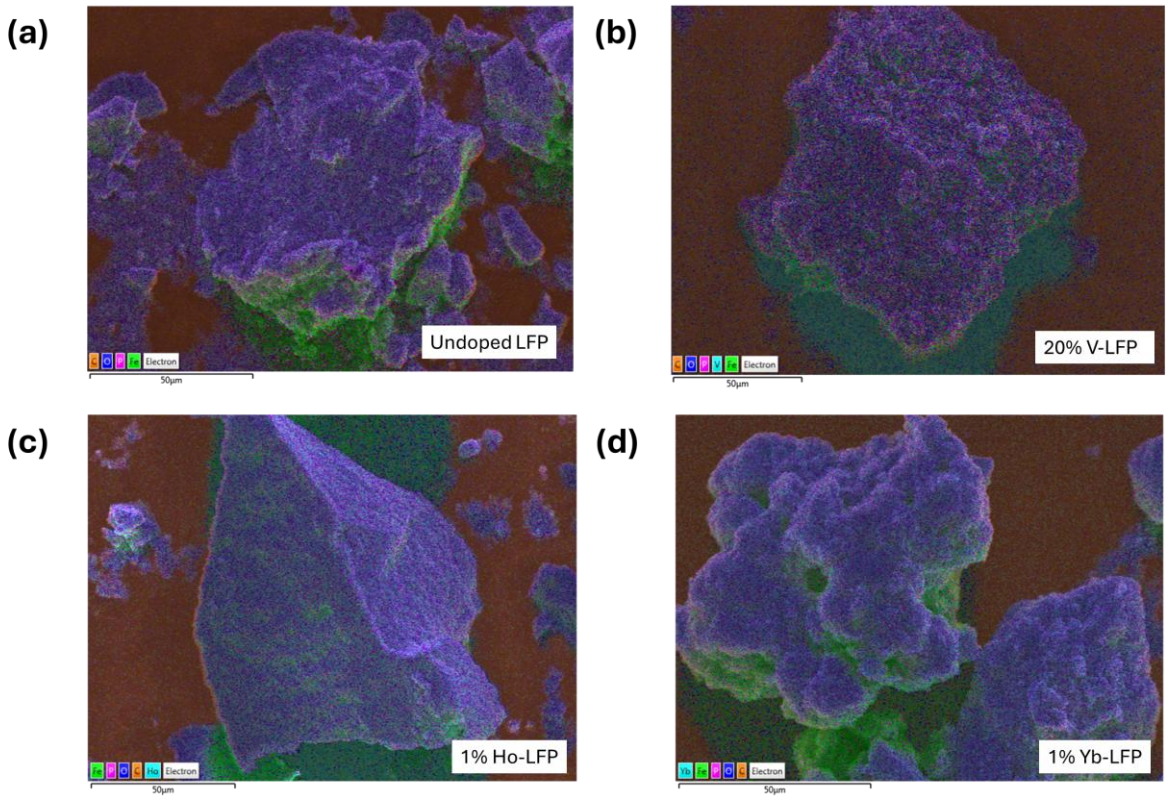

Figure A-1.11: SEM images of grains of (a) Undoped LFP, (b) 20% V-LFP, (c) 1% Ho-LFP, and (d) 1% Yb-LFP.

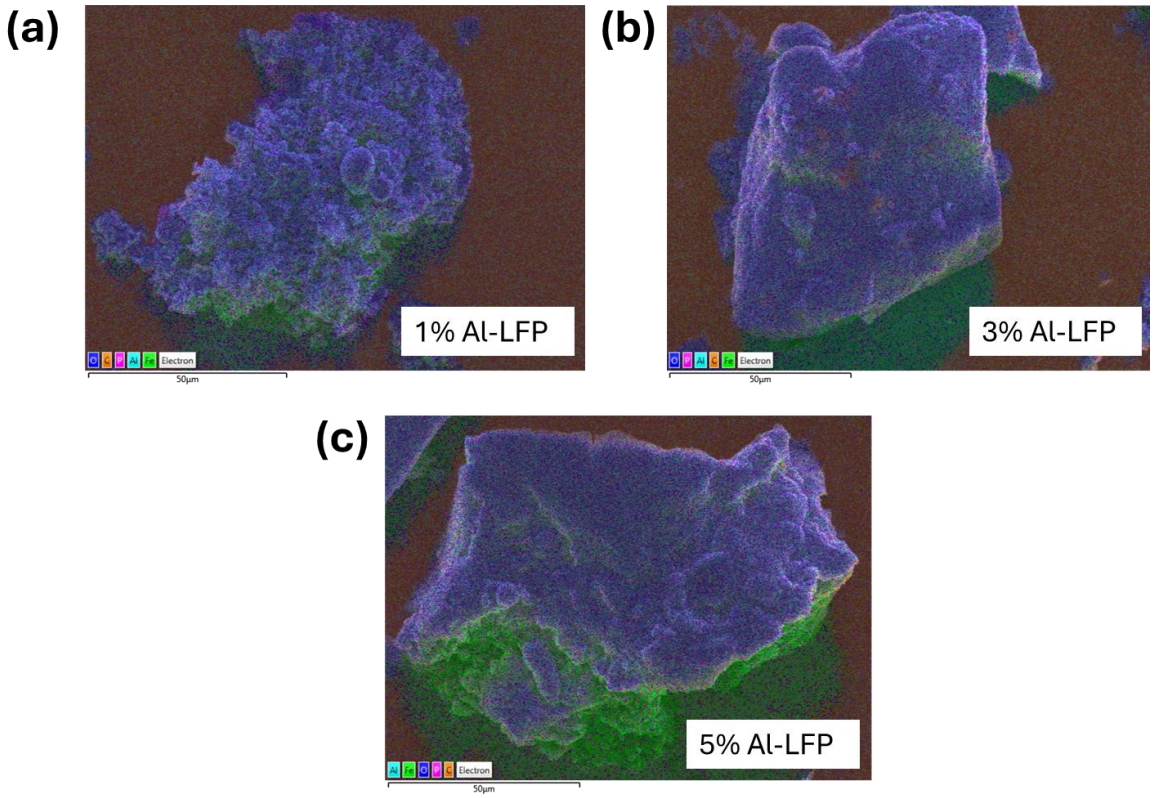

Figure A-1.12: SEM images of grains of (a) 1% Al-LFP, (b) 3% Al-LFP, and (c) 5% Al-LFP.

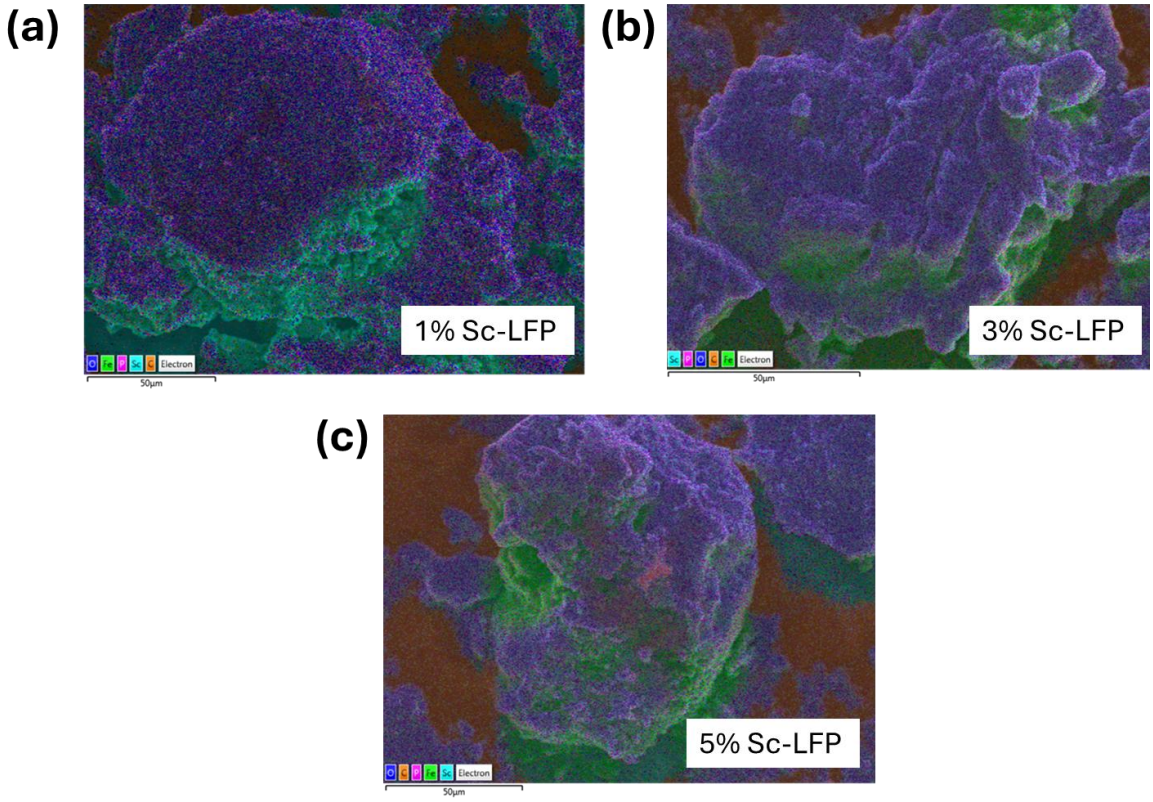

Figure A-1.13: SEM images of grains of (a) 1% Sc-LFP, (b) 3% Sc-LFP, and (c) 5% Sc-LFP.

The setup and sample holder for XAS measurements at BM28 is presented in **Figure A-1.14** where the detector proximity for data collection can also be seen.

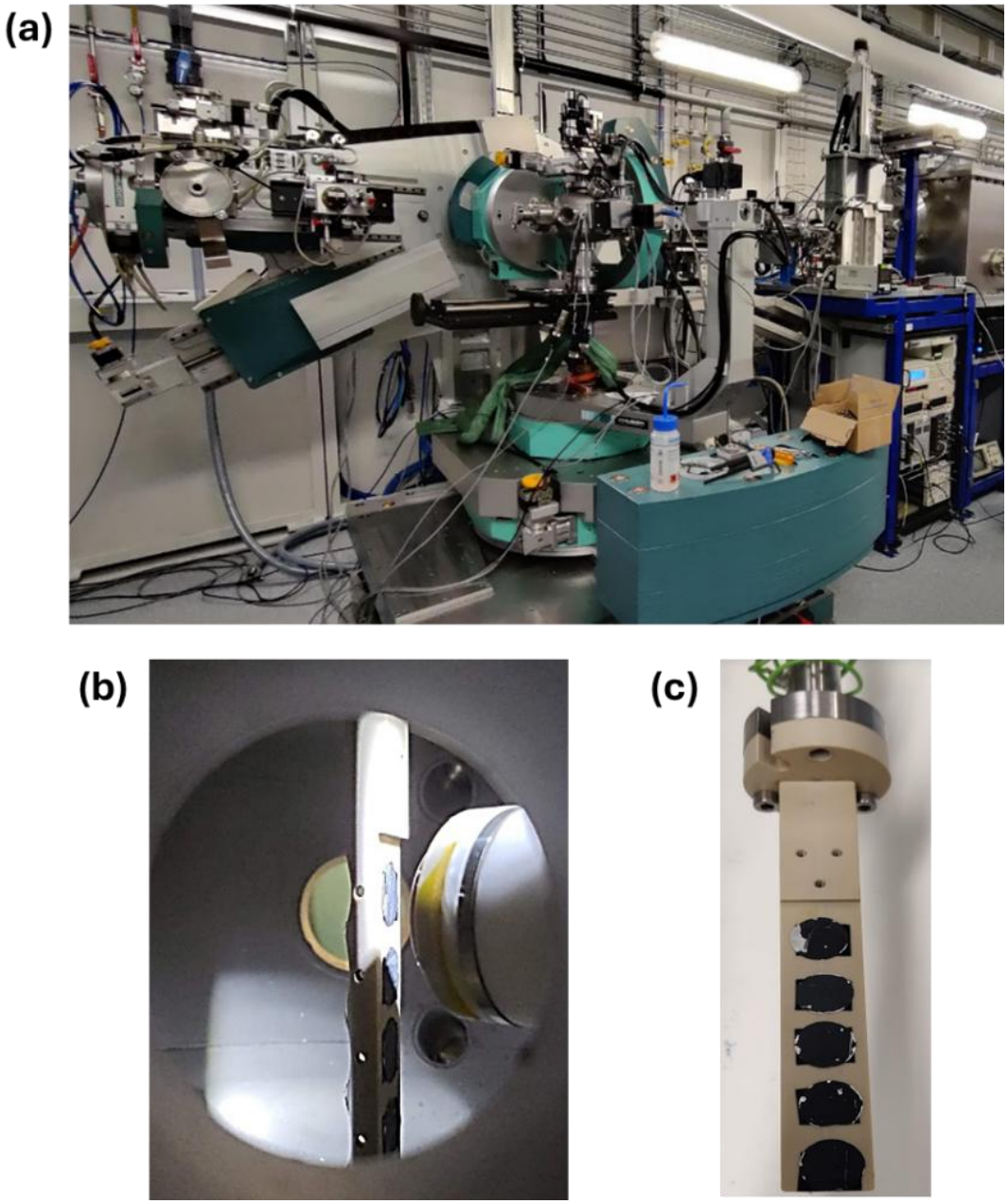

Figure A-1.14: (a) Setup of BM28 at XMaS at the ESRF XAS; (b) Detector measuring XAS on ex situ cathodes under vacuum; (c) Ex situ cathodes as placed on sample holder.

A correlation between Fe–O bond distance, Debye-Waller factor, and SOC is plotted in **Figure A-1.15** for the Ho-LFP samples measured.

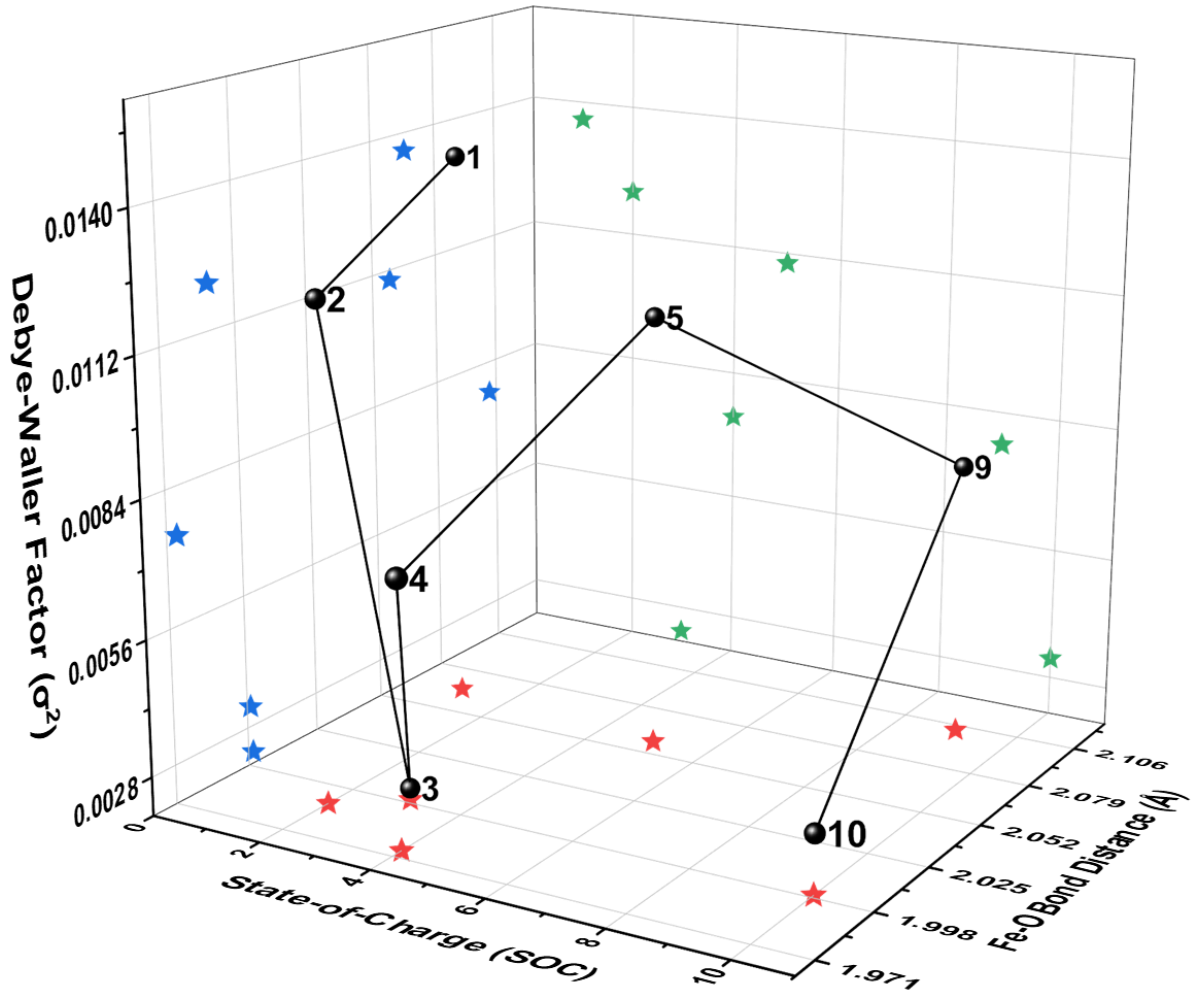

Figure A-1.15: Graph of Debye-Waller factor vs SOC vs Fe-O bond distance for all Ho-LFP samples. The balls represent each sample, whilst the different coloured stars represent the correlation between each set of axes.

Detailed Ho-O bond lengths and Debye-Waller factors for all measured SOCs of Ho-LFP obtained from Ho L_{III}-Edge EXAFS using Artemis software[117] are listed in **Table A-1.2**.

Table A-1.2: Ho-O bond lengths obtained from the radial distribution function by fitting the Ho L_{III}-edge EXAFS.

Sample	Ho-O (Å)	Debye-Waller factor (σ^2)
Ho-LFP OCV	2.295	0.00002
Ho-LFP SOC2	2.266	0.00198
Ho-LFP SOC3	2.266	0.00091
Ho-LFP SOC4	2.272	0.00028
Ho-LFP SOC5	2.285	0.00089
Ho-LFP SOC9	2.291	0.00001
Ho-LFP SOC10	2.257	0.00065

Detailed V-O bond lengths and Debye-Waller factors for all measured SOCs of V-LFP obtained from V K-Edge EXAFS using Artemis software[117] are listed in **Table A-1.3**.

Table A-1.3: V-O bond lengths obtained from the radial distribution function by fitting the V K-edge EXAFS.

Sample	V-O (Å)	Debye-Waller factor (σ^2)
V-LFP OCV	2.007	0.00149
V-LFP SOC2	2.008	0.00001
V-LFP SOC3	1.990	0.00021
V-LFP SOC4	2.008	0.00093
V-LFP SOC5	2.016	0.00001
V-LFP SOC9	2.027	0.00006
V-LFP SOC10	1.996	0.00004

From the first derivative plots of the P K-edge for all samples at different SOCs (**Figure A-1.16**), it is clear that there is a trend observed which further supports the E_o shift seen in the XANES spectra. The same shift is observed, accompanied by a

change in the shape of the crest from a doublet in the discharged SOCs to a singlet in the charged SOCs.

The shift from double peak to single peak is clearly noted in the transitory SOCs, where SOCs 2 and 4 present with a shoulder peak as the shift from lower to higher energies occurs. This complements the XANES portion of the spectra since these intermediary SOCs fall in between the discharged and charged SOCs well, indicating that there is a mix of Fe^{2+} and Fe^{3+} as the lithium is de/intercalated within the LFP crystal lattice.

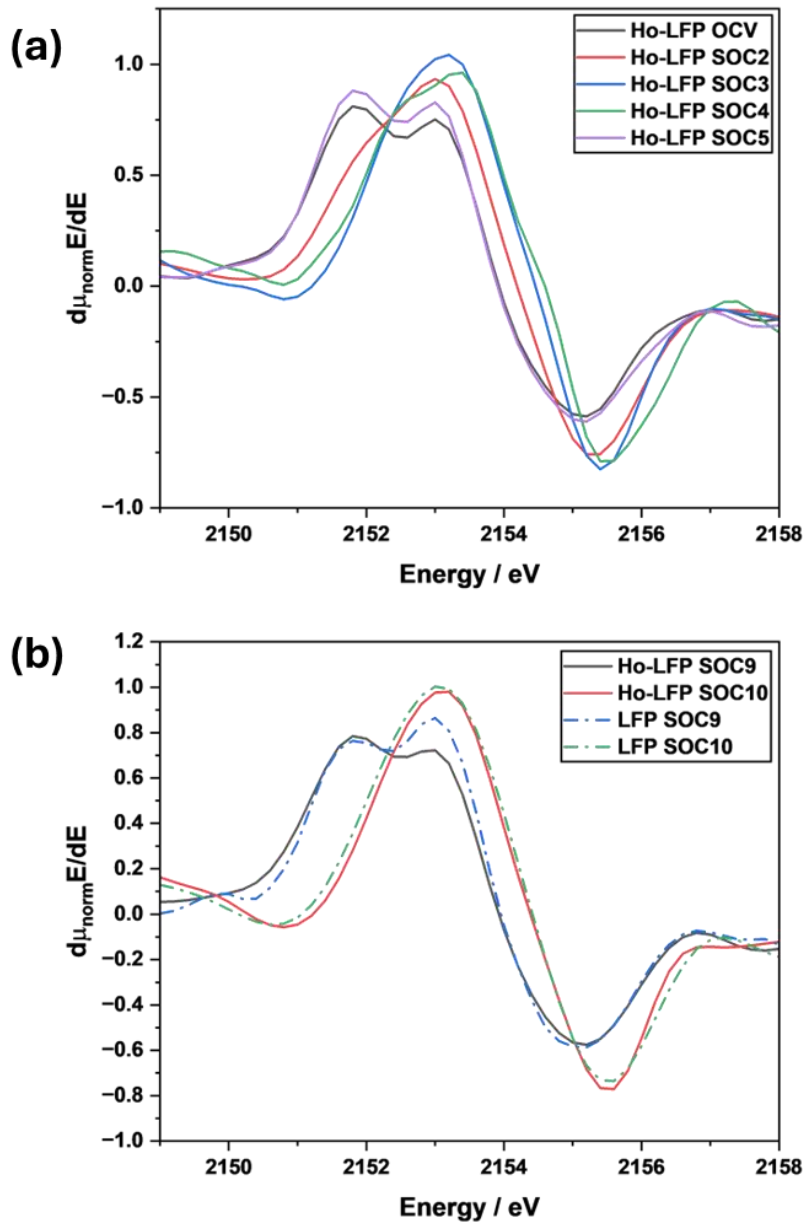

Figure A-1.16: First derivative plots of the P K-edge XANES of (a) Ho-LFP during the first charge-discharge cycle; (b) Ho-LFP and LFP during the fifth charge-discharge cycle.

APPENDIX 2

Microwave-Assisted Synthesis of LFP

An alternate synthesis of LFP was attempted in the earlier stages of this PhD, where a microwave reactor was implemented in the procedure. The methodology was adapted from the work by Bezerra *et al.*[186] whereby a one-pot synthesis containing all reagents is employed then placed in the microwave reactor at a set temperature for an amount of time.

Lithium acetate ($CH_3CO_2Li{\cdot}2H_2O$, Sigma-Aldrich), 85% phosphoric acid (H_3PO_4, ThermoFisher Scientific), and iron(II) sulphate ($FeSO_4{\cdot}7H_2O$, Sigma-Aldrich) were used as the starting materials in a stoichiometric ratio of 2.5 : 1 :1, with deionised water as the solvent. The lithium acetate was first dissolved in room temperature deionised water with stirring under N_2 atmosphere, then the phosphoric acid was added dropwise until a white precipitate of lithium phosphate (Li_3PO_4) formed. Iron(II) sulphate was then added and the reaction was stirred until a green suspension form. This was introduced into a borosilicate reaction vessel and heated in a microwave reactor at 200 °C for varying times. The resulting product was then washed several times with deionised water and dried in a vacuum oven overnight for analysis.

A study was carried out where different reaction times were implemented in the microwave reactor from 5 minutes until 30 minutes in increments of 5 minutes, correspondingly labelled A through F (**Figure A-2.1**), with A being the shortest irradiation time and F being the longest.

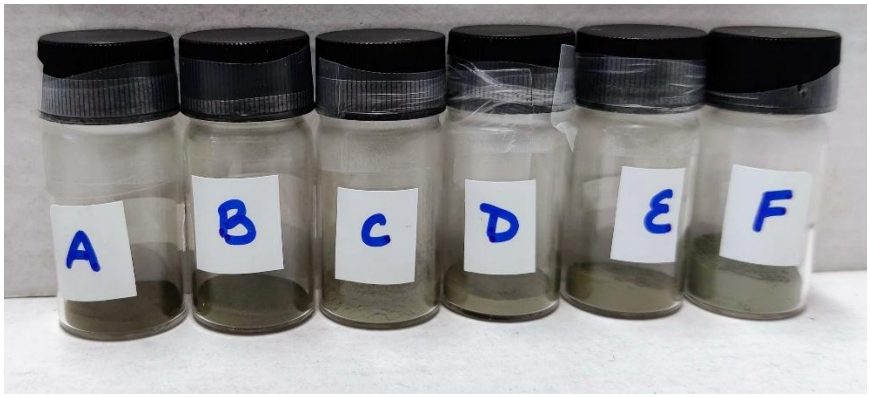

Figure A-2.1: Samples A – F after being dried in a vacuum oven overnight.

XRD was performed to assess the sample purity (**Figure A-2.3)**, and SEM-EDX was carried out to gain an insight on sample morphology (**Figure A-2.4**). There were noticeable differences in particle morphology as a function of irradiation time. The trend identified that particle size decreased with increasing irradiation. Another notable feature was the stacking growth of platelets, which was less observed in the more irradiated samples. The growth of individual particles may be limited due to the shorter irradiation times, thus resulting in grouped particle growth and stacking of particle layers, which is less observed in the more irradiated particles.

When carbon-coated and implemented as a cathode *vs* Li/Li^+ anode with 1M $LiPF_6$ in 1:1 v/v EC : DMC electrolyte, the outcome was poorly with discharge capacities ranging from 2 – 16 mAh g^{-1} and showing no clear charge/discharge plateaus regardless of irradiation time, reagents, or solvents used (**Figure A-2.2**). It was due to this that efforts were directed towards the hydrothermal synthesis route and focusing on cation doping through this method.

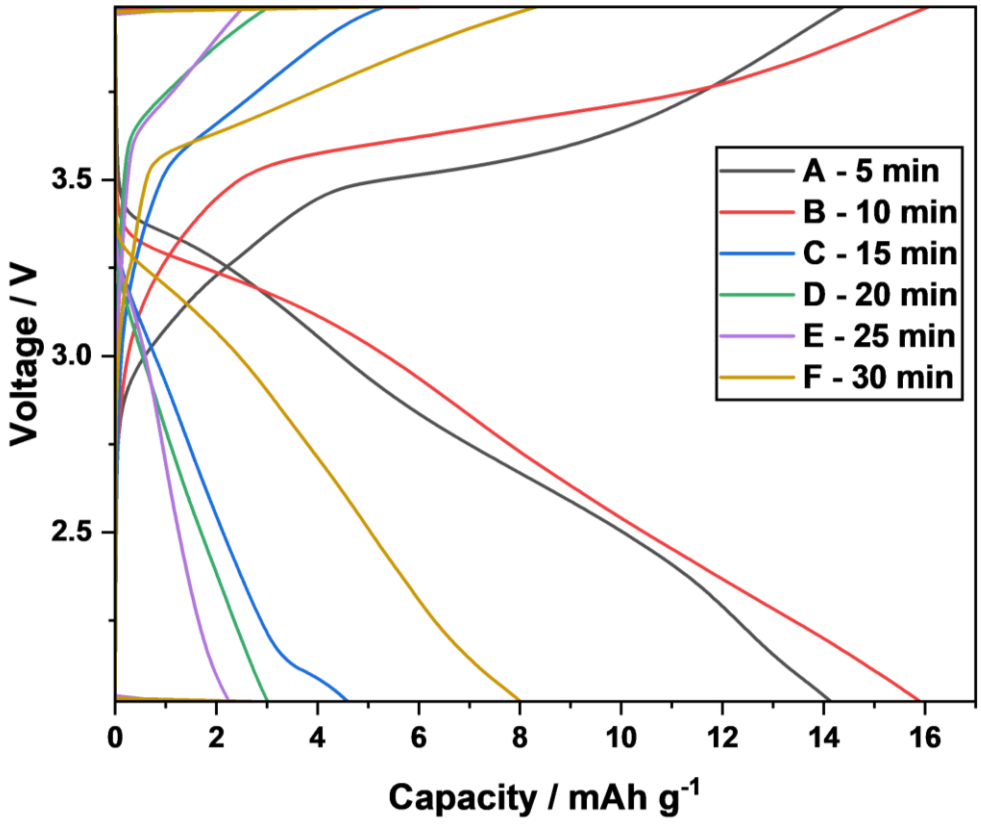

Figure A-2.2: Galvanostatic cycling curves implementing samples A – F as cathodes vs. Li/Li⁺ anode.

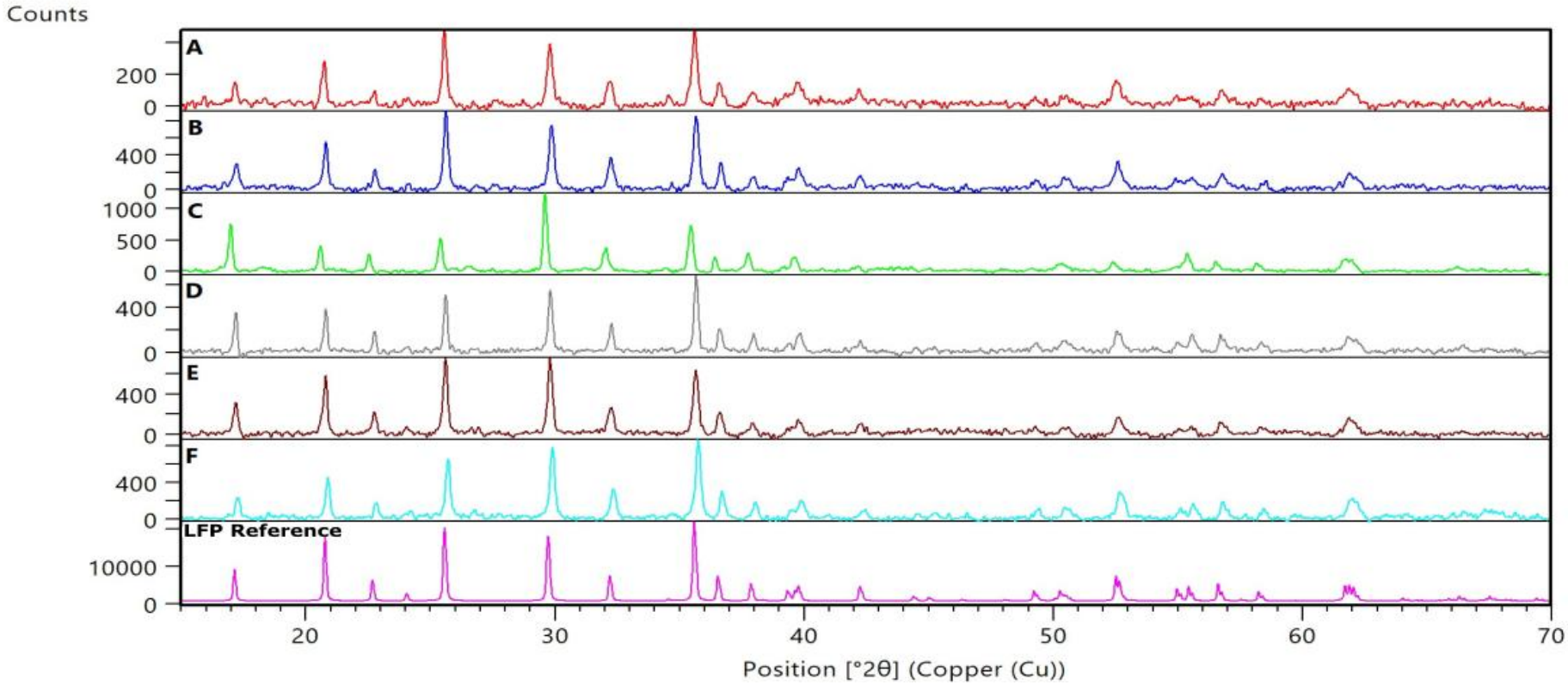

Figure A-2.3: XRD patterns for samples A – F compared with the reference LFP pattern.[187]

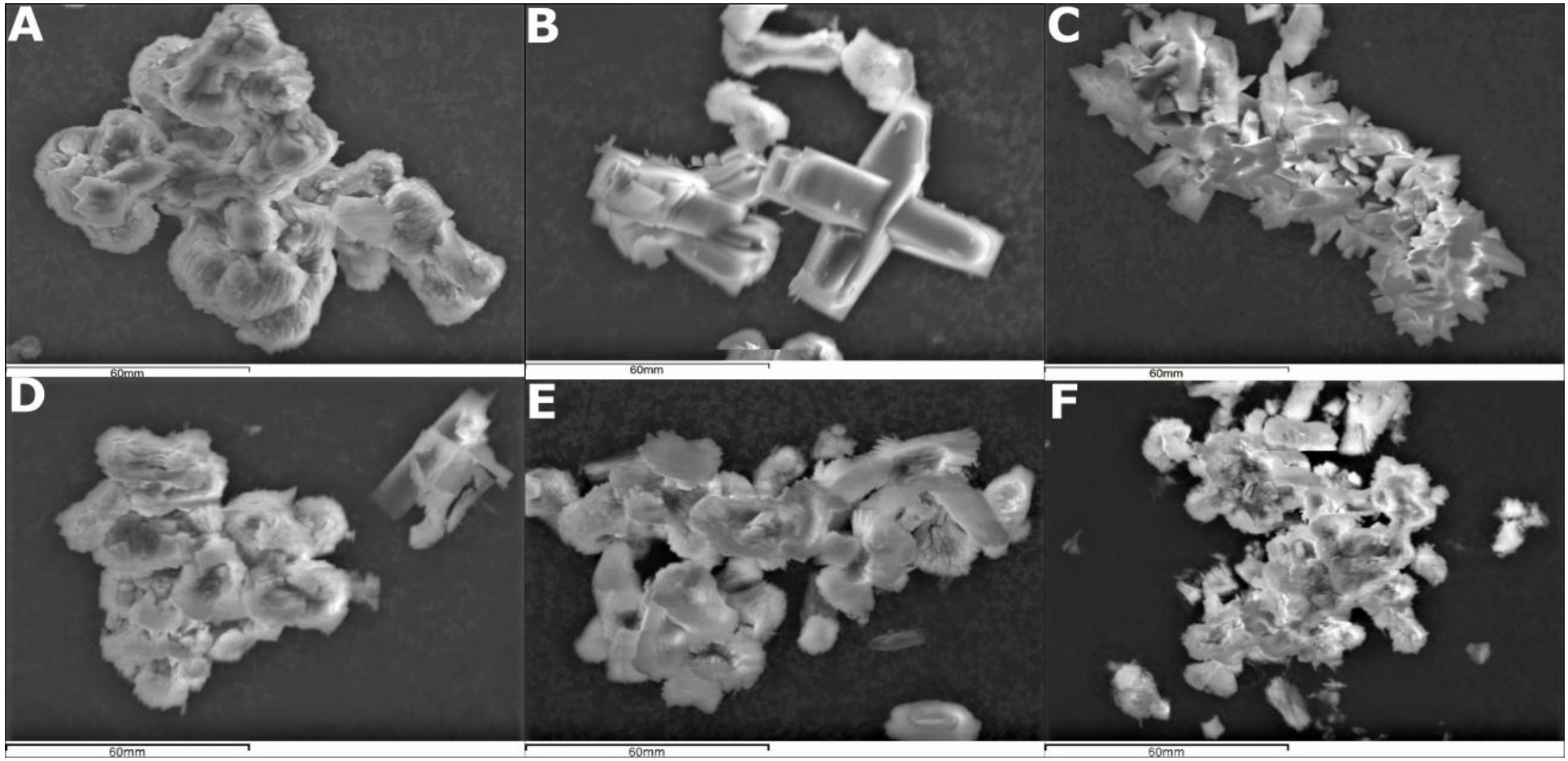

Figure A-2.4: SEM-EDX imaging of samples A – F.

